Development of tuberculosis imaging probes based on sugars and proteins



Raja Muhammad Naseer Khan

Pembroke College

University of Oxford

A thesis submitted for the degree of *Doctor of Philosophy*

Hilary 2020

Contents

Author Declaration VII

Abstract VIII

Acknowledgements IX

List of Common Abbreviations XI

1 Chapter 1: Introduction 1

1.1 Need for Imaging of Tuberculosis 1

1.2 Current TB Diagnosis 5

1.3 Overview of Molecular Imaging Modalities 6

1.3.1 Pros and Cons of Molecular Imaging Modalities 7

1.4 PET/CT Imaging Modality 8

1.5 Radiolabelling Approaches with Fluorine-18 (^{18}F) 10

1.6 Radiolabelled Macromolecules in TB Imaging 12

1.7 [^{18}F] FDG PET/CT Imaging in TB Diagnosis 13

1.7.1 Limitation of [^{18}F] FDG PET/CT in TB Diagnosis and Monitoring the Response to Treatment 15

1.8 Trehalose based Bacteria Specific Imaging Probes 17

1.8.1 Trehalose 17

1.8.2 Trehalose Analogues as Potential TB imaging probes 19

1.9 Trehalose Biosynthesis in Nature 22

1.9.1 Approaches to trehalose analogue synthesis 23

1.9.1.1 Chemical synthesis of trehalose analogues 23

1.9.1.2 Chemo-enzymatic synthesis of Trehalose analogues 25

1.10 Conclusions and Aims of this Thesis 27

1.11 Overview of the thesis 28

1.12 References 30

2 Chapter 2: Enzymatic Transformation of 2-[^{18}F]Fluoro-2-deoxy-D-glucose ([^{18}F]FDG) to 2-deoxy-2-[^{18}F]Fluoro-trehalose ([^{18}F]FDT) for PET Imaging of Tuberculosis 46

2.1 Introduction 46

2.2 Results and Discussion 50

2.2.1 Enzyme Expression, Purification and Characterisation and initial enzymatic activity assessment 50

2.2.2 Enzyme Kinetic Parameters 64

2.2.3 Enzyme Reaction optimization, Scale-up, Purification and Characterization 69

2.2.4 Characterisation and quality control of FDT batch 77

2.2.5 Synthesis and quality control of [^{18}F] FDT 83

2.2.5.1 Optimisation of Radiosynthesis for Animal Studies 86

2.2.5.2 Automated Radiosynthesis 87

2.2.5.3 Specific Activity Calculation 92

2.3 Conclusions 93

2.4 Experimental Procedures 95

2.4.1 General Biology Experimental Procedures 95

2.4.2 Preparation of Lysogeny Broth Agar Plates 95

2.4.3 Transformation 96

2.4.4 DNA Preparation 96

2.4.5 SDS-PAGE 96

2.4.6 Western-Blot 97

2.4.7 Protein Mass Spectrometry 97

2.4.8 Circular Dichroism (CD) Spectroscopy 99

2.4.9 Liquid Chromatography-mass spectrometry for Small Molecule Analysis 99

2.4.10 High Performance Liquid Chromatography (HPLC) for Enzyme Reaction Analysis 100

2.4.11 Expression, Purification and Characterisation of TreT *P. horikoshii* Enzyme 101

2.4.12 Expression, Purification and Characterisation of TreT *T. tenax* Enzyme 102

2.4.13 Expression and Purification of OtsAB Fusion from Crocosphaera watsonii ..103
2.4.14 Plasmid Design and Trial Expression of OtsAB Fusion Enzyme.....104
2.4.14.1 Western Blotting of OtsAB Fusion Protein Samples.....105
2.4.15 Large Scale Expression of OtsAB Fusion Protein.....106
2.4.15.1 Determination of Protein Concentration.....106
2.4.15.2 Enzymatic Reaction of OtsAB fusion Protein.....107
2.4.16 Detection of Trehalose by LC-MS for TreT and OtsAB Fusion enzyme.....107
2.4.17 Reaction Comparison between TreT homologues.....108
2.4.18 Reversible Reaction with TreT *P. horikoshii* 109
2.4.19 Enzyme Scale-up in Sf9 cell expression.....109
2.4.19.1 Experimental procedures to make P1 baculovirus for OtsA and OtsB.....111
2.4.19.2 Expression and Purification of C-terminally tagged, recombinant OtsA.....112
2.4.19.3 Expression and purification of recombinant OtsB 113
2.4.19.4 Small sale synthesis of [^{19}F]FDT from Hexokinase, OtsA and OtsB 114
2.4.20 General Chemistry Experimental Procedures.....114
2.4.21 Radio-HPLC Method.....115
2.4.22 Radio-TLC Method.....116
2.4.23 Luna-NH_2 Purification Method.....116
2.4.24 OtsA Enzyme kinetic assay 117
2.4.25 TreT *P. horikoshii* Enzyme Kinetic Assay 117
2.4.26 TreT *T. tenax* Enzyme Kinetic Assay.....118
2.4.27 OtsAB Enzyme Kinetic Assay.....119
2.4.28 OtsB Enzyme Kinetics.....119
2.4.29 Chemoenzymatic Reaction Optimisation and Scale-up.....120
2.4.30 Chemoenzymatic Synthesis of FDT 121
2.4.31 Purification and Characterisation of FDT.....122
2.4.32 Stability Testing of FDT Solution in HEPES Buffer.....122
2.4.33 Stability Testing of FDT Solid.....123

2.4.34 Endotoxicity Testing of FDT Solution 123
2.4.35 Determination of Purity by ^{1}H NMR 123
2.4.36 ^{23}Na-NMR Quantification 124
2.4.37 TreT *P. horikoshii* Screening Experiment 124
2.4.38 Reaction with TreT *T. tenax* enzyme 125
2.4.39 3-Enzyme-3-step one pot hot synthesis 125
2.4.40 2-Steps-2-enzyme one pot hot synthesis 126
2.4.41 Automation of [^{18}F]FDT Synthesis 127
2.4.42 Chemoenzymatic synthesis of [^{18}F]FDT for the animal studies 127
2.4.43 Specific Activity Analysis of [^{18}F]FDT 128
References 129
2.5 Supplementary Figures 134
3 Chapter 3: Pre-clinical Studies Using [^{19}/^{18}F]FDT 169
3.1 Introduction 169
3.2 Results and Discussions 171
3.2.1 LC-MS Method Development for [^{19}F]FDT Detection 171
3.2.2 Sample Preparation 174
3.2.3 *In vitro* and *In vivo* detection of [^{19}F]FDT 175
3.2.4 *In vivo* labelling of TMM in *M. tuberculosis* infected tissue 177
3.2.5 Characterization of FDT uptake timing, reproducibility, and association with bacterial numbers 179
3.2.6 FDT uptake in M. tuberculosis-infected marmosets and cynomolgus macaques 181
3.2.7 Biodistribution and toxicity assessment of FDT 185
3.2.8 Toxicity Studies 187
3.3 Conclusions 187
3.4 Experimental 188

3.4.1 Animals and ethics assurance 188
3.4.2 In vitro detection of [^{19}F]FDT 189
3.4.3 In vivo detection of [^{19}F] FDT 189
3.4.4 PET/CT instrumentation, probe administration, and image acquisition 189
3.4.5 Uptake / Time course analysis PET/CT data analysis 190
3.4.6 Biodistribution in Rhesus and Marmosets 191
3.4.7 Metabolism analysis and Detection of labeled mono and dimycolates 192
3.4.8 Toxicity studies 192
3.5 References 195
3.6 Supplementary Figures 200
4 Chapter 4: Copper-64 Labelled Monocyte Chemoattractant Protein-1 (MCP-1) as an Imaging Agent 203
4.1 Introduction 203
4.2 CCL2 Radiolabelling Methods 205
4.3 Results and Discussions 209
4.3.1 Synthesis of Aha 209
4.3.2 Aha incorporation into MCP-1, Purification and Characterisation 210
4.3.3 CuAAC and SPAAC Reactions with Aha0Aha64 212
4.3.4 CuAAC and SPAAC Reactions with Aha 64 215
4.3.5 Sequential Labelling of Aha0Aha64 217
4.3.6 Labelling of Copper-Chelator with CCL2-Aha 218
4.3.7 Chemical Synthesis and Labelling of CCL2-Aha64 with DFO-C6-DBCO 221
4.3.8 CCR2 Binding Studies on Selected Aha Modifications 223
4.3.9 Biophysical Characterisation of Aha modified MCP-1 225
4.4 Conclusions 227
4.5 Experimental 228

4.5.1 General 228
4.5.2 In-solution Digestion for proteomics 229
4.5.3 Zip Tip Protocol for sample clean up 230
4.5.4 LC-MS/MS Data Acquisition on Orbitrap Elite 231
4.5.5 LC-MS/MS data analysis 231
4.5.6 β-arrestin recruitment 232
4.5.7 Expression, Purification and characterisation of CCL2-WT 233
4.5.8 Incorporation of L-Azidohomoalanine into CCL2 WT 235
4.5.9 Enzymatic cleavage of N-terminal Aha 239
4.6 Protein Modification using CCL2-Aha0Aha64 241
4.6.1 CCL2-Aha0Aha64 through SPACC chemistry 241
4.6.2 CCL2-Aha0Aha64 through CuAAC Chemistry 244
4.6.3 CCL2-Aha64 labelling through SPAAC Chemistry 246
4.6.4 CCL2-Aha64 Reaction with alkyne PEG4-biotin 248
4.6.5 Sequential Selective labelling of CCL2-Aha with two biotin tags 250
4.6.6 Site-selective labelling of CCL2-Aha with Cu chelator CB-TE1A1P 252
4.6.7 CCL2-Aha64 Labelling with DFO-C6-DBCO 255
4.7 Chemical Synthesis of Azidohomoalanine (Aha)[29] 257
4.7.1 (S)-2-(N-tert-butoxycarbonyl)-3-azidopropanoic acid allyl ester (Boc-Dab-OH) 257
4.7.2 Synthesis of Boc-Aha 257
4.7.3 Synthesis of Aha 258
4.7.4 Chemical Synthesis of DFO-C6-DBCO[38] 259
4.8 References 264

Author Declaration

The work presented in this Thesis was conducted at the Chemical Research Laboratory under the supervision of Professor Benjamin G. Davis. All the work is my own, except where otherwise stated, and has not been submitted for any other degree at this or any other university.

In Chapter 2, the radio synthesis of 2-[^{18}F] -fluoro-2-deoxy-d-trehalose was carried out at the National Institute of Health (NIH) in collaboration with Dr Clifton Barry's lab. Radiosynthesis for animal imaging was carried out by members of Barry's group (Dr Yong-Mo Ahn and Dr Wendy Marriner) and automation was also carried out by Dr Falguni Bhattacharyya at the NIH. For the Baculovirus expression plasmid was provided by Dr Yong-Mo Ahn from Barry's group and the expression carried out in collaboration with Prof. Kim Naysmith group in the Department of Biochemistry and Prof. Nicola Burgess-Brown group at the SGC.

In chapter 3, PET imaging work was carried out by members of Barry's lab, under the directorship of Dr Laura E. Via at NIH. All the enzyme expression and cold compound syntheses were carried out in chemistry research laboratory by me.

In Chapter 4, CCL2 wt plasmid was made by Dr Ritu Raj and Dr Yiqun Geng and did the initial protein expression and optimisation. CCR2 binding cell assays were carried out by Vincent Luscombe in the department of pathology in collaboration with Prof. David Grieves. Radiolabelling of modified CCL2 variants and subsequent PET imaging is being done in collaboration with Prof. Carolyn Anderson group at the University of Pittsburgh.

Where stated that a compound had been previously formed in the group and/or no experimental data is given for a compound, this has been formed by another member of Prof. Ben Davis group.

Abstract

Tuberculosis (TB) is one of the oldest known human diseases, caused by *Mycobacterium tuberculosis*. The techniques currently employed for diagnosis are generally insensitive and non-specific. Positron emission tomography (PET) combined with computed tomography (CT) is used extensively in clinics and is among the advanced molecular imaging modalities for disease diagnosis and for monitoring the response to treatment.

In this thesis we described new probes based on sugars and proteins. We used an optimised biocatalytic approach for the synthesis of 2-fluoro-2-deoxy-D-trehalose (FDT). We scaled up synthesis for pre-clinical studies giving strong consideration to the expression host for enzymes. The use of rare biocatalytic methods employed in the synthesis was unique for the development of a radioisotope probe.

We then sought to develop an LC-MS based method for the detection of FDT *in vitro* and *in vivo*. Toxicity of the synthesised sugar compound was assessed in two different animal models. FDT administered to naïve marmosets labeled very little tissue in the lung, but when the animals were infected with *M. tuberculosis*, the tubercular lesions took up the radiolabelled FDT and [^{18}F] FDT monomycolate was isolated from tubercular lesions indicating that the probe reached the site of bacterial incorporation. In addition, FDT labelling of tubercular lesions was reduced with 4-drug standard TB treatment in marmosets. This work has permitted the development of specific PET imaging probe for TB diagnosis towards the clinic.

We demonstrated that a convergent protein synthesis using a "tag-and-modify" approach allowed the creation of homogenous, modified CCL2 variants bearing dual labels. We incorporated an unnatural amino acid azidohomoalanine (Aha) in the wild type CCL2 to obtain modified variants. Through initial work we have shown the successful modification of various potential PET imaging probes for TB diagnosis.

Acknowledgements

There are a number of people without whose help, guidance and support this thesis would almost certainly not exist. Firstly, I would like to thank my supervisor, Prof. Ben Davis, for giving me the opportunity to work in his group and on this amazing project. I enjoyed significant freedom to develop the project as I wished, whilst equally appreciated his guidance when needed. I would also like to thank my collaborator at the National Institute of Health Dr Clifton Barry III for his continual guidance and advice, providing different and interesting perspectives on my work, and also for allowing me the opportunity to work at NIH as part of my DPhil. I would like to thank Dr Laura E. Via from Barry group for extensive collaboration on this project, her regular guidance and support throughout and managing my stay at NIH. In addition I would like to thank Dr Dale Keiswetter for allowing me to work in his lab and providing me training in radiosynthesis.

I would also like to thank my other collaborators who helped in various studies during my DPhil: Prof. Daniel Anthony at the Department of Pharmacology and Dr Kim Walls for their support in *in vivo* studies; Prof. David Grieves and Vincent Luscombe for activity assays, James Collier from Department of Biochemistry and Shubhashish Mukhopadhy from Burgess Brown group for their assistance in enzymes expression in insect cells. I would also like to thank Prof. Carolyn Anderson and members of her group at the University of Pittsburgh for their ongoing collaboration on CCL2 imaging work.

Much of the work described herein would have been substantially more challenging than it already was without the excellent work carried out on by previous group members both from BGD and Barry's group. In this regard, I extend my thanks to Dr. Seung Seo Lee, Dr. Francois D'Hooge, Dr. Wendy Marriner, Dr. Yong-Mo Ahn, Dr Falguni, Dr. Ritu Raj, Dr. Yiqun-Yang and Sarah Faulkner.

The work in this thesis owes a great deal to a number of departmental staff. In particular, I thank Dr. James Wickens and Elisabete Pires and rest of the mass spectrometry team for helping me with LC-MS and LC-MS/MS related queries. Equally, I am extremely grateful to the NMR team: Prof. Tim Claridge, Dr. Nader Amin, Dr. Barbara Odell, and Tina Jackson.

There are a lot of people in the research group, past and present, who I would like to thank for a number of reasons. Firstly, I am grateful to all of you who took the time to proofread sections of this thesis: Dr. Laura E. Via, Dr. Andrew Giltrap, Dr. Sebastian Galan, Brian Josephson, Mateusz Imiolek, Aziz Khan, Aaisha Khan, Adeline Poh, Tobi Arisa, Abirami Lakshminaray and Jack Ren. Secondly, I thank past and present members of BGD group who helped me with various experiments special mention to Dr Nan Yan, Yiqun Geng and all members of ICL team (past and present). Thirdly, I'd simply like to thank all the members of the group during my time there, for making the group such a great place to be both in and out of work, whilst also providing support in tough times. I would also like to extend my thanks to Pembroke College for their travel grants during my time of DPhil.

Finally, I would like to thank my family members who supported me throughout my DPhil. Last but not least, enormous thanks to my wife Shagufta, my boy Haaris and girl Anayah who stood with me like a rock through the entire duration of my DPhil. It has been a journey where you all 3 suffered a lot because of me and I can't thank enough for all of you. I promise things will get back to normal.

I dedicate my thesis to both my mum and dad without their guidance and efforts I would not have manged thus far.

List of Common Abbreviations

ADP	Adenosine diphosphate
ATP	Adenosine triphosphate
BCG	Bacillus Calmette–Guérin
CB-TE1A1P	1,4,8,11-tetraazacyclotetradecane-1-(methanephosphonic acid)-8-
CFU	Colony forming unit
CID	Collision induced decomposition
CT	Computed tomogrpahy
DAB	(S)-4-Amino-2-(tert-butoxycarbonylamino)butanoic acid,
DBCO-PEG4-Biotin	Dibenzocyclooctyne-PEG4-biotin
DFO	Deferoxamine
DIPEA	N, N-Diisopropylethylamine
DMF	Dimethylformamide
DNA	Deoxyribonucleic acid
DTT	Dithiothreitol
EPTB	Extra pulmonary TB
FA	Formic acid
FDA	Food and Drug Administration
FDG	2-Deoxy-2-fluoro-D-glucose
FDG6P	Fluoro-Deoxy-glucose-6-phosphate

FDT	2-Deoxy-2-fluoro-D-trehalose
FDT6P	Fluoro-Deoxy-trehalose-6-phosphate
FITC	Fluorescein-5-isothiocyanate
GBq	Giga becquerel
Glc	Glucose
GT	Glycosyl transferase
HATU	(1-[Bis(dimethylamino)methylene]-1H-1,2,3-triazolo[4,5-b]
HIV	Human Immuno Defeciencey
IGRA	Interferon gamma release assay
IND	Investigational new drug
INH	Isoniazid
IPTG	Isopropyl β- d-1-thiogalactopyranoside
keV	kilo electron volt
LC-MS	Liquid chromatography mass spectrometry
M. tuberculosis	*Mycobacterium tuberculosis*
MDR	Multi drug resistant
MIP	Maximum intensity projection
MRI	Magnetic resonance imaging
NMM	N-methylmorpholine
NTA	Nitrilotriacetic acid

PCR	Polymerase chain reaction
PET	Positron emission tomography
PPT	Protein precipitation method
PTB	Pulmonary TB
ROI	Regions of interest
SDS-PAGE	Sodium dodecyl sulfate–polyacrylamide gel electrophoresis
SF9	*Spodoptera frugiperda* (cell type)
SIR	Selected ion recording
SPE	Solid phase extraction
SPECT	Single photon emission tomography
SUV	Standarised uptake value
TB	Tuberculosis
TDM	Trehalose dimycolate
THPTA	Tris-(3-hydroxypropyltriazolylmethyl) amine
TMM	Trehalose monomycolate
TPP	Trehalose phosphatase
TPS	Trehalose-6-phosphate synthase
TreP	Trehalose phosphorylase
TreS	Trehalose synthase
TreT	Trehalose glycosyltransferring synthase

TreY	Maltooligosyltrehalose synthase
TSPO	Translocator protein
TST	Tuberculin skin test
UDP	Uridine diphosphate
UDP-Glc	Uridine diphosphate glucose
WHO	World Health Organisation
WT	Wild type
XDR	Extensively drug resistant

1 Chapter 1: Introduction

1.1 Need for Imaging of Tuberculosis

Tuberculosis (TB) is an airborne disease, which has caused millions of human deaths over the centuries. According to the latest report by world health organisation (WHO) approximately 1.6 million people died of TB infection in 2018 alone. 10.6 million new cases of TB were reported in the same year, of which more than 0.5 million cases were related to drug resistant TB[1]. Most human tuberculosis is caused by *Mycobacterium tuberculosis (M. tuberculosis)*, which is a bacillus that can replicate and promote lesions throughout the body. It can be difficult to distinguish *M. tuberculosis* from diseases as diverse as cancer or skin disease. Even in pulmonary tuberculosis (PTB), cases of TB can manifest as sputum-negative TB because the bacteria were not detected in pulmonary secretions by traditional staining methods[1, 2], making a definitive diagnosis problematic. A key obstacle in developing new diagnostics, vaccines and antibiotics for TB is the lack of TB specific probes that can be used to assess the disease at the latent phase and monitor the response to treatment.

The general perception is that TB is a disease of the past. However, the fact remains that although it is not prevalent in the most advanced countries i.e., in Europe and North America. It has spread and concentrated to other parts of the world such as Africa, South America and Asia and remains a serious threat in the world's largest countries such as China, India and Russia (**Figure 1.1**)[3]. The high burden of disease is associated with poverty as it transmits most readily under poor ventilation conditions and the infection spreads faster with malnutrition[4]. In addition there is a significant issue involving human immunodeficiency viruses (HIV) TB co-infections, which causes significant problems[5].

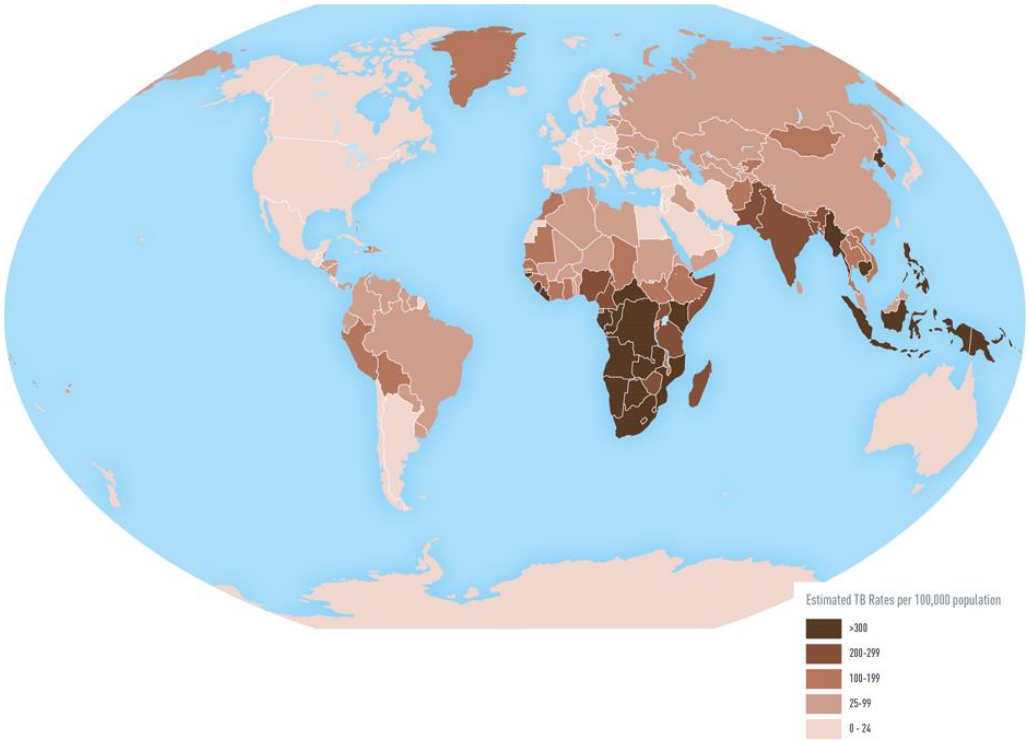


Fig. 1.1. Global burden of tuberculosis (adopted from with permission[6]).

TB was discovered by two physicians Jean-Antoni Villeman and Robert Koch who were the first people to identify TB as an infectious disease caused by mycobacterium[7]. The causative agent of tuberculosis, *M. tuberculosis* is a rod-shaped acid fast bacterium that is extremely slow growing. *M. tuberculosis* is carried in airborne particles, called droplet nuclei. Infection droplet nuclei are generated when the person carrying TB coughs, sneezes or shouts. The disease is then transmitted into other individuals, reaches the lung of the new host and resides into the macrophages if the droplets are of appropriate size. It then leads the macrophages into taking in *M. tuberculosis* and forms big aggregates called granuloma (**Figure1.2**)[8].

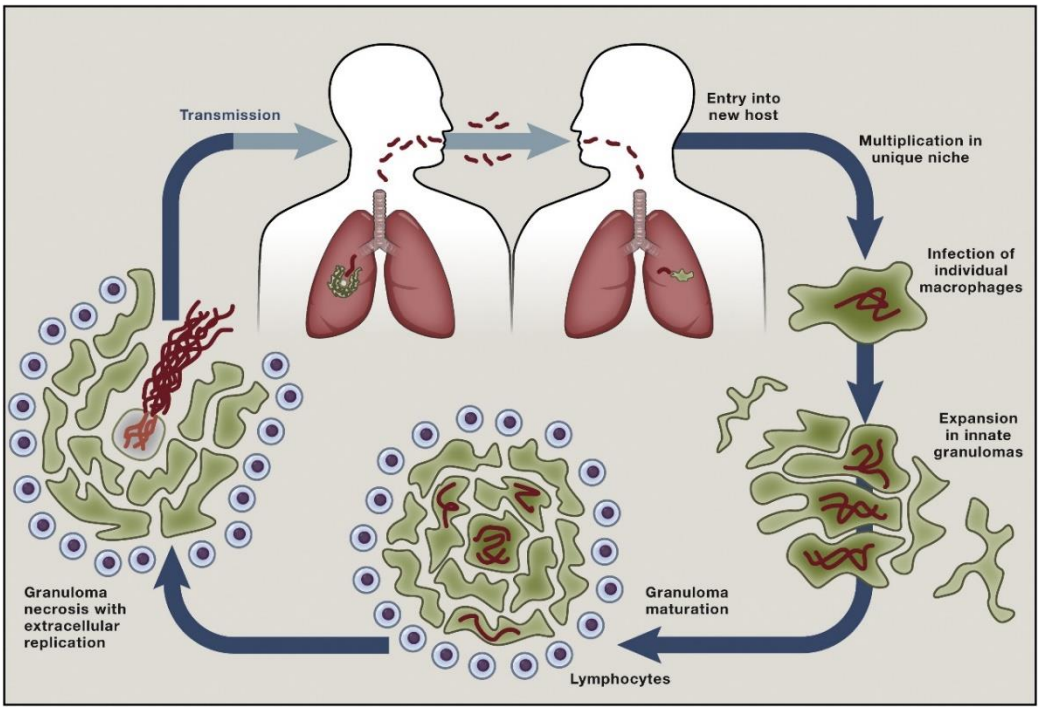
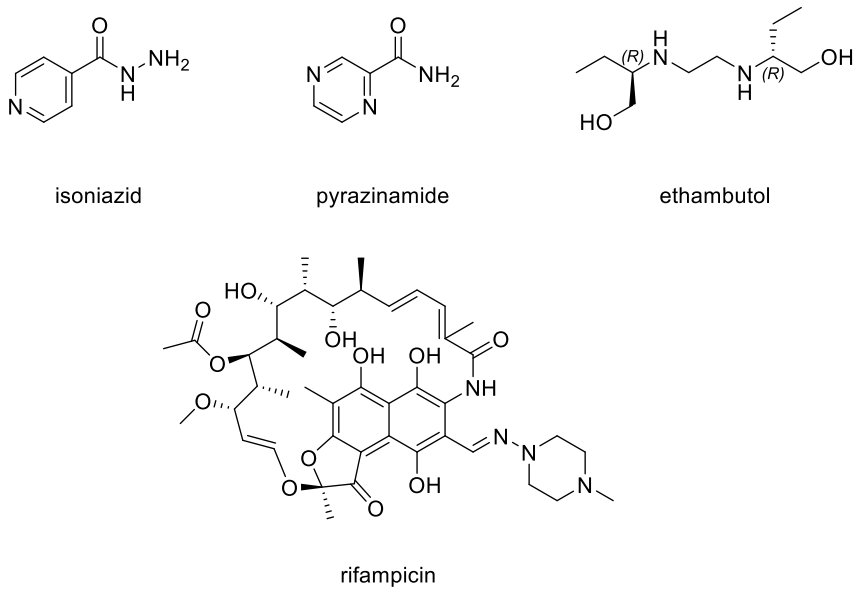


Figure 1.2. Pathogenic life cycle of *M. tuberculosis*. *M. tuberculosis* infection initiates when few tubercule bacilli dispersed in the air from a patient with active pulmonary TB. The bacteria then starts replicating actively inside the macrophages and diffuse to nearby cells and organs. A new round of macrophage recruitment to the original infected macrophage is initiated, forming the granuloma. As adaptive immunity develops, the granuloma can restrict bacterial growth. However, under many circumstances, the infected granuloma macrophages can undergo necrosis, forming a necrotic core that supports bacterial growth and transmission to the next host (used with permission from[8]).

M. tuberculosis is notorious for its high level of drug resistance, a characteristic traditionally attributed to its greasy, impermeable and hydrophobic cell envelope, which is also known as the "mycomembrane". The cell envelope consists of arabinogalactan attached to the peptidoglycan layer and to the inner leaflet of the mycolic-acid, containing mycomembrane. This thick layer prevents entry of most substances including potential drugs and probes into the bacterial cytoplasm[9, 10].

Anti-TB treatment aims to cure patients, prevents complications and death, avoids relapse and reduces transmission to other individuals. In order to address these challenges, the treatment approach to TB requires the use of multiple drugs. Usually treatment is carried out in two phases, an intensive phase aimed at reducing the bacterial burden, followed by a sterilising consolidation phase, both of which involve the use of multiple drugs[11].



Scheme 1.1. First line anti-TB antibiotics

Currently, overall duration of treatment is at least 6 months for simple drug-susceptible TB strains[11]. An intensive phase is carried out with four drugs (isoniazid, rifampicin, pyrazinamide and ethambutol) daily for two months followed by a 4-month consolidation phase with two drugs daily (isoniazid and rifampicin).

Although the treatment success rate for drug-susceptible TB exceeds 85% at a global level, the outcome is much poorer for patients with drug resistant TB (50% on average)[12]. Successful treatment outcome is far lower in extensively drug resistant (XDR) TB cases when compared with multi-drug resistant (MDR) TB[13]. Increasing cases of MDR and XDR TB, have led to a

push for discovery of the anti-TB drugs that are effective against drug resistant TB and allow effective management of the disease.

Aggarwal *et al.*[14] reported the structure-based development of a lead compound, TAM16, which targets polyketide synthase 13, an enzyme which performs the final assembly step in the mycolic acid synthesis. They claim that this lead compound is active against MDR and XDR *M. tuberculosis* strains *in vitro*. In murine TB infection models, it shows efficacy equal to INH. In addition, TAM16 shows 100-fold lower frequency of resistance when compared with INH[14].

The only current licensed vaccine against TB is the century old, bacillus Calmette-Guerin (BCG)[15] vaccine. Although this vaccine is highly effective in young children, it shows variable efficacy against adult pulmonary TB[16-18]. A key challenge in developing new vaccines is to control the vaccine response in different populations as highlighted in a recently concluded phase IIB trial of the anti-TB vaccine MVA85A[19].

1.2 Current TB Diagnosis

Robert Koch first used sputum microscopy in 1882 to identify TB and this remains the mainstay for the diagnosis of active TB in many parts of the world. Although cheap and accessible, this technique suffers from low sensitivity (45-80%) and is operator dependent. Sputum culture, the gold standard for active TB diagnosis, has greater specificity (98%) but is time consuming. In addition, sputum is difficult to collect from infants and children. As well as this, poor sample quality means all typical TB diagnostics to have low sensitivity. A significant portion of today's TB burden is due to extra-pulmonary TB (ETB), especially with HIV co-infection. Therefore a non-sputum based diagnostic strategy is needed, ideally a type of diagnostic test which can be used to diagnose all forms of tuberculosis[20].

Advances in culture media and improvement of automation has shortened the time of detection of *M. tuberculosis*. For instance, radiometric liquid culture using a broth with radiolabelled ^{14}C-palmitate as a carbon source has been available for many years. However, this is an expensive method, and as a result has lower adoption in developing countries[21]. Therefore, new fully automated systems that do not use radiometry for the detection of growth have been developed such as MB/BacT (Biomerieux), BACTEC 9000 (Becton Dickinson) and the mycobacterial growth indicator tube (MGIT; Becton Dickinson[22-25]. DNA amplification by polymerase chain reaction (PCR) is another rapid, sensitive method which has been used for the detection of TB[26-28]. However, these methods have limited sensitivity, are time consuming, expensive, and highly operator dependent.

For latent TB diagnosis in low incidence settings, immunodiagnostics tests such as tuberculin skin test (TST) or interferon gamma release assay (IGRA) are recommended[22-24]. However, immune compromising conditions, including HIV co-infection reduce the sensitivity of TST and IGRA and lower the cut-off for a positive TST[29]. Replacement of TST by IGRA is not recommended in middle-to-high incidence settings due to poor reproducibility, low efficacy in children and low sensitivity[30,31].

Due to limitations in the existing TB diagnostic strategies, researchers have explored molecular imaging based techniques for TB detection and diagnosis described in the next section.

1.3 Overview of Molecular Imaging Modalities

Over the past few decades, imaging has revolutionised the field of medicine. Advances in molecular imaging have allowed for non-invasive visualisation and quantification of both cellular and sub-cellular biological and pathophysiological processes within cells[32,33]. Imaging modalities are used both in research and clinical settings for diagnosis and monitoring response

to treatment. Development of new imaging agents, ligands and probes have significantly advanced the applications of molecular imaging techniques. Among the molecular imaging techniques currently employed in clinical and research settings are: Positron emission tomography (PET)[34,35], single photon emission tomography (SPECT)[35]; fluorescence and bioluminescent imaging[36], computed tomography (CT)[37], magnetic resonance imaging (MRI) [38], X-ray and ultrasound[39, 40].

1.3.1 Pros and Cons of Molecular Imaging Modalities

Most of the molecular imaging modalities are non-invasive, sensitive and extremely fast. However, there are limitations in that some of the modalities will either administer a radioactive probe to the patient (PET & SPECT) or the equipment used transmits radiation into the body (X-ray and CT). In addition, contrast agents used for MRI, CT and optical imaging can cause allergies to certain patients. Therefore when considering using molecular imaging modalitie, risks should be considered as well as benefits. A summary of the various properties of molecular imaging modalities is given in Table 1.

Table 1: Pros and Cons of Molecular imaging modalities (adapted from[41,33,42])

Imaging Modality	Spatial Resolution	Depth of Penetration	Temporal resolution	Sensitivity (mol/L)	Molecular Probe
PET	1-2 mm	No Limit	sec-min	10^{-11}–10^{-12}	ng
SPECT	0.3-1 mm	No Limit	min	10^{-10}–10^{-11}	ng
Fluorescence	2-3 mm	< 1 mm	sec-min	10^{-9}–10^{-12}	ng-μg
MRI	50-250 μm	No limit	min-hrs	10^{-3}–10^{-5}	μg-mg
X-ray CT	25-150 μm	No Limit	min	Unknown	mg

Plain chest radiography and computed tomography are mainstays for diagnosing probable pulmonary TB, whereas MRI and CT could add value in diagnosing extra pulmonary TB such as neural and skeletal TB. These modalities are non-specific and unable to provide definitive diagnosis due to the similar presentation of other infectious diseases, and the heterogeneous presentation of TB, particularly in HIV/TB co-infected patients with low CD4 counts[43].

1.4 PET/CT Imaging Modality

Integrated PET with CT (PET/CT), allows the non-invasive quantitative assessment of biochemical and functional processes with clear registration to the anatomical location. It is a type of radionuclide imaging, where a small amount of radiotracer is injected intravenously into the patient and after successful biodistribution; images of the areas of the tracer uptake are obtained. In PET/CT imaging, natural biological molecules can be labelled with a radionuclide that emits a positron upon decay[44]. Once the positron collides with a nearby electron, they annihilate each other to produce energy in the form of two 511 keV gamma rays, which are emitted in directions ~ 180° apart (**Figure 1.3**) for PET imaging process. One of the most commonly used PET radiotracer employed in clinical settings is [^{18}F]-2-Deoxy-2-fluoro-D-glucose ([^{18}F]FDG).

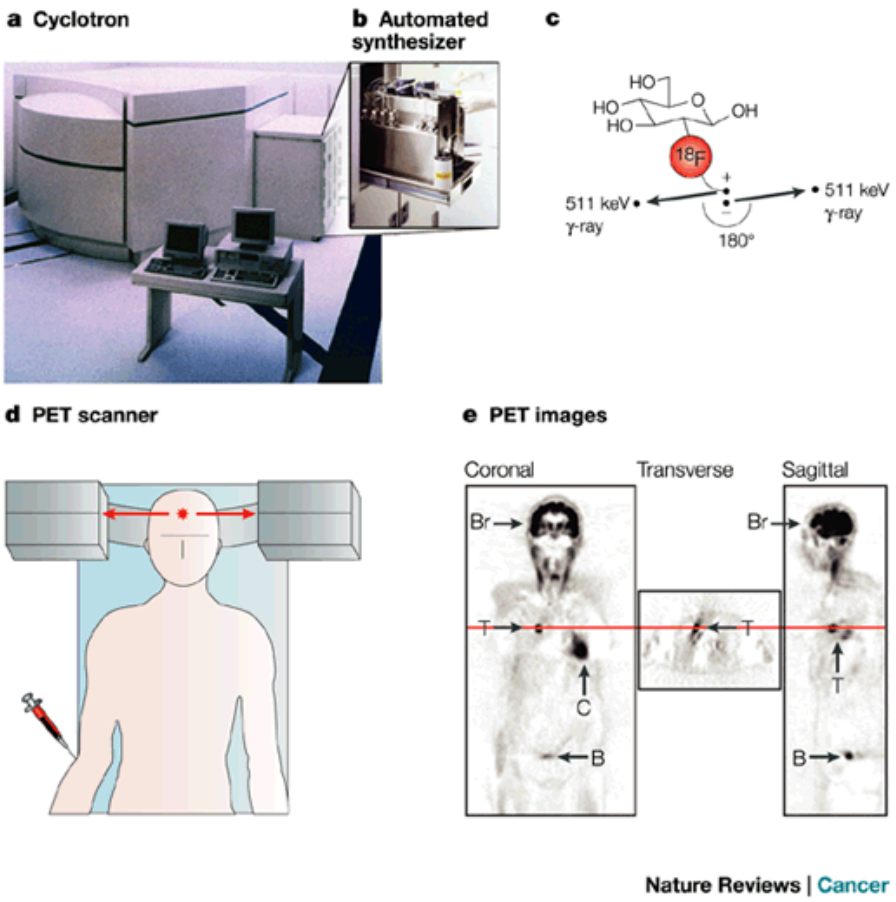


Figure 1.3. PET imaging process: **a)** A PET radionuclide is produced on the cyclotron by the bombardment of proton or deutron **b)** Automated synthesis units are used to conjugate the radionuclide to a tracer molecule of interest to produce the radiopharmaceutical. **c)** The molecule e.g., 2-[^{18}F] fluoro-2-deoxy-D-glucose [^{18}F]FDG, after synthesis is injected intravenously in a trace amount into a subject of interest. The radionuclide then decays by emitting a positron from its nucleus. The positron loses energy and eventually annihilates with a nearby electron to produce two gamma-rays that are 180° apart[43]**.** The PET scanner can detect the coincident γ-rays, and images can be reconstructed showing the anatomical location(s) and concentration of the tracer of interest. **e)** Cross-sectional [^{18}F]FDG PET images of a patient are shown 40 minutes after injection with [^{18}F]FDG with visible tumour uptake near to the lung[44] (used with permission).

The most commonly used PET isotopes include ^{15}O, ^{13}N, ^{11}C and ^{18}F. Other isotopes such as ^{64}Cu, ^{62}Cu, ^{124}I, ^{76}Br, ^{82}Rb and ^{68}Ga are less commonly used. However, there has been

significant interest in ^{68}Ga from the radiopharmacy community in recent years due to its reasonable half-life (68 min) and its accessibility.

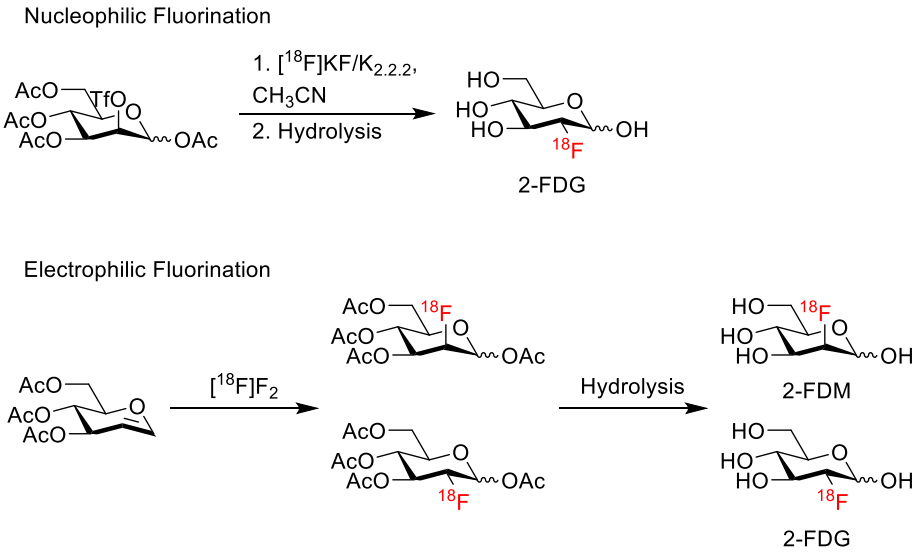
Table 2: Characteristics of the commonly used PET radionuclides[45,46-48]

Radionuclide	Half-life, $t_{1/2}$	Nuclear reaction	Target	Product	Decay product
^{15}O	2.04 min	$^{15}N(d,n)^{15}O$	$N_2(+O_2)$	$[^{15}O]O_2$	^{15}N
^{13}N	9.97 min	$^{16}O(p,\alpha)^{13}N$	H_2O	$[^{13}N]NOx$	^{13}C
^{11}C	20.4 min	$^{14}N(p,\alpha)^{11}C$	$N_2(+O_2)$	$^{11}C[CO_2]$	^{11}B
^{18}F	110 min	$^{18}O(p,n)^{18}F$	$[^{18}O]H_2O$	$^{18}F^-$	^{18}O
^{68}Ga	68 min	$^{68}Ge(p,n)^{68}Ga$	^{68}Ge	$^{68}GaCl_3$	^{68}Zn
^{64}Cu	12.3 h	$^{64}Ni(p,n)^{64}Cu$	^{64}Ni	$^{64}CuCl_2$	^{64}Zn
^{89}Zr	78.4 h	$^{89}Y(p,n)^{89}Zr$	^{89}Y-foil	^{89}Zr-oxalate	^{89}Y

1.5 Radiolabelling Approaches with Fluorine-18 (^{18}F)

Fluorine is the most electronegative element in the group VII members of the periodic table. Due to its small radius, it mimics the properties of the hydroxyl group[49]. The substitution of hydroxyl group for fluorine, increases the lipophilicity thereby enhancing the cellular absorption, and alters the molecular conformational structure[49]. The radioactive isotope of fluorine i.e. ^{18}F was initially produced by proton irradiation of ^{20}Ne[50]. However, with the introduction of PET imaging system, the current and the most common production method for the radionuclide is via the proton bombardment of ^{18}O water in a low energy cyclotron unit (**Table 2**). Irradiation of ^{18}O water with protons for 1-2 hours gives rise to 185-370 GBq of aqueous $^{18}F^-$ ion.

The produced radionuclide, can be used to radiolabel trace amount of target molecules either by direct or indirect fluorination. The direct fluorination approach is the introduction of ^{18}F to the tracer molecule in a single step, the indirect fluorination on the other hand requires a prosthetic group that conjugates to the radiolabelled intermediate[51]. [^{18}F]FDG can be synthesised either by nucleophilic or electrophilic substitution (**Scheme 1.2**). However, the nucleophilic fluorination method is far superior and most commonly used in the routine production of [^{18}F]FDG as this method yields the product with higher specific activity[51]. The electrophilic fluorination method on the other hand leads to the formation of products with far less specific activity (106-fold less than the nucleophilic products)[52]. The lower specific activity is due to the need for the addition of [^{19}F]F_2 gas as a carrier to extract the [^{18}F]F_2 from the target[52]. Therefore, [^{18}F]FDG produced using this method cannot be used for PET studies where high specific activity is crucial, such as ligand receptor binding[52]. The schematic overview of both nucleophilic and electrophilic fluorination is depicted in **Scheme 1.2**.



Scheme 1.2. [^{18}F]FDG synthesis by nuleophilic and electrophilic fluorination methods[52].

1.6 Radiolabelled Macromolecules in TB Imaging

Macromolecules such as peptides and proteins have long been studied for various pathological processes. Radiolabelled peptides, small proteins, and antibody fragments have been used predominantly for infection and inflammation imaging. These molecules have also been used in pre-clinical and clinical settings to diagnose TB. Lee *et al.*[53] used ^{131}I sodium iodide (NaI) labelled bacillus calmette-guerin (BCG)-specific F(ab)2 in a rabbit model. They were able to demonstrate tuberculosis lesions through immunoscintigraphy, however, the radionuclide ^{131}I used in the study has a very long half ($t_{1/2}$ = 8 days) and emits significant amount of β-rays, making it more suitable for therapy than imaging. Similarly, another commonly used SPECT radionuclide, ^{99m}Tc labelled human polyclonal imunoglobin G (IgG) has been successfully used in identifying inflammation and infection processes in human and animal models[54]. In a study carried out by Heffernan *et al.*[54] ^{99m}Tc IgG images correctly identified 95% of a varied range of infection locations.

The monocyte chemoattractant protein-1 (MCP-1/CCL2) is a member of the CC chemokine family that regulates migration and infiltration of the monocytes, memory T lymphocytes, and natural killer cells[55, 56]. As discussed earlier, TB is characterised by granuloma formation at the site of infection[57]. Granuloma consists of many different types of cells, including infected and uninfected macrophages, CD4, CD8, T cells and B cells.[58]. It has been hypothesized that higher levels of macrophages in granulomas might indicate a more active form of disease. CCR2 receptors are found in high concentrations in activated macrophages. As MCP-1 is a natural ligand for CCR2, a radionuclide labelled MCP-1 may act as a potent imaging agent for macrophages and hence allow for diagnosis of TB. Strategies towards this end will be discussed in chapter 4.

1.7 [^{18}F] FDG PET/CT Imaging in TB Diagnosis

[^{18}F] FDG is a well-established probe in cancer imaging to stage disease and predict outcomes to the treatment (**Fig. 1.4**). The use of PET/CT with [^{18}F]FDG as the probe in TB diagnosis, and to assess treatment response, is also well documented. Diagnostic studies based on [^{18}F] FDG have focused on determining the extent of TB disease, differentiating TB from cancer and differentiating active TB from latent TB. The uptake of [^{18}F]FDG in inflammatory cells such as neutrophils and activated macrophages enables the use of this imaging modality in real time assessment of disease activity. Goo *et al.*[59] studied 10 consecutive patients suffering from pulmonary TB. Tracer uptake was seen in 9 out of 10 patients. Kim *et al.*[60] evaluated the potential role of double-phase acquisition of [^{18}F]FDG PET/CT in differentiating active pulmonary TB from other malignant or infected tissues. A total of 25 patients enrolled for the study, and the PET/CT scans were obtained at 60 min and 120 min post-injection. In all patients active tuberculum showed statistically significant higher values of SUV than those of inactive tuberculum with greater sensitivity and specificity. These preliminary results suggested that areas of active TB can be differentiated from inactive TB infection by imaging at two time points.

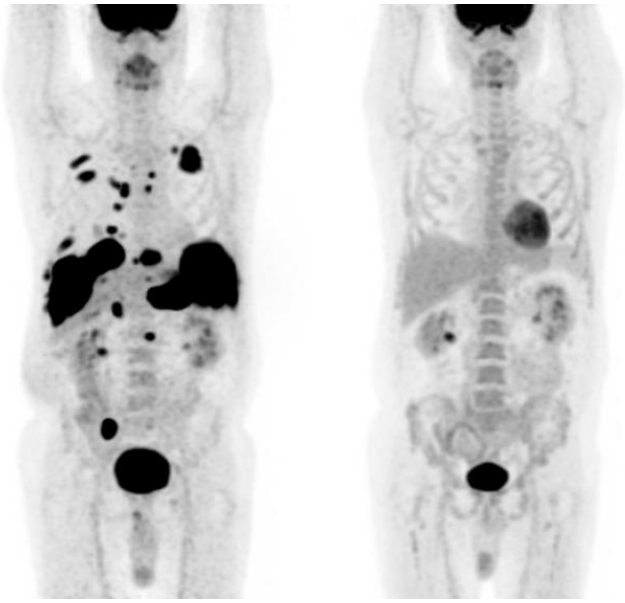


Fig. 1.4. [^{18}F] FDG PET/CT imaging in monitoring the response to treatment. Shown above are the [^{18}F] FDG PET scans from a patient with diffuse large B-cell lymphoma. PET/CT scan on the left show the disease stage at the beginning. While the the scan on the right has been taken after 4 cycles of chemotherapy. Images shown post treatment indicate that tumours are no longer taking up [^{18}F[FDG (used from[61] with permission).

[^{18}F]FDG PET/CT has shown diagnostic potential in extra pulmonary tuberculosis such as in diagnosing musculoskeletal tuberculosis, central nervous system TB and abdominal TB, although the published data indicates non-specificity and variation in the diagnosis[62].

The diagnosis of active PTB is a major challenge, especially in individuals with severe immunosuppression, such as those co-infected with HIV. PTB presentation in HIV-positive patients differs from that of HIV-negative patients as these patients show atypical radiographic patterns. [^{18}F]FDG PET/CT may allow for early diagnosis of extra pulmonary TB. This technique detects more extra pulmonary TB lesions than the use of CT alone.

The ability of PET/CT imaging to quantify tracer uptake can be useful in monitoring the response to therapy. [^{18}F]FDG uptake has been successfully used both in animal and TB

infection models for this purpose[63-66]. Davis *et al.*[63] have shown a clear correlation between the reduction of [^{18}F]FDG uptake in the lungs and successful administration of a bactericidal drug in mouse models of TB. Several studies carried out in patients show reductions in [^{18}F]FDG uptake as they progress through the course of antibiotic treatments[64-67]. Martinez *et al.*[66] used [^{18}F]FDG PET/CT to monitor the early response to treatment both in pulmonary and extra-pulmonary TB in 21 patients. The patients underwent PET/CT scans at day 0 and day 30 after one month of treatment. A decrease of approximately one-third in SUV_{max} has been reported after 1 month of anti-TB treatment in most patients. Lefebvre *et al.*[68] reported that of 18 patients with lymph node TB, [^{18}F]FDG PET/CT correctly identified TB clearance in nine patients and treatment failure in two patients.

1.7.1 Limitation of [^{18}F] FDG PET/CT in TB Diagnosis and Monitoring the Response to Treatment

PET imaging has the potential to significantly improve the diagnosis of TB due to its high sensitivity. However, [^{18}F]FDG PET/CT is the recognised PET radiotracer which is currently being used for imaging TB infection in patients. The use of [^{18}F]FDG PET/CT is not optimal because it lacks specificity for bacteria, such as *M. tuberculosis*, and has high uptake in mammalian cells[69]. [^{18}F]FDG PET/CT cannot distinguish TB infection from other pathologies such as cancer and inflammation. In addition, this tracer is unable to diagnose the disease at the early stages before significant lung pathology has occurred[70, 71].

Due to the limitations of [^{18}F]FDG in TB diagnosis, significant research efforts have focused on the evaluation of other radio tracers which could allow specific detection of *M. tuberculosis*. Weinstein *et al.* evaluated 2-[^{18}F]-fluoroisonicotinic acid hydrazide as a PET/CT diagnostic probe for TB in mice models. They showed that the radiotracer extensively distributed and

rapidly accumulated at the site of infection in animals, including TB lesions. No comparable uptake was seen in healthy animals after the injection of the tracer[72].

Iodine radionuclides are used extensively in the field of nuclear medicine for both diagnosis and treatment of various diseases. Therefore, a number of research groups have radiolabelled a ligand, DPA-713 with SPECT radionuclide [^{125}I]. DPA-713 is the ligand for the translocator protein, (TPSO). TPSO is highly expressed in immune cells such as microglia and macrophages. Upon injection of the radiotracer in healthy and infected mouse models, the infected mice showed clear uptake in sites of TB infection, whereas uninfected animals or animals with blocking showed little or no uptake[72]. When this radiotracer was compared with [^{18}F]FDG in the same animals, [^{125}I]DPA-713 showed a discrete signal at the site of infection, whereas [^{18}F]FDG signal was very diffuse indicating the non-specificity of [^{18}F]FDG [72].

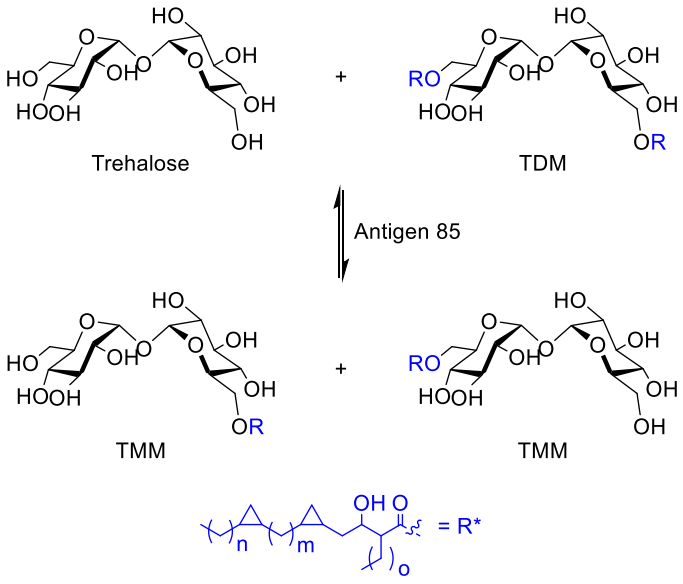
Foss *et al.* reported another [^{125}I] anti-C3d-mAb for imaging of *M. tuberculosis* in mouse models[73]. [^{125}I]3d29 monoclonal antibody (mAb) was used as a control and both radiotracers were injected in healthy and infected mice. The infected mice showed discrete uptake of the radiotracer, [^{125}I]anti-C3d-mAb at the site of the infection when imaged 24 hours post injection, while there was no reported uptake in healthy animals [73].

Recently, Ning *et al.,* investigated the potential of [^{18}F] maltohexaose ([^{18}F]MH) for the imaging of bacterial infection in rats[74]. They showed that radiotracer was retained in infected animals but cleared in non-infected tissues[74]. While comparing the sensitivity and specificity of this new tracer with [^{18}F]FDG, they reported that [^{18}F]MH not only detected the infection at the earlier stage but was also more effective in imaging bacterial infection[74].

1.8 Trehalose based Bacteria Specific Imaging Probes

1.8.1 Trehalose

The non-mammalian disaccharide sugar trehalose (α-D-glucopyranosyl-α-D-gluco-pyranoside) is comprised of two glucose moieties linked *via* reducing anomeric centres (**Scheme 1.3**). Trehalose is widely distributed in bacteria, yeast, fungi, insects, invertebrates and plants. Apart from acting as carbon and energy source, trehalose acts as a protective agent. It is commonly found in the cell wall structure of many bacteria. Under physiological stress and other adverse conditions, organisms increase trehalose production, signifying its role as a protective agent[75,76]. In addition, trehalose is used as a preservative in the food, pharmaceutical and cosmetic industries[77]. In plants, the trehalose biosynthetic precursor, trehalose-6-phosphate has been involved in plant growth regulation and development[78]. Trehalose is also abundant in *M. tuberculosis*[79].



Scheme 1.3. Antigen 85 A, B and C catalyse the transesterification of trehalose, TDM and TMM[80].

In *M. tuberculosis*, trehalose not only serves as a source of energy but also acts as a stress protector[75]. Although, the precise 3D structure of the bacterial cell wall remains understudied,

the outer membrane, also known as the mycomembrane contains lipids, glycolipids, trehalose dimycolate (TDM) and trehalose monomycolate (TMM) (**Figure 1.6**) [81]. TMM and TDM possess long lipid chains (C60-C90), known as mycolic acids, that are critical for *M. tuberculosis* cell viability and are also associated with virulence and persistence within the host[82]. Trehalose can be incorporated into the mycomembrane via two metabolic pathways. The first pathway involves transport of the sugar molecule into the cytoplasm of the cell via the SugABC-LpqY transporter protein complex[83]. Inside the cell, the sugar is converted to TMM and transported out of the cell via the Mmpl3 transporter system into the outer membrane[84]. In the second pathway, trehalose is anchored into the *M. tuberculosis* cell wall as TMM or TDM by the action of extracellular proteins Antigen 85 (Ag85) A-C. All Ag85 isoforms catalyse the reversible transesterification reaction between two units of TMM, generating TDM and free trehalose (**Scheme 1.3, Figure 1.5**). Ag85 can also covalently introduce mycolates into the arabinogalactan to form the base polymer of the cell wall[85, 86].

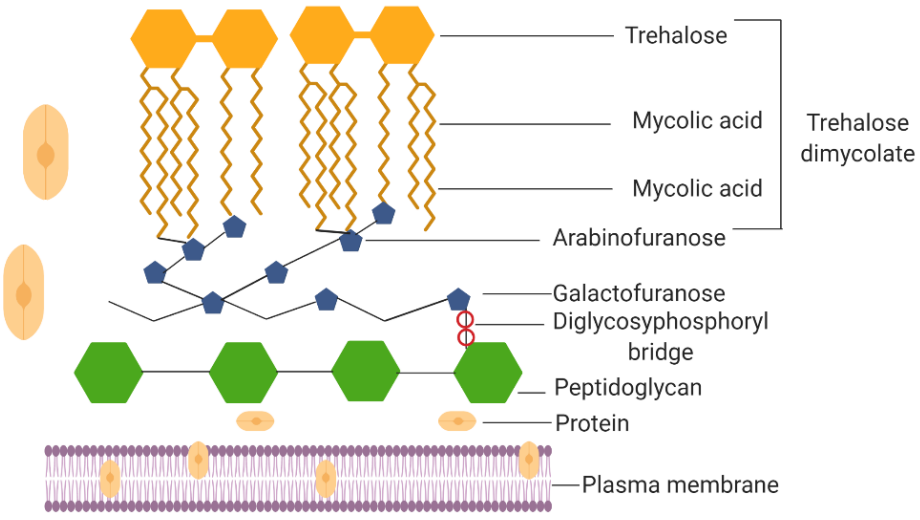


Figure 1.5. Schematic representation of mycobacterial cell wall. This figure shows the plasma membrane is the peptidoglycan to which is attached the galactofuranose and arabinofuranose through a diglycosyphosphoryl bridge. Trehalose and trehalose mycolates associates to the outer most portion of the membrane. Figure recreated from [87].

1.8.2 Trehalose Analogues as Potential TB imaging probes

In recent years, several groups including the Davis group have found that modified trehalose analogues, including fluorine, alkyl, azido and fluorogenic derivatives can be metabolically incorporated into the mycobacterial outer membrane as trehalose mycolates[88-90]. Antigen 85 proteins are promiscuous and process a variety of trehalose analogues and hence can be used to introduce reporter molecules in the cell wall of bacteria which possess a mycomembrane[88-90].

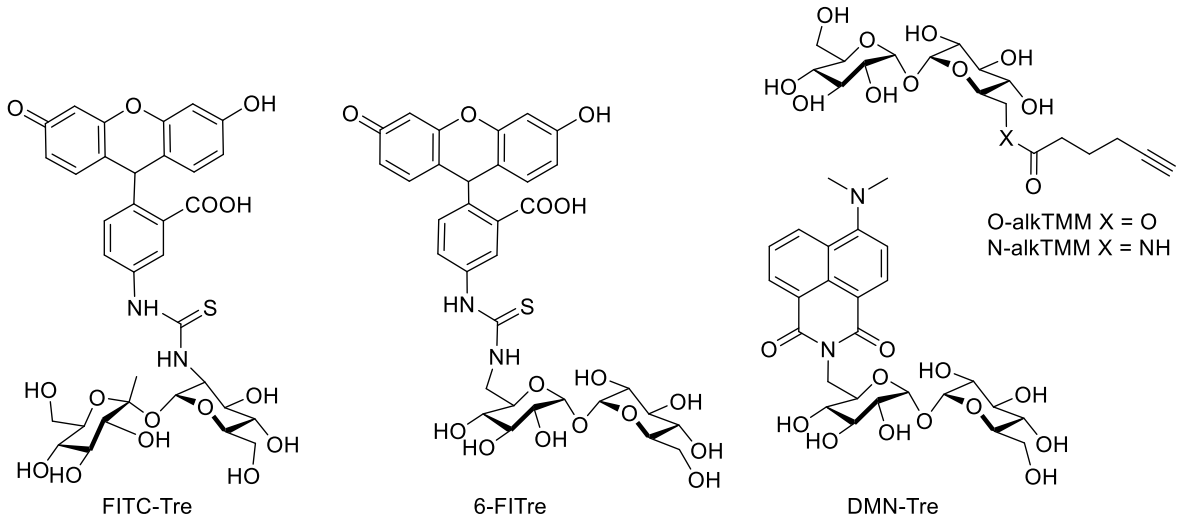
Backus *et al.*[88] first reported the specific labelling of *M. tuberculosis* using a fluorescent agent, fluorescein isothiocyanate (FITC) trehalose (tre) (**Scheme 1.4**) both *in vitro* and in the macrophages during infection. Through a new Ag85 substrate assay, they found that the Ag85 A-C could tolerate extensive modifications on the trehalose scaffold[88]. Although this probe, and most importantly the methodology, opened new research avenues, it had its own limitations. For example, it showed poor efficiency when labelling different bacterial species including mycobacteria. In addition, poor sensitivity was reported with corynebacteria for labelling glycolipids. It has been speculated that the anomeric methyl group, a directing group, may compromise the processing of FITC-tre by the Ag85 complex[90].

Swarts *et al.*[91], reported the synthesis and metabolic labelling of glycolipids of azido analogues of trehalose. They installed the azido group at all possible positions with native stereochemistry. These compounds showed effective metabolic labelling, however, these analogues have limitations in that that they get transformed to additional classes of trehalose metabolites, which complicates data analysis[90]. Furthermore, the secondary reagent used to conjugate a fluorescent probe could result in non-specific interactions, due to the limited access to mycomembrane[90]. Swarts and co-workers also installed the alkyne functionalised trehalose

analogues (alkTMM) into the mycomembrane[89]. This approach also requires secondary labelling reagents as well as a Cu catalyst for click chemistry that may be cytotoxic.

Bertozzi and co-workers used the fluorescein trehalose analogues with slight modification to FITC-Tre and reported that these molecules are recognised by mycolyltransferases of diverse mycobacterial species[90]. They reasoned that the reagents used in this work showed improved metabolic efficiency compared to FITC-tre (**Scheme 1.4**)[90]. These analogues showed strong metabolic labelling with the highest labelling observed with 6-FITre (**Scheme 1.4**). This approach was also limited as un-metabolised probe needed to be removed to eliminate background fluorescence

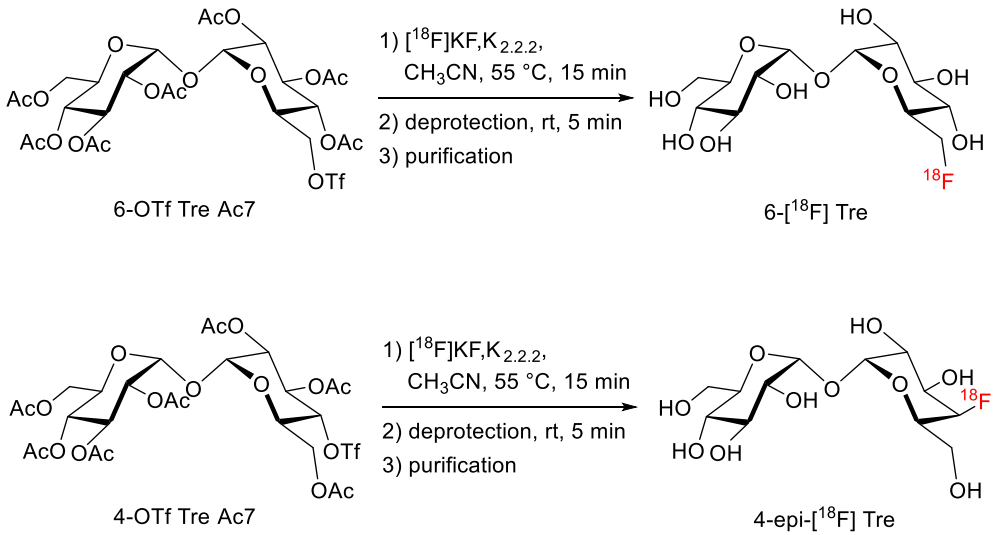
In order to overcome this problem, Kamariza *et al.*[92] hypothesised that the trehalose probe whose fluorescence signal is specifically activated by metabolic incorporation into the mycomembrane would overcome this limitation[92]. They developed 4-N,N-dimethylamino-1, 8-naphthalimide (DMN), conjugated to trehalose (**Scheme 1.4**), collectively called DMN-Tre for the detection of *M. tuberculosis* from the sputum samples of TB patients. They showed that this probe selectively labels live *M. tuberculosis* cells and observed reduction in the fluorescence signal when the probe was exposed to front line TB drugs[92].



Scheme 1.4: Trehalose based compounds recetly developed and tested in pre-clinical settings for TB diagnosis.

Recently, Heather *et al.*[93] have developed a quencher-trehalose-fluorophore (QTF), a fluorogenic probe for imaging mycolyltransferase activity. This probe is an analogue of the mycolyltransferase donor, TMM. It is hydrolysed by mycolyltransferases to provide real-time fluorescent signal of these enzymes activity and mycolic acid membrane assembly[93]. Unlike, the previously discussed fluorescent agents, this new probe does not require washing steps and reports on mycobacterial cell wall assembly in live bacteria in real time[93].

In the Davis group, chemical synthesis of fluorinated trehalose analogues at position 4 and 6 has been accomplished[88]. These compounds were then radiolabelled from their triflate precursors using nucleophilic fluorination (**Scheme 1.5**) and tested in animal models as potential PET diagnostic probes for TB (unpublished work).

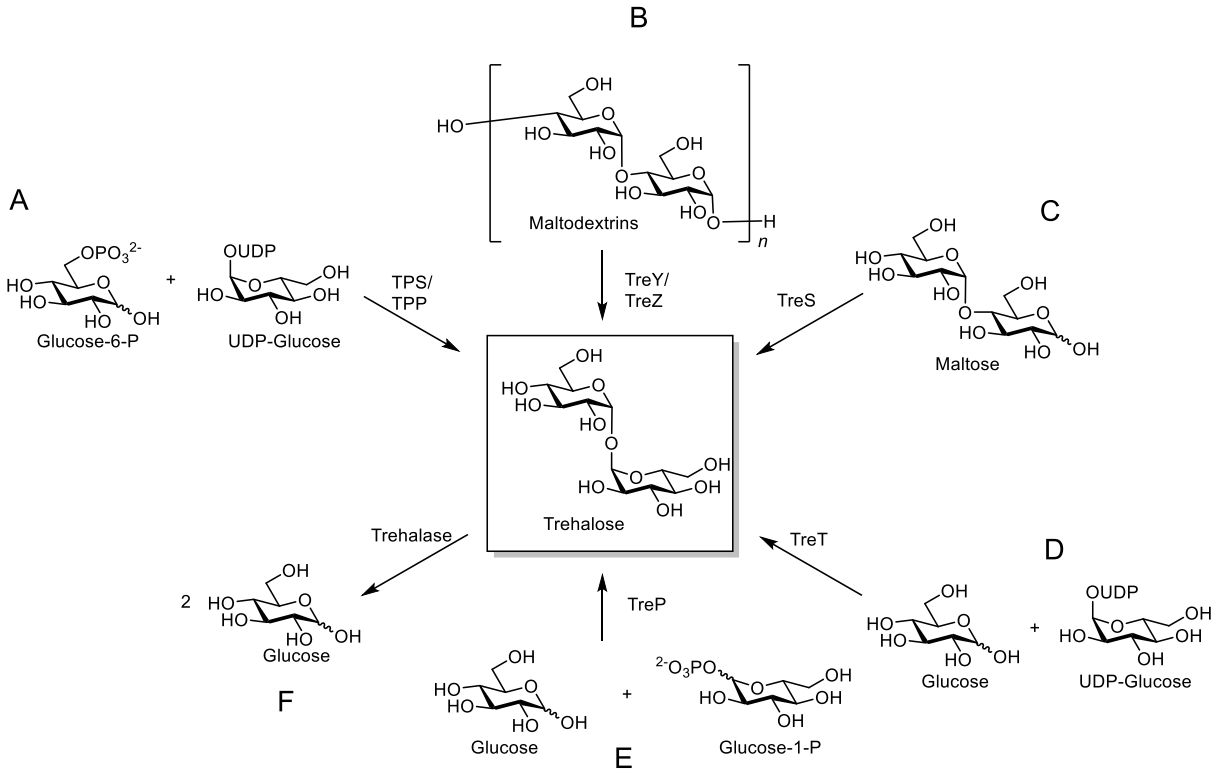


Scheme 1.5 Radiosynthesis of 4-epi-[^{18}F] Tre and 6-[^{18}F]-Tre from corresponding triflate precursors.

Animal testing carried out in rabbits indicated that 6-FDT was completely metabolised by rabbits 2 h post injection, whereas, in 4-FDT the rate of metabolism was slower, but after 3 h, 30 % of the radiotracer was metabolised by rabbits.

1.9 Trehalose Biosynthesis in Nature

To date, there are five natural biosynthetic pathways for trehalose[94]. The best known one involves a glycosyltransferase and a specific phosphatase. The glycosyltransferase is trehalose-6-phosphate synthase (TPS), which is called OtsA in *E. coli*. This enzyme transfers a glucose (Glc) moiety from uridine diphosphate glucose (UDP-Glc) to glucose-6-phosphate (G6P) to yield trehalose-6-phosphate (T6P), which subsequently undergoes hydrolysis by trehalose-6-phosphate phosphatase (also called OtsB in *E. coli*) (**Scheme 1.6A**)[79, 95]. In the TreY-TreZ pathway, maltooligosyltrehalose synthase (TreY) converts the terminal alpha-1, 4 glycosidic linkage into maltooligosyltrehalose. Maltooligosyltrehalose, trehalose hydrolase, TreZ, then hydrolytically liberates trehalose (**Scheme 1.6B**)[96]. Another trehalose biosynthesis pathway based on trehalose synthase (TreS), isomerises maltose to trehalose(**Scheme 1.6C**)[97]. The fifth pathway, found in both bacteria and archea, utilizes the trehalose synthesising glycosyltransferase, TreT, which converts glucose and UDP-glucose into trehalose in a single step with the release of UDP (**Scheme 1.6D**)[98]. The trehalose phosphorylase (TreP) pathway, which has been reported for fungi[99], and the protista Euglena[100] catalyses the formation of trehalose from glucose-1-phosphate and glucose *in vitro* (**Scheme 1.6E**)[101].



Scheme 1.6. Known Trehalose Biosynthesis (A-E) and Degradation (F) Pathways[102].

The trehalose biosynthesis pathways described above, as well as pathways for incorporating trehalose into *M. tuberculosis* cell wall, have important implications for development and applications of trehalose analogues. The presence of trehalose in pathogens and its absence in mammalian metabolism makes the development of trehalose based diagnostics an attractive research avenue. In this context, the trehalose biosynthetic pathways have the potential to be adopted for the chemo-enzymatic synthesis of trehalose analogues, the core work of this thesis.

1.9.1 Approaches to trehalose analogue synthesis

1.9.1.1 Chemical synthesis of trehalose analogues

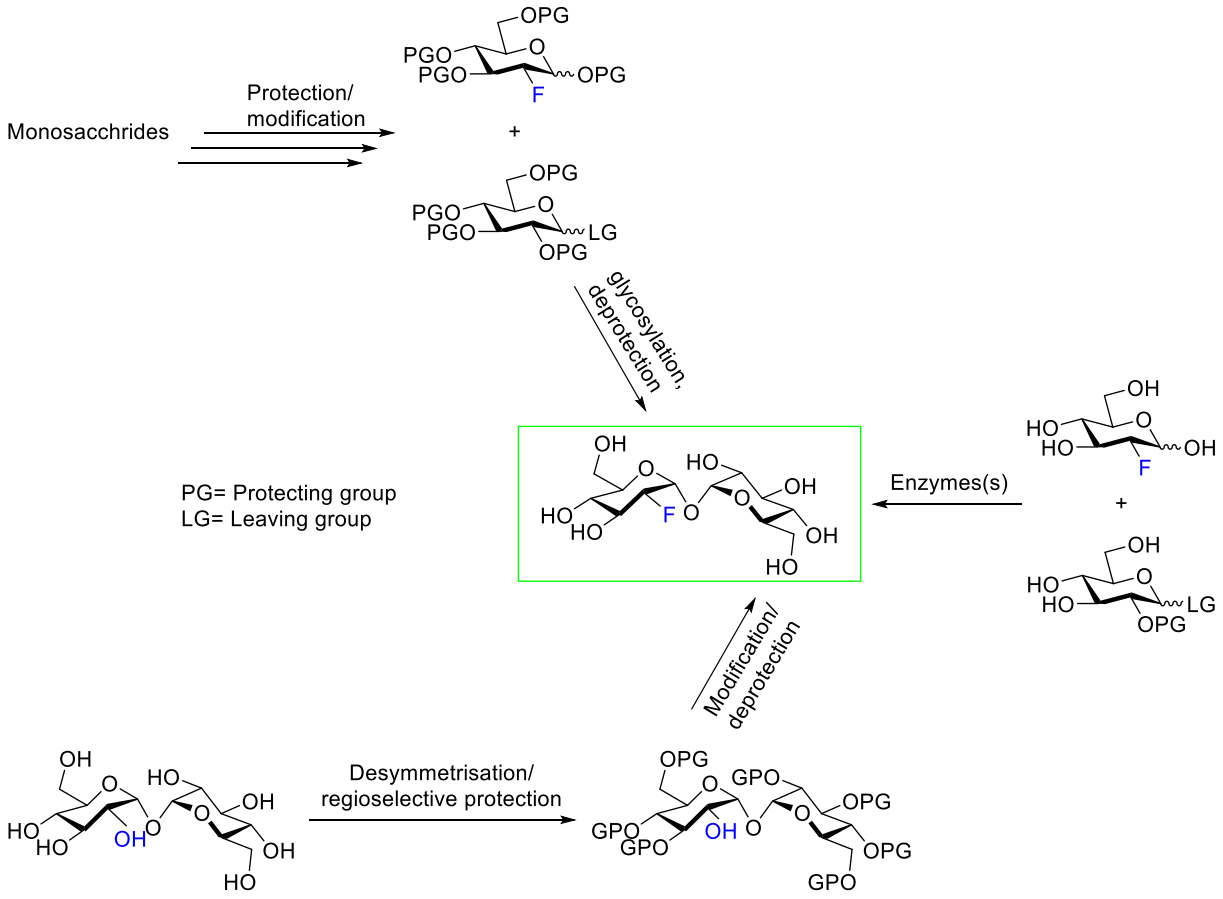
Chemical synthesis of trehalose derivatives is challenging. Trehalose analogues can be synthesised through two basic strategies i). Modification of the trehalose scaffold or regio-

selective synthesis[103-105] and ii) coupling of monosaccharide units to produce trehalose analogues or chemical glycosylation (**Scheme 1.7**)[106-108].

Synthesis beginning with trehalose based approaches involve regioselective functionalisation of native trehalose, which is abundant and inexpensive. The main challenges include differentiation of similarly reactive hydroxyl groups as well as desymmetrization to form unsymmetrical analogues. These reactions are generally inefficient and the isomeric products are very difficult to separate. Most modifications based on this approach have been at the 4- and the 6- positions because of ease of modifications, whereas modification at 2- and 3- positions have been limited to deoxy sugars only.

Synthesis beginning with monosaccharides requires that two stereo-centres are at the relatively unfavourable alpha configuration. Pratt *et al.*[108] reported the synthesis of trehalose analogues based on intramolecular aglycone delivery for stereo-selective formation of the 1,1-α, α-glyosidic bond. Although this approach offers the advantage of exclusively yielding the alpha and alpha linkage there can be challenges in synthesising various building blocks. Glycosylation of ketosides capitalises on the inherent tendency for the ketoside sugars to form the alpha, alpha linkage, but incorporates an extra, methyl group at the anomeric position[109]. Dehydrative glycosylation[110] affords alpha selectivity but results in the synthesis of 2', 2'-dideoxy analogues, preventing further modification at the 2-position.

Due to significant challenges in the chemical synthesis of trehalose, it is now synthesised chemoenzymatically.



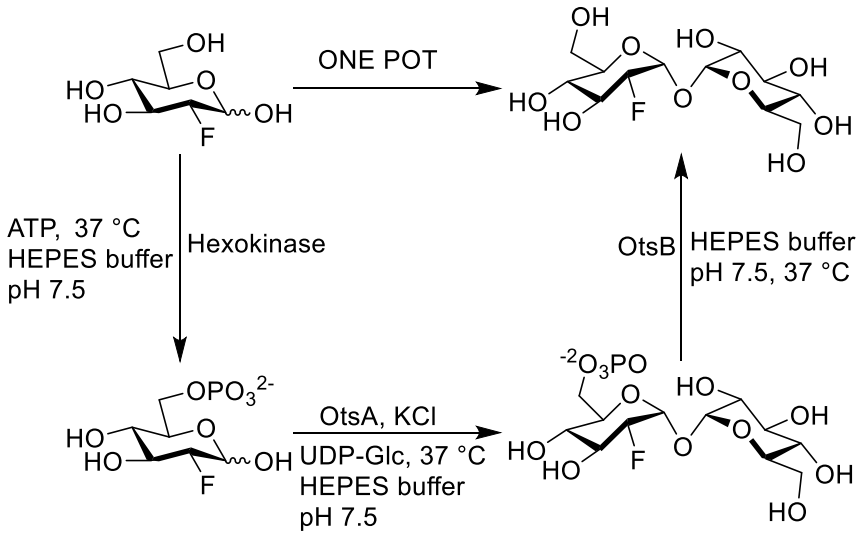
Scheme 1.7. Overview of the Synthetic Approaches for the Trehalose Analogues. Chemical synthesis may involve synthesis from monosaccharides, through selective protection and/or modification, followed by glycosylation and deprotection. In addition, trehalose analogues can be synthesised chemically from trehalose, through regio-selective protection and modification and de-protection approaches. Chemo-enzymatic synthesis on the other hand offers, one-pot, stereo-selective trehalose analogues in aqueous conditions.

1.9.1.2 Chemo-enzymatic synthesis of Trehalose analogues

The trehalose biosynthesis pathways in nature allows for the development of chemo-enzymatic methods to produce trehalose and trehalose analogues for a variety of applications. Trehalose forming enzymes are capable of forming the challenging 1,1-alpha,alpha glycosidic bond with

precise stereo-selectivity. In addition the reaction is carried out in aqueous conditions utilising, simple and unprotected substrates.

Among these pathways, the TPS/TPP pathway converts, glucose-6-phosphate and UDP-glucose to trehalose over two steps. This pathway has been exploited for the chemo enzymatic synthesis of trehalose analogues by modifying either of the substrates. Backus *et al.*[88] first reported the synthesis of 2-deoxy-2-fluoro-D-trehalose [^{19}F] FDT. For this synthesis 2-deoxy-2-fluoro-D-glucose (FDG) was used as the substrate and phosphorylated with commercially available Hexokinase at the 6-position to generate the intermediate (FDG6P), which then reacts with UDP-Glucose in the presence of OtsA to form 2-deoxy-2-fluoro-D-trehalose-6-phosphate (FDT6P). Subsequent dephosphorylation by an alkaline phosphatase, such as TPP or OtsB afforded the desired [^{19}F]FDT (**Scheme 1.8**). This synthesis was quite efficient (63% yield in final two steps), indicating the potential of this approach for the synthesis of trehalose analogues.



Scheme 1.8. [^{19}F]FDT synthesis from hexokinase, OtsA and OtsB enzyme. This is a three steps, three enzyme strategy whereby hexokinase catalyses the phosphorylation of FDG to yield FDG6P. FDG6P reaction is catalysed by OtsA in the presence of UDP-Glc as a donor substrate to yield FDT6P.

OtsB enzyme further catalyses the dephosphorylation of FDT6P to yield FDT. HEPES buffer solution contains 50 mM HEPES, 100 mM NaCl and 10 mM $MgCl_2$, pH 7.5

1.10 Conclusions and Aims of this Thesis

TB remains a global healthcare challenge and with increasing risks of MDR and XDR TB, newer diagnostics and treatments are urgently sought. Current standard of care for TB involves treatment with four drugs for six months and this requires huge amount of resources and personal commitments from patients. Shortening the treatment from six months to even four months could add significant value. The diagnostic techniques currently employed in clinical settings are insensitive and time consuming. Even, among the most sensitive molecular imaging techniques, the PET probe, [^{18}F]FDG is non-specific to the TB lesions. Therefore, there needs a diagnostic probe which is highly sensitive and specific to the TB lesions, that could be used to not only diagnose TB at the earliest phase but also can aid in monitoring the response to treatment.

As shown in this review, one of the unique features of the mycobacteria is their incorporation of trehalose into TMM and TDM in their outer membrane structure. We have hypothesized that radiolabeled FDT would be a substrate for the antigen 85 complex enzymes *in vivo* allowing radiolabeled FDT to selectively label tissues containing mycobacteria. In this thesis we described our exploration of three chemo-enzymatic strategies to synthesize [^{18}F]FDT from [^{18}F]FDG. Having identified the best enzymatic synthesis approach, we reported the scale-up of the enzymes in the Baculovirus system, and optimization of the [^{18}F]FDT labeling reaction for automated synthesis. We characterized the performance of the probe in two preclinical models of *M. tuberculosis* infection and demonstrated that serial imaging can provide evidence of response to treatment, Further, we determined the basic biodistribution of the probe in naïve monkeys and conducted toxicity testing to support the likely safety of the

FDT probe for use in evaluating and monitoring known mycobacterial infections. In addition to radiolabeled sugar, we explored the potential radiolabeling of modified MCP-1 with a PET radionuclide copper-64 to target macrophages *in vivo*. With having two different approaches, the overall goal was develop a specific PET imaging probe for the diagnosis of TB.

1.11 Overview of the thesis

Chapter 2:

In this chapter, we have synthesised [^{18}/^{19}F]FDT from three different enzymatic approaches. We expressed key biosynthetic enzymes (TreT, OtsA, OtsB and OtsAB fusion enzymes) and determined the kinetic parameters for each. We scaled-up the synthesis of [^{19}F]FDT using Hexokinase, OtsA and OtsB enzyme, and this allowed for a multi-gram synthesis of this compound. We also expressed the OtsA and OtsB enzymes in Sf9 insect cells, optimised and scale-up the expression.

Chapter 3:

In this chapter we demonstrated the *in vitro* and *in vivo* stability of FDT. In addition, we have shown that the compound has no toxicity effects when tested in two different animal species. From the radiotracer, [^{18}F]FDT, injection and subsequent PET/CT imaging, we were able to determine the biodistribution, uptake in TB infected cells and effectively monitor the response to treatment. From the blocking studies, we demonstrated that unlabelled FDT can block the uptake of radiolabelled FDT.

Chapter 4:

Described herein were the methods to incorporate the unnatural amino acid, azidohomoalanine (Aha) into the MCP-1 protein and carry out subsequent click chemistry reactions. We demonstrated the installation of various modifications including a potential cross-bridge

chelator. This labelled protein will then subsequently be used in radiolabelling with the PET radionuclide, copper-64 (^{64}Cu) which will allow for imaging of macrophages in animal models. In addition we confirmed the exact site of modifications by LC-MS/MS analysis. From the activity assays and CD analysis it was possible to determine the sites at which modifications may have a detrimental effect on activity.

1.12 References

1. World Health Organisation; Global tuberculosis report 2019. *World Health Organisation* **2019.**

2. Steingart, K. R.; Henry, M.; Ng, V.; Hopewell, P. C.; Ramsay, A.; Cunningham, J.; Urbanczik, R.; Perkins, M.; Aziz, M. A.; Pai, M., Fluorescence versus conventional sputum smear microscopy for tuberculosis: a systematic review. *The Lancet Infection Diseases* **2006,** *6* (9), 570-581.

3. Migliori, G. B.; Centis, R.; Lange, C.; Richardson, M. D. A.; Sotgiu, G., Emerging epidemic of drug-resistant tuberculosis in Europe, Russia, China, South America and Asia: current status and global perspectives. *Current Opinion in Pulmonary Medicine* **2010,** *16* (3), 171-179.

4. Oxlade, O.; Murray, M.; Tuberculosis and poverty: why are the poor at greater risk in India? *PLoS One* **2012,** *7* (11), e47533.

5. Pawlowski, A.; Jansson, M.; Sköld, M.; Rottenberg, M. E.; Källenius, G.; Tuberculosis and HIV co-infection. *PLoS Pathogens* **2012,** *8* (2), e1002464.

6. World Health Organisation., Global tuberculosis report 2017. *World Health Organisation, Geneva, Switzerland* **2017.**

7. Drobniewski, F. A.; Caws, M.; Gibson, A.; Young, D., Modern laboratory diagnosis of tuberculosis. *The Lancet Infectious Diseases* **2003,** *3* (3), 141-147.

8. Cambier, C. J.; Falkow, S.; Ramakrishnan, L., Host evasion and exploitation schemes of Mycobacterium tuberculosis. *Cell* **2014,** *159* (7), 1497-509.

9. Daffe, M.; Etienne, G., The capsule of Mycobacterium tuberculosis and its implications for pathogenicity. *Tubercle and lung disease : The Official Journal of the International Union against Tuberculosis and Lung Disease* **1999,** *79* (3), 153-69.

10. Vincent, A. T.; Nyongesa, S.; Morneau, I.; Reed, M. B.; Tocheva, E. I.; Veyrier, F. J., The Mycobacterial Cell Envelope: A Relict From the Past or the Result of Recent Evolution? *Frontiers in Microbiology* **2018,** *9*, 2341.

11. World Health Organisation; Treatment of tuberculosis: Guidelines. *World Health Organization* **2010**.

12. World Helath Organisation., Global TB Programme, *WHO, Geneva, Switzerland*. **2016**.

13. Migliori, G. B.; Sotgiu, G.; Gandhi, N. R.; Falzon, D.; DeRiemer, K.; Centis, R.; Hollm-Delgado, M. G.; Palmero, D.; Perez-Guzman, C.; Vargas, M. H.; D'Ambrosio, L.; Spanevello, A.; Bauer, M.; Chan, E. D.; Schaaf, H. S.; Keshavjee, S.; Holtz, T. H.; Menzies, D., Drug resistance beyond extensively drug-resistant tuberculosis: individual patient data meta-analysis. *The European Respiratory Journal* **2013,** *42* (1), 169-179.

14. Aggarwal, A.; Parai, M. K.; Shetty, N.; Wallis, D.; Woolhiser, L.; Hastings, C.; Dutta, N. K.; Galaviz, S.; Dhakal, R. C.; Shrestha, R.; Wakabayashi, S.; Walpole, C.; Matthews, D.; Floyd, D.; Scullion, P.; Riley, J.; Epemolu, O.; Norval, S.; Snavely, T.; Robertson, G. T.; Rubin, E. J.; Ioerger, T. R.; Sirgel, F. A.; van der Merwe, R.; van Helden, P. D.; Keller, P.; Bottger, E. C.; Karakousis, P. C.; Lenaerts, A. J.; Sacchettini, J. C., Development of a Novel Lead that Targets M. tuberculosis Polyketide Synthase 13. *Cell* **2017,** *170* (2), 249-259.e25.

15. Kaufmann, S. H.; Lange, C.; Rao, M.; Balaji, K. N.; Lotze, M.; Schito, M.; Zumla, A. I.; Maeurer, M.; Progress in tuberculosis vaccine development and host-directed therapies—a state of the art review. *The Lancet. Respiratory Medicine* **2014,** *2* (4), 301-320.

16. Trunz, B. B.; Fine, P.; Dye, C., Effect of BCG vaccination on childhood tuberculous meningitis and miliary tuberculosis worldwide: a meta-analysis and assessment of cost-effectiveness. *Lancet* **2006,** *367* (9517), 1173-80.

17. Colditz, G. A.; Berkey, C. S.; Mosteller, F.; Brewer, T. F.; Wilson, M. E.; Burdick, E.; Fineberg, H. V., The efficacy of bacillus Calmette-Guerin vaccination of newborns and infants in the prevention of tuberculosis: meta-analyses of the published literature. *Pediatrics* **1995,** *96* (1 Pt 1), 29-35.

18. Davenne, T.; McShane, H., Why don't we have an effective tuberculosis vaccine yet? *Expert Review of Vaccines* **2016,** *15* (8), 1009-13.

19. Tameris, M. D.; Hatherill, M.; Landry, B. S.; Scriba, T. J.; Snowden, M. A.; Lockhart, S.; Shea, J. E.; McClain, J. B.; Hussey, G. D.; Hanekom, W. A.; Mahomed, H.; McShane, H., Safety and efficacy of MVA85A, a new tuberculosis vaccine, in infants previously vaccinated with BCG: a randomised, placebo-controlled phase 2b trial. *Lancet* **2013,** *381* (9871), 1021-8.

20. Grosset, J.; Mycobacterium tuberculosis in the extracellular compartment: an underestimated adversary. *Antimicrobial Agents and Chemotherapy* **2003,** *47* (3), 833-836.

21. Kirihara, J. M.; Hillier, S. L.; Coyle, M. B., Improved detection times for Mycobacterium avium complex and Mycobacterium tuberculosis with the BACTEC radiometric system. *Journal of Clinical Microbiology* **1985,** *22* (5), 841-5.

22. Pfyffer, G. E.; Cieslak, C.; Welscher, H. M.; Kissling, P.; Rusch-Gerdes, S., Rapid detection of mycobacteria in clinical specimens by using the automated BACTEC 9000 MB system and comparison with radiometric and solid-culture systems. *Journal of Clinical Microbiology* **1997,** *35* (9), 2229-34.

23. Pfyffer, G. E.; Welscher, H. M.; Kissling, P.; Cieslak, C.; Casal, M. J.; Gutierrez, J.; Rusch-Gerdes, S., Comparison of the Mycobacteria Growth Indicator Tube (MGIT) with radiometric and solid culture for recovery of acid-fast bacilli. *Journal of Clinical Microbiology* **1997,** *35* (2), 364-8.

24. Chew, W. K.; Lasaitis, R. M.; Schio, F. A.; Gilbert, G. L., Clinical evaluation of the Mycobacteria Growth Indicator Tube (MGIT) compared with radiometric (Bactec) and solid media for isolation of Mycobacterium species. *Journal of Medical Microbiology* **1998,** *47* (9), 821-7.

25. Hanna, B. A.; Ebrahimzadeh, A.; Elliott, L. B.; Morgan, M. A.; Novak, S. M.; Rusch-Gerdes, S.; Acio, M.; Dunbar, D. F.; Holmes, T. M.; Rexer, C. H.; Savthyakumar, C.; Vannier, A. M., Multicenter evaluation of the BACTEC MGIT 960 system for recovery of mycobacteria. *Journal of Clinical Microbiology* **1999,** *37* (3), 748-52.

26. Lebrun, L.; Espinasse, F.; Poveda, J. D.; Vincent-Levy-Frebault, V., Evaluation of nonradioactive DNA probes for identification of mycobacteria. *Journal of Clinical Microbiology* **1992,** *30* (9), 2476-8.

27. Stender, H.; Lund, K.; Petersen, K. H.; Rasmussen, O. F.; Hongmanee, P.; Miorner, H.; Godtfredsen, S. E., Fluorescence In situ hybridization assay using peptide nucleic acid probes for differentiation between tuberculous and nontuberculous mycobacterium species in smears of mycobacterium cultures. *Journal of Clinical Microbiology* **1999,** *37* (9), 2760-5.

28. Suffys, P. N.; da Silva Rocha, A.; de Oliveira, M.; Campos, C. E.; Barreto, A. M.; Portaels, F.; Rigouts, L.; Wouters, G.; Jannes, G.; van Reybroeck, G.; Mijs, W.; Vanderborght, B., Rapid identification of Mycobacteria to the species level using INNO-LiPA Mycobacteria, a reverse hybridization assay. *Journal of Clinical Microbiology* **2001,** *39* (12), 4477-82.

29. Pai, M.; Denkinger, C. M.; Kik, S. V.; Rangaka, M. X.; Zwerling, A.; Oxlade, O.; Metcalfe, J. Z.; Cattamanchi, A.; Dowdy, D. W.; Dheda, K.; Banaei, N., Gamma interferon release assays for detection of Mycobacterium tuberculosis infection. *Clinical Microbiology Reviews* **2014,** *27* (1), 3-20.

30. Herrera, V.; Perry, S.; Parsonnet, J.; Banaei, N., Clinical Application and Limitations of Interferon-γ Release Assays for the Diagnosis of Latent Tuberculosis Infection. *Clinical Infectious Diseases* **2011,** *52* (8), 1031-1037.

31. Getahun, H.; Matteelli, A.; Abubakar, I.; Aziz, M. A.; Baddeley, A.; Barreira, D.; Den Boon, S.; Borroto Gutierrez, S. M.; Bruchfeld, J.; Burhan, E.; Cavalcante, S.; Cedillos, R.; Chaisson, R.; Chee, C. B.; Chesire, L.; Corbett, E.; Dara, M.; Denholm, J.; de Vries, G.; Falzon, D.; Ford, N.; Gale-Rowe, M.; Gilpin, C.; Girardi, E.; Go, U. Y.; Govindasamy, D.; A, D. G.; Grzemska, M.; Harris, R.; Horsburgh, C. R., Jr.; Ismayilov, A.; Jaramillo, E.; Kik, S.; Kranzer, K.; Lienhardt, C.; LoBue, P.; Lonnroth, K.; Marks, G.; Menzies, D.; Migliori, G. B.; Mosca, D.; Mukadi, Y. D.; Mwinga, A.; Nelson, L.; Nishikiori, N.; Oordt-Speets, A.; Rangaka, M. X.; Reis, A.; Rotz, L.; Sandgren, A.; Sane Schepisi, M.; Schunemann, H. J.; Sharma, S. K.; Sotgiu, G.; Stagg, H. R.; Sterling, T. R.; Tayeb, T.; Uplekar, M.; van der Werf, M. J.; Vandevelde, W.; van Kessel, F.; van't Hoog, A.; Varma, J. K.; Vezhnina, N.; Voniatis, C.; Vonk Noordegraaf-Schouten, M.; Weil, D.; Weyer, K.; Wilkinson, R. J.; Yoshiyama, T.; Zellweger, J. P.; Raviglione, M., Management of latent Mycobacterium tuberculosis infection: WHO guidelines for low tuberculosis burden countries. *The European Respiratory Journal* **2015,** *46* (6), 1563-76.

32. Wu, M.; Shu, J., Multimodal Molecular Imaging: Current Status and Future Directions. *Contrast Media & Molecular imaging* **2018,** *2018*, 1382183.

33. Willmann, J. K.; van Bruggen, N.; Dinkelborg, L. M.; Gambhir, S. S., Molecular imaging in drug development. *Nature reviews. Drug Discovery* **2008,** *7* (7), 591-607.

34. Chen, Z. Y.; Wang, Y. X.; Lin, Y.; Zhang, J. S.; Yang, F.; Zhou, Q. L.; Liao, Y. Y., Advance of molecular imaging technology and targeted imaging agent in imaging and therapy. *BioMed Research International* **2014,** *2014*, 819324.

35. Maisonial, A.; Kuhnast, B.; Papon, J.; Boisgard, R.; Bayle, M.; Vidal, A.; Auzeloux, P.; Rbah, L.; Bonnet-Duquennoy, M.; Miot-Noirault, E.; Galmier, M. J.; Borel, M.; Askienazy, S.; Dolle, F.; Tavitian, B.; Madelmont, J. C.; Moins, N.; Chezal, J. M., Single photon emission computed tomography/positron emission tomography imaging and targeted radionuclide therapy of melanoma: new multimodal fluorinated and iodinated radiotracers. *Journal of Medicinal Chemistry* **2011,** *54* (8), 2745-66.

36. Hadjipanayis, C. G.; Jiang, H.; Roberts, D. W.; Yang, L., Current and future clinical applications for optical imaging of cancer: from intraoperative surgical guidance to cancer screening. *Seminars in Oncology* **2011,** *38* (1), 109-18.

37. Kim, T.; Lee, N.; Arifin, D. R.; Shats, I.; Janowski, M.; Walczak, P.; Hyeon, T.; Bulte, J. W. M., In Vivo Micro-CT Imaging of Human Mesenchymal Stem Cells Labeled with Gold-Poly-L-Lysine Nanocomplexes. *Advanced Functional Materials* **2017,** *27* (3).

38. Peldschus, K.; Ittrich, H., Magnetic resonance imaging of metastases in xenograft mouse models of cancer. *Methods in Molecular Biology* **2014,** *1070*, 213-22.

39. Lee, H. W.; Singh, T. D.; Lee, S. W.; Ha, J. H.; Rehemtulla, A.; Ahn, B. C.; Jeon, Y. H.; Lee, J., Evaluation of therapeutic effects of natural killer (NK) cell-based immunotherapy in mice using in vivo apoptosis bioimaging with a caspase-3 sensor. *FASEB Journal : official publication of the Federation of American Societies for Experimental Biology* **2014,** *28* (7), 2932-41.

40. Lee, H. W.; Gangadaran, P.; Kalimuthu, S.; Ahn, B. C., Advances in Molecular Imaging Strategies for In Vivo Tracking of Immune Cells. *BioMed Research International* **2016,** *2016*, 1946585.

41. Sinusas, A. J.; Bengel, F.; Nahrendorf, M.; Epstein, F. H.; Wu, J. C.; Villanueva, F. S.; Fayad, Z. A.; Gropler, R. J., Multimodality cardiovascular molecular imaging, part I. *Circulation. Cardiovascular Imaging* **2008,** *1* (3), 244-56.

42. Pysz, M. A.; Gambhir, S. S.; Willmann, J. K., Molecular imaging: current status and emerging strategies. *Clinical Radiology* **2010,** *65* (7), 500-16.

43. Skoura, E.; Zumla, A.; Bomanji, J., Imaging in tuberculosis. *International Journal of Infectious Diseases* **2015,** *32*, 87-93.

44. Gambhir, S. S., Molecular imaging of cancer with positron emission tomography. *Nature reviews. Cancer* **2002,** *2* (9), 683-93.

45. Miller, P. W.; Long, N. J.; Vilar, R.; Gee, A. D., Synthesis of 11C, 18F, 15O, and 13N radiolabels for positron emission tomography. *Angewandte Chemie* **2008,** *47* (47), 8998-9033.

46. Zhernosekov, K. P.; Filosofov, D. V.; Baum, R. P.; Aschoff, P.; Bihl, H.; Razbash, A. A.; Jahn, M.; Jennewein, M.; Rosch, F., Processing of generator-produced 68Ga for medical application. *Journal of Nuclear Medicine* **2007,** *48* (10), 1741-8.

47. Kasbollah, A.; Eu, P.; Cowell, S.; Deb, P., Review on production of 89Zr in a medical cyclotron for PET radiopharmaceuticals. *Journal of Nuclear Medicine Technology* **2013,** *41* (1), 35-41.

48. Xie, Q.; Zhu, H.; Wang, F.; Meng, X.; Ren, Q.; Xia, C.; Yang, Z., Establishing Reliable Cu-64 Production Process: From Target Plating to Molecular Specific Tumor Micro-PET Imaging. *Molecules* **2017,** *22* (4).

49. Ismail, F. M. D., Important fluorinated drugs in experimental and clinical use. *Journal of Fluorine Chemistry* **2002,** *118* (1), 27-33.

50. Casella, V.; Ido, T.; Wolf, A. P.; Fowler, J. S.; MacGregor, R. R.; Ruth, T. J., Anhydrous F-18 labeled eslemental flurine for radiopharmaceutical preparation. *Journal of Nuclear Medicine* **1980,** *21* (8), 750-7.

51. Jacobson, O.; Kiesewetter, D. O.; Chen, X., Fluorine-18 radiochemistry, labeling strategies and synthetic routes. *Bioconjugate Chemistry* **2015,** *26* (1), 1-18.

52. Coenen, H. H., Fluorine-18 labeling methods: Features and possibilities of basic reactions. *Ernst Schering Research Foundation Workshop* **2007,** (62), 15-50.

53. Lee, J. D.; Shin, K. H.; Cho, S. N.; Shin, J. S.; Lee, M. G.; Yang, W. I.; Park, C. Y.; Yoo, H. S.; Lee, J. T.; Awh, O. D., Immunoscintigraphy in the detection of tuberculosis with radiolabelled antibody fragment against Mycobacterium bovis bacillus Calmette-Guerin: a preliminary study in a rabbit model. *European Journal of Nuclear Medicine* **1992,** *19* (12), 1011-5.

54. Jimenez-Heffernan, A.; Villanueva, J. L.; Moral, A.; Rebollo, A.; Gonzalez, F. M.; Urena, M.; Lopez-Ruiz, J. M.; Llamas-Elvira, J. M.; Mateo, A., Detection of inflammation/infection with human polyclonal immunoglobulin G labelled with 99Tcm. *The British Journal of Radiology* **1994,** *67* (800), 770-4.

55. Deshmane, S. L.; Kremlev, S.; Amini, S.; Sawaya, B. E., Monocyte chemoattractant protein-1 (MCP-1): an overview. *Journal of interferon & cytokine research : The Official Journal of the International Society for Interferon and Cytokine Research* **2009,** *29* (6), 313-26.

56. Zhang, Y. J.; Rutledge, B. J.; Rollins, B. J., Structure/activity analysis of human monocyte chemoattractant protein-1 (MCP-1) by mutagenesis. Identification of a mutated

protein that inhibits MCP-1-mediated monocyte chemotaxis. *The Journal of Biological Chemistry* **1994,** *269* (22), 15918-24.

57. Sadek, M. I.; Sada, E.; Toossi, Z.; Schwander, S. K.; Rich, E. A., Chemokines induced by infection of mononuclear phagocytes with mycobacteria and present in lung alveoli during active pulmonary tuberculosis. *American Journal of Respiratory Cell and Molecular Biology* **1998,** *19* (3), 513-21.

58. Gonzalez-Juarrero, M.; Turner, O. C.; Turner, J.; Marietta, P.; Brooks, J. V.; Orme, I. M; immunity, Temporal and Spatial Arrangement of Lymphocytes within Lung Granulomas Induced by Aerosol Infection withMycobacterium tuberculosis. *Infection and Immunity* **2001,** *69* (3), 1722-1728.

59. Goo, J. M.; Im, J. G.; Do, K. H.; Yeo, J. S.; Seo, J. B.; Kim, H. Y.; Chung, J. K., Pulmonary tuberculoma evaluated by means of FDG PET: findings in 10 cases. *Radiology* **2000,** *216* (1), 117-21.

60. Kim, I. J.; Lee, J. S.; Kim, S. J.; Kim, Y. K.; Jeong, Y. J.; Jun, S.; Nam, H. Y.; Kim, J. S., Double-phase 18F-FDG PET-CT for determination of pulmonary tuberculoma activity. *European Journal of Nuclear Medicine and Molecular Imaging* **2008,** *35* (4), 808-14.

61. Farwell, M. D.; Pryma, D. A.; Mankoff, D. A., PET/CT imaging in cancer: current applications and future directions. *Cancer* **2014,** *120* (22), 3433-45.

62. Yu, W.-Y.; Lu, P.-X.; Assadi, M.; Huang, X.-L.; Skrahin, A.; Rosenthal, A.; Gabrielian, A.; Tartakovsky, M.; Wáng, Y. X. J., Updates on (18)F-FDG-PET/CT as a clinical tool for tuberculosis evaluation and therapeutic monitoring. *Quant Imaging Med Surg* **2019,** *9* (6), 1132-1146.

63. Davis, S. L.; Nuermberger, E. L.; Um, P. K.; Vidal, C.; Jedynak, B.; Pomper, M. G.; Bishai, W. R.; Jain, S. K., Noninvasive pulmonary [18F]-2-fluoro-deoxy-D-glucose positron

emission tomography correlates with bactericidal activity of tuberculosis drug treatment. *Antimicrobial Agents and Chemotherapy* **2009,** *53* (11), 4879-84.

64. Demura, Y.; Tsuchida, T.; Uesaka, D.; Umeda, Y.; Morikawa, M.; Ameshima, S.; Ishizaki, T.; Fujibayashi, Y.; Okazawa, H., Usefulness of 18F-fluorodeoxyglucose positron emission tomography for diagnosing disease activity and monitoring therapeutic response in patients with pulmonary mycobacteriosis. *European Journal of Nuclear Medicine and Molecular Imaging* **2009,** *36* (4), 632-9.

65. Park, I. N.; Ryu, J. S.; Shim, T. S., Evaluation of therapeutic response of tuberculoma using F-18 FDG positron emission tomography. *Clinical Nuclear Medicine* **2008,** *33* (1), 1-3.

66. Martinez, V.; Castilla-Lievre, M. A.; Guillet-Caruba, C.; Grenier, G.; Fior, R.; Desarnaud, S.; Doucet-Populaire, F.; Boue, F., (18)F-FDG PET/CT in tuberculosis: an early non-invasive marker of therapeutic response. *The International Journal of Tuberculosis and Lung Disease* **2012,** *16* (9), 1180-5.

67. Park, Y. H.; Yu, C. M.; Kim, E. S.; Jung, J. O.; Seo, H. S.; Lee, J. H.; Hur, S. C.; Kim, S. Y.; Lee, H. Y., Monitoring Therapeutic Response in a Case of Extrapulmonary Tuberculosis by Serial F-18 FDG PET/CT. *Nuclear Medicine and Molecular Imaging* **2012,** *46* (1), 69-72.

68. Lefebvre, N.; Argemi, X.; Meyer, N.; Mootien, J.; Douiri, N.; Sferrazza-Mandala, S.; Schramm, F.; Weingertner, N.; Christmann, D.; Hansmann, Y.; Imperiale, A., Clinical usefulness of (18)F-FDG PET/CT for initial staging and assessment of treatment efficacy in patients with lymph node tuberculosis. *Nuclear Medicine and Biology* **2017,** *50*, 17-24.

69. Glaudemans, A. W.; Signore, A., FDG-PET/CT in infections: the imaging method of choice? *European Journal of Nuclear Medicine and Molecular Imaging* **2010,** *37* (10), 1986-91.

70. Sathekge, M.; Maes, A.; Kgomo, M.; Pottel, H.; Stolz, A.; Van De Wiele, C., FDG uptake in lymph-nodes of HIV+ and tuberculosis patients: implications for cancer staging. *The quarterly journal of nuclear medicine and molecular imaging : official publication of the Italian Association of Nuclear Medicine (AIMN) [and] the International Association of Radiopharmacology (IAR), [and] Section of the So* **2010,** *54* (6), 698-703.

71. Corstens, F. H.; van der Meer, J. W., Nuclear medicine's role in infection and inflammation. *Lancet* **1999,** *354* (9180), 765-70.

72. Foss, C. A.; Harper, J. S.; Wang, H.; Pomper, M. G.; Jain, S. K., Noninvasive molecular imaging of tuberculosis-associated inflammation with radioiodinated DPA-713. *The Journal of Infectious Diseases* **2013,** *208* (12), 2067-74.

73. Foss, C. A.; Kulik, L.; Ordonez, A. A.; Jain, S. K.; Michael Holers, V.; Thurman, J. M.; Pomper, M. G., SPECT/CT Imaging of Mycobacterium tuberculosis Infection with [(125)I]anti-C3d mAb. *Molecular Imaging and Biology* **2019,** *21* (3), 473-481.

74. Ning, X.; Seo, W.; Lee, S.; Takemiya, K.; Rafi, M.; Feng, X.; Weiss, D.; Wang, X.; Williams, L.; Camp, V. M.; Eugene, M.; Taylor, W. R.; Goodman, M.; Murthy, N., PET imaging of bacterial infections with fluorine-18-labeled maltohexaose. *Angewandte Chemie* **2014,** *53* (51), 14096-14101.

75. Singer, M. A.; Lindquist, S., Thermotolerance in Saccharomyces cerevisiae: the Yin and Yang of trehalose. *Trends in Biotechnology* **1998,** *16* (11), 460-8.

76. Elbein, A. D.; Pan, Y. T.; Pastuszak, I.; Carroll, D., New insights on trehalose: a multifunctional molecule. *Glycobiology* **2003,** *13* (4), 17r-27r.

77. Ohtake, S.; Wang, Y. J., Trehalose: current use and future applications. *Journal of Pharmaceutical Sciences* **2011,** *100* (6), 2020-53.

78. Avonce, N.; Leyman, B.; Mascorro-Gallardo, J. O.; Van Dijck, P.; Thevelein, J. M.; Iturriaga, G., The Arabidopsis trehalose-6-P synthase AtTPS1 gene is a regulator of glucose, abscisic acid, and stress signaling. *Plant Physiology* **2004,** *136* (3), 3649-59.

79. Kalscheuer, R.; Koliwer-Brandl, H., Genetics of Mycobacterial Trehalose Metabolism. *Microbiology Spectrum* **2014,** *2* (3).

80. Backus, K. M.; Boshoff, H. I.; Barry, C. S.; Boutureira, O.; Patel, M. K.; D'Hooge, F.; Lee, S. S.; Via, L. E.; Tahlan, K.; Barry, C. E.; Davis, B. G., Uptake of unnatural trehalose analogs as a reporter for Mycobacterium tuberculosis. *Nature Chemical Biology* **2011,** *7* (4), 228-235.

81. Hoffmann, C.; Leis, A.; Niederweis, M.; Plitzko, J. M.; Engelhardt, H., Disclosure of the mycobacterial outer membrane: cryo-electron tomography and vitreous sections reveal the lipid bilayer structure. *Proceedings of the National Academy of Sciences of the United States of America* **2008,** *105* (10), 3963-7.

82. Barry, C. E., 3rd; Mdluli, K., Drug sensitivity and environmental adaptation of mycobacterial cell wall components. *Trends in Microbiology* **1996,** *4* (7), 275-81.

83. Kalscheuer, R.; Weinrick, B.; Veeraraghavan, U.; Besra, G. S.; Jacobs, W. R., Jr., Trehalose-recycling ABC transporter LpqY-SugA-SugB-SugC is essential for virulence of Mycobacterium tuberculosis. *Proceedings of the National Academy of Sciences of the United States of America* **2010,** *107* (50), 21761-6.

84. Grzegorzewicz, A. E.; Pham, H.; Gundi, V. A.; Scherman, M. S.; North, E. J.; Hess, T.; Jones, V.; Gruppo, V.; Born, S. E.; Kordulakova, J.; Chavadi, S. S.; Morisseau, C.; Lenaerts, A. J.; Lee, R. E.; McNeil, M. R.; Jackson, M., Inhibition of mycolic acid transport across the Mycobacterium tuberculosis plasma membrane. *Nature Chemical Biology* **2012,** *8* (4), 334-41.

85. Jackson, M.; Raynaud, C.; Laneelle, M. A.; Guilhot, C.; Laurent-Winter, C.; Ensergueix, D.; Gicquel, B.; Daffe, M., Inactivation of the antigen 85C gene profoundly affects the mycolate content and alters the permeability of the Mycobacterium tuberculosis cell envelope. *Molecular Microbiology* **1999,** *31* (5), 1573-87.

86. Puech, V.; Bayan, N.; Salim, K.; Leblon, G.; Daffe, M., Characterization of the in vivo acceptors of the mycoloyl residues transferred by the corynebacterial PS1 and the related mycobacterial antigens 85. *Molecular Microbiology* **2000,** *35* (5), 1026-41.

87. Tonge, P. J., Another brick in the wall. *Nature Structural Biology* **2000,** *7* (2), 94-6.

88. Backus, K. M.; Boshoff, H. I.; Barry, C. S.; Boutureira, O.; Patel, M. K.; D'Hooge, F.; Lee, S. S.; Via, L. E.; Tahlan, K.; Barry, C. E., 3rd; Davis, B. G., Uptake of unnatural trehalose analogs as a reporter for Mycobacterium tuberculosis. *Nature Chemical Biology* **2011,** *7* (4), 228-35.

89. Foley, H. N.; Stewart, J. A.; Kavunja, H. W.; Rundell, S. R.; Swarts, B. M., Bioorthogonal Chemical Reporters for Selective In Situ Probing of Mycomembrane Components in Mycobacteria. *Angewandte Chemie* **2016,** *55* (6), 2053-7.

90. Rodriguez-Rivera, F. P.; Zhou, X.; Theriot, J. A.; Bertozzi, C. R., Visualization of mycobacterial membrane dynamics in live cells. *Journal of the American Chemical Society* **2017,** *139* (9), 3488-3495.

91. Swarts, B. M.; Holsclaw, C. M.; Jewett, J. C.; Alber, M.; Fox, D. M.; Siegrist, M. S.; Leary, J. A.; Kalscheuer, R.; Bertozzi, C. R., Probing the mycobacterial trehalome with bioorthogonal chemistry. *Journal of the American Chemical Society* **2012,** *134* (39), 16123-6.

92. Kamariza, M.; Shieh, P.; Ealand, C. S.; Peters, J. S.; Chu, B.; Rodriguez-Rivera, F. P.; Babu Sait, M. R.; Treuren, W. V.; Martinson, N.; Kalscheuer, R.; Kana, B. D.; Bertozzi,

C. R., Rapid detection of Mycobacterium tuberculosis in sputum with a solvatochromic trehalose probe. *Science Translational Medicine* **2018,** *10* (430).

93. Hodges, H. L.; Brown, R. A.; Crooks, J. A.; Weibel, D. B.; Kiessling, L. L. J. P. o. t. N. A. o. S., Imaging mycobacterial growth and division with a fluorogenic probe. *PNAS* **2018,** *115* (20), 5271-5276.

94. Avonce, N.; Mendoza-Vargas, A.; Morett, E.; Iturriaga, G., Insights on the evolution of trehalose biosynthesis. *BMC Evol Biol* **2006,** *6*, 109-109.

95. Zaparty, M.; Tjaden, B.; Hensel, R.; Siebers, B., The central carbohydrate metabolism of the hyperthermophilic crenarchaeote Thermoproteus tenax: pathways and insights into their regulation. *Archives of Microbiology* **2008,** *190* (3), 231-45.

96. Maruta, K.; Mitsuzumi, H.; Nakada, T.; Kubota, M.; Chaen, H.; Fukuda, S.; Sugimoto, T.; Kurimoto, M., Cloning and sequencing of a cluster of genes encoding novel enzymes of trehalose biosynthesis from thermophilic archaebacterium Sulfolobus acidocaldarius. *Biochimica et Biophysica Acta* **1996,** *1291* (3), 177-81.

97. Nishimoto, T.; Nakano, M.; Nakada, T.; Chaen, H.; Fukuda, S.; Sugimoto, T.; Kurimoto, M.; Tsujisaka, Y., Purification and properties of a novel enzyme, trehalose synthase, from Pimelobacter sp. R48. *Bioscience, Biotechnology, and Biochemistry* **1996,** *60* (4), 640-4.

98. Qu, Q.; Lee, S. J.; Boos, W., TreT, a novel trehalose glycosyltransferring synthase of the hyperthermophilic archaeon Thermococcus litoralis. *The Journal of Biological Chemistry* **2004,** *279* (46), 47890-7.

99. Eis, C.; Nidetzky, B., Characterization of trehalose phosphorylase from Schizophyllum commune. *The Biochemical Journal* **1999,** *341 (Pt 2)*, 385-93.

100. Belocopitow, E.; Marechal, L. R., Trehalose phosphorylase from Euglena gracilis. *Biochimica et Biophysica Acta* **1970,** *198* (1), 151-4.

101. Walmagh, M.; Zhao, R.; Desmet, T., Trehalose Analogues: Latest Insights in Properties and Biocatalytic Production. *International Journal of Molecular Sciences* **2015,** *16* (6), 13729-45.

102. O'Neill, M. K.; Piligian, B. F.; Olson, C. D.; Woodruff, P. J.; Swarts, B. M., Tailoring Trehalose for Biomedical and Biotechnological Applications. *Pure Appl Chem* **2017,** *89* (9), 1223-1249.

103. Hadfield, A. F.; Hough, L.; Richardson, A. C. J. C. R., The synthesis of 6-deoxy-6-fluoro-α, α-trehalose and related analogues. **1978,** *63*, 51-60.

104. Hadfield, A. F.; Hough, L.; Richardson, A. C. J. C. R., The syntheses of 4, 6-dideoxy-4, 6-difluoro-and 4-deoxy-4-fluoro-α, α-trehalose. *Carbohydrate Research* **1979,** *71* (1), 95-102.

105. Lin, F. L.; van Halbeek, H.; Bertozzi, C. R., Synthesis of mono-and dideoxygenated α, α-trehalose analogs. *Carbohydrate Research* **2007,** *342* (14), 2014-2030.

106. Leigh, C. D.; Bertozzi, C. R., Synthetic studies toward Mycobacterium tuberculosis sulfolipid-I. *The Journal of Organic Chemistry* **2008,** *73* (3), 1008-17.

107. Rodriguez, M. A.; Boutureira, O.; Matheu, M. I.; Diaz, Y.; Castillon, S.; Seeberger, P. H., Synthesis of 2-iodoglycals, glycals, and 1,1'-disaccharides from 2-Deoxy-2-iodopyranoses under dehydrative glycosylation conditions. *The Journal of Organic Chemistry* **2007,** *72* (23), 8998-9001.

108. Pratt, M. R.; Leigh, C. D.; Bertozzi, C. R., Formation of 1,1-alpha,alpha-glycosidic bonds by intramolecular aglycone delivery. A convergent synthesis of trehalose. *Organic Letters* **2003,** *5* (18), 3185-8.

109. Gómez, A. M.; Pedregosa, A.; Valverde, S. n.; López, J. C. J. T. l., Stereoselective synthesis of substituted exo-glycals from 1-exo-methylene pyranoses. *Tetrahedron Letters* **2003,** *44* (32), 6111-6116.

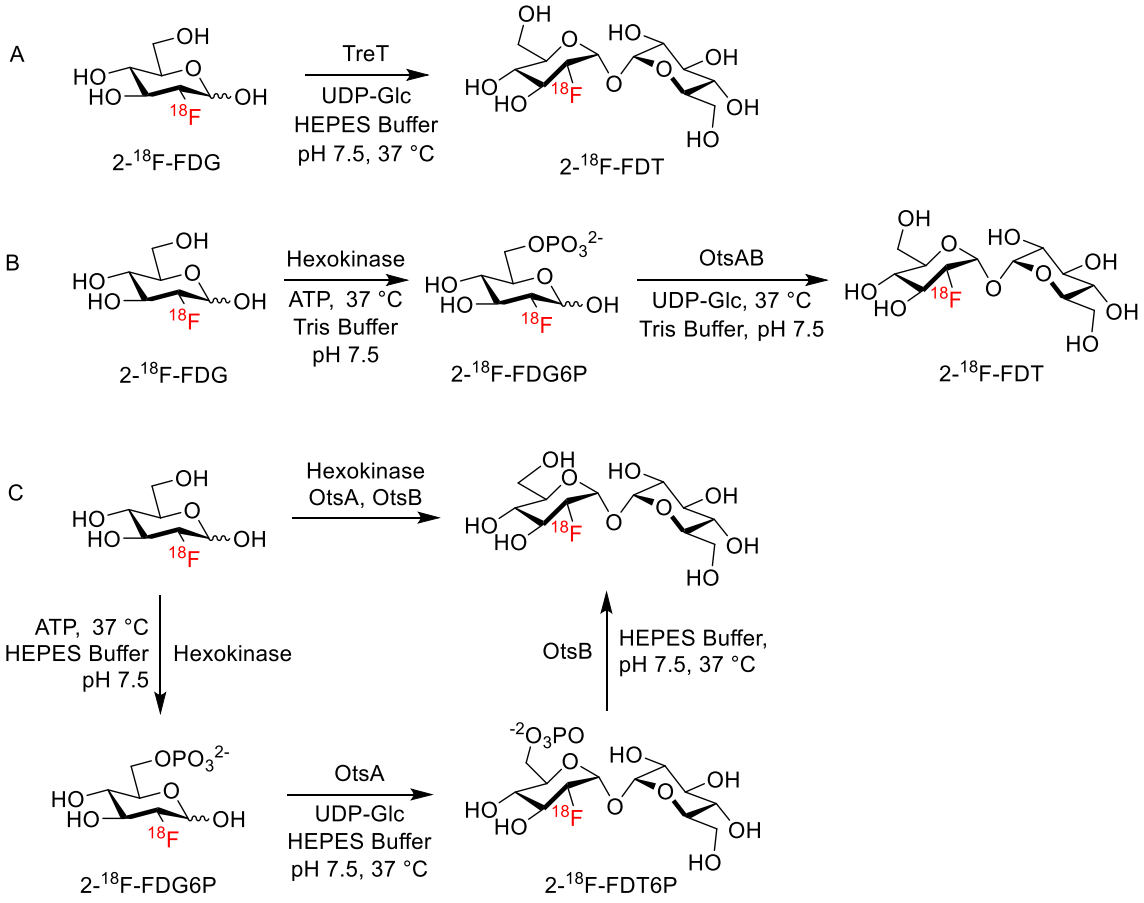
110. Eliseo, T.; Ragona, L.; Catalano, M.; Assfalg, M.; Paci, M.; Zetta, L.; Molinari, H.; Cicero, D. O., Structural and dynamic determinants of ligand binding in the ternary complex of chicken liver bile acid binding protein with two bile salts revealed by NMR. *Biochemistry* **2007,** *46* (44), 12557-67.

2 Chapter 2: Enzymatic Transformation of 2-[^{18}F]Fluoro-2-deoxy-D-glucose ([^{18}F]FDG) to 2-deoxy-2-[^{18}F]Fluoro-trehalose ([^{18}F]FDT) for PET Imaging of Tuberculosis

2.1 Introduction

As discussed previously, the ultimate goal of this project is to develop a specific PET imaging agent for the diagnosis of TB. Herein, we describe the strategies we employed to synthesise and characterise 2-deoxy-2-[^{18}F] fluoro-trehalose ([^{18}F]FDT). We preferred an enzymatic synthesis approach over the chemical synthesis due to ease of synthesis in aqueous conditions, with less purification steps needed to get stereoselective product. This approach allows the synthesis and purification of [^{18}F]FDT in a reasonable time compatible with the short half-life of [^{18}F]FDG (110 min)[1]. We explored three strategies as laid down in **Scheme 2.1**.

Strategy **2.1A** is based on the use of trehalose glycosyltransferring synthase (TreT) enzyme. This enzyme uses glycosyl acceptor (N-glucose(s) and glycosyl donor (diphosphate glucose(s)) to yield trehalose analogues in a single step. TreT enzymes have been found in various organisms such as *Thermococus litoralis*[2], *Pyrococus horikoshii* (*P. horikoshii*)[3], *Thermoproteus tenax* (*T. tenax*)[4] and *Rubrobacter xylanophilus*[5]. These enzymes have high thermal stability with an optimum stability temperature of up to 86 ^{o}C reported for *T. litoralis*[4]. TreT from both *T. litoralis* and *R. xylanophilus* utilizes a highly expensive donor substrate, adenosine diphosphate glucose (ADP-Glc) and are reversible[2], therefore, we opted against using these enzymes for the synthesis of [^{18}F]FDT.



Scheme 2.1. Enzymatic synthesis approaches employed for the synthesis of [^{18}F]FDT. A) Enzymatic synthesis of [^{18}F]FDT from TreT enzymes. This strategy utilizes two substrates, a donor (uridine diphosphate glucose (UDP-Glc)) and an acceptor (FDG). With utilizing a single enzyme, TreT, the product is obtained in a single step. HEPES buffer solution contains 50 mM HEPES, 100 mM NaCl and 10 mM $MgCl_2$, pH 7.5. **B**) Enzymatic synthesis of [^{18}F]FDT from hexokinase and an OtsAB fusion enzyme. In this strategy, hexokinase catalyses the phosphorylation of FDG and the OtsAB fusion enzyme subsequently catalyses the glycosylation reaction and hydrolysis of the phosphate group to yield the neutral sugar. HEPES buffer solution contains 50 mM HEPES, 100 mM NaCl and 10 mM $MgCl_2$, pH 7.5 **C**) [^{18}F]FDT synthesis from hexokinase, OtsA and OtsB enzyme. This is a three steps, three enzyme strategy whereby hexokinase catalyses the phosphorylation of FDG to yield FDG6P. FDG6P reaction is catalysed by OtsA in the presence of UDP-Glc as a donor to yield FDT6P. OtsB enzyme further catalyses the dephosphorylation of FDT6P to yield FDT. HEPES buffer solution contains 50 mM HEPES, 100 mM NaCl and 10 mM $MgCl_2$, pH 7.5.

TreT from *P. horikoshii* catalyses the synthesis of trehalose and its analogues from nucleoside diphosphate (NDP)-glucose and glucose[3]. This enzyme uses various NDP-glucose as donor substrates such as UDP-Glc, ADP-Glc and GDP-Glc and can process monosaccharides other than glucose[6]. While this enzyme has also been reported as reversible, the reversible kinetic parameters reported[6] indicate the forward reaction is favoured. The properties of *P. horikoshii* make this enzyme an ideal candidate to be used in the synthesis of FDT.

TreT from *T. tenax*[4] was also considered as it only catalyses the formation of trehalose analogues from the corresponding donor and acceptor molecules. TreT from *T.tenax* cannot degrade trehalose as it is unidirectional[4]. In addition, it can process monosaccharides other than glucose as an acceptor, therefore recently, this enzyme has been used in the synthesis of a wide range of disaccharides sugars[7].

We explored strategy **2.1B** to synthesise [^{18}F]FDT from [^{18}F]FDG. This approach makes use of two enzymes: The commercially available yeast hexokinase (EC 2.7.1.1) which catalyses the phosphorylation of the glucose analogues[8-10]. This enzyme has been extensively studied for the phosphorylation of unprotected carbohydrates[8]. Hexokinase uses metabolic intermediates as reagents and water/buffer as solvents to catalyse the regioselective phosphorylation of the unprotected sugars[8]. On the other hand, phosphorylation by chemical methods requires numerous protection and deprotection steps[11]. Chemical synthesis often involves multi-step syntheses and extensive purification in each step, resulting in low yield of the product[12]. Hexokinase has broad substrate specificity and catalyses the phosphorylation of a number of deoxy and deoxyfluoro analogues of D-glucose, with slight kinetic preference for α-glucopyranose over β-glucopyranose[8, 13].

The other enzymes used in this strategy is the fusion of trehalose-6-phosphate synthase (TPS also called OtsA in *E. coli*. For convenience we will refer this enzyme as OtsA thoughout this thesis) and trehalose-6-phosphate phosphates (TPP also called OtsB in *E. coli.* We will refer

this OtsB throughout)[14-17] (**2.1C**). OtsAB fusion enzyme has been studied only in a few organisms[18, 19], where bacteria accumulate trehalose from the single enzyme OtsAB under osmotic stress conditions[18, 19]. Although the current studies are only limited to G6P as an acceptor substrate, with advantage of two enzymes synthesis over three enzyme synthesis, we nevertheless investigated this approach.

Finally, strategy **2.1C** uses 3 enzymes i.e. hexokinase, OtsA and OtsB for the overall synthesis of [^{18}F]FDT from [^{18}]FDG. As discussed in the previous section, hexokinase catalyses the phosphorylation of FDG to FDG6P. OtsAB pathway is the most well-known pathway for the synthesis of trehalose in bacteria. OtsA is a glycosyltransferase that transfers a glucose (Glc) moiety from uridine diphosphate glucose (UDP-Glc) to glucose-6-phosphate to yield trehalose-6-phosphate (T6P), which subsequently undergoes the hydrolysis of the phosphate upon the action of OtsB[14-17]. In previous work by Dr Seung Seo Lee, the synthesis of trehalose analogues had been achieved using OtsA and alakaline phosphatase instead of OtsB[16]. Dr Ritu Raj managed to obtain a soluble protein by cloning the plasmid into pDB-His-MBP vector, resulting in the soluble protein in high expression yield.

Although, the OtsAB system has been used successfully for the synthesis of trehalose analogues[16], one of the key challenges identified with this system was the potential for endotoxicity to be introduced during the preparation of [^{18}F]FDT when using *E. coli* as the expression host for OtsA and OtsB. There is the risk of carried contamination from *E. coli* cell wall components that act as endotoxins[20].

In this chapter, we show three strategies (Scheme **2.1 A, B and C**) to synthesise small and large scale 'cold' ([^{19}F]FDT) and radiolabelled FDT. We opted to choose the 'cold' material for the reaction optimisation and scale-up. Although, for the radio synthesis the amount of FDG used is a few nM, the key objective of the thesis was to perform pre-clinical studies using 'cold' or 'hot' FDT. We needed 3 g of 'cold' FDT for toxicity and blocking studies. Therefore a 'cold'

synthesis was optimised and scaled-up to provide enough material for the intended studies. The next part of the thesis will discuss and describe the experiments we carried out to choose **2.1C** as our preferred route of synthesis. We determined kinetic parameters of enzymes involved in the synthesis. We aim to address the challenges associated with previous synthesis of FDT by carrying out enzyme expression and optimisation in insect cells instead of *E. coli*.

2.2 Results and Discussion

2.2.1 Enzyme Expression, Purification and Characterisation and initial enzymatic activity assessment

TreT analogues

We expressed, purified and characterised two analogues of TreT; TreT *P. horikoshii* and TreT *T. tenax.* For TreT *P. horikoshii* expression (**Section 2.4.11**), plasmid DNA was synthesised by Dr Seung S. Lee as per the literature method[21]. The plasmid was encoded with *XbaI* and a *PstI* restrictions sites with containing 6 x Histidines at the C- terminus of the protein. After confirming the DNA sequence, the histidine-tagged protein was expressed in *E. coli* BL21 (DE3) cells and after purification by size exclusion on FPLC and characterisation by SDS-PAGE and LC-MS, the protein of interest was obtained in the overall expression yield of 3 mg/L of culture. The purified protein showed a single protein band on SDS-PAGE gel (**Fig. 2.1 A**). The molecular weight of the protein was found to be 50508 Da by LC-MS (**Fig. 2.1 C**), consistent with the expected size of the protein, as analysed by DNA sequence.

Similarly, plasmid DNA for the TreT *T. tenax* was designed as described by T. kouril *et al.*[4] and synthesised via Gen script by cloning into the expression vector pET 24(C^+) encoding a C-terminus His-tag via *NcoI* and *BamHI* restrictions sites. After confirming the sequence through Sanger sequence analysis, the protein was expressed in *E. coli* BL21 (DE3) cells (**Section**

2.4.12). Expressed protein was then purified by Ni-NTA and characterised by SDS-PAGE and LC-MS (**Fig. 2.1 B & D**). The Expected mass of protein (48114 Da) was confirmed by both SDS-PAGE and LC-MS. The expression yield of TreT *T. tenax* was found to be 2 mg/L of the culture.

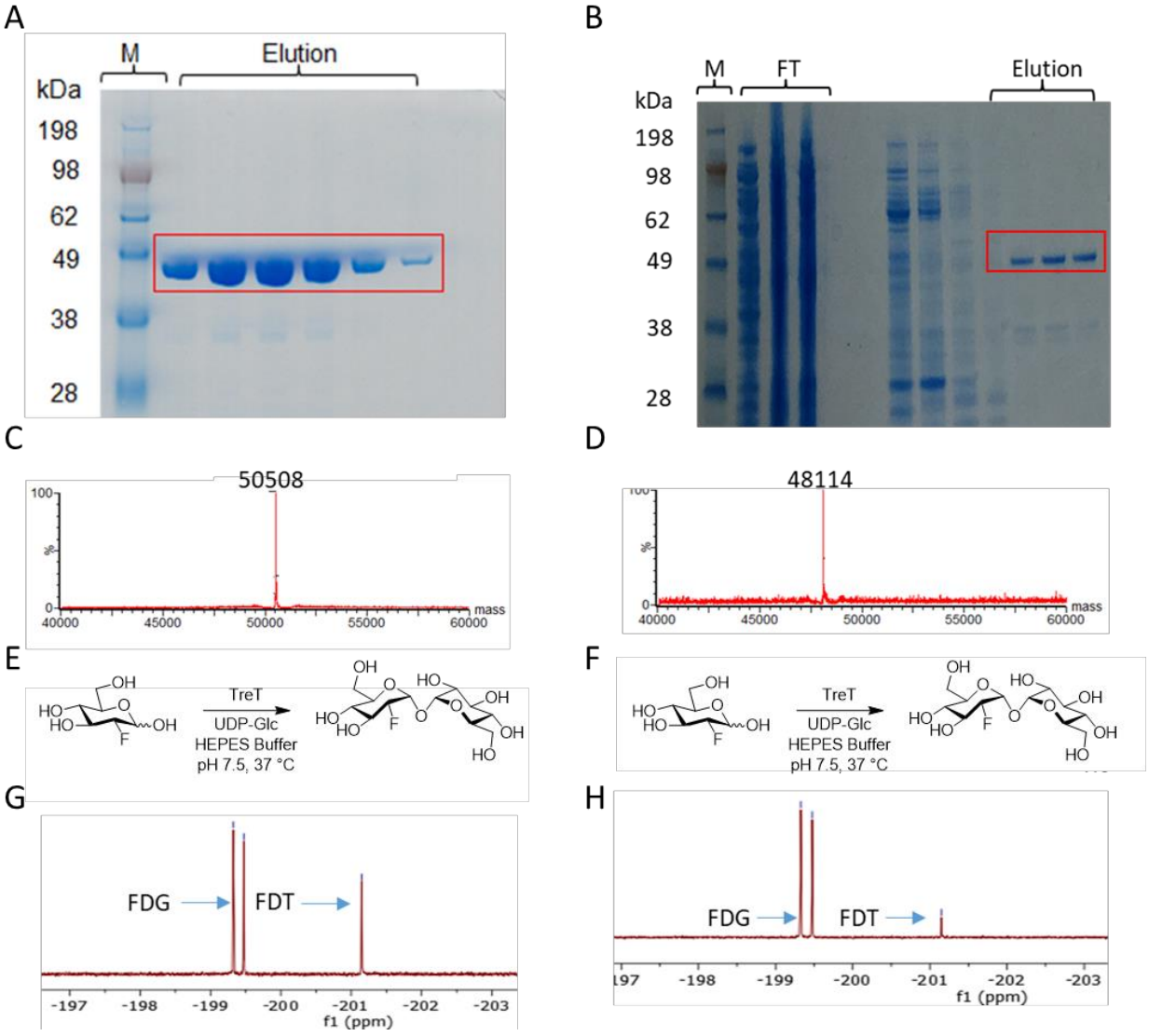


Figure. 2.1: Details of TreT homologue purification, characterisation and enzyme reactions. A, C, E &G). TreT *P. horikoshii* enzyme characterisation by SDS-PAGE and LC-MS. The schematic of the enzyme reaction and characterisation by ^{19}F-NMR spectroscopy. Similarly Fig. **B, D, F &H**) represent TreT *T. tenax* characterisation by SDS-PAGE and LC-MS, followed by the enzyme reaction scheme and characterisation by ^{19}F-NMR spectroscopy. With both TreT, "cold" FDG has two anomers, the α-anomer and a β-anomer.

With fully characterised enzymes in hand, we sought to test the enzyme activity for the synthesis of trehalose and trehalose analogues i.e. [^{19}F]FDT in one-pot. We developed an LC-MS method to characterise our chemo-enzymatic reaction based on previously published work[22] (**Section 2.4.9**). This method allowed the separation of monosaccharides sugars from the corresponding disaccharides. In addition to LC-MS method, for sugars containing fluorine, ^{19}F-NMR was also used to analyse the reaction products. Initially, we used the LC-MS method to monitor the formation of trehalose from glucose using both TreT analogues (**Figure 2.2 A & B**). We then attempted a small scale reaction for both the TreT homologues and analysed by ^{19}F-NMR spectroscopy (**Figure 2.1 G & H**). We obtained the desired product i.e. [^{19}F]FDT from both reactions indicating the enzyme activity under the tested conditions. TreT *P. horikoshii* yielded more product when compared with TreT *T. tenax*, although none of the reactions reached completion under the non-optimised conditions.

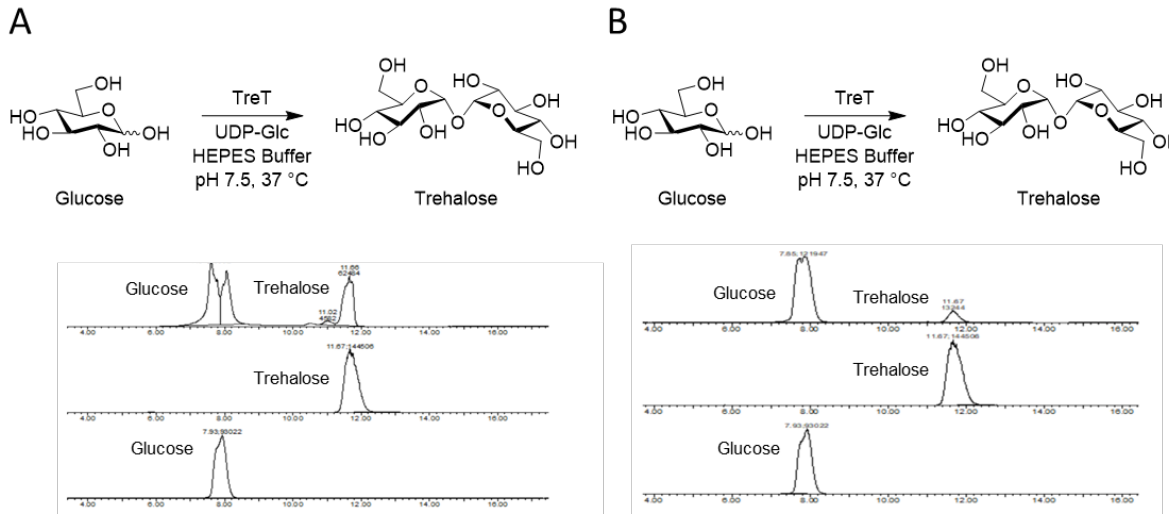


Figure 2.2. LC-MS based characterisation of trehalose formation from glucose using TreT enzymes. A). Trehalose formation scheme and LC-MS chromatogram from TreT *P. horikoshii* reaction. B). Trehalose formation scheme and LC-MS chromatogram from TreT *T. tenax* reaction. In both cases trehalose and glucose standard samples were also run.

To compare the enzymes performance, we then set out to carry out 10 mM scale reactions under the same conditions. (**Methods section 2.4.17).** TreT *P. horikoshii* performed far better than the TreT *T. tenax* (**Figure 2.3**) with around 45% conversion (3.89 mM of FDT) over 2 hours as compared to 17% (0.89 mM of FDT) conversion in the case of *T. tenax*. TreT *T. tenax* reacts slowly, with reported unidirectional properties[4], in theory should perform better than TreT *P. horikoshii*, that is reversible[23].

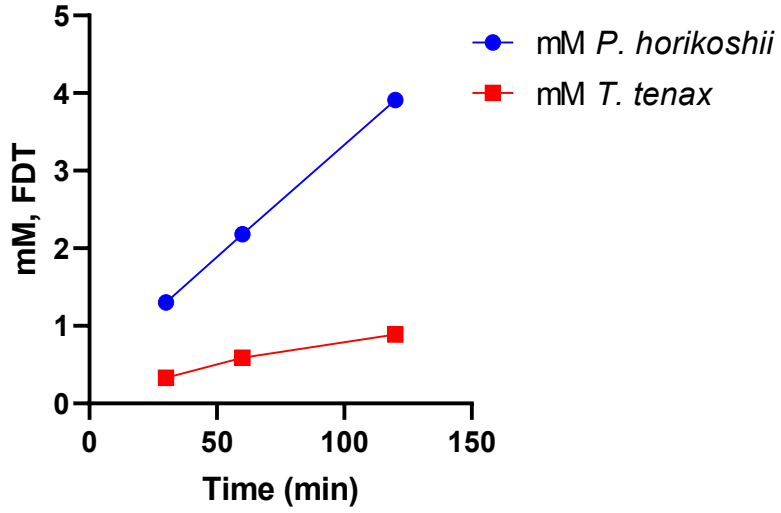


Figure 2.3. TreT homologues enzyme reaction comparison. TreT *P. horikoshii* yielded more product than the corresponding TreT *T. tenax*. Reaction were analysed by ^{19}F-NMR spectroscopy from the samples taken after 30 min, 60 min and 120 min post reaction with n= 1

As [^{18}F]FDG is a non-specific tracer for TB, it is crucial to have a synthetic method for specific probe synthesis which will not make [^{18}F]FDG or the reaction will be compromised due to product or substrate inhibition. While TreT enzymes are quite an attractive option for the synthesis of [^{18}F]FDT analogues, challenges, such as slow reaction rates, reversibility and the low enzyme yields could hinder the progress of them becoming ideal biocatalysts for FDT radiosynthesis. As from our initial reaction, TreT *P. horikoshii*, performed better, we sought to

investigate the concentration dependent reversibility of this enzyme. The kinetic parameters reported for reversible reaction favour the forward reaction[5]. Initially we tested the concentrations of [^{19}F]FDT substrate from 1 – 10 mM while maintaining the fixed UDP concentration at 20 mM. We observed no reversible reaction after 1 h of incubation as shown in **Fig. 2.4B**.

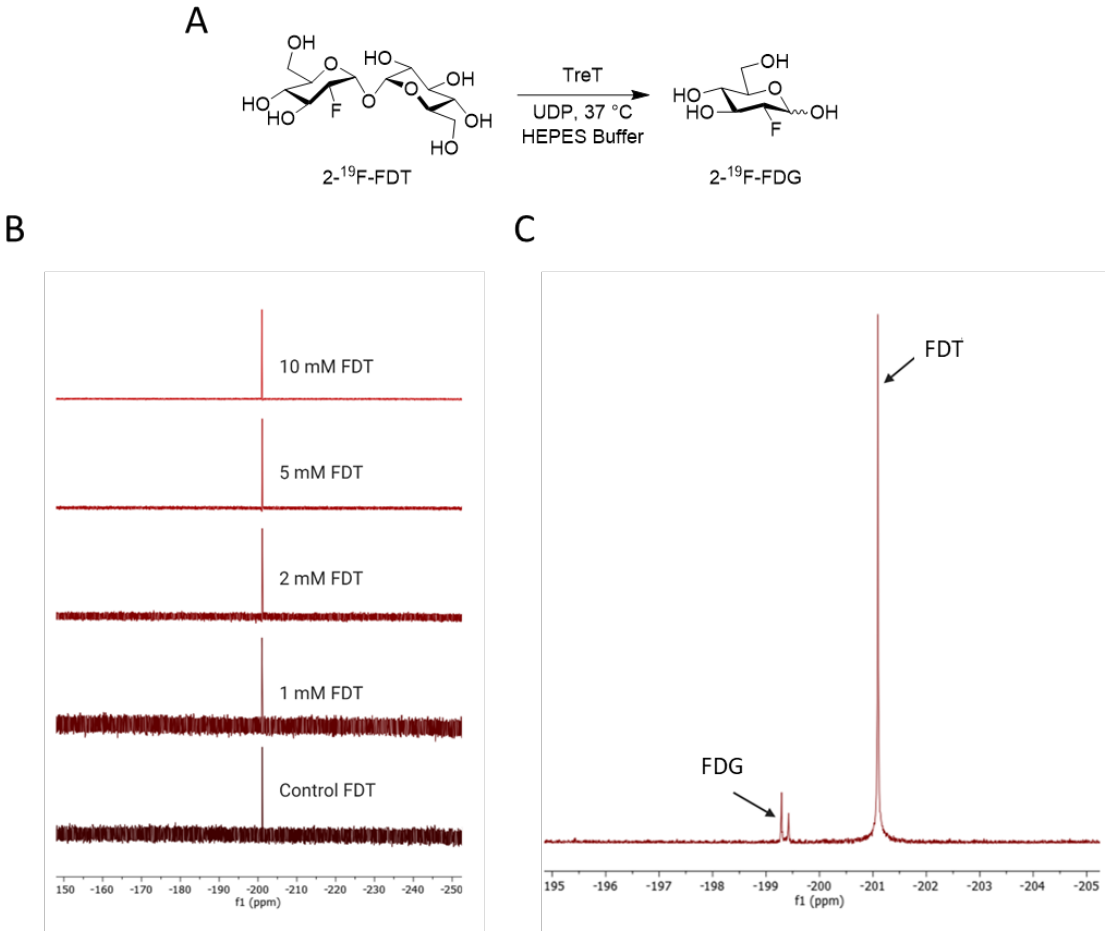


Figure. 2.4. Testing the reversibility of TreT *P. horikoshii* enzyme. A) Schematic of the reversible reaction where [^{19}F]FDT and UDP are used as the substrate and [^{19}F]FDG and UDP-Glc are the products. **B**) ^{19}F-NMR spectra (500 MHZ) of the control and reversible reactions tested at various FDT concentration with UDP concentration maintained at 20 mM and **C**) At the higher UDP concentration (80 mM) and [^{19}F]FDT concentration (20 mM), the reversible product, FDG observed after 2 hours of incubation.

We also tested the reversibility of this enzyme at higher substrate concentration i.e. [^{19}F]FDT 20 mM and fixed UDP concentration at 80 mM (**Section 2.4.18**). We did indeed observe approx. 10% reversible reaction (relative ^{19}F-NMR integration) when incubated for 2 h at 37 °C as shown in **Fig. 2.4C.**

In summary, we expressed, purified and characterised two homologues of TreT. The expression yields of both enzymes were low (2-3 mg/L), although, both enzymes were active, TreT *P. horikoshii* was reversible when FDT substrate concentration approaches 20 mM. This is not problematic for the radio synthesis of FDT but is an issue for reaction scale-up. On the other hand, the TreT *T. tenax* enzyme reacted slower than the *P. horikoshii*, indicating the need for higher amount of enzyme and longer reaction times.

OtsAB Fusion enzyme

In addition to TreT enzymes, an OtsAB fusion enzyme was also expressed and purified in *E. coli*. (**Section 2.4.13 and 2.4.15**). The plasmid for this enzyme was kindly donated by the Prof. Martin Hagemann group[18]. From the sequence analysis of plasmid DNA, presence of His-tag and the exact molecular mass of the enzyme could not be confirmed as reported[18]. We attempted the trial expression without success.

From the literature review, we found another report of this enzyme expression. To our knowledge, there is only one published report for an OtsAB fusion expression in *Myxococcus xanthus*[19]. We sought to design a new plasmid based on this method using the pColdI vector. This vector allows for the expression of protein at lower temperature, giving better yields for enzymes which are difficult to express otherwise[24].

Small scale expression trials, analysed using western blotting, indicated the presence of His-tagged protein (**Fig. 2.5A, section 2.4.14.1**). For these experiments, cultures were induced at

different optical density (OD_{600}) values, OD_{600} 0.4 and 0.6. Isopropyl β-D-1-thiogalactopyranoside (IPTG) concentrations for protein induction were also varied at 0.5 mM and 1.0 mM. Finally, expression times were kept from 6-48 h. In the light of trial expression results, large scale expression of protein was carried out in 1 litre culture at 15 ^{o}C for up to 48 h. SDS-PAGE analysis and LC-MS confirmed the protein of interest (**Fig. 2.5B & D**).

The expression yields for this biocatalyst were very low (0.1 mg/mL). The enzyme showed precipitation upon storage. We attempted several times to synthesise [^{19}F]FDT from FDG using hexokinase and the fusion enzyme but failed at each occasion.

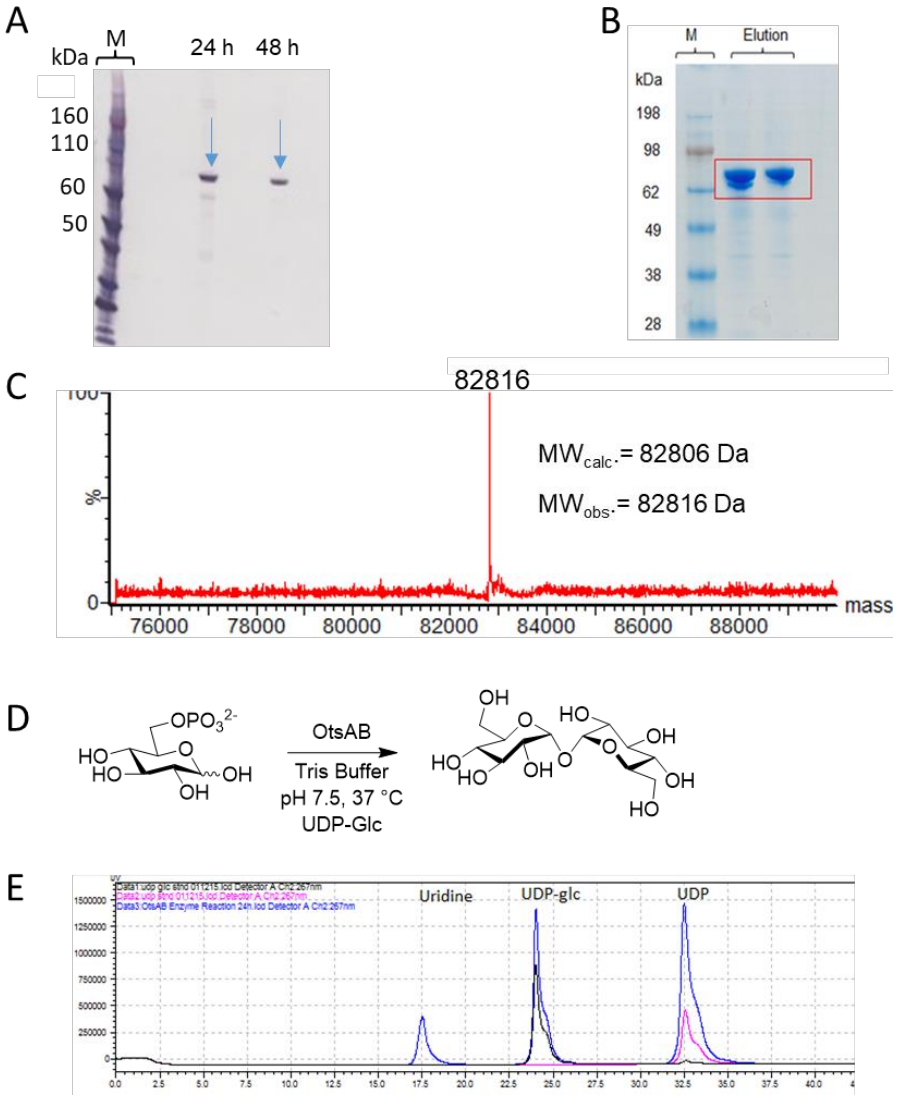


Figure 2.5. OtsAB fusion enzyme optimisation and expression. **A**) Small scale expression with different IPTG concentrations and OD_{600}, values. A His-tagged protein at the expected molecular weight was visualised by wetern blotting after probing with anti-His monoclonal antibody after 24 h and 48 h of incubation at 15 °C. IPTG concentration of 0.5 mM and OD_{600} of 0.4 were the relatively best conditions as compared to IPTG concentration 1 mM and OD_{600} 0.6. **B**) SDS-PAGE characterisation of the large scale (1L) expression of protein. **C**) LC-MS characterisation of OtsAB fusion enzyme where the expected mass after N-terminus Met cleavage is observed **D**) Reaction scheme for the enzyme reaction of OtsAB fusion enzyme. and **E**). HPLC chromatogram of the glucose-6-phosphate reaction in the presence of UDP-Glc and OtsAB fusion enzyme. The reaction monitoring by HPLC confirmed the UDP release which is one of the product of this enzyme catalysis.

OtsA and OtsB

For the expression of OtsA and OtsB enzymes, plasmid DNA was designed based on the pFastbac vector system (**see methods 2.4.19**). Analyses of the gene sequences of both the OtsA and OtsB from *E. coli* and insect cells revealed the identical protein sequence (**Appendix A1).** Bac-to-Bac baculovirus expression system was used for small and large scale expression of the proteins[25]. The overall process of insect cells expression using Bac-to-Bac system is shown in **Figure 2.6**.

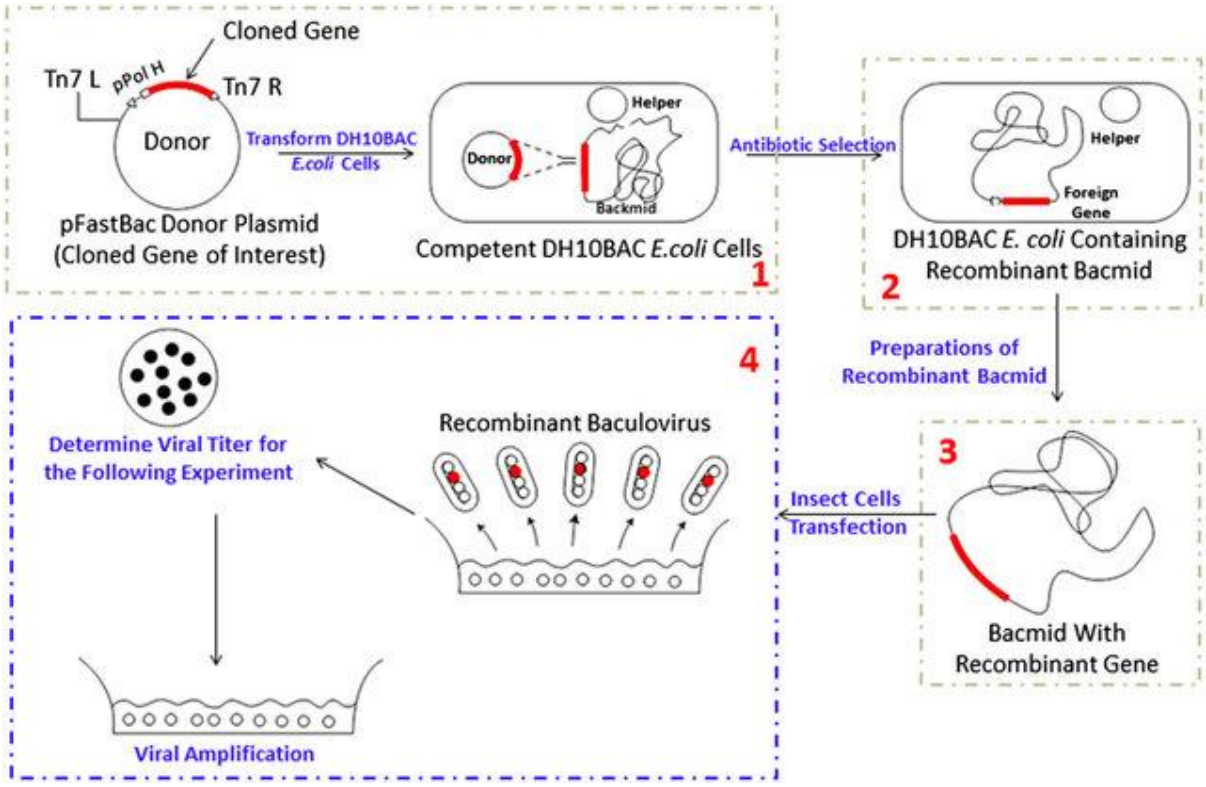


Figure.2.6. Diagram of Bac-to-Bac expression system; Step 1 Construction of donor plasmid; **Step 2** Generation fo bacmid DNA**; Step 3;** Recombinant bacmid DNA preparation, purification and confirmation using PCR method; **Step 4;** Production of recombinant baculovirus P1 and further amplification of P1 virus to generate P2 viral stock (used with permission[26]).

From the respective plasmid DNA, we prepared the recombinant bacmid DNA for both the enzymes by transforming the donor plasmids into DH10Bac competent cells that contained

bacmid DNA of baculovirus. Since the correct insertion of mini-Tn7 site into the mini-attTn7 attachment site on the bacmid DNA will disrupt the expression of LacZ peptide that absorbs the X-gal dye from the medium. Therefore, we performed blue-white selection to screen the correct colonies that contained the recombinant bacmid DNA. The blue colonies contained the empty bacmid or the mixture of empty and recombinant bacmid while the white colonies only contained the recombinant bacmid DNA of OtsA and OtsB (**Figure 2.7 A & B**). The resulting recombinant bacmid DNA was verified by the PCR method (**Figure 2.7C**) and transfected into Sf9 insect cells with cellfectin II reagent in 6-well plate (**Figure 2.7D & E**). After incubation at 27 $^{\circ}$C for 3 days, the cells were harvested by centrifugation. The supernatant resulted in recombinant baculovirus particles (P1 baculovirus stock for OtsA and OtsB enzyme). We used the pellet to check the protein expression level. We used western-blotting to visualise the protein bands by probing with anti-His antibody. From the western blot results (**Figure 2.7F**), it appeared that 1.0 μg bacmid DNA of OtsA-2 and OtsB-2 were better conditions to get higher protein expression levels.

P1 viral stock (**Figure 2.7G**) is a small-scale, low titre stock. This stock was used to infect cells to generate high-titre P2 stocks (**Figure 2.7H**). The titre of initial viral stock obtained from transfecting Sf9 cells generally ranged from 1.0 x 10^6 to 2.0 x 10^6 cells/ml. Amplification of this stock allowed production of P2 viral stock with a cell density of 2.0 x 10^6 cells/ml. To make the P2 viral stock, 150 mL of sf9 cells with a cell density of 2.0 x 10^6 cells/ml were infected with the P1 viral stock of OtsA and OtsB enzymes, respectively. After incubation at 27 ^{o}C for 72 h, the P2 viral stock (in culture medium) was harvested by centrifugation. The supernatant after adding 2% FBS solution was stored at 4 °C and used for large scale protein expression. The pellet was used to confirm the protein expression and purification in a small scale by SDS-PAGE and LC-MS (**see Fig. 2.8 A & D**).

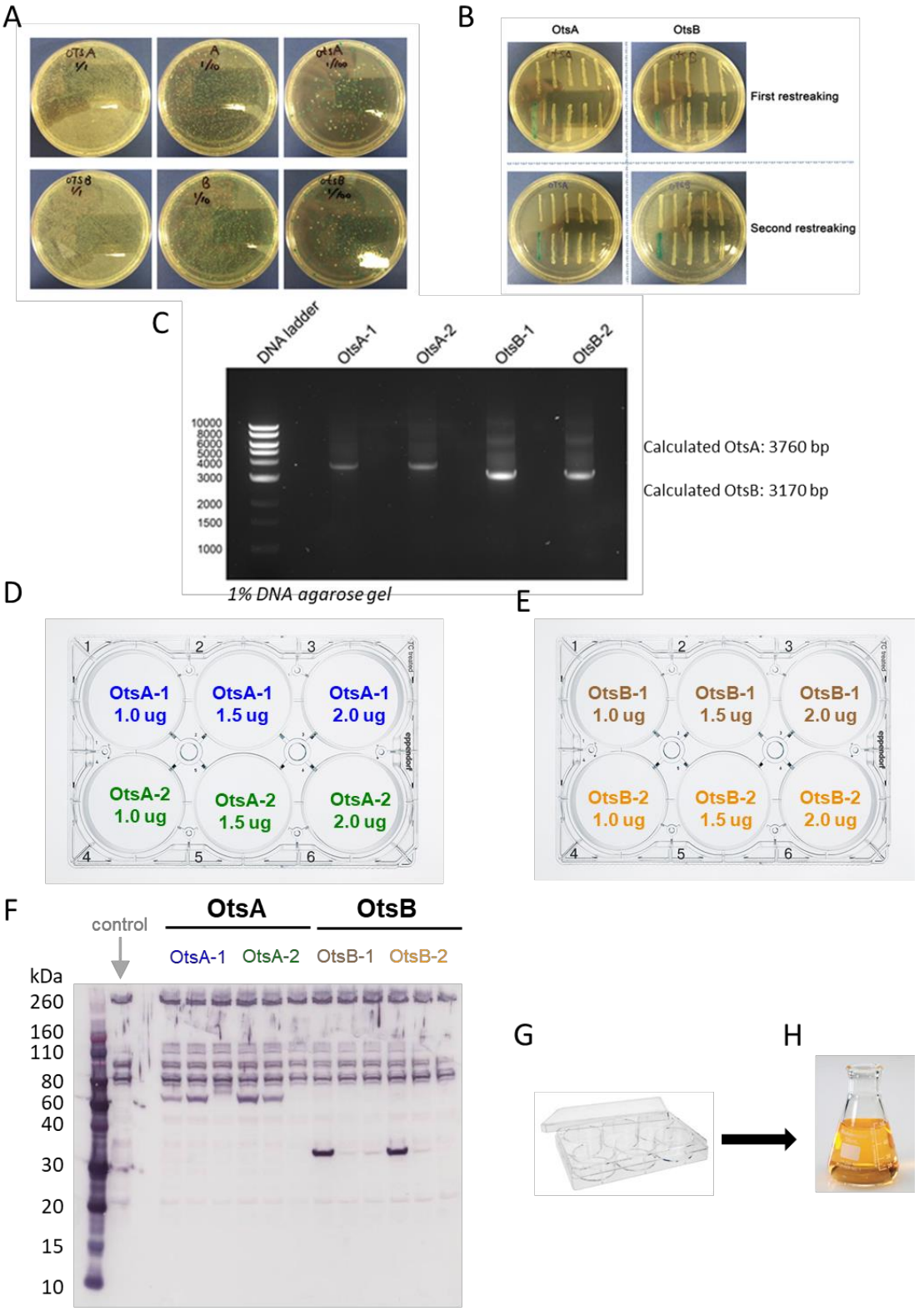


Figure 2.7. Schematic of the insect cell expression of TPS (OtsA in *E. coli*) and TPP (OtsB in *E. coli*) enzymes. **A**) LB-Agar plates for the blue & white selection colonies of plasmid DNA. **B**) Phenotype confirmation by streaking and re-streaking the colonies from A. **C**). 1 % Agarose gel for the

characterization of OtsA and OtsB bacmid DNA. **D & E**) Generation of P1 bacmid DNA for OtsA and OtsB enzymes. **F**) Western blot using anti-His tag antibody to characterize OtsA and OtsB protein from the pellet of P1 viral stock. **G & H**) P1 & P2 baculovirus of OtsA and OtsB enzymes.

After preparing the P2 viral stock, enough to infect 30 L Sf9 cells, we embarked on the challenge of scaling up the expression of both OtsA and OtsB. The key obstacle was to prevent the media from contamination during incubation. The scale-up for both of the enzymes was initially carried out up to 0.5 L of culture solution, and subsequently increased to 1.0 L. Insect cell culture (1 mL, cell density ~ 0.3 x 10^6 cells/ml) was added into 25 mL Sf900-II media and incubated at 27 °C. Prior to splitting the cells, the cell density and cell viability was checked. In this way, 0.5 mL x 2 of insect cell culture with a cell density of ~ 2.0 x 10^6 cells/mL and with cell viability of over 98% was obtained. Insect cells were infected with 1% the P2 viral stock of both OtsA and OtsB and after incubation at 27 °C for 3 days, cells were harvested by centrifugation and the pellet from each culture was purified by size exclusion chromatography on FPLC. The SDS-PAGE analysis and LC-MS confirmed the appearance of the desired protein (**Figure(s) 2.8 B, C, E & F**).

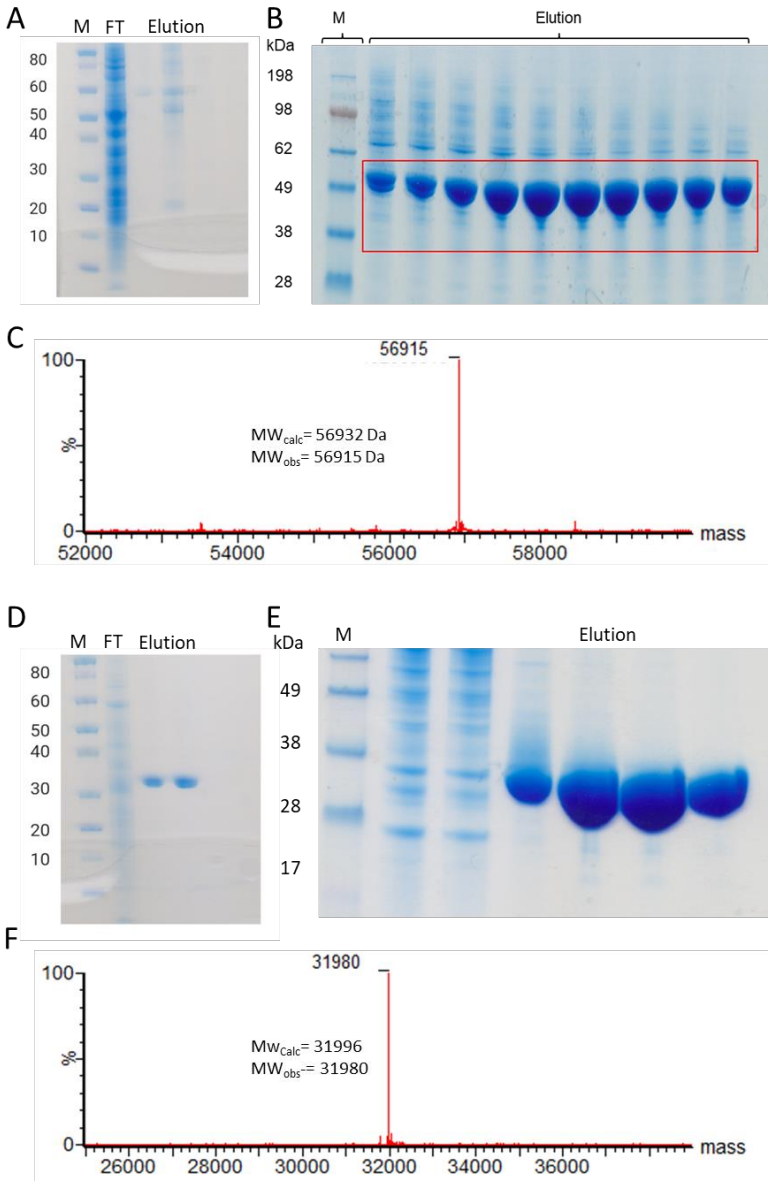


Figure 2.8. Small and large scale expression of OtsA and OtsB enzymes from insect cells. A) SDS-PAGE characterization of OtsA enzyme from the pellet of 50 mL culture. B) SDS-PAGE characterization of OtsA enzyme from 1 L culture. C) LC-MS characterization of OtsA enzyme. D) SDS-PAGE characterization of OtsB enzyme from the pellet of 50 mL culture. E) SDS-PAGE characterization of OtsB enzyme from the 1L scale expression culture. F) LC-MS characterization of OtsB enzyme.

The expression yield for the purified OtsA protein was found to be ~ 20 mg/L of culture and 15 mg/L of culture for OtsB. The expression yields obtained from these two enzymes were far superior to the corresponding TreT enzymes and the fusion construct of OtsAB enzyme.

A small scale synthesis based on OtsA and alkaline phosphatase enzyme was previously reported[16]. With the OtsB enzyme in hand, we attempted the small scale synthesis with using 3-enzymes-3-steps one-pot synthesis (**Figure 2.9A, methods section 2.4.19.4**) [^{19}F]FDT formation. We observed full conversion to the product within 30 min at 1 mM scale reaction by both ^{19}F-NMR (**Figure 2.9E**) and LC-MS (**Figure 2.9C**).

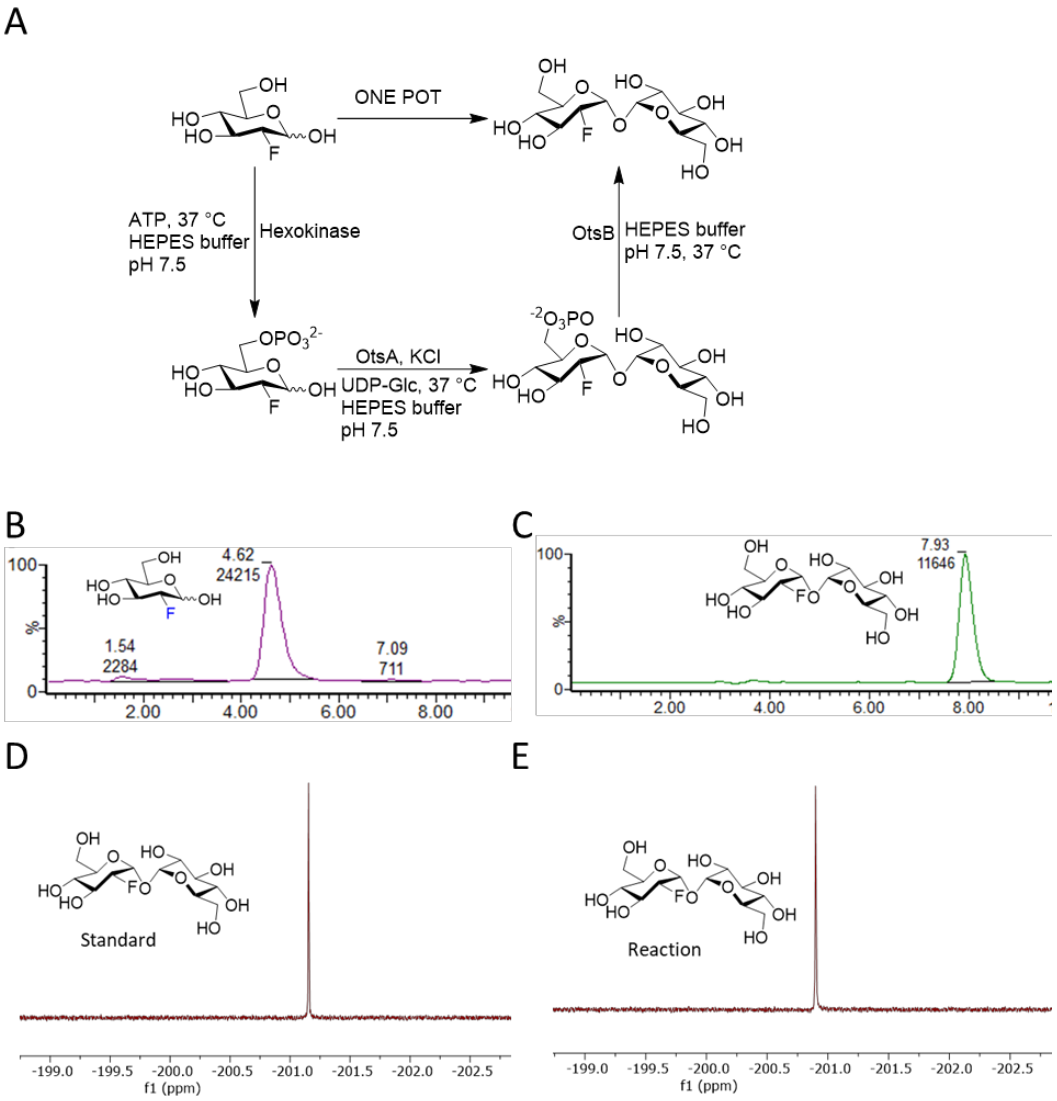


Figure. 2.9. Small scale synthesis of [^{19}F]FDT from 3-enzymes-3-steps-one pot synthesis. A) Reaction scheme for the synthesis of [^{19}F]FDT from FDG utilizing three enzymes in one-pot. **B**) LC-

MS analysis of the control FDG reaction. This reaction mixture did not contain hexokinase, therefore, no further reaction could occur. **C**) LC-MS integrated chromatogram of [^{19}F]FDT reaction sample, showing the formation of the product at rt 7.93 min. **D**) ^{19}F-NMR spectrum of [^{19}F]FDT standard sample. This sample is without the addition of enzymes at t=0 and **E**) ^{19}F-NMR of the 3-steps-3-enzymes reaction, showing the full conversion to the product within 30 min of reaction and no starting material (FDG) or the intermediate (FDG6P and FDT6P) left in the reaction mixture.

In summary, we were able to express, purify and characterise two homologues of TreT and OtsAB fusion enzymes in *E.coli*. Expression yields for TreT homologues were between 2-3 mg/L from of culture, whereas expression levels for the OtsAB fusion enzyme were very low i.e. 0.1 – 0.2 mg/L. We also expressed OtsA and OtsB in Sf9 insect cells, where we obtained expression yields of 20 mg/L for OtsA and 15 mg/L for OtsB.

We tested the small scale reactions using FDG and UDP-Glc substrates for the formation of [^{19}F]FDT. Among TreT homologues, *P. horikoshii* was efficient when compared with *T. tenax*. OtsAB fusion reaction did not happen utilizing these substrates. However, the reaction involving hexokinase, OtsA and OtsB did reach completion within 30 min. Both the reaction efficiency and higher expression yields make this enzyme system an ideal choice for further use in reaction scale-up and radiosynthesis of FDT. Next, we explored the kinetic parameters of all enzymes, to obtain additional information on the catalytic performance.

2.2.2 Enzyme Kinetic Parameters

The enzyme kinetic parameters of OtsA, TreT *P. horikoshii* were determined in a glycosyl transferase (GT)-continued spectrophotometric assay (**Section 2.4.4**)[27]. The decrease in NADH absorbance at 340 nm (ε340 = 6220 $M^{-1}cm^{-1}$) was measured at 25 °C in a 96 well plate using a spectrophotometer equipped with a thermostat (Spectra NanoStar). For TreT *T. tenax* we used

an HPLC method to determine the kinetics of UDP-Glc with fixed Glc concentration, whereas for variable Glc concentrations and fixed UDP-Glc concentration, we used the GT-continued assay instead. We used an HPLC method to elucidate the kinetic parameters of the OtsAB fusion enzyme. For the OtsB kinetics, a ^{1}H NMR method was used.

Using Michaelis-Menten[28] and/or Lineweaver-Burk[29] plots we compared the enzyme kinetic parameters of all glycosyltransferases i.e. OtsA, TreT and the OtsAB fusion enzyme (Table 1), OtsA showed superior binding to the substrates (K_m for UDP-Glc 1.40 ± 0.19 mMs^{-1}), although it was almost four times lower for the acceptor substrate (K_m for Glc-6P 4.88 ± 0.48 mMs^{-1}). In addition, the turnover number (k_{cat}) and catalytic effeciency (k_{cat}/K_m) for this enzyme was far better than the correpsoning TreT and fusion contstruct of OtsAB (**see Table 1**). We also compared the kinetic parameters of OtsA construct from Sf9 insect cells to the ones in *E. coli*[15] and from our data Sf9 insect cells showed better binding, had better catalytic effeciency and the higher turnover number as compared to the *E. coli* construct[15].

In addition, we also studied the substrate binding mechanism for OtsA enzyme by altering the concentration of donor substrate while keeping fixed concentrations of acceptor substrate (**Figure 2.10 1G**). We carried out our study at 5 fixed concentrations of acceptor substrates (**see methods 2.4.4**). The enzyme showed slight inhibition at 35 mM of acceptor substrate concentration which is contrary to the study carried out by Errey et al.[15] (**Figure 2.10C**). The Lineweaver-Burk plots intersected, indicating that OtsA followed a sequential binding mechanism involving a ternary enzyme-substrate complex. This notion is consistent with other glycosyltransferases. From these plots, it is difficult to distinguish the order of binding of substrates.

For the OtsB kinetics, initially we explored phosphate release assay to measure the amount of inorganic phosphate release during the trehalose-6-phosphate dephosphorylation. This amount is directly propotional to the amount of trehalose formed. However, we could not get this assay

working due to the background phosphate from the reagents used in the reaction. NMR method allowed the accurate quantification and subsequent analysis of kinetic parametrs. The K_m value observed (2.8 ± 0.7) is close to the *E. coli* construct (3.60 ± 0.8), however the k_{cat} value (740 ± 96) was different (286) from *E. coli* construct. The work on *E. coli* construct was carried out by Dr Yiqun Geng in Davis lab. For the OtsAB fusion we could not achieve reliable kinetics due to the unstability and less activity of the protein.

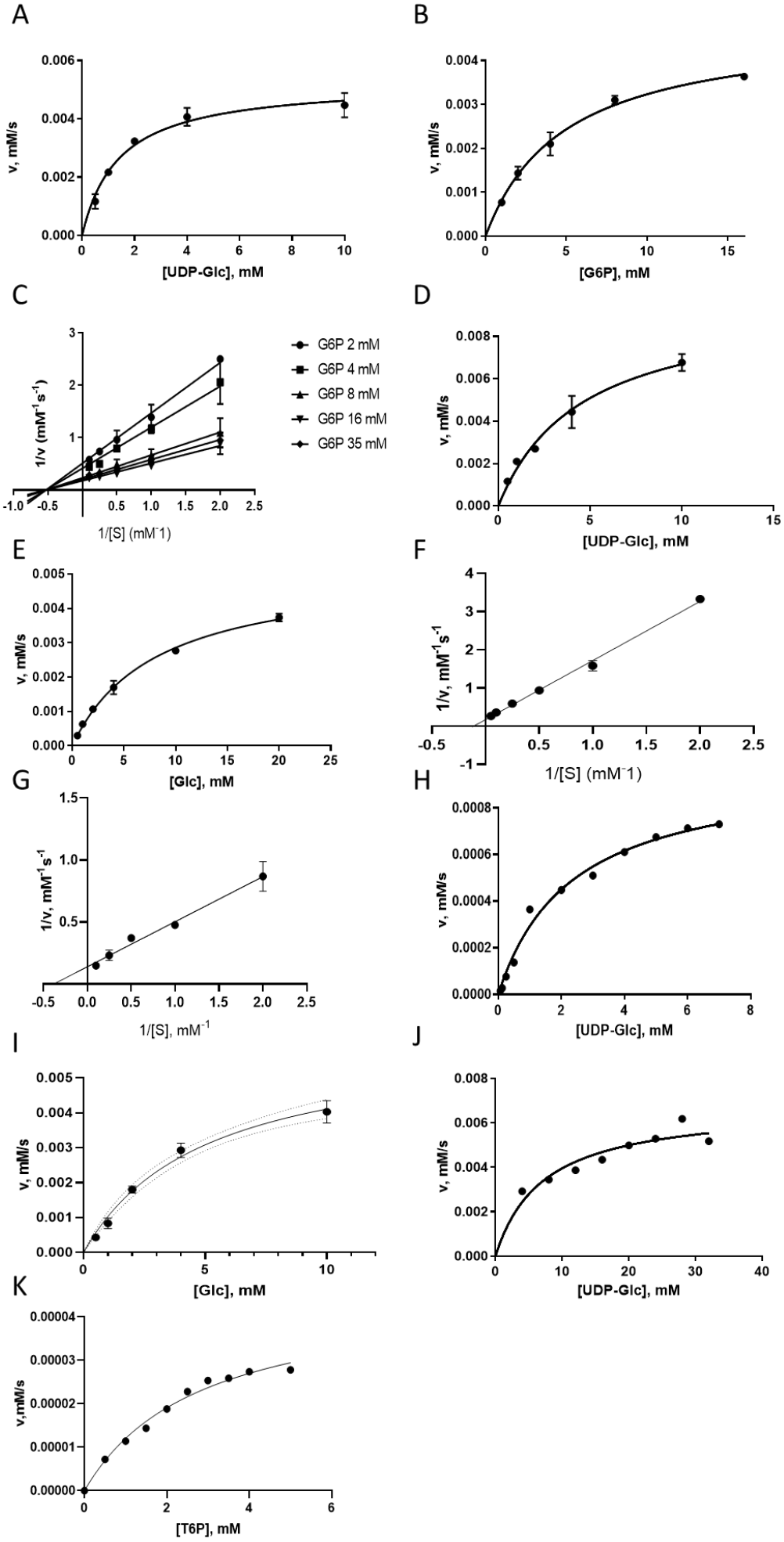

A
v, mM/s
[UDP-Glc], mM
B
v, mM/s
[G6P], mM
C
1/v (mM-1s-1)
1/[S] (mM-1)
G6P 2 mM
G6P 4 mM
G6P 8 mM
G6P 16 mM
G6P 35 mM
D
v, mM/s
[UDP-Glc], mM
E
v, mM/s
[Glc], mM
F
1/v, mM-1s-1
1/[S] (mM-1)
G
1/v, mM-1s-1
1/[S], mM-1
H
v, mM/s
[UDP-Glc], mM
I
v, mM/s
[Glc], mM
J
v, mM/s
[UDP-Glc], mM
K
v,mM/s
[T6P], mM

Fig. 2.10. Kinetic parameters donor and acceptor substrates of OtsA, TreT, OtsAB fusion enzyme and OtsB enzyme. A) Michaelis-Menten plot showing the activity of OtsA as a function of UDP-Glc with a fixed Glc-6P concentration, **B**) Michaelis-Menten plot showing the activity of OtsA as a function of Glc-6P with a fixed UDPG concentrations. **C**) Lineweaver-Burk (double reciprocal plot) showing the activity of OtsA as a function of UDP-Glc in the presence of series of fixed G6P concentrations. **D**) Michaelis-Menten plot showing the activity of TreT *P. horikoshii* as a function of UDP-Glc with a fixed Glc concentration. **E**) Michaelis-Menten plot showing the activity of TreT *P. horikoshi*i as a function of Glc with a fixed UDP-Glc concentrations. **F**) Lineweaver-Burk showing the activity of TreT *P. horikoshii* as a function of UDP-Glc in the presence of a fixed Glc concentration. **G**) Lineweaver-Burk (double reciprocal plot) showing the activity of TreT *P. horikoshii* as a function of Glc in the presence of a fixed UDP-Glc concentration. **H**) Michaelis-Menten plot showing the activity of TreT *T. tenax* as a function of UDP-Glc with a fixed Glc concentration, **I**). Michaelis-Menten plot showing the activity of TreT *T. tenax* as a function of Glc with a fixed UDP-Glc concentration. **J**). Michaelis-Menten plot showing the activity of OtsAB fusion as a function of UDP-Glc with a fixed G6P concentration. **K**). Michaelis-Menten plot showing the activity of OtsB as a function of T6P.

The comparison of the kinetic parameters of GT enzymes revealed the OtsA had better turnover number, substrate binding and catalytic efficiency. While TreT homologues and OtsAB fusion showed less favourable kinetic characteristics. Therefore, we decided to use the 3-enzyme system in the reaction optimisation, scale-up and [^{18}F]FDT synthesis.

Table 1: Kinetic Parameters of the Enzymes used in the [^{19}F] FDT Synthesis

Enzyme	Substrate	K_m (mM)	k_{cat} (s^{-1})	k_{cat}/K_m ($mM^{-1}s^{-1}$)
OtsA	UDP-Glc	1.40 ± 0.2	63.5 ± 2.5	45.3
OtsA	G6P	4.88 ± 0.5	57.5 ± 2.3	11.9
TreT *P. horikoshii*	UDP-Glc	4.55 ± 0.8	25.0 ± 2.0	5.5
TreT *P. horikoshii*	Glc	8.13 ± 0.6	13.6 ± 0.4	1.7
TreT *T. tenax*	UDP-Glc	2.31 ± 0.7	13.5 ± 1.4	6.2
TreT *T. tenax*	Glc	4.99 ± 1.3	10.3 ± 1.3	2.1
OtsAB	UDP-Glc	7.15 ± 5.7	-	-
OtsB	T6P	2.8 ± 0.7	740 ± 96	264

2.2.3 Enzyme Reaction optimization, Scale-up, Purification and Characterization

We sought to test the effect of increasing temperature on the protein structure and activity of both OtsA and OtsB enzymes. Although increasing the temperature may not have direct impact on the substrate binding and turnover number, it does increases the reaction rate. Therefore, knowledge of optimal temperature can be useful. In order to investigate the structural changes, we used the circular dichroism (CD) technique (**see section 2.4.8**). Both the enzymes were incubated at 25 °C, 37 °C, 45 °C and 50 °C and then analysed by CD to observe any changes in the secondary structure[30].

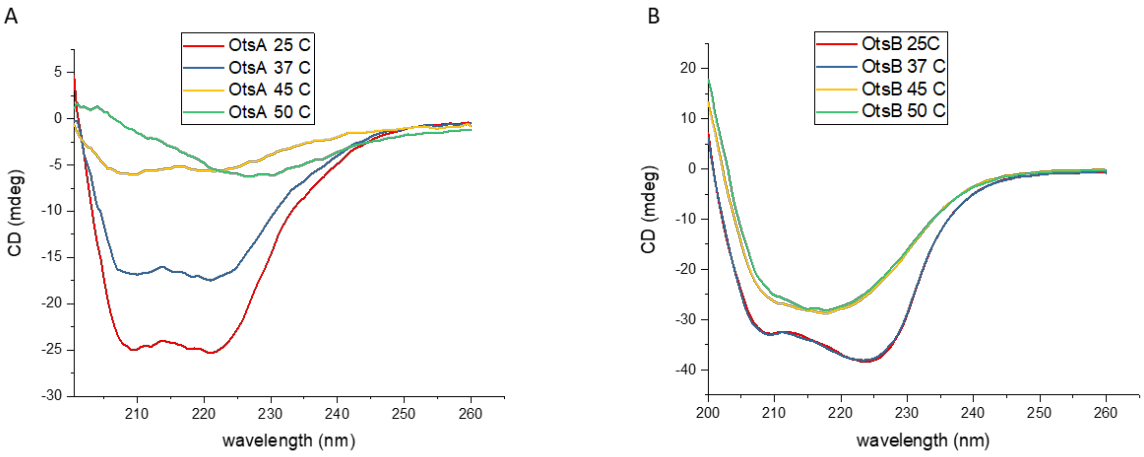


Fig. 2.11. CD spectra of otsA and OtsB enzymes. A). CD spectra of OtsA enzyme at 25 °C, 37 °C, 45 °C and 50 °C and **B**). CD spectra of OtsB enzyme at 25 °C, 37 °C, 45 °C and 50 °C.

OtsA enzyme showed maximum folding at 25 °C and maintained secondary structure at 37 °C but lost the secondary structure at 45 °C and above (**Fig. 2.11 A**). OtsB showed similar secondary structures properties having maintained maximum folding at 25 °C and 37 °C (**Fig. 2.11 B**).

We then set out to analyze the effects of enzyme and substrate concentrations and reaction duration of reactions. We observed the maximum amount of hexokinase enzyme needed for the conversion of 100 mg of FDG substrate to FDG6P was 5 mg. Whereas, the amount of ATP needed to be in slight excess (1.1 equiv.) compared to the acceptor substrate concentration (**Figure 2.12B**).

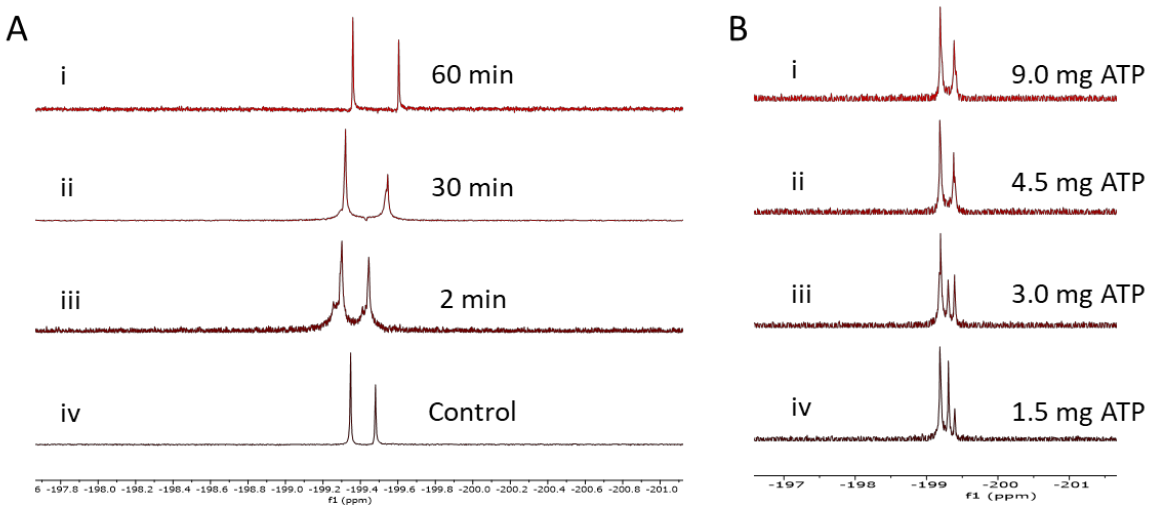


Figure 2.12. Testing the optimal amount of hexokinase and ATP needed for full conversion of FDG to FDG6P. **A**). Reaction monitoring from FDG to FDG6P using 5 mg hexokinase. Reaction completed after 60 min. **B**). Small scale reactions of FDG with ATP to determine the optimal amount of ATP needed for conversion of FDG to FDG6P. The amount of FDG was fixed at 5.6 mM or 1 mg, whereas ATP varied from 2.7 mM (1.5 mg), 5.4 mM (3 mg), 8.1 mM (4.5 mg) and 16.2 mM (9 mg). In conditions i and ii where concentration of ATP was higher than FDG, full conversion to FDG6P observed by ^{19}F-NMR spectroscopy.

With this information in hand, we switched our attention to determine the concentration of OtsA and OtsB enzyme needed for the catalysis of subsequent glycosylation of FDG6P to FDT6P and then dephosphorylation of FDT6P to FDT. We tested these reactions at 50 mg scale. We found out that the glycosylation step is slower and the optimum amount of OtsA enzyme needed was 18.2 µM. However, the dephosphorylation step was very fast with very little enzyme at 6.1 µM (**Figure 2.13 A & B**).

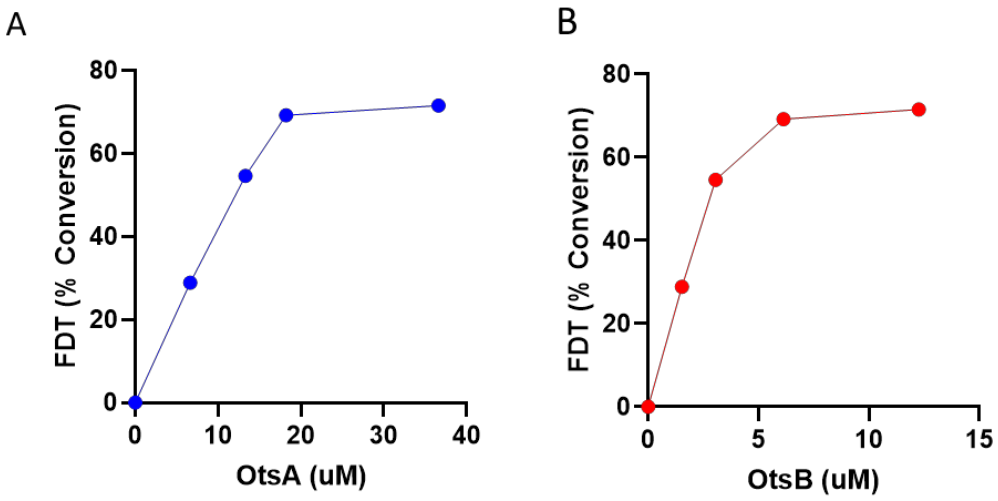


Figure 2.13. OtsA and OtsB enzyme optimum concentration determination. For optimum enzyme concentration determination, reaction with fixed substrate concentrations and all the other parameters incubated with varying enzyme(s) concentrations. **A**). OtsA concentrations varied from 6.65 µM to 36.6 µM. Optimum concentration of the enzyme was found to be 18.2 µM. **B**). OtsB concentrations varied from 1.53 µM to 12.26 µM. Optimum concentration was 6.1 µM.

In order to scale-up the enzymatic reaction, we set-up several reactions with varying FDG concentrations while fixing all the other parameters and monitored over time using ^{19}F-NMR (**see Table 2.1**).

As can be seen from **Figure 2.14B**, with increasing the amount of FDG, the formation of product slowed down, with significant amount of FDG6P left e.g. in 25 mg and 50 mg reaction, however, very little or no FDG and FDT6P remained unreacted. This indicated that the glycosylation step needed further optimisation.

Table 2.1: FDT reaction optimisation with varying substrate

Entry	FDG mg	ATP mg	UDP-Glc mg	hexokinas mg	OtsA mg	OtsB mg	Total Volume mL
1	6.25	21	37	5	3	0.4	2
2	12.5	42	37	5	3	0.4	2
3	25	84	37	5	3	0.4	2
4	50	168	37	5	3	0.4	2
5	50	168	168	5	3	0.4	2

We envisioned to use the slight excess amount of UDP-Glc to the calculated amount of acceptor substrate and tested this reaction at 50 mg scale again. This change resulted in better conversion to the product with almost 80% conversion in 18 h (**Figure 2.15**). We tested the reactions further under the same conditions at 100 mg and 200 mg scale. The conversion at 100 mg scale was slightly lower (~ 70% conversion in 18 h as compared to 50 mg scale but the 200 mg scale reaction did not proceed well and even with further enzyme and/or UDP-Glc addition did not add to the conversion and precipitation was observed. Therefore, we set out to synthesise our batches at 100 mg scale in order to obtain several grams of FDT.

For the reaction scale-up, conversion of FDG to 2-fluoro-2-deoxy-glucose-6-phosphate (FDG6P), catalysed by hexokinase, was quantitative. However, the glycosylation of FDG6P with UDP-Glc, catalysed by OtsA, proved to be a limiting step; average conversion of FDG6P to 2-fluoro-deoxy-trehalose-6-phosphate (FDT6P) was around 65 - 70% over 18 h. The final step in the chemo-enzymatic reaction sequence, the conversion of FDT6P to FDT, was also quantitative and completed in 2 h. Reaction progress through each step in the single pot was monitored by the measurement of the crude ^{19}F-NMR spectra (**Fig. 2.14 C**).

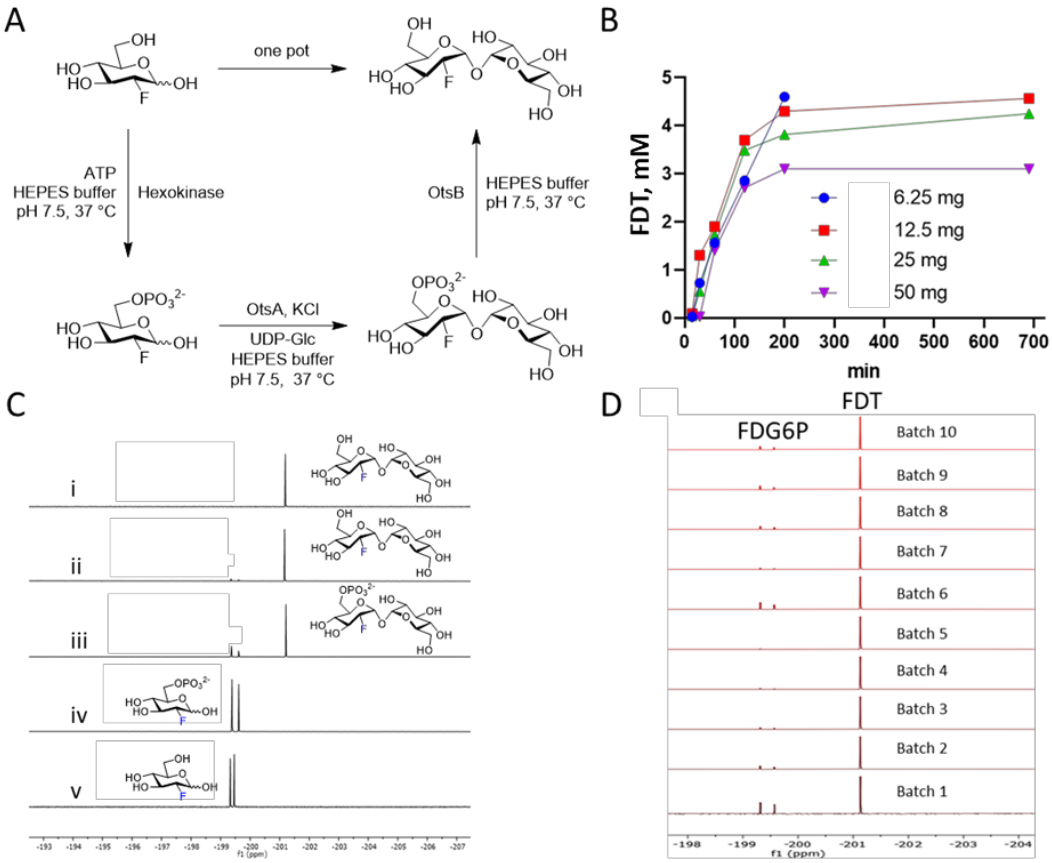


Figure 2.14. Reaction optimisation, scale-up and batch synthesis. A) Enzyme reaction scheme employed to synthesise [^{19}F]FDT**. B)** Reaction optimisation at different acceptor substrate quantities e.g. 6.25 mg , 12.5 mg, 25 mg and 50 mg of FDG reactions were monitored over 3 h period and the samples were taken 15 min, 30 min, 60 min, 120 min, 200 min and 690 min after starting the reaction. Initially the reaction was linear for all substrates. For 6.25 mg FDG reaction, the reaction completed in almost 3 hours and was linear throughout. However, for other concentrations, the reaction slowed down as the amount of substrate increased. **C**) Reaction monitoring of 3-step FDT synthesis from FDG by ^{19}F-NMR. NMR spectra **(i)** ^{19}F NMR spectrum of purified [^{19}F]FDT. **(ii)** Crude ^{19}F-NMR spectrum of [^{19}F]FDT with small amount of FDG6P still present. **(iii)** Crude ^{19}F-NMR spectrum FDT6P from FDG6P. **(iv)** Crude ^{19}F-NMR spectrum of FDG6P from FDG conversion. and **(v)** Control sample of FDG. **D**) Representative crude [^{19}F]FDT batches synthesised by 3-enzymes-3-steps, one-pot synthesis

After the completion of the one-pot batch synthesis, the enzymes used were precipitated by adding 2 mL of ethanol (EtOH), the mixture filtered and the filtrate was concentrated to produce a solid for further work up. During reactions, in order to maintain enzyme activity, high NaCl concentrations were used in buffers leading to the potential for NaCl carry-through in reaction mixtures of FDT**.** In order to reduce the amount of NaCl entering into the purification stage, the crude product obtained after EtOH precipitation was therefore dissolved in a 90:10 mixture of methanol /acetonitrile (MeOH/MeCN) to 'crash out' most NaCl. The resulting suspension was centrifuged and the supernatant filtered through a 0.45 μm syringe filter. The filtrate was concentrated and purified by flash column chromatography and applied in combined batches.

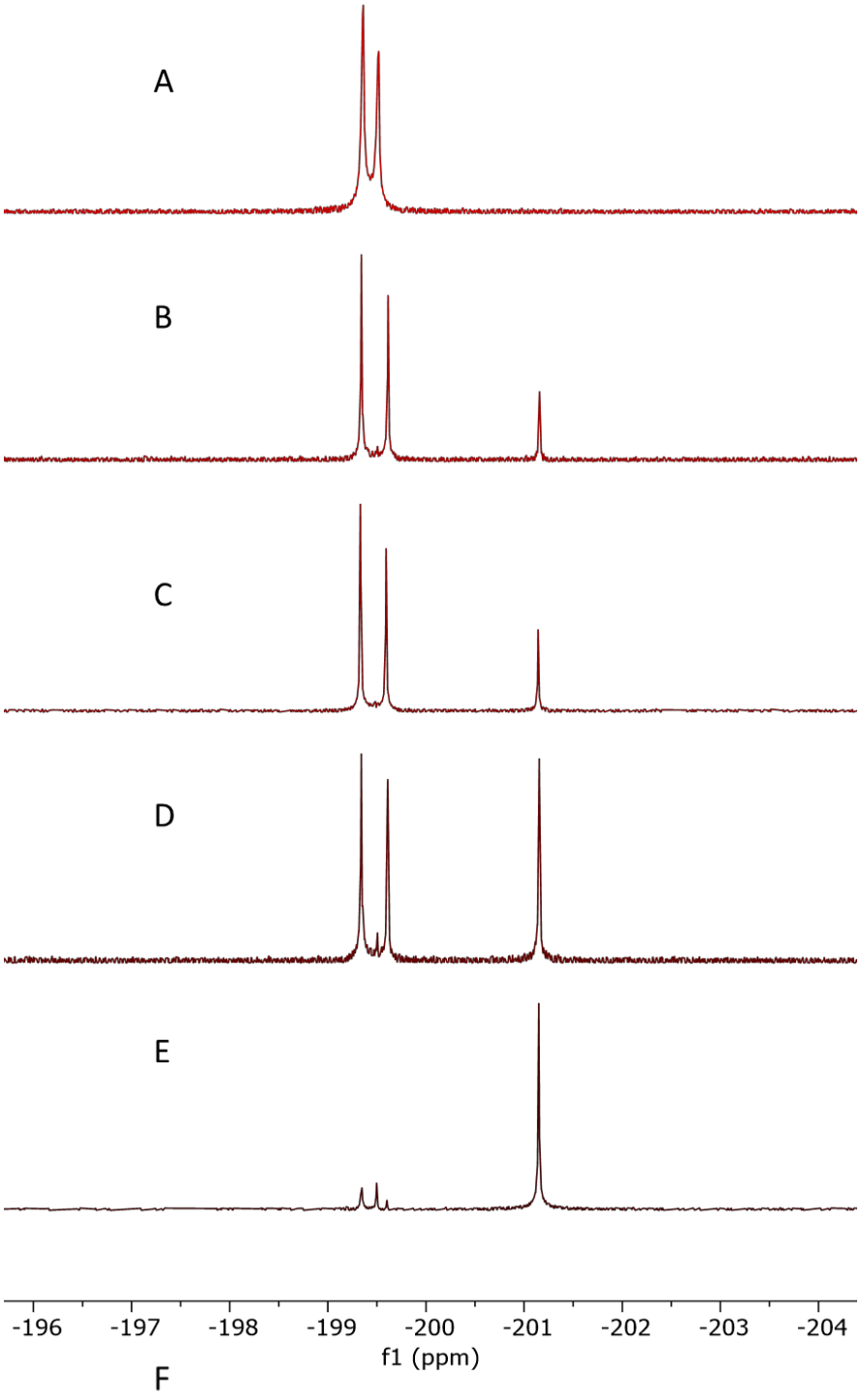

A
B
C
D
E
-196
-197
-198
-199
-200
-201
-202
-203
-204
f1 (ppm)
F
FDT, mM
15
10
5
0
0
500
1000
1500
Time (min)

Figure 2.15. Optimisation of Reaction with access amount of UDP-Glc. A). Control FDG reaction. **B**). ^{19}F-NMR spectrum of 50 mg reaction sample after 30 min. **C**). ^{19}F-NMR spectrum of 50 mg reaction sample after 60 min, comparing with non-optimised reaction, conversion is already better. **D**). ^{19}F-NMR spectrum of 50 mg reaction sample after 90 min, comparing with non-optimised reaction and **E**). ^{19}F-NMR spectrum of 50 mg reaction sample after overnight incubation. Conversion to the final FDT product is around 80% with FDG6P as the only intermediate left in the sample. **F**). Plot of the reaction time vs FDT concentration produced after time. The concentration was obtained from the standard calibration curve of the FDT solution run in the same machine under the same NMR parameters. The concentration shown here is not corrected for the dilution which is 10x the original concentration.

2.2.4 Characterisation and quality control of FDT batch

To determine the amount of enzyme leaching into the purified [^{19}F]FDT sample, we used various concentrations of OtsA and OtsB enzyme i.e. 1 mg/mL, 100 µg/mL, 10 µg/mL and 1 µg/mL and [^{19}F]FDT concentrations of 25 mg/mL and analysed by SDS-PAGE and Western blotting (**Fig. 2.16 A & B**). We did not detect any enzyme leached into the final product, even though we used a significantly concentrated sample of [^{19}F]FDT as compared to original enzyme concentration.

The purity of the final compound after purification was determined by quantitative ^{1}H-NMR, based on absolute concentration determination[31]. Such absolute concentration determination utilizes a known amount of reference compound; calibrants that are used contain the spin nucleus of interest and have resonances that do not overlap with the analyte[15]. Keeping in mind all of these parameters, maleic acid was chosen as an internal standard for quantification; maleic acid is soluble in D_2O and gives a singlet resonance at 6.30-6.40 ppm which does not interfere with the analytes studied here. Similar concentrations of the analyte and the internal standard were used. Both reagents were accurately weighed and dissolved in D_2O (0.5 mL) and

analysed by ^{1}H-NMR and the purity of the compound was calculated (**See Methods Section**). Upon quantification, the purity of the final product was found to be 88.4 ± 1 % (**Fig. 2.16C**, **Table. 2.2**).

Table 2.2. [^{19}F] FDT purity calculation results from quantitative ^{1}H-NMR analyses

I_x	I_{cal}	N_{cal}	N_x	M_x	M_{cal}	W_{cal}	W_x	P_{cal}	P_x
0.84	2	2	1	344.10	116.08	1.24 mg	3.48 mg	100 %	88.4 %

In **table 2.2**, I, N, M, W and P are the integrated area, number of nuclei, molecular mass, gravimetric weight and purity of the compound of interest (x) and the calibrant (cal), respectively.

For LC-MS analysis, an HILIC (hydrophilic interactions liquid chromatography)-based mode of separation was employed as a stationary phase and a 70:30 acetonitrile:water solvent combination used as a mobile phase. The flow rate was maintained at 0.4 mL / min and the total run time was 12 min. 5 µL of the sample was injected for both the blank and the **[^{19}F] FDT** sample. The LC-MS integrated chromatogram of the batch sample is shown in **Figure 2.16D**; the LC-MS chromatogram for both the batch and blank sample is shown in the supporting information (**Figure S26**).

The determined purity of 88% was further investigated by NMR spectroscopy; any residual organic contaminant was estimated <2%. Quantification of NaCl was performed by ^{23}Na-NMR analysis, based on a standard calibration curve for NaCl (**Figure 2.16E**). The quantified value of NaCl in 2.3 mg of [^{19}F]FDT was 12.6 % ± 1%, consistent with NaCl being the only major remaining impurity.

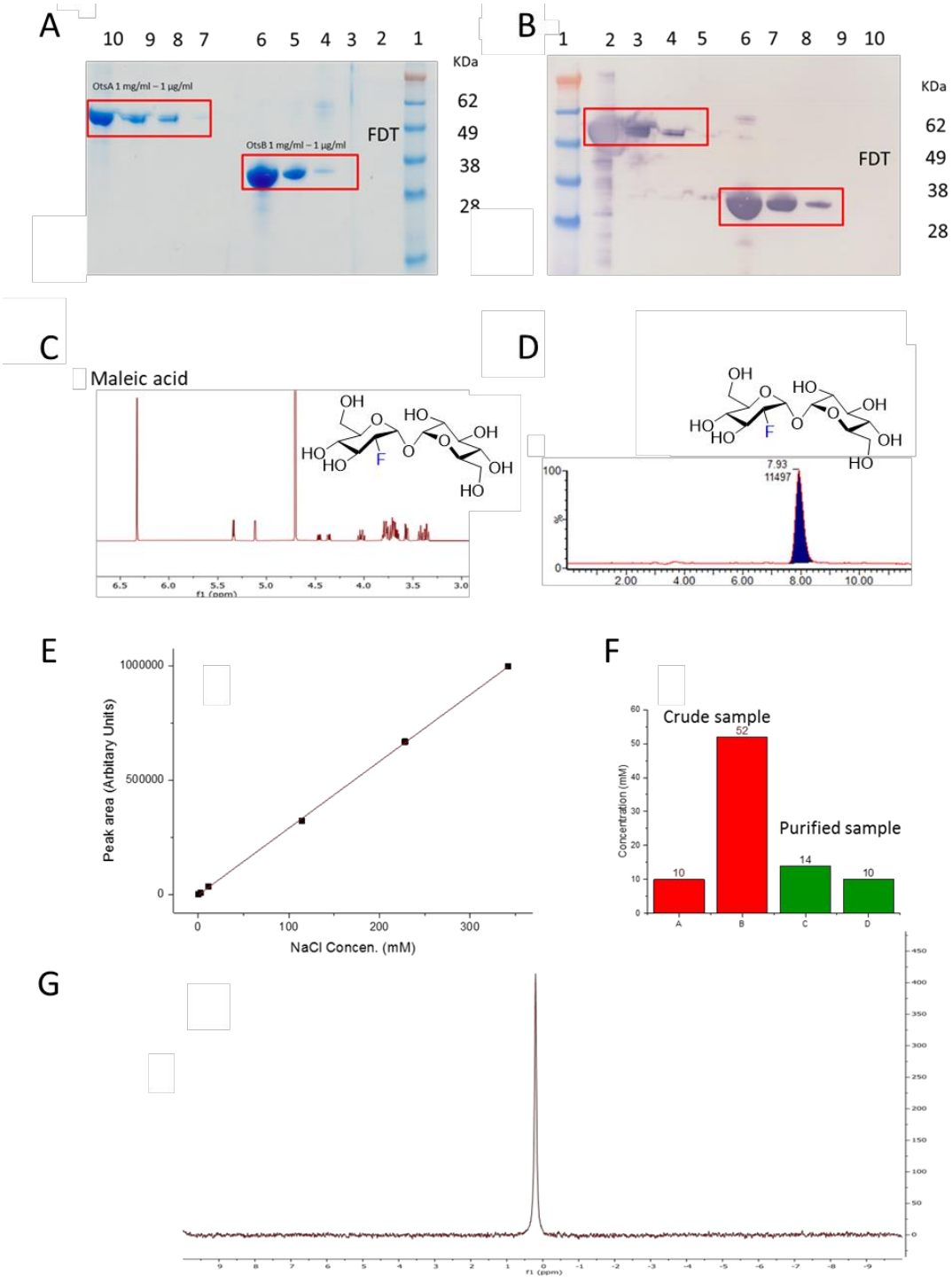


Figure 2.16. **FDT batch quantification and purity testing**. **A**) SDS-PAGE analysis for the detection of enzyme leaching in the final FDT batch. OtsA (lane 7-10) and OtsB (lane 3-6) with 1/10 serial dilutions loaded onto the SDS-PAGE. 25 mg/mL FDT from purified batch also loaded on the gel. No enzyme was detected in the FDT sample. **B**) Western blotting visualisation for the detection of enzyme leaching in the final FDT batch. OtsA (lane 2-5) and OtsB (lane 6-9) enzymes with 1/10 serial dilutions from 1mg/mL to 1 µg/mL loaded onto the SDS-PAGE. 25 mg/mL FDT (lane 10) from purified batch

also loaded. Visualisation was done with anti-His monoclonal antibody and no his-tagged protein was detected in the FDT sample. **C**). Processed quantitative ^{1}H-NMR spectrum of analyte FDT. Maleic acid as an internal standard. **D**) LC-MS Chromatogram of FDT. Retention times above; integral below for each noted peak. Peak at 7.93 min is FDT with major ESI^- m/z of 343. **E**) Standard calibration curve of NaCl; **F**) Concentrations in FDT samples (determined by ^{19}F-NMR and ^{23}Na-NMR) in the crude reaction mixture (red) and purified (green). Column A is the concentration of FDT in the crude reaction mixture determined by ^{19}F-NMR; column B shows the quantified value of NaCl as determined by ^{23}Na-NMR. Columns C & D are the corresponding measurements from the purified sample of FDT**.** All are calculated from samples dissolved in 0.5 mL D_2O. Total integrals from the peak area were used for calculation using intercept and slope from the calibration curve. **G**) Example ^{23}Na-NMR spectrum for quantitative yield calculation of NaCl in samples.

Further characterization (**See Methods for all**) included further NMR, IR and LC-MS analysis (**See supplementary Figs. S5-19).**

Elemental microanalysis of a solid [^{19}F]FDT batch was also performed. Analysis of CHN content (Elemental Microanalysis Ltd) used the Dumas combustion method. The results of the analysis are shown in **Table 2.3** and are consistent with moderately hygroscopic [^{19}F]FDT at 88% purity bearing <2% organic contaminant (possibly imidazole based on extended NMR analyses) and 10-12% NaCl impurity.

Table 2.3: Elemental Microanalysis Results for [^{19}F]FDT Samples

	Calculated, pure [^{19}F]-FDT (%)	Calculated, 88% [^{19}F]-FDT (%)	Found-1 (%) ± 0.3	Found-2 (%) ± 0.3	Average (%) ± 0.3	Deviation, from pure (%)	Deviation, from 88% (%)
C	41.86	36.84	35.63	35.52	35.58	- 6.28	- 1.26
H	6.15	5.41	5.80	5.72	5.76	- 0.39	+ 0.35
N	0	0	0.96	0.97	0.96	+ 0.96	+ 0.96

Control of heavy metals in the pharmaceutical products is crucial as higher intake could be toxic[32]. To that end we wished to test the components of Ni potentially leaching from Ni-NTA column into the final [^{19}F]FDT product. We also wanted to test the contents of Na, Mg and K (all metals used in the buffer solutions during enzyme preparations). To detect the metals potentially present in the purified [^{19}F]FDT sample or in the enzyme used for the synthesis of the [^{19}F]FDT, inductively coupled plasma mass spectrometry (ICP-MS)[33] based metal quantification of samples was carried out in the Department of Earth Sciences. Total 6 samples were analysed in duplicates i.e. OtsA, OtsB, 2x [^{19}F]FDT crude sample and 2 x [^{19}F]FDT purified samples. MilliQ water and 2 % HNO_3 were used as blank. The results are shown in **Table 2.4**. The data obtained showed excellent accuracy and precision when duplicates samples analysed.

Magnesium was only detected in the [^{19}F]FDT crude samples. Ni was detected in both OtsA and OtsB enzyme sample possibly leaching from the Ni-NTA column. However, the amount of Ni detected was well below the recommended daily intake[34]. The amount was almost 10 times more in OtsA sample than the OtsB. However, the amount present in either the [^{19}F] FDT crude or purified sample was minimal. The sodium content was high in [^{19}F]FDT samples, this was almost 2.5 times less than the amount present in the crude samples. Higher sodium

quantity, corresponds to the sodium quantification NMR. Potassium was only detected in crude [^{19}F]FDT samples as potassium was used as a salt during the reaction process.

Table 2.4: Metal Analysis in OtsA and OtsB enzyme and FDT Crude and Purified samples

Entry	Sample	Mg ng/g	Ni ng/g	Na ng/g	K ng/g	Dilution factor
1	Blank milliQ	Below DL	0.002	Below DL	Below DL	x1
2	Blank 2% HNO3	0.324	0.030	Below DL	Below DL	x1
3	OtsA	Below DL	11.49	67828.86	Below DL	x50
4	OtsB	Below DL	0.925	27093.77	Below DL	x50
5	FDT crude	501.20	0.128	8803.52	675.89	x10
6	FDT purified	Below DL	0.187	3638.73	664.97	x10

For toxicity studies, the [^{19}F]FDT doses needed to be prepared in advance in 50 mM HEPES buffer containing 7.5 mM $MgCl_2$. Therefore, stability for up to 21 days in this buffer system was determined (**Experimental section 2.5.10**). As shown from **Figure 2.17**, [^{19}F]FDT samples stored at room temperature and between 2 – 8 °C did not show any degradation over the period of testing. In addition, during the entire testing period, it was important that the solid stored at -20 °C does not degrade, therefore, we tested the stability of the solid sample as well whereby, the compound was stored at -20 °C and then samples (~ 8 mg) were dissolved in D_2O and analysed by ^{1}H-NMR spectroscopy to detect any degradation of the product. For the duration of testing the compound did not show any degradation (**Fig. 2.17 B**).

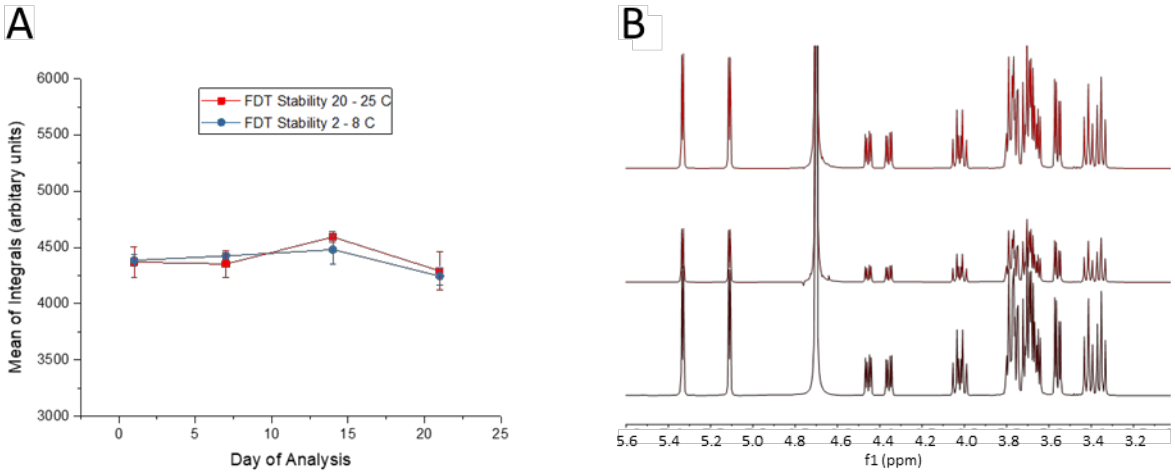


Figure 2.17. Stability testing data of [^{19}F]FDT in solution and solid. A) Plot of mean peak area of integrals and standard deviation against the day of testing for stability testing in solution at 20 -25 °C and 2-8 °C over 21 day period. Samples were stored in HEPES buffer (50 mM HEPES, 7.5 mM $MgCl_2$, pH 7.5) and run in triplicate. Sample analysis was done by ^{19}F-NMR spectroscopy. **B**). Stability testing of the solid FDT compound by ^{1}H NMR spectroscopy. Samples from -20 °C were dissolved in 0.5 mL D_2O and analysed by ^{1}H NMR.

In the upcoming section optimisation of the radiosynthesis and automation has been carried out by Dr Yong-Mo Ahn and Dr Falguni Bhattacharyya at NIH. I have done the synthesis in all different enzyme systems.

2.2.5 Synthesis and quality control of [^{18}F] FDT

After the successful large scale synthesis and purification of [^{19}F]FDT, we next sought to develop a protocol for the radio synthesis of [^{18}F]FDT from commercially available [^{18}F]FDG in all three enzymatic reactions (**Figure 2.18**).

The key challenge in the radiosynthesis is usually the significantly lower concentration of acceptor substrate [^{18}F]FDG which is typically in nao-molar range; the concentration range we

did not test under the 'cold' reaction conditions. However, this did not prove too problematic. We tested the reactions from 5-15 mCi and managed to get full conversion in 60 min for both the 3-steps-3-enzyme and 1-step-1-enzyme synthesis (**Figure 2.18C & D**). The reaction did not work in 2-steps-2-enzyme synthesis **(Figure 2.18B**). The reaction progress was monitored by radio-HPLC with two different analytical methods; i) A HILIC column based rapid and efficient analytical method with run time of 15 min and retention time (rt) of [^{18}F] FDG ~ 5 min and [^{18}F]FDT ~ 8 min and ii) A Glycan mapping column based analytical method with run time of 20 min. This method not only allowed the monitoring of [^{18}F]FDG (rt ~ 7 min) and [^{18}F]FDT (rt ~ 10 min) but also was effective in monitoring the phosphate intermediates as a single peak (rt ~ 12 min).

Once the chemo-enzymatic reactions completed, the enzymes in the reaction mixture were precipitated by adding EtOH. The filtrate was passed through a 5 μm filter and purified through luna-NH_2 cartridges. The product [^{18}F]FDT was eluted with EtOH. The non-decay corrected radiochemical yield for [^{18}F]FDT obtained from 3-steps-3-enzyme synthesis was 34% and from 1-step-1-enzyme synthesis was 33%. The radiochemical purity in both instances was >99%.

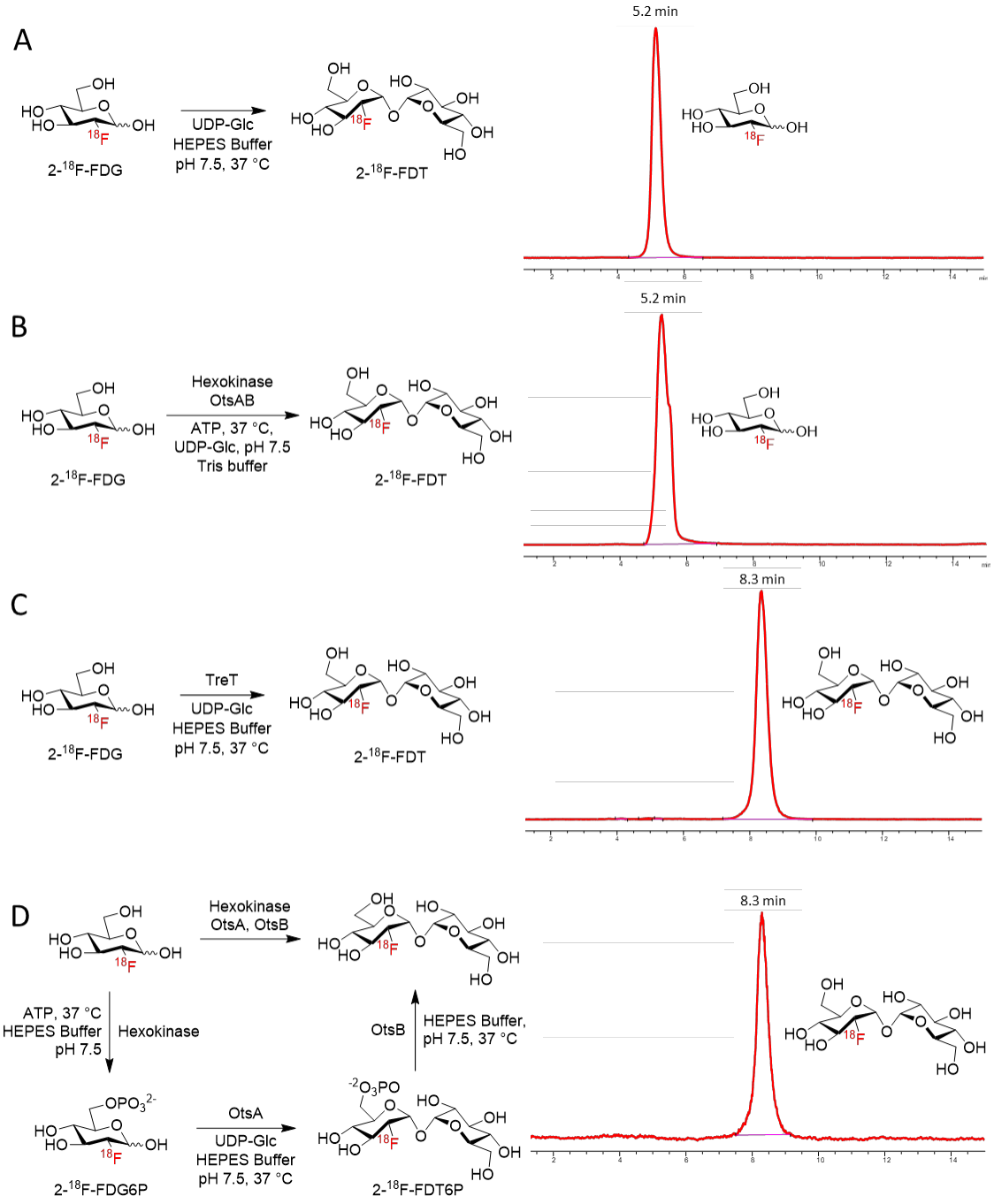


Figure 2.18. Enzymatic radio synthesis of [^{18}F]FDT. A) Schematic of control reaction, no enzyme was added in the reaction mixture. **B**) Schematic overview of attempted radiosynthesis of [^{18}F]FDT using 2-enzyme-2-step one-pot synthesis method which failed to yield any product and only [^{18}F]FDG observed after 2 h reaction. **C**) Schematic and radio-HPLC chromatogram of [^{18}F]FDT synthesized from TreT enzyme, full conversion to the product observed after 60 min of reaction. **D**). Schematic overview of [^{18}F]FDT synthesised from hexokinase, OtsA and OtsB enzyme and radio-HPLC chromatogram , full conversion to the product observed after 60 min of reaction.

2.2.5.1 Optimisation of Radiosynthesis for Animal Studies

After initial screening experiments, we attempted to optimize the 3-steps-3-enzyme reaction for efficient synthesis of [^{18}F]FDT. We tested the reduction of the overall reaction time to 30 min from 1 h with higher concentrations of the enzymes, OtsA, OtsB and hexokinase, to ensure >99% completion of the reaction (**Figure 2.19A**). Decreasing the reaction time did not affect the radiochemical yield, 2~5 mCi, within a range of the radioactivity of the final product from 1 h reaction and the purity of the final products. We also tested if there were any residual proteins from the reaction in the final product, due to the inclusion of higher concentration of the enzymes, and we confirmed that there were no protein carried over by western blot (> µg/reaction – i.e. sensitivity of assay) (**Figure 2.19B & C**) . Finally, this optimization confirmed that a 30 min reaction time, or overall 1 h to 1 h 15min processing time, was sufficient to make highly pure [^{18}F]FDT for the animal studies and these conditions were further applied to the automation of the radiosynthesis.

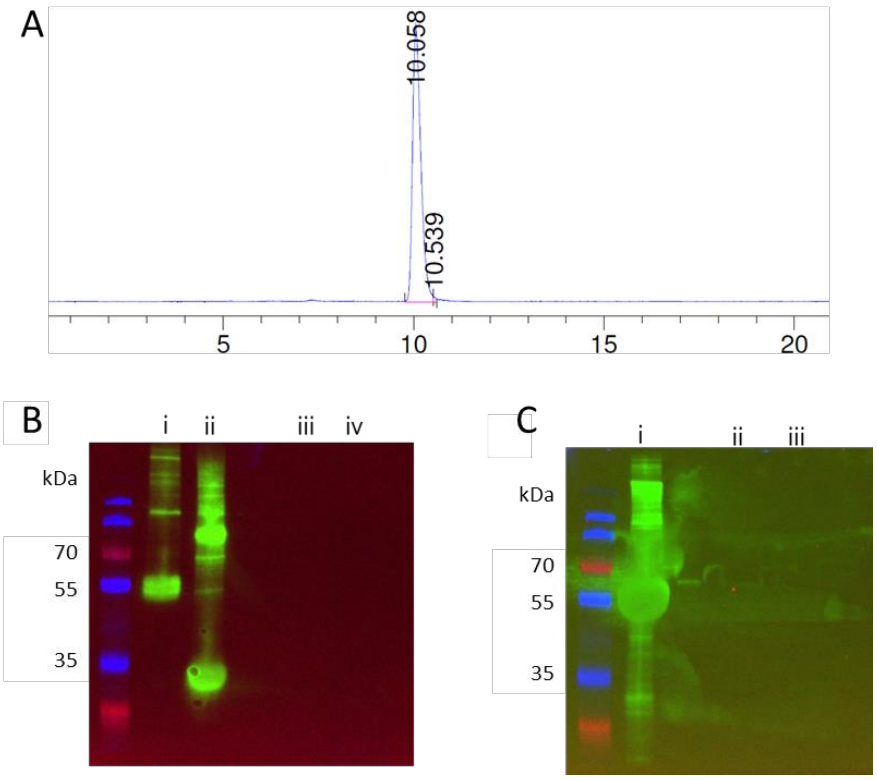


Figure 2.19. Quality control testing for [^{18}F]FDT batch. **A**) The purity of the 30 min reaction of [^{18}F] FDT by radio-HPL. **B**) Detection of OtsA and OtsB, using anti-His antibody. (**i**) OtsA enzyme; (**ii**) OtsB enzyme; (**iii**) Dilute [^{18}F]FDT sample and (**iv**) Concentrated [^{18}F]FDT sample **C**) Detection of hexokinase, using anti-hexokinase antibody. **C**). Detection of hexokinase in [^{18}F]FDT sample using anti-hexokinase antibody. (**i**) Hexokinase enzyme only; (**ii**) Dilute [^{18}F]FDT sample and (**iii**) Concentretaed [^{18}F]FDT sample. No enzymes detected in the [^{18}F]FDT samples.

2.2.5.2 Automated Radiosynthesis

After successful manual standardization of the procedure, a fully automated synthesis was performed in a GE Tracer lab FX-N module (**Figure 2.20**). Transformation of [^{18}F]FDG to [^{18}F]FDT and precipitation of enzymes were performed in Reactor 1. The reaction mixture was transferred to Reactor 2 through a 5 µm filter and stack of three luna-NH_2 cartridges for evaporation of ethanol and final formulation.

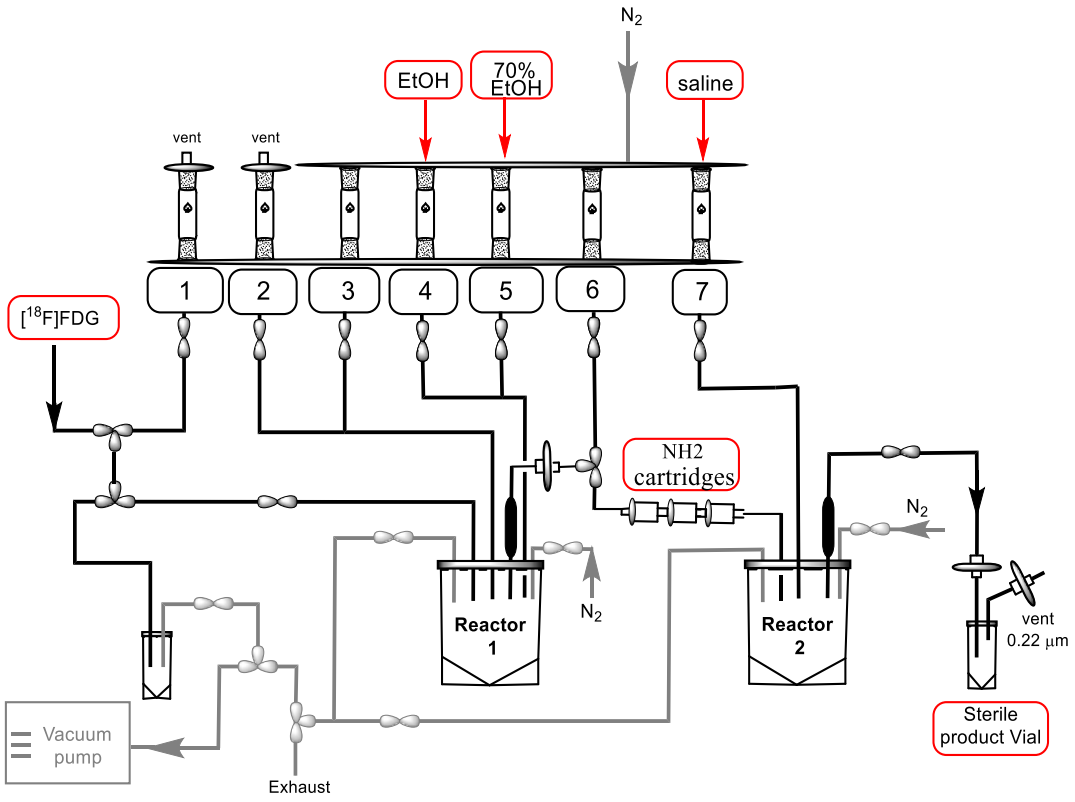


Figure 2.20. Schematic diagram of automated [^{18}F]FDT synthesis on GE FX-N pro module

The radiolabelling reactions were performed with 1480- 3700 MBq (40-100 mCi) of [^{18}F]FDG in 0.8 - 1.8 mL of saline. The higher overall decay-corrected radiochemical yield (**see Table 2.5**) was observed with a higher amount of [^{18}F]FDG starting material.

Table 2.5: Effect of amount of [^{18}F]FDG on the radiochemical yield

Entry	[^{18}F]FDG mCi	Volume mL	Volume reagents mL	[^{18}F]FDT mCi	Yield % decay corrected
1	40	0.8	0.3	9 (n=1)	31
2	60	1	0.3	13 (n=3)	30-41
3	100	1.8	0.3	44, 38 (n=2)	60, 51

In a typical reaction starting with 3700 MBq (100 mCi) of [^{18}F]FDG, 1628 MBq (44 mCi of [^{18}F]FDT was obtained in 50 min. The identity of the product was confirmed using LC-MS by co-injecting the [^{18}F]FDT with an authentic nonradioactive standard, FDT (**Figure 2.21**). The radiochemical purity was >98%, determined by radio-HPLC.

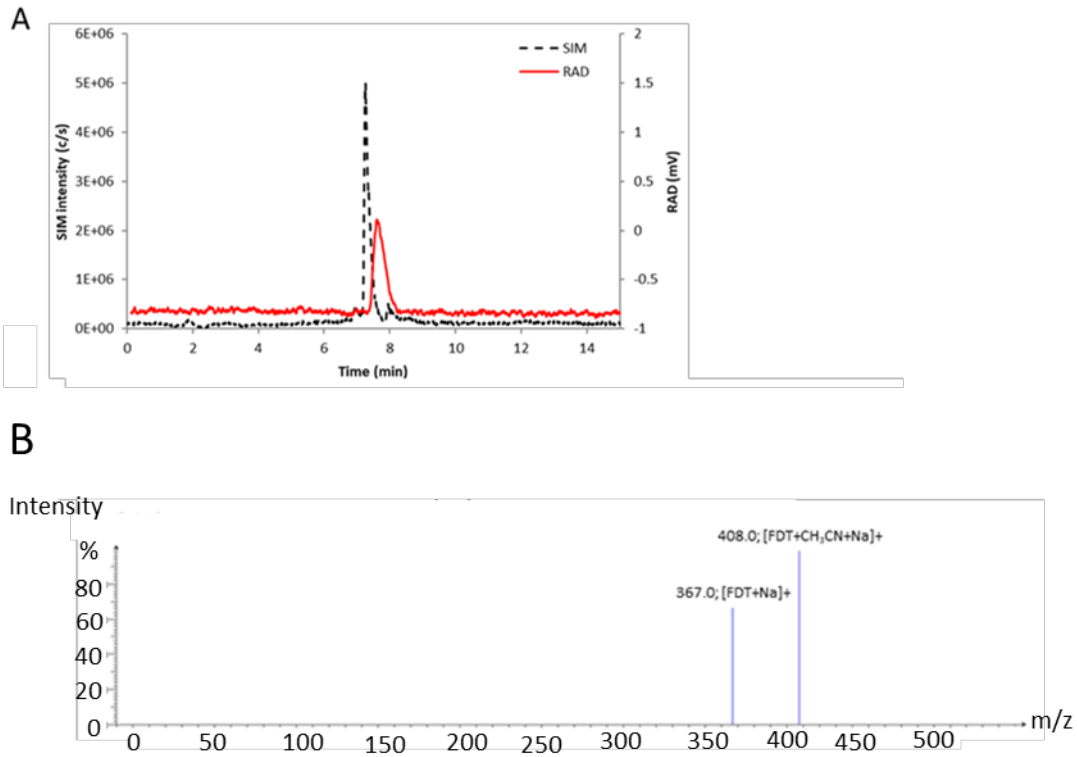


Figure 2.21. **LC-MS analysis of [^{18}F]FDT coinjected with nonradioactive standard FDT**. **A**) Solid line, in-line radiodetector; dotted line, UV detector at 254 nm. **B**) ESI$^+$ MS spectrum of FDT with m/z of 367.0 represntative of [FDT + Na]$^+$ and m/z of 408.0 indicative of [FDT+CH_3CN+Na]$^+$.

However, there was a major UV-peak at ~15 min. The HPLC retention time of this impurity peak perfectly matched with the rt of separately injected UDP-Glucose (**Figure 2.22**). Furthermore, mass-spec analysis (**Figure 2.23**) of the decayed radiolabelled FDT solution confirmed the presence of UDP-Glc in the solution.

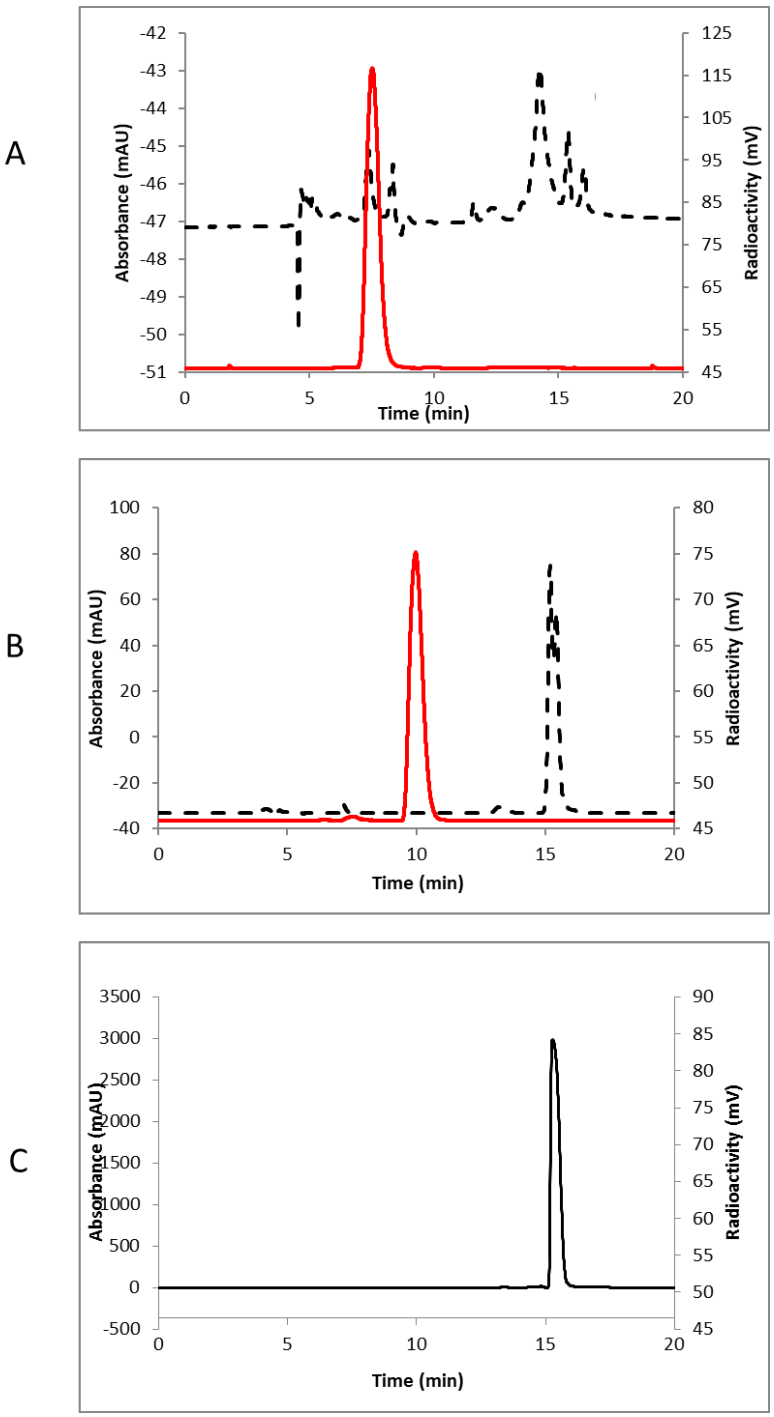
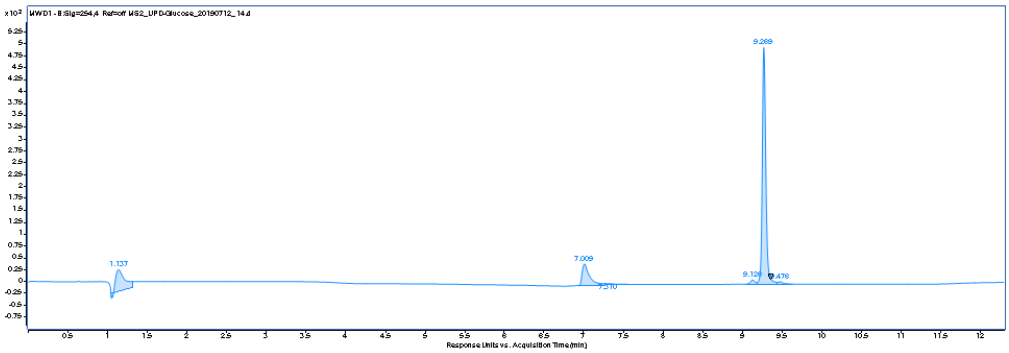
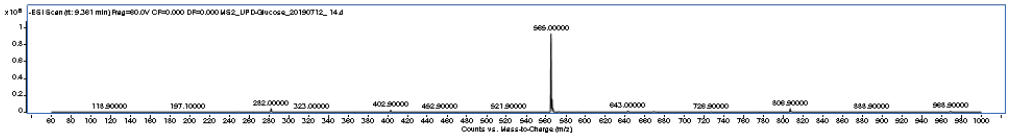


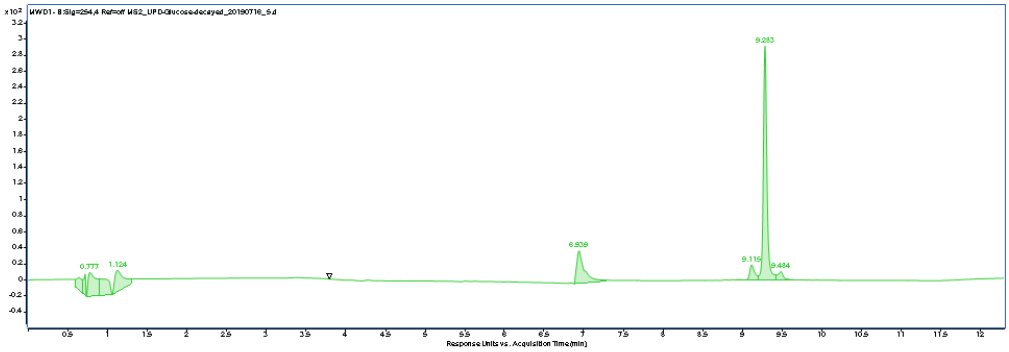
Figure 2.22. A) HPLC analysis of [^{18}F] FDG. **B**) [^{18}F] FDT and **C**) Pure UDP-Gl. 4.6 x 250 mm, 2.7 µm AdvanceBio Glycan Mapping Column; solvent A = 50 mM ammonium formate, pH 4.5, solvent B = acetonitrile; Flow rate = 0.5 mL/min; gradient 0-15 min 68-62% B; 15-20 min 62-68% B. Retention. Red line, in-line radiodetection; black line, UV detection at 254 nm.

A





B



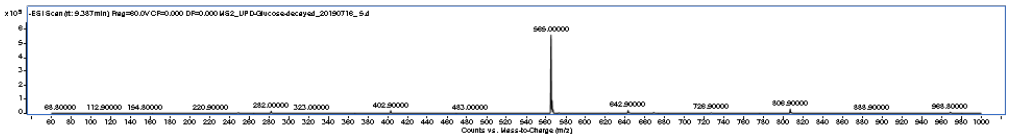


Figure 2.23. Mass Spec (ESI) analysis of **A**) Pure UDP-Glc; **B**) Decayed [^{18}F]FDT solution. Mass calculated for UDP-glucose-1H ($C_{15}H_{23}N_2O_{17}P_2$) 565.05, observed 565

Recently, S. Peña-Zalbidea *et al.*[35] reported the automated synthesis of [^{18}F]FDT using *T. tenax* TreT as an enzyme. However, a fully automated synthesis including purification of the final product has not been reported in this literature.

2.2.5.3 Specific Activity Calculation

Since the quantification of FDT is required to have FDA-approval for the clinical study to test FDT as a PET radiotracer scan, the amount of FDT was determined via an enzymatic assay as reported previously[36]. The active ingredient, [^{18}F]FDT has a molecular formula of $C_{12}H_{21}{}^{18}FO_{10}$ with a molecular weight of 343.29 Daltons. [^{18}F]FDT decays into 2-[^{18}O]-trehalose. Then, 2-[^{18}O]-trehalose can be hydrolysed to 2 D-Glucose (D-Glc) by trehalase. The production of D-Glc can be monitored by Glucose Oxidase assay. In this assay, glucose oxidase reacts with D-Glc to form D-gluconolactone and H_2O_2. In the presence of horseradish peroxidase (HRP), the H_2O_2 then reacts with the dye in a 1:1 stoichiometry to generate the red-fluorescent oxidation product that can be detected. The amount of D-Glc can be converted to the amount of trehalose. Utilizing this assay, we detected and analysed the amount of the cold starting material, [^{18}O] Glucose, and the final product, [^{18}O] trehalose. Depending on the [^{18}F] FDG quality, the average amount of [^{18}F]FDT synthesized using the chemo enzymatic synthesis was 0.21 μmol and the specific activity was 26.4 Ci/mmol. With this quantification result, the toxicology study on this molecule has been designed and subsequent toxicity studies carried out.

Table 2.6: Specific activity of calculations of [^{18}F]FDT

Entry	[^{18}F]FDG mCi	The total [^{18}F]FDT (μmol)	Specific activity (Ci/mmol)
1	3.1	0.14	11.0
2	5.0	0.15	15.9
3	4.6	0.13	17.0
4	1.7	0.1	16.5
5	2.1	0.26	8.3
6	4.9	0.08	59.6
7	3.5	0.13	26.6
8	3.9	0.05	86.8
9	2.7	0.14	19.8
10	4.4	0.45	9.8
11	12.7	0.66	19.3

2.3 Conclusions

To summarise the chapter, we have attempted three biocatalytic approaches for the synthesis of FDT. While we have been successful with two of those strategies i.e. the one-enzyme and three-enzymes strategy, we have found the three-enzymes system far more efficient. This was due to the superior kinetic characteristics, higher enzyme expression yields and faster reactions at or near the physiological pH and temperature range. We have used this method to scale-up the reaction and prepared several batches of [^{19}F]FDT with a maximum batch size of 100 mg. The procedure has been reproducible and that allowed us to synthesise up to 3 g of the compound using this method. In addition, we have been able to apply the 'cold' synthesis protocols for the [^{18}F]FDT synthesis. We have successfully achieved the [^{18}F]FDT synthesis

by both TreT enzymes and hexokinase, OtsA and OtsB enzyme systems. The faster reactions of 30 min to 1 h for 'hot' synthesis suited well with the short half-life of ^{18}F. We then successfully applied optimised 'hot' synthesis conditions for the automated radiosynthesis of [^{18}F]FDT. The 'cold' FDT synthesised has been used to test the toxicity of this compound in animal species (discussed further in chapter 3). In addition, the [^{18}F]FDT has been used in several pre-clinical applications to be discussed in Chapter 3.

We show here the rare biocatalytic approaches to the synthesis of radiotracer. The strategies employed are highly advantageous where complex organic reactions can be carried out in aqueous conditions. In addition purification strategies employed make use of minimal organic solvents which can be evaporated in a short time. With the conventional [^{18}F]FDG synthesis, acetonitrile is used as part of the reaction. Due to toxicity issues, not only does acetonitrile have to be removed from the reaction mixture, but also a separate quality control test based on gas chromatography is required by regulatory authorities to ensure that the product is safe for the sterile injection. Due to the short half-life of ^{18}F, requirement for longer QC time is not desirable, therefore biocatalytic approaches would add greater value to future radiotracer development. While there are advantages for using biocatalytic approaches, there are of course challenges associated with these syntheses. Among those issues, the choice of expression host for the enzyme is important. Enzymes expressed in *E. coli* require extensive purification for endotoxins and the subsequent purification step could hamper enzyme activity. Therefore, enzyme expression in insect cells could be a useful alternative solution, however, insect cells can amplify viruses that may infect humans. To manufacture products for human use, the cell lines used for enzyme expression should be free of contamination.

The future work in this area is to take the automated synthesis from GLP lab to a good manufacturing practice (GMP) laboratory. This will allow the synthesis of [^{18}F]FDT for phase 0 and Phase 1 clinical trials. In addition, enzyme reactions can be explored in a biocatalytic

flow system and that in essence could allow efficient synthesis of [^{18}F]FDT due to easier purification of products, automation, and the potential of re-using the enzyme. This radiotracer has a great potential to be used as a specific PET imaging probe for the diagnosis of TB and monitoring the response to treatment.

2.4 Experimental Procedures

2.4.1 General Biology Experimental Procedures

All prepared biological solutions and equipment, such as media, plastic and glassware, used in the handling of microbial cultures were autoclaved at 121 °C. All biological work was performed in a BASSAIRE Class II Laminar Flow Cabinet. Bacterial cultures were incubated in Innova® 42 incubator Shaker Series. Centrifugation was performed in Avanti Jxn-30 Centrifuge for cell harvesting and post sonicated cell cultures, and Megafuge Centrifuge was used for protein concentration and DNA samples. Micro centrifugation was performed on Eppendorf Centrifuge 5424 R. Gel electrophoretic analysis was performed on the following equipment: Invitrogen XCell SureLockTM and BioRad Power Pac Basic (200 V used, 50 min.) with using MOPS/MES as buffer.

2.4.2 Preparation of Lysogeny Broth Agar Plates

Lysogeny broth (LB, 6.25 g) and agar (2.5 g) were both added to water (250 mL) and the mixture was autoclaved. After cooled to ~45 ºC, a stock solution of appropriate antibiotic was added and the agar was poured into plates and allowed to settle. Stored at 4 ºC.

2.4.3 Transformation

Plasmid stock (1 μL, 10 ng) and cell stock (20 μL) mixed in 14 mL polyene tube and incubated on ice for 30 min, the mixture was then heat shocked to 42 °C for 45 s then incubated on ice for 2 min. Super optimal broth with catabolic repression (SOC) medium (200 μL) was added and the mixture was incubated at 37 °C for 1h. The mixture was plated on agar plates with the appropriate antibiotic (2 plates, one with 100 μL one with 25 μL). Plates were then incubated overnight (37 °C).

2.4.4 DNA Preparation

A single colony was picked and placed into 5 mL of lysogeny broth (LB) with the appropriate antibiotic. The culture was shaken at 37 °C overnight. Cells were pelleted by centrifugation (4700 rpm, 20 min, 4 °C) then DNA preparation carried out according to the instructions provided with the QIAGEN QIAPrep spin miniprep kit. The DNA concentration is determined by nanodrop and Sanger sequencing performed by Source Bioscience. Sequence analysis was performed by using source bio edit.

2.4.5 SDS-PAGE

Sodium dodecyl sulfate – polyacrylamide gel electrophoresis (SDS-PAGE) was carried out to check the purity of all proteins. These were carried out using 4 – 12% bis-Tris polacrylamide gels with either MOPS or MES buffer. To the protein sample (8 μL) was added 2 × SDS loading buffer (3 μL 80 mM Tris-HCl buffer pH 6.8, 8% v/v glycerol, 40 μM bromophenol blue, 80 mM SDS, 2% β-mercapethanol). The solution was then heated to 95 ºC for 10 min. The sample was then applied to a well in the gel. The gel was then run at 200 V for 1 h and then visualised

by the addition of Coomassie InstantBlue dye (Gentaur) and gentle stirring for 2 h at room temperature.

2.4.6 Western-Blot

SDS-PAGE was done as before, but using a Pre-Stained protein ladder and the gel was not stained with InstantBlue dye. Instead, the gel was electroblotted onto a membrane for 7 min using an iBlot machine. The membrane was then washed with 50 mM Tris-HCl, 150 mM NaCl and 0.05% Tween 20, pH 7.6 (TBS-T + 5% BSA w/v , 45 mL) for 1 h. The membrane was further washed with TBS-T + 5% BSA w/v, 45 mL and monoclonal anti-polyHistidine-alkaline phosphatase antibody produced in mouse (Sigma, 16 μL). The membrane was then rocked for 4 h at room temperature. After this time, the solution was removed and the membrane washed with TBST buffer (3 × 20 mL). BCIP/NBT alkaline phosphate substrate (Sigma Aldrich, 4 mL) was added and the membrane was gently rocked until protein bands could be seen (~15 min). The membrane was then washed with water.

2.4.7 Protein Mass Spectrometry

Various machines used for protein LC-MS. In all cases solvent A was water and solvent B was acetonitrile with both containing 0.1% formic acid.

1) Waters LCT Classic coupled to a Shimadzu 20 Series HPLC using a Thermo Proswift (250 x 4.6 mm x 5 μm) column. Electrospray source parameters were as follows: capillary voltage 3000 V; cone voltage 25 V. Spectra were calibrated to at least 17 matched peaks of the multiply charged ion series of equine myoglobin run under equivalent conditions. The gradient program is shown below; a flow rate of 0.4 ml/min was used throughout.

Time (min)	% Solvent A	% Solvent B	Flow rate (mL/min)
0.0	95	5	0.4
1.0	95	5	0.4
7.0	5	95	0.4
11.0	5	95	0.4
12.0	95	5	0.4
17.0	95	5	0.4

2) Waters Xevo G2-QS QToF MS coupled to a Water Acquity UPLC using a Thermo Proswift (250 x 4.6 mm x 5 μm) column. Electrospray source parameters were as follows: capillary voltage 3000 C; cone voltage 20 V. Spectra were calibrated through use of an internal lock-spray. The gradient program is shown below; a flow rate of 0.3 ml/min was used throughout.

Time (min)	% Solvent A	% Solvent B	Flow rate (mL/min)
0.0	95	5	0.4
1.0	95	5	0.4
7.0	5	95	0.4
8.0	5	95	0.4
8.1	95	5	0.4
10.0	95	5	0.4

The electrospray source was operated with a capillary voltage of 3.2 kV and a cone voltage of 35 V. Nitrogen was used as the nebulizer and desolvation gas at a total flow of 600 l hr^{-1}. Spectra were calibrated using a calibration curve constructed from a minimum of 16 matched peaks from the multiply charged ion series of equine myoglobin obtained at a cone voltage of 35 V. Data was processed using MassLynx software (v. 4.1 from Waters) according to the manufacturer's instructions.

2.4.8 Circular Dichroism (CD) Spectroscopy

For CD measurement, protein was buffer exchanged into phosphate buffer (10 mM potassium phosphate, pH 7.5). Measurements were made at room temperature using a Chirascan CD-spectrometer (Applied Photophysics) using 0.1 cm quarz cuvette. Background readings were taken with using 0.2 mL of buffer only, followed by protein samples measured at concentrations of 0.2 mg/mL. Scans were run using 0.5 s per time point and 0.5 nm increments, scanning from 185 to 280 nm. Data reported is the mean average of 3 results.

2.4.9 Liquid Chromatography-mass spectrometry for Small Molecule Analysis

Liquid chromatography–mass spectrometry (LC–MS) for quantification of trehalose and glucose was performed on the LC-MS Quattro instrument coupled with agilent technologies HPLC system, using a TOSOH TSKgel Amide-80 column (4.6 mm x 250 mm, 5µM, 80 Å). Solvent A (CH_3CN) and (H_2O) with a volume ratio of 70:30 were used as the isocratic mobile phase at a flow rate of 1.0 mL / min. The MS file was programme as 20 min for each sample. The electrospray source was operated with a capillary voltage of 3.0 kV and a cone voltage of 20 V. Nitrogen was used as the nebulizer and desolvation gas at a total flow of 500 Lh^{-1}. The data was acquired by single ion recording (SIR) of m/z 341 for trehalose and m/z 179 for

glucose in negative mode and processed using MassLynx software (v. 4.1 from Waters) according to the manufacturer's instructions.

2.4.10 High Performance Liquid Chromatography (HPLC) for Enzyme Reaction Analysis

All of the enzyme reactions were analysed by HPLC for UDP-glucose consumption and UDP release. For the analysis, few different stationary and mobile phases were used to optimise the separation between UDP and UDP-glucose (Summarised in table S1). Method 3 was selected as a method of choice because it gave the best separation between the two phosphate sugars.

Table S1: Summary of different HPLC conditions for enzymatic reaction analysis

Method	Mobile Phase	Stationary Phase	Gradient	Flow rate (mL/min)	Run time (min)	UV detection (λ)
1	A. H_2O B.Ammonium formate 300 mM	waters spherisorb 5 µm SAX 4.6 x 250 nm	5-100% B linear gradient	1	30	262
2	A.H_2O B.H_2KPO_4 100 mM	waters spherisorb 5 µm SAX 4.6 x 250 nm	5-100% B linear gradient	1	30	262
3	A. H_2O B. H_2KPO_4 1M	Phenomenex Luna NH_2 4.6 x 250 nm	0-100% linear gradient over 60 min, 61-65 min, 100% A	0.6	65	262

2.4.11 Expression, Purification and Characterisation of TreT *P. horikoshii* Enzyme

The DNA plasmid from group plasmid bank was verified by sequencing from source bio-science. The plasmid encoded a C-terminal 6 x Histidine tag (His-tag) on the protein. The plasmid was transformed into *E.coli* (BL21 DE3) cells and plated on LB agar containing 50 mg/mL kanamycin. One of the resulting grown colony was inoculated into 10 mL LB media containing 10 µL of kanamycin (50 mg/mL) solution and left incubating overnight (37 °C, 200 rpm).

To express the TreT protein, 10 mL grown culture was inoculated into 1 L of LB media containing 1 mL of kanamycin solution (50 mg/mL) and left incubating (37 °C, 200 rpm). OD_{600} was measured every one hour and once the inoculated culture reached the mid-log phase, it was induced with 1 mL of IPTG solution (final concentration = 1 mM) and grown in shaking incubator overnight (37 °C, 200 rpm).

Cells were then harvested by centrifugation (4700 rpm, 20 min, 4 °C) and the pellet was resuspended in 30 mL lysis buffer (300 mM NaCl, 50 mM NaH_2PO_4, 20 mM imidazole). One protein inhibitor tablet, 25 mg lysozyme and 5 mg of DNase was also added into the lysate and lysis reaction was carried out on rotating platform (60 min, 4 °C). Lysed cells were sonicated (5 x 30 s, 30 s pulse on, 60 s pulse off, 75% amplitude). Sonicated cells were centrifuged (21000 x g, 20 min, 4 °C) to clarify the lysate. Supernatant was then filtered (0.45 µm and 0.2 µm filter). Next supernatant was loaded on a 50 mL FPLC loop and purified by Ni-NTA chromatography using 5 mL His-trap HP column and eluted with 15 column volumes of elution buffer (300 mM NaCl, 50 mM NaH_2PO_4, 250 mM imidazole). Protein samples were concentrated using viva spin at 10 kDa MWCO. Elution buffer was exchanged for 300 mM NaCl, 50 mM HEPES, pH 7.5. Protein samples were then characterised by SDS-PAGE to verify protein purity and LC-MS to confirm the mass of the protein.

2.4.12 Expression, Purification and Characterisation of TreT *T. tenax* Enzyme

2 x 1 L cultures of TreT *T. tenax* protein were expressed in BL21 (DE3) cells. Expression was carried out by inoculating 10 mL cultured BL21 (DE3) transformed with plasmid DNA into 1 L of LB media. 1 mL of Kanamycin sulphate solution (50 mg / mL) was used as the resistance antibiotic. Both the flasks were shaken at 200 rpm and 37 °C for 3 hours when the OD_{600} value reached to 0.6. At tHis stage protein induction was carried out by using 1.0 mL of IPTG solution (final concentration = 1 mM), post induction both flasks were then kept overnight in the

shaking incubator. Cells were then harvested by centrifugation (4700 rpm, 20 min, 4 °C), and the pellet was resuspended in 30 mL lysis buffer (300 mM NaCl, 50 mM NaH_2PO_4, 20 mM imidazole). One protein inhibitor tablet, 25 mg lysozyme and 5 mg of DNase was also added into the lysate and lysis reaction was carried out on rotating platform (60 min, 4 °C). Lysed cells were sonicated (5 x 30 s, 30 s pulse on, 60 s pulse off, 75% amplitude). Sonicated cells were centrifuged (21000 x g, 20 min, 4 °C) to clarify the lysate. Supernatant was then filtered (0.45 μm and 0.2 μm filter). Next supernatant was loaded on a 50 mL FPLC loop and purified by Ni-NTA chromatography using 5 mL His-trap HP column and eluted with 15 column volumes of elution buffer (300 mM NaCl, 50 mM NaH_2PO_4, 250 mM imidazole).

FPLC fractions were then analysed by SDS-PAGE. Fraction containing potential protein were concentrated using viva spin at 10 kDa MWCO and centrifuging at 8000 x g. Protein concentration was determined by nanodrop and characterisation was done with mass spectrometry and SDS-PAGE.

2.4.13 Expression and Purification of OtsAB Fusion from Crocosphaera watsonii

Plasmid for the OtsAB fusion protein was kindly donated by Prof. Hageman group at the University of Rostock, Germany. The plasmid DNA was transformed into XL10 gold cells. After transformation DNA was plated for ampicillin agar plates supplemented with glycine betaine (5 mM) NaCl (2 % w/v) and sorbitol (250 mM). The grown colonies were cultured overnight in 5 mL of LB media. DNA was extracted from these cultures by centrifugation (4700 rpm, 20 min, 4 °C) and purified using Qia Spin Mini prep Kit Protocol. DNA concentration was then determined using nanodrop and samples were submitted to source boscience for sequence analysis.

2 x 1 L flasks containing sterile LB media (25 g/L) and ampicillin solution (1 mL, 100 mg/L) were inoculated with 10 mL of overnight expression culture each. Flask 2 was supplemented with glycine betaine (5 mM), sorbitol (250 mM) and NaCl solution (2% w/v). Both flasks were then incubated at 37 °C in the shaking incubator at 200 rpm. OD600 was measured every hour until it reached to 0.55. Temperature was reduced to 20 °C and when the OD600 reached to 0.6, 1 mL solution of arabinose (20 mg / mL) was added into each flask to start the process of protein induction. Both flask were then kept overnight at 20 °C in the shaking incubator (200 rpm).

Cells were harvested by centrifugation (4700 rpm, 40 min, 4 °C) lysed with start buffer (20 mM Tris/HCl, 200 mM NaCl and 20 mM imidazole pH 7.8) The lysis reaction was carried out for 2 h while rotating slowly and at 4 °C. Post lysis cells were sonicated (Fisher scientific sonicator; 5 cycles: 30 s pulse on and 60 s pulse off with 40% amplitude), centrifuged (10000 rpm, 40 min, 4 °C) and the supernatant was filtered with 0.45 µm & 0.22 µm filter respectively. The filtrate was then purified with Akta FPLC (His-trap HP 5 mL Column; Elution Buffer: 20 mM Tris / HCl, 200 mM NaCl and 250 mM imidazole). Purification process was carried out equal to the 15 column volumes with increasing concentration of imidazole i.e. from 0-100%. The fraction containing potential protein content were analysed with SDS-PAGE.

2.4.14 Plasmid Design and Trial Expression of OtsAB Fusion Enzyme

N-terminus His-tagged OtsAB fusion protein plasmid DNA was transformed into BL21 (DE3) cells. The grown colonies were inoculated into the LB media (10 mL) containing 10 µL of ampicillin (100 mg/mL) solution incubated overnight in the shaking incubator (37 °C, 200 rpm). Small scale expression trial was carried out by pipetting 250 µL of grown culture in 20 mL of LB media in 6 different 50 mL falcon tube. 20 µL of ampicillin solution was also added. Tube 1 & 2 were used as control (0.4 OD_{600} and 0.6 OD_{600}); tube 3 & 4 were induced with 0.5

mM and 1 mM IPTG solution when OD_{600} value was 0.4 and 0.6 respectively. A similar process was repeated for tube 5 & 6. 1 mL of sample was taken from each tube at 0 min, before adding IPTG solution, 4 h, 16 h, 24 h and 48 h post IPTG induction.

Cells were then harvested from liquid culture by centrifugation (10,000 x g, 10 min, 4 °C). The cell solution was decanted and the pellet was allowed to drain completely. 100 µL of bugbuster reagent was added into each of the sample and the cell pellet was completely re-suspended by vortexing slowly. Cells were then incubated at a shaking platform for 20 min at room temperature. Insoluble cell debris was removed by centrifugation (16000 x g, 20 min, 4 °C). Supernatant was transferred into a fresh tube and analysed by SDS-PAGE.

2.4.14.1 Western Blotting of OtsAB Fusion Protein Samples

8 µL of protein sample and 2 µL of loading dye was added into 1.5 mL Eppendorf tube. The samples were heated between 90-100 °C for 10 min and then centrifuged for 10-20 s on a table top centrifuge. The SDS-PAGE (4-12% Bis-Tris gel, Invitrogen) was loaded into the holder and 800 mL of MOPS buffer was added into it.

Using iblot machine the gel was electro blotted to a membrane using P3 programme for 7 min. The membrane was transferred into the blocking solution (2 g BSA into 40 mL of TBST solution), left with gentle rocking for 60 min. The membrane was then rinsed with TBST buffer solution (20 mL x 3); probed with antibody (16 µL monoclonal anti-polyHistidine-alkaline phosphate antibody produced in mouse and 0.5 g BSA in 50 mL TBST buffer solution) by gently rocking overnight at 4 °C. The next morning membrane was then rinsed with TBST buffer solution (20 mL x 3) and the bands were visualised by adding BCIP / NBT alkaline phosphate substrate.

2.4.15 Large Scale Expression of OtsAB Fusion Protein

N-terminus His-tagged OtsAB fusion protein plasmid DNA (2 µL) was transformed into BL21 (DE3) cells (20 µL). The grown colonies were inoculated into the LB media (10 mL) containing 10 µL of ampicillin solution (100 mg/mL) incubated overnight in the shaking incubator (37 °C, 200 rpm). Large scale expression was carried out by inoculating 10 mL of grown culture in 1000 mL of LB media in 2 different 2L conical flasks. 1000 µL of ampicillin solution (100 mg/mL) was also added. Both flasks were then incubated in the shaking incubator (37 °C, 200 rpm) until the OD_{600} reached at 0.4. Cells were then incubated at 15 °C for further 30 min and then induced by adding IPTG solution (1 mL, 1 mM) and incubated for further 24 h at 15 °C.

After 24 h cells were harvested by centrifugation (9000 rpm, 20 min, 4 °C) and lysed with lysis buffer (50 mM Tris, 50 mM imidazole and 150 mM NaCl, pH 7.5) for 30 min at room temperature. Lysis was carried out by adding lysozyme (25 mg), DNase (5 mg) and 1 protein inhibitor tablet. Post lysis cells were sonicated (60% amplitude, 6 cycles of 30 s pulse on, 60 s off). Sonicated cells were then centrifuged to get rid of cell debris (20000 rpm, 20 min, 4 °C) and filtered through 0.45 µm and 22 µm filter and loaded onto FPLC loop for purification using His-trap HP 5 mL column as stationary phase and eluted with 15 column volumes of elution buffer (50 mM Tris. 150 mM NaCl, 500 mM imidazole).

FPLC fractions were then visualised by SDS-PAGE method and fraction containing potential protein were concentrated through Vivaspin (5 mL, 30 kDa MWCO) by centrifugation (5000 x g, 15 min, 4 °C). Protein samples were then characterised by LC-MS.

2.4.15.1 Determination of Protein Concentration

Protein concentration was determined by BCA method. In summary working reagent was prepared by mixing solution A & B with A:B ratio of 50:1 (3 mL:60 µL). BSA standard

solutions were prepared from the stock solution if BSA (2 mg / mL dissolved in H_2O) by serial dilutions so that the final concentrations were 0.06125 mM, 0.125 mM, 0.25 mM, 0.5 mM, 0.75 mM, 1.0 mM, 1.5 mM and 2.0 mM. 10 µL of standard solution and 200 µL of working reagent were pipetted into 96 well plate followed by 3 unknown protein sample solution (i.e. x 1, x 0.5 and x 0.9 diluent). All samples were then then incubated at 37 °C for 30 min and then assayed at 562 nm by spectrophotometer. Protein concentration determined through this method was found to be 0.1 mg/mL.

2.4.15.2 Enzymatic Reaction of OtsAB fusion Protein

To test the protein activity enzymatic reaction was carried out. 20 µL Glucose-6-phosphate (20 mM); 20 µL of UDP-glucose (20 mM), 1.25 µL of manganese chloride (2.5 mM) and 20 µL of enzyme (0.23 µM) were added into 1.5 mL Eppendrof tube. The total reaction volume was adjusted to 100 µL by adding Tris/NaCl buffer (50 mM Tris; 150 mM NaCl, pH 7.5). Reaction was started by adding the enzyme solution and stopped by placing on ice and quenched by adding 20 µL acetonitrile solution. Reaction was carried out on the thermoshaker (37 °C, 700 rpm) and continued for 24 h.

2.4.16 Detection of Trehalose by LC-MS for TreT and OtsAB Fusion enzyme

In order to detect the trehalose LC-MS method was used as described in the general experimental condition. Standard solutions for glucose and trehalose were analysed along with the samples. For TreT reaction UDP-glucose was used in excess and 8 mM glucose was used as a substrate. Enzyme concentration, metal ion concentration and buffer amounts were kept the same as in the case UDP-Glucose and UDP reaction.

For OtsAB fusion reaction, total reaction volume was 100 µL. In 1.5 mL Eppendorf tube were added: glucose-6-phosphate 2 µL (10 mM), $MnCl_2$ 1.25 µL (2.5 mM) and 0.23 µM enzyme was used. UDP-Glucose concentration was maintained at 50 µL (50 mM). Reaction was made up to 100 µL by adding Tris/HCl buffer solution (50 mM, pH 7.5).

2.4.17 Reaction Comparison between TreT homologues

To demonstrate the yield of FDT from TreT enzyme reactions, we tested the reaction for both homologues. Equimolar amount of starting substrate and enzyme concentration was used (**see Table S2**). All the other parameters and reagents concentration was kept constant so that yield for FDT formation from each enzyme system can be compared.

In summary reaction volume was maintained to 500 µL and HEPES buffer (50 mM HEPES, pH 7.5, 200 mM NaCl and 10 mM $MgCl_2$) was used to make up the required volume. Reactions were initiated by adding the enzyme and then incubated at 37 ^oC, 700 rpm on the thermoshaker. 150 µL of reaction samples were taken after 30 min, 60 min and 120 min respectively from each reaction mixture. Reaction were stopped by incubating the reaction mixture at 100 ^oC for 5 min and further diluted to 500 µL with D_2O solution, centrifuged and stored for the analysis.

Sample analysis was carried out using 500 MHz NMR spectrometer (AVB500) and ^{19}F-NMR signal for the formation of FDT were sought as compared to FDG peaks in all the reaction mixtures.

Table S2: Reagents details for enzyme comparison reaction

Enzyme	FDG (mM)	UDP-Glc (mM)	$MgCl_2$ (mM)	Enzyme (μM)	HEPES Buffer (mM)
TreT *P. horikoshii*	10	20	10	1.2	50 mM, pH 7.5
TreT *T. tenax*	10	20	10	1.2	50 mM, pH 7.5

2.4.18 Reversible Reaction with TreT *P. horikoshii*

To test the reversibility of TreT *P. horikoshii*, we set-up small scale reactions from 1-10 mM of [^{19}F]FDT with fixed UDP concentration of 20 mM. In 1.5 mL Eppendorf tube were added the following: UDP 20 mM, [^{19}F]FDT 1 mM, 2 mM, 5 mM and 10 mM with a further 1 mM control reaction. Reaction volume was made up to 100 μL with HEPES buffer solution (50 mM HEPES, 200 mM NaCl, 10 mM $MgCl_2$, pH 7.5). Reactions were initiated by adding TreT enzyme and incubated at 37 °C for 2 h. A further reaction with higher amount of UDP substrate (80 mM) and [^{19}F] FDT (20 mM) was also set-up as above. Reactions were analysed by [^{19}F]-NMR spectroscopy.

2.4.19 Enzyme Scale-up in Sf9 cell expression

The coding sequence of *E. coli* OtsA (CAA48913.1) and OtsB (CAA48912.1) was optimized according to *S. frugiperda* MNPV codon usage. The DNA fragment was then cloned into the EcoRV restriction enzyme site of the pUC57 plasmid. PUC57-OtsA and OtsB and pFastBac transfer vector were digested with BamHI and NotI, respectively, and then ligated to create pFastBac-otsA and OtsB constructs. The constructs were transformed into *E. coli* DH5α. Correct insertion of the genes was confirmed by

PCR amplification with pUC/M13 standard primers, by PCR amplification with pUC/M13 standard primers — 5- CCCAGTCACGACGTTGTAAAACG-3 (forward) and 5- AGCGGATAACAATTTCACACA GG (reverse) and by DNA sequencing with pFastBac standard primers. The accurate transfer vector was transfected into competent *E. coli* DH10Bac containing a helper plasmid for transposition into the expression bacmid.

In order to obtain a reasonable expression level of OtsA and OtsB proteins, the Bac-to-Bac baculovirus expression system was selected. We prepared the recombinant bacmid DNA of baculovirus of OtsA and OtsB. This was achieved by transforming both donor plasmids of OtsA and OtsB into DH10Bac competent cells. The cells were incubated at 37 °C, 250 rpm for 4 h. 100 µL competent cells were then plated on LB agar plates containing 50 µg/mL kanamycin, 7 µg/mL gentamicine, 10 µg/mL tetracycline, 80 µg/mL X-gal and 40 µg/mL IPTG with a series of dilution (1/1, 1/10 and 1/100) and incubated at 37 °C for 48 h. In order to confirm the colony phenotype and purify the recombinant bacmid DNA, 9 white colonies and and one blue colony of OtsA and OtsB were re-streaked on a fresh agar palte with all the antibiotics, X-gal and IPTG and incubated at 37 °C for further 48 h. After 48 h, two white colonies of OtsA and OtsB were selected for overnight liquid culture in LB-broth media containing 50 µg/mL kanamycin, 7 µg/mL gentamicine, 10 µg/mL tetracycline. The bacmid DNA containing the OtsA and OtsB gene was extracted by purelink plasmid extraction kit (Invitrogen). Since the recombinant bacmid DNA is greater than 135 kb in size, restriction analysis is difficult to perform. So, the PCR analysis was utilized to verify the presence of OtsA and OtsB genes in the recombinant bacmids. A set of primers (M13-forward and M13-reverse) was synthesized to perform the PCR analysis of recombinant bacmid DNA. The PCR results of recombinant bacmid DNA were checked by 1% DNA agarose gel. For OtsA, the inserted gene is 1460 bp on donor plasmid pFastBac1-OtsA, so the expected DNA size after PCR for OtsA recombinant bacmid DNA is around 3760 bp (1460 bp + 2300 bp); while for OtsB, the

inserted gene is 870 bp on donor plasmid pFastBac1-OtsB, so the expected DNA size after PCR for OtsB recombinant bacmid DNA is around 3170 bp (870 bp + 2300 bp). From the bacmid DNAs, the P1 baculovirus of OtsA and OtsB were made by SF9 cells in 6-well culture plates.

Frozen Sf9 cells were recovered according to the manual provided by Gibco Companyref. In summary, frozen vial of Sf9 cells were quickly thawed at 37 °C water bath (1~2 minutes) and then entire contents of the vial transferred into a 100 mL conical flask containing 25 mL pre-warmed (27 °C) Sf-900 II SFM medium. Flask was then incubated at 27 °C with shaking (150 rpm) in incubator-shaker for 4 days. After 4-day culture, Sf9 cell number were counted and calculated the cell density under microscope. In order to make a large volume (150 mL) of Sf9 cell culture dilution of 25 mL Sf9 cells with fresh Sf-900 II SFM medium in a 300 mL conical flask was carried out and the Sf9 cells cultured until its density reach 2~3 × 10^6/mL for further use in baculovirus preparation.

2.4.19.1 Experimental procedures to make P1 baculovirus for OtsA and OtsB

Sf9 cells were added to each well of two into 6-well plates. The total cell number in each well was maintained at 8 × 10^5 and the total volume in each well was kept to 2.0 mL. Cellfectin II stock solution was prepared by diluting Cellfectin II reagent with Grace's insect medium. Bacmid DNA solution for OtsA and OtsB was then prepared. The transfection solution was then prepared by mixing bacmid DNA solution with cellfectin II stock solution and added into each well in 6-well plate and incubated at 27 °C for 5 hours. Post incubation transfection solution was removed from each well and added fresh Sf-900 II SFM medium and incubated for 3 days at 27 °C The P1 baculovirus (in supernatant) was harvested by centrifugation for OtsA and OtsB. The P1 baculovirus are in the culture medium and the Sf9 cell pellets were used to check protein expression level. Fetal bovine serum (FBS) was then added to each P1

baculovirus solution to reach 2% final. The P1 baculovirus stock solution were then stored in cold-room avoiding light.

Preparation of P2 and P3 baculovirus for OtsA and OtsB: In order to make baculovirus stock for large scale protein expression, and to increase virus titer, it was essential to prepare P2 and P3 baculovirus stocks from P1 virus of OtsA and OtsB. To make P2 baculovirus, total 150 mL Sf9 cells with a cell density of 2.0×10^6 cells/mL was infected by P1 baculovirus of OtsA or OtsB, respectively. The 150 mL infection culture composition: 1% P1 baculovirus of OtsA or OtsB, 1% FBS, Sf9 cells with a cell density of 2.0×10^6 cells/mL. After infection at 27 °C with shaking (150 rpm) for 72 hours, the P2 baculovirus (in culture medium) was harvested by centrifugation at 1100 rpm for 10 minutes at room temperature. In order to make P2 virus stock solution, FBS was added (final concentration 2%), then the solution was filtered by syringe filter (0.45 μm) and stored in cold-room avoiding light. The similar preparation procedures were applied for making P3 baculovirus as preparation of P2 baculovirus, except using P2 baculovirus stock solution to replace P1 virus for cell infection.

2.4.19.2 Expression and Purification of C-terminally tagged, recombinant OtsA

Insect cells were grown in serum-free medium to a density of 2×10^6 cells/mL and a cell viability of greater than 95%. The cell culture (1 L) was transfected with the viral stock, 2.8 x 10^6 cells/mL. At 72 h post-infection, the cells were harvested by centrifugation. After freeze/thaw cycle, the pellet was resuspended in lysis buffer (100 mM HEPES, 200 mM NaCl, 10 mM imidazole, 10 mM $MgCl_2$, 1 mM βME). DNase 3 mg and 1x Complete® protease inhibitor cocktail was also added into the protein pellet and lysed using a homogenizer. Cell debris was removed by centrifugation and the cell free extract passed through a 0.45 μm membrane filter. The filtrate was applied to a Ni–NTA column equilibrated in lysis buffer. After removal of the cell debris by centrifugation, the protein of interest was purified with a linear gradient of 10–300 mM imidazole in 100 mM HEPES, 200 mM NaCl, 10 mM $MgCl_2$, 1

mM βME, pH 7.5, using Ni-NTA. Protein samples were exchanged into 100 mM Hepes, 150 mM NaCl, 10 mM $MgCl_2$, pH 7.5, using a Hiload^{TM} 26/60 Superdex^{TM} 200 desalting column. The sample was passed through an Acrodisc Mustang E membrane (Pall #MSTG25E3) to reduce endotoxin to 1.9 EU/mL. After the addition of 10% glycerol, the aliquots containing the recombinant enzyme were flash frozen, and stored at −80 °C.

2.4.19.3 Expression and purification of recombinant OtsB

Insect cells were grown in serum-free medium to a density of 2×10^6 cells/mL and a cell viability of greater than 95%. The cell culture (1 L) was transfected with the viral stock, $2.0x10^6$ cells/mL. At 72 h post-infection, the cells were harvested by centrifugation. After freeze/thaw cycle, the pellet was resuspended in lysis buffer (50 mM Tris-HCl, 200 mM NaCl, 5 mM $MgCl_2$, 30 mM imidazole, 1 mM βME). DNase 3 mg, 1x Complete® protease inhibitor cocktail was also added in the pellet and lysed using a homogenizer. Cell debris was removed by centrifugation and the cell free extract passed through a 0.45 μm membrane filter. The filtrate was applied to a Ni–NTA column equilibrated in lysis buffer. After removal of the cell debris by centrifugation, the protein of interest was purified with a linear gradient of 10–300mM imidazole in 50 mM Tris-HCl, 200 mM NaCl, 5 mM $MgCl_2$, 1 mM βME, pH 7.5, using Ni-NTA. The fractions with potential protein were concentrated using Vivaspin (5 MWCO) and then desalted on Hiload^{TM} 26/60 Superdex^{TM} 200 with 50 mM Tris-HCl, 5 mM $MgCl_2$, 100 mM NaCl, pH 7.5. The sample was passed through an Acrodisc Mustang E membrane (Pall #MSTG25E3) to reduce endotoxin to 1.9 EU/mL. After the addition of 10% glycerol, the aliquots containing the recombinant enzyme were flash frozen, and stored at −80 °C. SDS–PAGE analysis revealed the presence of a protein with the correct molecular weight.

2.4.19.4 Small sale synthesis of [^{19}F]FDT from Hexokinase, OtsA and OtsB

In order to test the small scale synthesis of FDT from 3-enzymes systems, in a 1.5 mL Eppendorf tube were added the following, [^{19}F]FDG 1mM, ATP 10 mM, UDP-Glc 20 mM, KCl 100 mM, hexokinase 2 mg, OtsA 1 mg and OtsB 0.3 mg in 50 mM HEPES buffer solution containing 100 mM NaCl and 10 mM $MgCl_2$. The reaction was incubated at 37 °C, 400 rpm and monitored by ^{19}F-NMR and LC-MS. Full conversion was achieved in 30 min. A control sample of FDG with no enzyme added was also analysed.

2.4.20 General Chemistry Experimental Procedures

Proton nuclear magnetic resonance spectra (^{1}H NMR) were recorded on a Bruker AVX 500 (500 MHZ), a Bruker AVB 500 (500 MHz) or a Bruker AVB 400 (400 MHZ) spectrometer as indicated. Carbon nuclear magnetic resonance (^{13}C NMR) spectra were recorded on the same spectrometer as described above. ^{19}F-NMR spectra were recorded on a Bruker AVX500, AVB500, AV600 and AVB400. NMR spectra were fully assigned using COSY and HSQC. All chemical shifts are quoted on the δ scale in ppm using residual solvents as the internal standards. Coupling constants (*J*) are reported in Hz with the following splitting abbreviations: s = singlet, d = doublet, t = triplet, q = quartet, and m = multiplet.

Infrared (IR) Spectra were recorded on a Bruker Tensor 27 Fourier Transform Spectrometer using KBr discs for solids and crystals. Absorption maxima (νmax) are reported in wave number (cm^{-1}) and classified as strong (s) or broad (br).

Low-resolution mass spectrometry (LRMS) were recorded using an agilent 6120 Quadrupole spectrometry using electrospray ionisation (ESI) in either positive or negative mode. High resolution mass spectra (HRMS) were recorded on a Thermo Orbitrap Exactive mass spectrometer. The instrument is calibrated with a standard calibration mix from thermo before

the run. Liquid Chromatography – Mass spectrometry (LC-MS) analysis was carried out on a Waters Quattro Micro – MS with electrospray ionization operating in negative mode (ESI) interface with Agilent HPLC system and Waters 2777 auto sampler with 4-valve injector module. MS analysis was under the control of micro mass Masslynx 4.1 software.

Thin layer chromatography (TLC) was carried out using aluminium backed sheets coated with 60F254 silica gel (Merck). Visualization of the silica plates was achieved using a UV lamp (λmax = 254 nm), and/or ammonium molybdate 5% in 2M H_2SO_4. Column chromatography was carried out using Geduran ® Si 60 silica gel (Merck). Mobile phases are reported in ratio of solvents (e.g. 4:1 petrol/ethyl acetate).

2.4.21 Radio-HPLC Method

Radio-HPLC analysis was carried out in a Bioscan radio-HPLC system (flow count) coupled with agilent 1200 HPLC system. Two analytical methods were used for the analysis of the depletion of starting material and formation of the product. In method 1, initially isocratic elution of 75:25 acetonitrile/water mobile phase combination was used with TSK gel normal phase HILIC column (phase amide -80, 10 cm x 4.6 mm x 5 μm) as stationary phase. The flow rate was maintained at 0.4 mL/min. This system resulted in the [^{18}F]FDG retention time of ~ 5.6 min and [^{18}F]FDT of 11.4 min. The mobile phase combination was then slightly adjusted to 70:30 acetonitrile/water and hence retention time of [^{18}F]FDG was 4.9 min and [^{18}F]FDT was ~ 8.3 min. The total run time was 15 min.

The method 2 allowed the clear separation of phosphate sugars as well as analysis of [^{18}F]FDG and [^{18}F]FDT. In This method Advanced Glycan Mapping column (4.6 x 250 mm, 2.7 μm) was used as the stationary phase. The mobile phase was the gradient of two solvent system; solvent

A= 50 mM ammonium formate, pH 4.5 and solvent B= acetonitrile. Flow rate was maintained at 0.5 mL/min and the total run time was 20 min.

2.4.22 Radio-TLC Method

Radio-TLC analysis was carried out in a Bioscan AR-2000 radio-TLC scanner. Silica gel plates 150 Å Silica Gel HL 250 cm 10 x 20 cm were used as the stationary phase and the 75:25 acetonitrile/water combination was used as the mobile phase. Once the strip developed to the 10 cm mark, was scanned by the radio-TLC scanner and analysed.

2.4.23 Luna-NH_2 Purification Method

[^{18}F]FDT was purified by Sep-Pak cartridges. Sep-Pak Aminopropyl (NH_2) plus short cartridge (Waters, WAT020535, 360 mg) used as the stationary phase. The cartridge was pre-rinsed with 1 mL EtOH and then twice with 3 mL per wash sterile water for injection. A 10 mL syringe was attached to the cartridge with plunger removed to the 5 μm filter. 1 mL of EtOH was loaded on to the syringe.

The reaction mixture was diluted with 2 mL of EtOH. This mixture was poured into the above syringe with filter. Reaction vial was rinsed with further 1 mL of EtOH and transferred to the syringe. The contents of the syringe were filtered through 5 μm syringe tip filter to remove precipitate. Eluent was loaded onto the NH_2 cartridge and eluted without washing at a very low flow rate. Mixture was then concentrated first by evaporation and then by heating at 60 °C with a nitrogen flush. Finally the mixture was diluted with sterile water and filtered through sterile filter and drawn into the syringe.

2.4.24 OtsA Enzyme kinetic assay

The OtsA enzyme kinetic assay were measured through a NADH-linked GT-continued spectrophotometric assay. The decrease in absorbance of NADH at 340 nm (ε340 = 6220 $M^{-1}cm^{-1}$) was measured at 25 °C using a spectrophotometer equipped with a thermostat. To determine the kinetic parameters of UDP-Glc, various UDP-Glc cocentrations (0.5 mM, 1 mM, 2 mM, 4 mM and 10 mM) were used at the fixed G6P concentration. The G6P concentrations were fixed at 2 mM, 4 mM, 8 mM, 16 mM and 35 mM. The reaction mixture contained 100 mM HEPES (pH 7.5), 10 mM $MgCl_2$, 300 mM KCl, 1 mM potassium phosphoenolpyruvate, 300 μM NADH, 17 units of pyruvate kinase, and 24 units of lactate dehydrogenase in a total volume of 200 μL at 25 °C as well as a fixed G6P concentration and variable UDP-Glc concentration. For G6P assay, UDP-Glc concentration was fixed at 10 mM, whereas, G6P concentration varied (1 mM, 2 mM, 4 mM, 8 mM, 16 mM and 32 mM). After incubation for 5 min at 25 °C, reactions were initiated by the addition of OtsA (final concentration 83 nM).Then absorbance of the reaction mixture at 340 nm was recorded continuously.

2.4.25 TreT *P. horikoshii* Enzyme Kinetic Assay

TreT *P. horikoshii* enzyme kinetic assay were measured through a NADH-linked GT-continued spectrophotometric assay. The decrease in absorbance of NADH at 340 nm (ε340 = 6220 $M^{-1}cm^{-1}$) was measured at 37 °C using a spectrophotometer equipped with a thermostat. To determine the kinetic parameters of UDP-Glc, various UDP-Glc cocentrations (0.5 mM, 1 mM, 2mM, 4 mM and 10 mM) were used at the fixed Glc concentration. The Glc concentration was fixed at 50 mM. The reaction mixture contained 100 mM HEPES (pH 7.5), 10 mM $MgCl_2$, 300 mM KCl, 1 mM potassium phosphoenolpyruvate, 300 μM NADH, 17 units of pyruvate kinase, and 24 units of lactate dehydrogenase in a total volume of 200 μL at 37 °C as well as a fixed Glc concentration and variable UDP-Glc concentration. For Glc assay, UDP-Glc

concentration was fixed at 20 mM, whereas, Glc concentration varied (0.5 mM, 1 mM, 2 mM, 4 mM, 10 mM). After incubation for 5 min at 25 °C, reactions were initiated by the addition of TreT (final concentration 662 nM).Then absorbance of the reaction mixture at 340 nm was recorded continuously.

2.4.26 TreT *T. tenax* Enzyme Kinetic Assay

In order to determine kinetic parameters (k_{cat}, K_m) of TreT *thermoproteus tenax* enzyme, UDP-Glc concentrations were varied from 0.03125 mM – 7 mM

In 1.5 mL Eppendorf tube were added glucose 50 µl (50 mM), $MgCl_2$ 20 µl (10 mM), TreT enzyme 4 µl, Hepes buffer varied volumes (50 mM, pH 7.5) to make up the total volume to 100 µl. Different volumes of UDP-glucose were added to the reaction mixture so that the final concentration of UDP-glucose in the reaction mixture was 0.01325, 0.06125, 0.125, 0.50, 1.00, 2.00, 3.00, 4.00, 5.00, 6.00 and 7.00 mM. Reactions were started by adding 4 µl enzyme and immediately placing on the thermoshaker at 70 °C. Each reaction was heated for 10 min and reactions were stopped by placing on ice and quenched by adding 20 µl acetonitrile to precipitate the protein. Reactions were then flash freezed with nitrogen and stored at -20 °C. Prior to HPLC analysis each reaction mixture was centrifuged at 13000 rpm for 20 min. HPLC analysis was carried out by HPLC method 3 as specified in **Table S1.**

The kinetic parameters of TreT *T.tenax* were also determined based on the variable acceptor substrate concentrations by GT-continued assay as described for TreT P. horikoshii under the similar conditions. The amount of UDP-Glc was fixed at 20 mM and Glc concentration varied (0.5 mM, 1 mM, 2 mM, 4 mM and 10 mM). The reactions were incubated at 37 °C for 5 min and then enzyme (662 nM) added and reaction rates determined.

2.4.27 OtsAB Enzyme Kinetic Assay

OtsAB kinetic parameters were determined using HPLC method 3 as specified in Table S1. We used variable UDP-Glc concentrations (2 mM, 4 mM, 8 mM, 16 mM and 32 mM) at a fixed G6P concentration of 80 mM. After adding the enzyme (1.23 μM), reactions were incubated for 5 min at 37 °C in a thermoshaker. Reactions were then quenched by adding acetonitrile, centrifuged (13000 rpm, 10 min) and analysed by HPLC. A standard calibration curve of UDP was also generated under the same reaction and analysis conditions. From the resulting UDP calibration curve, unknown concentrations from enzymatic reactions were determined and plotted against the concentrations of G6P substrate to obtain the K_m and V_{max} values.

2.4.28 OtsB Enzyme Kinetics

For the OtsB enzyme kinetics we used ^{1}H NMR spectroscopy. We chose the ^{1}H proton in the anomeric region of the spectra for the analysis. Initially we analysed standard samples of trehalose-6-phosphate and trehalose. For the kinetic assay, we incubated several concentrations of T6P (0.5 mM, 1.0 mM, 1.5 mM, 2.0 mM, 2.5 mM, 3.0 mM, 3.5 mM, 4.0 mM and 5.0 mM). Reaction was initiated by adding 10 μL of OtsB and incubated at 37 °C for 10 min. After 10 min, reactions were stopped by boiling at 95 °C for 5 min and then analysed by ^{1}H NMR using D_2O as a solvent. The standard calibration curve for trehalose was also generated and using this calibration curve unknown concentrations of resulting trehalose from an enzymatic reaction were obtained, divided by time to get rates which were then subsequently plotted against original substrate concentrations to get K_m and k_{cat}.

2.4.29 Chemoenzymatic Reaction Optimisation and Scale-up

During reaction optimisation we tested the effect of ATP concentrations to the conversion of FDG to FDG6P initially at 1 mg scale. We set-up four different reactions in 1.5 mL Eppendorf tubes as shown in Table S3:

Table S3. Testing ATP concentrations for the conversion of FDG to FDG6P

Entry	FDG (mM)	ATP (mM)	$MgCl_2$ (mM)	Enzyme (mg)	HEPES Buffer (mM)
1	5.55	2.75	10	5	50 mM, pH 7.5
2	5.55	5.50	10	5	50 mM, pH 7.5
3	5.55	8.25	10	5	50 mM, pH 7.5
4	5.55	16.5	10	5	50 mM, pH 7.5

Reactions were incubated at 37 °C for 1 h at 400 rpm in a thermoshaker and then analysed by ^{19}F-NMR spectroscopy to observe the conversion.

To test the OtsA and OtsB enzymes needed for a reaction, we tested several concentrations of OtsA (6.65 μM, 13.3 μM, 18.2 μM and 36.6 μM) and OtsB (1.53 μM, 3.06 μM, 6.13 μM, 12.26 μM) in a 50 mg scale while maintaining all the other reaction parameters constant. Reactions were incubated at 37 °C at 400 rpm for 1 h and then analysed by ^{19}F-NMR spectroscopy.

In order to further optimise the enzymatic reaction conditions using 3 enzyme synthesis method, we tested various substrate concentrations i.e. with fixed enzyme concentrations. In summary in a 50 mL falcon tube were added FDG (various FDG concentrations i.e. 6.25 mg, 12.5 mg, 25 mg and 50 mg), ATP with equivalent or slight excess molar concentration to FDG, hexokinase 5 mg (680 U), UDP-Glc (37 mg with final concentration of 30 mM), OtsA enzyme

(2 mg, 18 μM), OtsB (0.4 mg, 6.2 μM) and KCl (100 mM). Reaction volume was made up to 2 mL by HEPES buffer solution (HEPES 50 mM, pH 7.5, 100 mM NaCl, $MgCl_2$ 10 mM). Reactions were incubated at 37 °C and samples were taken after 15 min, 30 min, 60 min, 120 min, 200 min and 690 min, diluted with D_2O and analysed by ^{19}F-NMR spectroscopy. 50 mg reaction was further optimised with additional UDP-Glc (168 mg, 138 mM) and analysed by ^{19}F-NMR.

2.4.30 Chemoenzymatic Synthesis of FDT

In a 50 mL sterile falcon tube were added; FDG (100 mg, 367 mM), ATP (320 mg, 368 mM) and $MgCl_2$ (5 mg). The contents were dissolved in HEPES buffer solution containing 100 mM NaCl (100 mM, 1 mL, pH 7.5). The pH was then adjusted to 8.0 with NaOH. Hexokinase (0.6 mL) was added to the reaction mixture to initiate the reaction. The reaction mixture was incubated at 30 °C, 50 rpm for 1-2 hours. Phosphorylation of FDG to FDG6P was monitored by TLC and ^{19}F-NMR spectroscopy. Full conversion to FDG6P was observed within 2 hours for each batch synthesized.

Within the same pot, UDP-Glc (200 mg, 110 mM), KCl (100 mM) and OtsA enzyme (26 μM) was added. The total reaction was then adjusted to 3 mL. The reaction mixture was incubated to similar conditions as above for 24 h to allow appropriate conversion to FDT6P. The conversion of FDG6P to FDT6P was monitored by ^{19}F-NMR spectroscopy. The average maximum conversion after 24 h was between 65-70 %. After 24 h, in the same reaction mixture OtsB enzyme (6.23 μM) was added. The pH was adjusted to 8.0 and reaction mixture was incubated at 37 °C, 50 rpm. Reaction progress was monitored by TLC and ^{19}F-NMR. The Reaction was usually complete within 2 hours.

2.4.31 Purification and Characterisation of FDT

The enzymes from crude reaction mixture were precipitated by either heating the mixture at 95 °C for 10 min or adding 2 mL EtOH and isolated by centrifugation (Viva spin, 10,000 MWCO) and/or filtration. The resulting filtrate was lyophilized and the crude mixture was further precipitated with MeOH/MeCN 90:10 solution and then purified by flash column chromatography. For purification normal phase silica was used as stationary phase and mixture of Ethyl acetate: Iso-propanol and water (48%/48%/4%) were used as mobile phase. FDT was separated from residual FDG6P and residual FDG. The fractions containing FDT were pooled, concentrated and then lyophilised to dryness. The Lyophilisation step was repeated for a further 2-3 times to get rid of any residual water. The freeze dried compound was then characterised by proton (^{1}H NMR), carbon (^{13}C NMR), fluorine (^{19}F NMR) and ESI-MS. $[\alpha]_D^{25}$ + 128.9 (c 1.00, H_2O). ^{1}H NMR (500 MHz, D_2O) δ 5.33 (d, *J* = 3.9 Hz, 1H, H-1), 5.11 (d, *J* = 3.7 Hz, 1H, H-1′), 4.40 (ddd, *J* = 49.0, 9.6, 3.9 Hz, 1H, H-2), 4.02 (dt, *J* = 13.2, 9.4 Hz, 1H, H-3), 3.79 – 3.62 (m, 7H, H-5, H-6a, H-6b, H-3′, H-5′, H-6a′, H-6b′), 3.56 (dd, *J* = 9.9, 3.7 Hz, 1H, H-2′), 3.41(t, *J* = 9.7 Hz, 1H, H-4) , 3.35 (t, *J* = 9.4 Hz, 1H, H-4′) ppm. ^{13}C NMR (125 MHz, D_2O) δ 94.0 (C-1′), 91.2 (d, $J_{F,C-1}$ = 21.8 Hz, C-1), 89.5 (d, $J_{F,C-2}$ = 186.6 Hz, C-2), 72.6 (C-3′), 72.2 (C-5 and C-5′), 71.4 (d, $J_{F,C-3}$ = 15.8Hz, C-3) 70.9 (C-2′), 69.6(C-4′), 69.1 (d, *J* = 8.0 Hz, C-4), 60.5 (C-6 or C-6′), 60.3 (C-6 or C-6′) ppm. ^{19}F NMR (470 MHz, D_2O) δ – 201.18 ppm. IR (neat) ν 3264 (OH), 1647, 1409, 1150, 1103, 990, 948, 841, 802, 705 cm^{-1}. ESI-MS: ESI-MS calculated for $C_{12}H_{21}F_1O_{10}Na_1$ [M + Na] 367.1011, found 367.1011.

2.4.32 Stability Testing of FDT Solution in HEPES Buffer

In order to establish the storage conditions of the final formulation of an injection, small scale stability testing of the final formulation was carried out. In summary, FDT sample was dissolved in HEPES Buffer solution (50 mM, pH 7.5) containing 7.5 mM $MgCl_2$. One portion

of the dissolved solution was stored at room temperature (20 – 25 °C) and the other portion was stored between 2-8 °C. Samples were taken at day 0, 3, 5, 7 and 10 and analysed by ^{19}F NMR spectroscopy in triplicate. The means of the obtained integrals are then plotted against the day of testing. In addition, spectras were observed for any additional peaks as well.

2.4.33 Stability Testing of FDT Solid

In order to ensure that the compound will be stable throughout the testing period, on-going stability testing of the FDT sample from solid was also investigated over three months period. Material for testing was stored at - 20 °C and periodic testing was carried out by dissolving ~ 8 mg of smaple in D_2O and then subsequently analysed by ^1H NMR spectroscopy.

2.4.34 Endotoxicity Testing of FDT Solution

Endotoxicity testing of the solution was outsourced to Lonza. FDT (10 mg) was dissolved in endotoxin free water in a 15 mL falcon tube (endotoxin free) supplied by the Lonza. Samples were then analysed by Lonza and the endotoxicity levels reported were ≤0.05 EU/mL of the solution.

2.4.35 Determination of Purity by ^1H NMR

Purity of the final compound was determined by ^1H NMR spectroscopy by determining relative concentration of the substance as compared to impurities. Known quantity of FDT was dissolved in D_2O and quantified by ^1H NMR spectroscopy. Maleic acid was used as an internal standard.

2.4.36 ^{23}Na-NMR Quantification

In order to determine the amount of salt (NaCl) in the FDT compound we used ^{23}Na-NMR in AVX500 instrument. We generated the calibration curve of NaCl solution of known concentration and then run the FDT samples using the same parameters as NaCl standards. The amount of Na was calculated from the standard calibration curve as an unknown and then from molar ration of Na:FDT the amount of salt then determined.

2.4.37 TreT *P. horikoshii* Screening Experiment

In 2 mL Eppendorf tube were added UDP-Glc (30 mM), TreT enzyme (0.7 mg). Reaction was started by adding [^{18}F] FDG (500 µL, 14.1 mCi/mL). Reaction volume was made up to 1 mL by adding HEPES buffer solution (100 mM HEPES, 10 mM $MgCl_2$, pH 7.5). The reaction was incubated at 37 oC in a thermoshaker and monitored by radio-HPLC. Once [^{18}F]FDG fully converted to [^{18}F]FDT, the reaction mixture was purified by Luna-NH_2 cartridge method as described in the method section.

TreT *P. horikoshii* Reaction with larger volume: This reaction was intended to look at any potential inhibition of an enzyme due to higher saline concentration in the reaction mixture. In a 2 mL Eppendorf were added UDP-Glc (30 mM), TreT enzyme (0.7 mg). Total reaction volume was adjusted to 1.6 mL by adding HEPES buffer solution (HEPES 100 mM, $MgCl_2$ 10 mM, pH 7.5). Reaction was started by adding [^{18}F]FDG solution (1mL, 13.8 mCi). Reaction was incubated at 37 °C for 60 min and monitored by radio-HPLC. Once full conversion observed, reaction mixture was purified by Luna-NH_2 cartridge method.

TreT *P. horikoshii* Reaction at higher temperature: As the TreT enzyme is a thermophile, we sought to test the reaction at higher temperature (60 °C). In a 2 mL Eppendorf tube were added, UDP-Glc (30 mM), TreT enzyme (0.2 mg, 3.3 μM), $MgCl_2$ (20 mM). Reaction was started by adding [^{18}F]FDG (500 μL, 7.5 mCi). Reaction was incubated at 60 °C in a thermoshaker and progress was monitored by radio-HPLC. Reaction was stopped after 25 min and purified by Luna-NH_2 cartridge. The non-decay corrected radiochemical yield was found to be 52%.

2.4.38 Reaction with TreT *T. tenax* enzyme

In 2 mL Eppendorf tube were added UDP-Glc (30 mM), TreT enzyme (0.7 mg). Reaction was started by adding [^{18}F]FDG (500 μL, 14.1 mCi/mL). Reaction volume was made up to 1 mL by adding HEPES buffer solution (100 mM HEPES, 10 mM $MgCl_2$, pH 7.5). The reaction was incubated at 37 °C in a thermoshaker and monitored by radio-HPLC. Once [^{18}F]FDG almost fully converted to [^{18}F]FDT, the reaction mixture was purified by Luna-NH_2 cartridge method as described in the method section.

2.4.39 3-Enzyme-3-step one pot hot synthesis

Initial Screening Experiment: For the initial screening experiment, in a 2 mL Eppendorf were added UDP-Glc (20 mM), ATP (10 mM), OtsA (3.7 μM, 0.21 mg), OtsB (0.1 mg, 2.5 μM), hexokinase (1 mg, 128 U). The reaction was started by adding [^{18}F]FDG (300 μL, 8.2 mCi). The reaction volume was adjusted to 1 mL with using HEPES buffer solution (HEPES 100 mM, $MgCl_2$ 10 mM and NaCl 100 mM). The reaction was incubated at 37 °C in a thermoshaker and monitored by radio-HPLC. The reaction progressed slowly under the given conditions and after 45 min the conversion was ~ 20%. The purification was not attempted at this stage.

Reaction Optimisation: To further optimise the reaction, in a 2 mL Eppendorf tube were added UDP-Glc (30 mM), ATP (10 mM), hexokinase (2 mg, 256 U), OtsA (4 μM, 0.25 mg), OtsB (0.1 mg, 2.5 μM). The reaction was started by adding [^{18}F]FDG (250 μL, 5.15 mCi). Reaction volume was adjusted to 1 mL by adding HEPES buffer solution (HEPES 100 mM, $MgCl_2$ 10 mM and 100 mM NaCl, pH 7.5). Reaction was incubated at 37 °C on a thermoshaker. Reaction completed in 2 hrs and at this point reaction was stopped and purified by Luna-NH_2 cartridge method. The non-decay corrected purified yield for this reaction was only 12% and hence needed further optimisation.

Scale-up and further optimisation: In an attempt to further scale-up and optimise the reaction conditions to reduce the overall reaction time, we carried out further optimisation. In a 2 mL Eppendorf tube were added UDP-Glc (30 mM), ATP (10 mM), hexokinase (5 mg, 640 U), OtsA (0.7 mg, 12.3 μM), OtsB (0.4 mg, 12.5 μM). [^{18}F] FDG (500 μL, 15.6 mCi) was added to the reaction mixture to start the reaction. Final volume of reaction was adjusted to 1 mL by adding HEPES buffer solution and incubated at 37 °C in a thermoshaker. Reaction progress was monitored by radio-HPLC and stopped after 60 min when fully converted to the product and purified by Luna-NH_2 cartrdige method.

2.4.40 2-Steps-2-enzyme one pot hot synthesis

In a 2 mL Eppendorf tube were added UDP-Glc (30 mM), ATP (10 mM), OtsAB fusion enzyme (0.1 mg. 1.3 μM), hexokinase (2 mg, 256 U). The reaction was started by the ddition of [^{18}F]FDG (250 μL, 3.5 mCi). The reaction volume was adjusted to 1 mL by adding HEPES buffer solution (HEPES 100 mM, $MgCl_2$ 10 mM, NaCl 100 mM, pH 7.5). The reaction was

started by incubating at 37 °C and monitored by radio-HPLC. The reaction did not work under the conditions described above even after 90 min of incubation.

In an another attempt, higher enzyme concentrations were added into the reaction mixture and incubated for 2 hrs at 37 ^{o}C but there was no conversion at all.

2.4.41 Automation of [^{18}F]FDT Synthesis

[^{18}F] FDG (1480- 3700 MBq; 40-100 mCi in 0.8 -1.8 mL) was transferred under vacuum to the Reactor 1 containing 100 µL 1 M HEPES buffer, pH 7.6, 20 µL 1 M $MgCl_2$, 20 µL 1 M ATP, 60 µL 1 M UDP-Glucose, ~50 µL OtsA (1 mg), ~50 µL OtsB (1 mg), 20 µL hexokinase (5 mg). The reaction mixture was incubated for 30 min at 45 ^{o}C and ethanol was added (3 - 6 mL). The reaction mixture was passed through the filter (5 µm) and a stack of three NH_2-cartridges and collected in Reactor 2. An additional 1 mL 75% ethanol in water was added to rinse the Reactor 1 and transferred into the Reactor 2. The combined solution was concentrated under nitrogen at 60 ^{o}C for 10 min. 2 mL saline was added to the Reactor 2. The final [^{18}F] FDT solution was transferred to the product vial through a sterile filter (0.22 µm). The quality of the product was determined by analytical radio-HPLC (Condition: 4.6 x 250 mm, 2.7 µm AdvanceBio Glycan Mapping Column; solvent A = 50 mM ammonium formate, pH 4.5, solvent B = acetonitrile; Flow rate = 0.5 mL/min;gradient 0-15 min 68-62% B; 15-20 min 62-68% B). Identity of the compound was confirmed by LC-MS.

2.4.42 Chemoenzymatic synthesis of [^{18}F]FDT for the animal studies

For the animal studies, [^{18}F]FDG (20-30 mCi in 0.8 -1 mL) was injected to the reaction mixture containing 100 µL 1 M HEPES buffer, pH 7.6, 20 µL 1 M $MgCl_2$, 20 µL 1 M ATP, 60 µL 1 M UDP-GlC, ~50 µL OtsA (1 mg), ~50 µL OtsB (1 mg), 20 µL hexokinase (5 mg). The

reaction mixture was incubated at 37 °C for 30 min. After 30 min, the mixture was diluted with absolute ethanol (4 mL) and passed through a 5 μm syringe filter. The eluent was passed slowly through an amine Sep-Pak SPE cartridge at a flow rate of 1-2 drops per second. The eluent was then concentrated in vacuo. The resulting solution was filter-sterilized into a sterile vial for delivery. Identity of the compound was confirmed by LC-MS.

2.4.43 Specific Activity Analysis of [^{18}F]FDT

The radioactivity of the final products, [^{18}F]FDT, was obtained using the radiation detector. To quantify the mass of the cold [^{18}F]FDT in a form of [^{18}O] trehalose, the modified version of the trehalose quantification enzymatic assay was performed. A trehalose standard calibration curve (linear fit, R2 = 0.9984) was generated, following the enzymatic assay[36] using known concentrations of trehalose. The cold masses of [^{18}F]FDT from the syntheses were calculated based on this calibration curve. Then, the specific activity of the final product was calculated, following the definition, radioactivity/a unit mass of the compound.

References

1. Gaspar, L.; Reich, M.; Kassai, Z.; Macasek, F.; Rodrigo, L.; Kruzliak, P.; Kovac, P., Long-term quality assurance of [(18)F]-fluorodeoxyglucose (FDG) manufacturing. *American Journal of Nuclear Medicine & Molecular Imaging* **2016,** *6* (3), 154-165.

2. Qu, Q.; Lee, S.-J.; Boos, W.; TreT, a novel trehalose glycosyltransferring synthase of the hyperthermophilic archaeon *Thermococcus litoralis*. *Journal of Biological Chemistry* **2004,** *279* (46), 47890-47897.

3. Ryu, S. I.; Park, C. S.; Cha, J.; Woo, E. J.; Lee, S. B., A novel trehalose-synthesizing glycosyltransferase from Pyrococcus horikoshii: molecular cloning and characterization. *Biochemical and Biophysical Research Communications* **2005,** *329* (2), 429-36.

4. Kouril, T.; Zaparty, M.; Marrero, J.; Brinkmann, H.; Siebers, B., A novel trehalose synthesizing pathway in the hyperthermophilic Crenarchaeon *Thermoproteus tenax*: the unidirectional TreT pathway. *Archives of Microbiology* **2008,** *190* (3), 355-69.

5. Nobre, A.; Alarico, S.; Fernandes, C.; Empadinhas, N.; da Costa, M. S., A unique combination of genetic systems for the synthesis of trehalose in Rubrobacter xylanophilus: properties of a rare actinobacterial TreT. *Journal of Bacteriology* **2008,** *190* (24), 7939-46.

6. Ryu, S.-I.; Kim, J.-E.; Kim, E.-J.; Chung, S.-K.; Lee, S.-B. J. P. b., Catalytic reversibility of *Pyrococcus horikoshii* trehalose synthase: Efficient synthesis of several nucleoside diphosphate glucoses with enzyme recycling. *Process Biochemistry* **2011,** *46* (1), 128-134.

7. Urbanek, B. L.; Wing, D. C.; Haislop, K. S.; Hamel, C. J.; Kalscheuer, R.; Woodruff, P. J.; Swarts, B. M., Chemoenzymatic synthesis of trehalose analogues: rapid access to chemical probes for investigating mycobacteria. *ChemBiochem* **2014,** *15* (14), 2066-70.

8. Chenault, H. K.; Mandes, R. F.; Hornberger, K. R., Synthetic Utility of Yeast Hexokinase. Substrate Specificity, Cofactor Regeneration, and Product Isolation. *The Journal of Organic Chemistry* **1997,** *62* (2), 331-336.

9. Salas, M.; Vinuela, E.; Sols, A., Spontaneous and enzymatically catalysed anomerization of glucose-6-phosphate and anomeric specificity of related enzymes. *The Journal of Biological Chemistry* **1965,** *240*, 561-8.

10. Viola, R. E.; Raushel, F. M.; Rendina, A. R.; Cleland, W. W., Substrate synergism and the kinetic mechanism of yeast hexokinase. *Biochemistry* **1982,** *21* (6), 1295-302.

11. Wang, C. C.; Lee, J. C.; Luo, S. Y.; Kulkarni, S. S.; Huang, Y. W.; Lee, C. C.; Chang, K. L.; Hung, S. C., Regioselective one-pot protection of carbohydrates. *Nature* **2007,** *446* (7138), 896-9.

12. Joseph, A. A.; Chang, C. W.; Wang, C. C., Simple one-pot regioselective 6-O-phosphorylation of carbohydrates and trehalose desymmetrization. *Chemical Communications* **2013,** *49* (98), 11497-9.

13. Raushel, F. M.; Cleland, W. W., The substrate and anomeric specificity of fructokinase. *The Journal of Biological Chemistry* **1973,** *248* (23), 8174-7.

14. Gibson, R. P.; Turkenburg, J. P.; Charnock, S. J.; Lloyd, R.; Davies, G. J., Insights into trehalose synthesis provided by the structure of the retaining glucosyltransferase OtsA. *Chemistry & Biology* **2002,** *9* (12), 1337-46.

15. Errey, J. C.; Lee, S. S.; Gibson, R. P.; Martinez Fleites, C.; Barry, C. S.; Jung, P. M.; O'Sullivan, A. C.; Davis, B. G.; Davies, G. J., Mechanistic insight into enzymatic glycosyl transfer with retention of configuration through analysis of glycomimetic inhibitors. *Angewandte Chemie* **2010,** *49* (7), 1234-7.

16. Backus, K. M.; Boshoff, H. I.; Barry, C. S.; Boutureira, O.; Patel, M. K.; D'Hooge, F.; Lee, S. S.; Via, L. E.; Tahlan, K.; Barry, C. E., 3rd; Davis, B. G., Uptake of unnatural trehalose analogs as a reporter for Mycobacterium tuberculosis. *Nature Chemical Biology* **2011,** *7* (4), 228-35.

17. Klutts, S.; Pastuszak, I.; Edavana, V. K.; Thampi, P.; Pan, Y. T.; Abraham, E. C.; Carroll, J. D.; Elbein, A. D., Purification, cloning, expression, and properties of mycobacterial trehalose-phosphate phosphatase. *The Journal of Biological Chemistry* **2003,** *278* (4), 2093-100.

18. Pade, N.; Compaore, J.; Klahn, S.; Stal, L. J.; Hagemann, M., The marine cyanobacterium Crocosphaera watsonii WH8501 synthesizes the compatible solute trehalose by a laterally acquired OtsAB fusion protein. *Environmental Microbiology* **2012,** *14* (5), 1261-71.

19. Kimura, Y.; Kawasaki, S.; Tuchimoto, R.; Tanaka, N., Trehalose biosynthesis in Myxococcus xanthus under osmotic stress and during spore formation. *Journal of Biochemistry* **2014,** *155* (1), 17-24.

20. Stewart, I.; Schluter, P. J.; Shaw, G. R., Cyanobacterial lipopolysaccharides and human health - a review. *Environmental Health* **2006,** *5*, 7.

21. Ryu, S.-I.; Park, C.-S.; Cha, J.; Woo, E.-J.; Lee, S.-B. J. B.; communications, b. r., A novel trehalose-synthesizing glycosyltransferase from *pyrococcus horikoshii*: molecular cloning and characterization. *Biochemical and Biophysical Research Communication* **2005,** *329* (2), 429-436.

22. Griffiths, C. A.; Sagar, R.; Geng, Y.; Primavesi, L. F.; Patel, M. K.; Passarelli, M. K.; Gilmore, I. S.; Steven, R. T.; Bunch, J.; Paul, M. J.; Davis, B. G., Chemical intervention in plant sugar signalling increases yield and resilience. *Nature* **2016,** *540* (7634), 574-578.

23. Woo, E. J.; Ryu, S. I.; Song, H. N.; Jung, T. Y.; Yeon, S. M.; Lee, H. A.; Park, B. C.; Park, K. H.; Lee, S. B., Structural insights on the new mechanism of trehalose synthesis by trehalose synthase TreT from *Pyrococcus horikoshii*. *Journal of Molecular Biology* **2010,** *404* (2), 247-59.

24. Qing, G.; Ma, L. C.; Khorchid, A.; Swapna, G. V.; Mal, T. K.; Takayama, M. M.; Xia, B.; Phadtare, S.; Ke, H.; Acton, T.; Montelione, G. T.; Ikura, M.; Inouye, M., Cold-shock induced high-yield protein production in *Escherichia coli*. *Nature Biotechnology* **2004,** *22* (7), 877-82.

25. Anderson, D. J. F., Rapid generation of recombinant baculoviruses and expression of foreign genes using the Bac-to-Bac baculovirus expression system. **1996,** *17*, 53-58.

26. Sui, D.; Wang, K.; Park, H.; Chae, J., Bright field microscopic cells counting method for BEVS using nonlinear convergence index sliding band filter. *BioMedical Engineering OnLine* **2014,** *13* (1), 147.

27. Gosselin, S.; Alhussaini, M.; Streiff, M. B.; Takabayashi, K.; Palcic, M. M., A continuous spectrophotometric assay for glycosyltransferases. *Analytical Biochemistry* **1994,** *220* (1), 92-7.

28. Johnson, K. A.; Goody, R. S., The Original Michaelis Constant: Translation of the 1913 Michaelis–Menten Paper. *Biochemistry* **2011,** *50* (39), 8264-8269.

29. Lorsch, J. R., Chapter One - Practical Steady-State Enzyme Kinetics. In *Methods in Enzymology*, Lorsch, J., Ed. Academic Press: **2014**; Vol. 536, pp 3-15.

30. Greenfield, N. J., Using circular dichroism spectra to estimate protein secondary structure. *Nature Protocols* **2006,** *1* (6), 2876-2890.

31. Bharti, S. K.; Roy, R., Quantitative 1H NMR spectroscopy. *TrAC Trends in Analytical Chemistry* **2012,** *35*, 5-26.

32. Abernethy, D. R.; DeStefano, A. J.; Cecil, T. L.; Zaidi, K.; Williams, R. L.; Metal Impurities in Food and Drugs. *Pharmaceutical Research* **2010,** *27* (5), 750-755.

33. Şahan, Y.; Basoglu, F.; Gücer, S., ICP-MS analysis of a series of metals (Namely: Mg, Cr, Co, Ni, Fe, Cu, Zn, Sn, Cd and Pb) in black and green olive samples from Bursa, Turkey. *Food Chemistry* **2007,** *105* (1), 395-399.

34. Abernethy, D. R.; Destefano, A. J.; Cecil, T. L.; Zaidi, K.; Williams, R. L., Metal impurities in food and drugs. *Pharmaceutical Research* **2010,** *27* (5), 750-5.

35. Pena-Zalbidea, S.; Huang, A. Y.; Kavunja, H. W.; Salinas, B.; Desco, M.; Drake, C.; Woodruff, P. J.; Vaquero, J. J.; Swarts, B. M., Chemoenzymatic radiosynthesis of 2-deoxy-2-[(18)F]fluoro-d-trehalose ([(18)F]-2-FDTre): A PET radioprobe for in vivo tracing of trehalose metabolism. *Carbohydrate Research* **2019,** *472*, 16-22.

36. Carillo, P.; Feil, R.; Gibon, Y.; Satoh-Nagasawa, N.; Jackson, D.; Bläsing, O. E.; Stitt, M.; Lunn, J. E., A fluorometric assay for trehalose in the picomole range. *Plant Methods* **2013,** *9* (1), 21.

2.5 Supplementary Figures

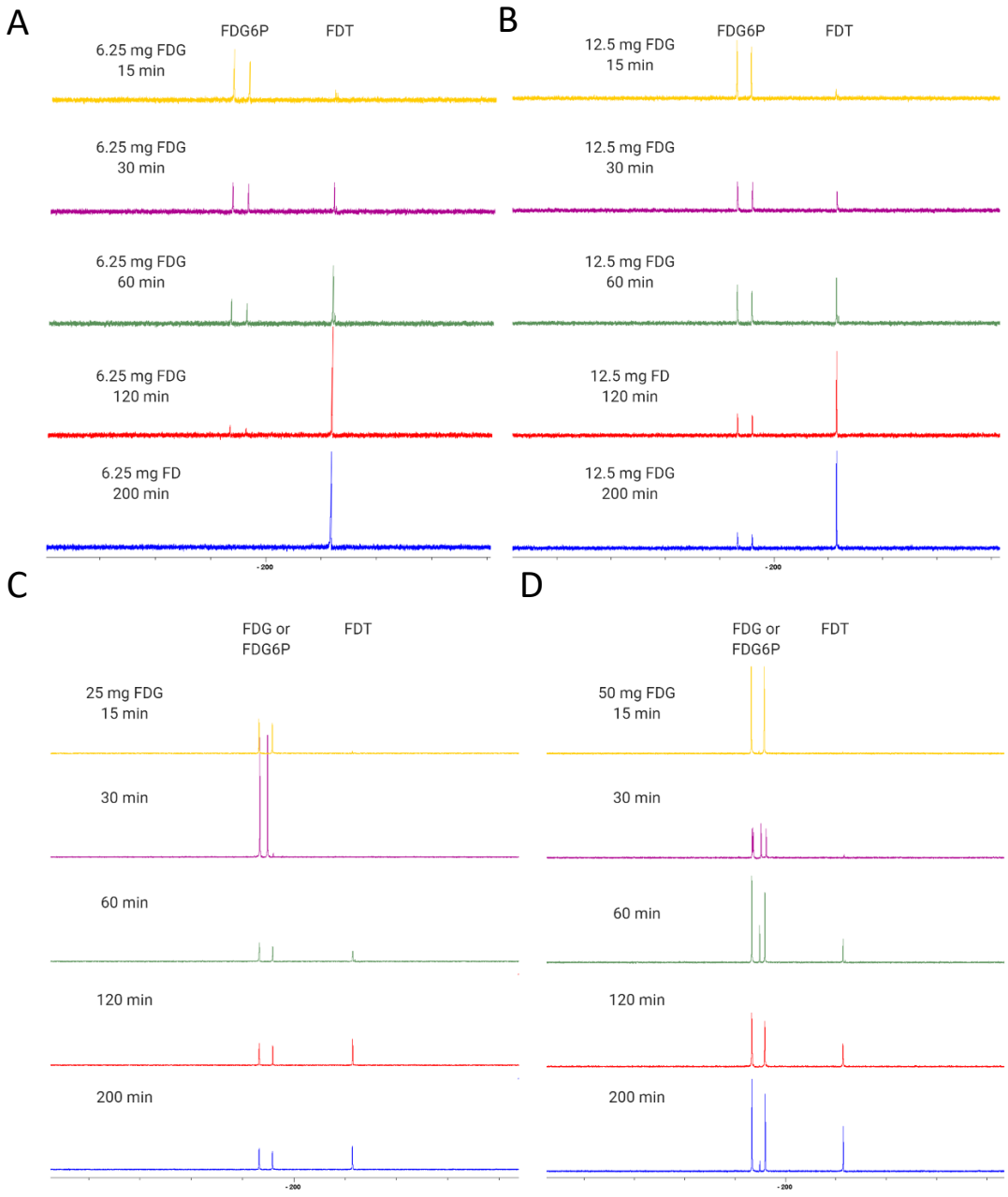


Figure S1. [^{19}F] FDT Reaction optimisation and monitoring by ^{19}F-NMR spectroscopy. A). 6.25 mg FDG reaction catalysis by Hexokinase, OtsA and OtsB. Samples were taken 15 min, 30 min, 60 min, 120 min and 200 min post reaction and reaction was more than 95% complete after 2 h. B). 12.5 mg FDG sample with similar monitoring time as above. After 3 h, there was 10% of FDG6P remained uncatalysed. C). 25 mg FDG sample catalysed and reaction monitored as A, after 3h, 20 min there was about 45% intermediate remained uncatalysed and D). 50 mg FDG sample catalysed and analysed as above, the conversion was 30% after 3h, 20 min. The glycosylation reaction was the limiting step and

the amount of UDP-glc was kept constant at 30 mM which was significantly less for 25 mg FDG substrate and 50 mg FDG substrate.

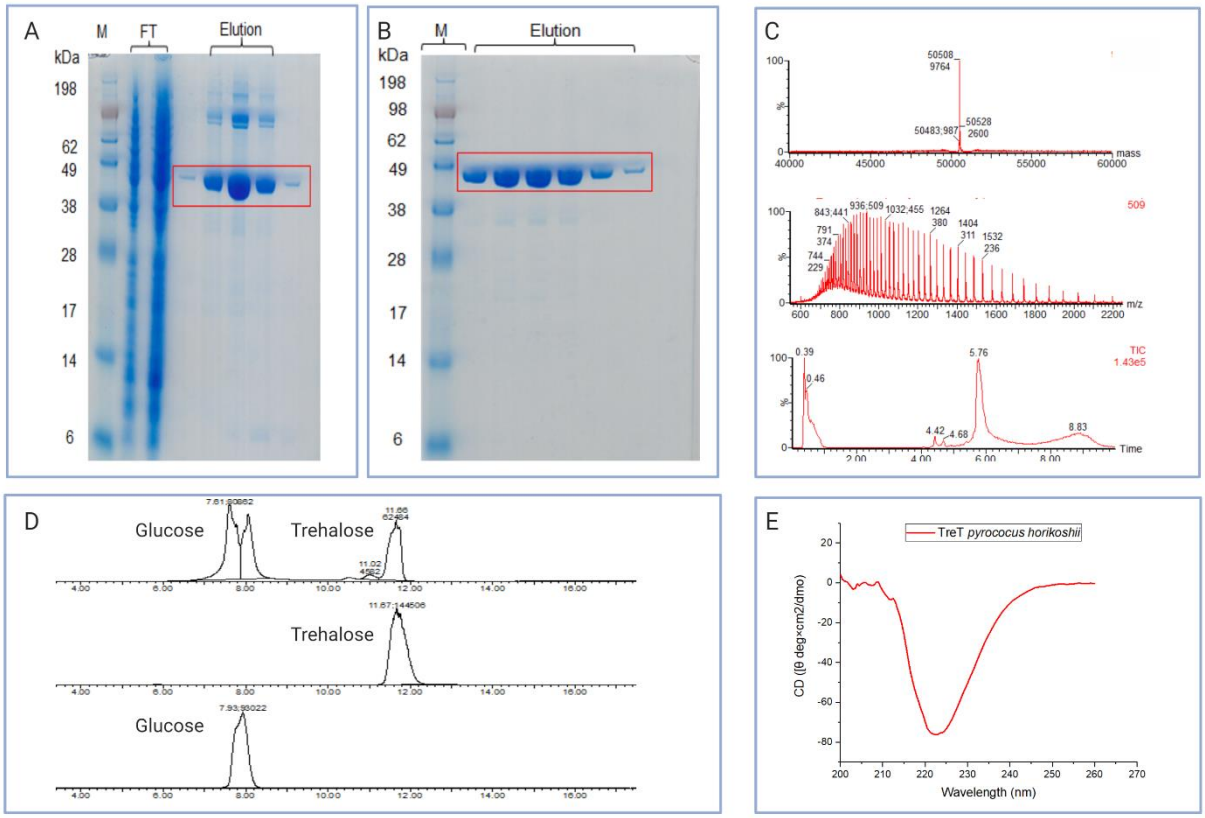


Figure S2: TreT *P. horikoshii* enzyme characterization and reaction analysis. A). SDS-Gel from FPLC purification of TreT *P. horikoshii* showing the characteristic band of the enzyme around 50 kDa. B). SDS-Gel of TreT *P. horikoshii* from SEC purification confirming the band at 50 kDa reprenstative of the enzyme; C). LC-MS characterization of TreT *P. horikoshii*, from top to bottom: deconvoluted spectra, ion series and the chromatogram of the sample; D). Enzyme reaction analysis of *P. horikoshii* by LC- MS. We have used standard samples for both the starting material (glucose) and the final product (trehalose) and confirmed by LC-MS analysis that the enzyme is active; E). Circular dichroism (CD) spectra of *P. horikoshii.*

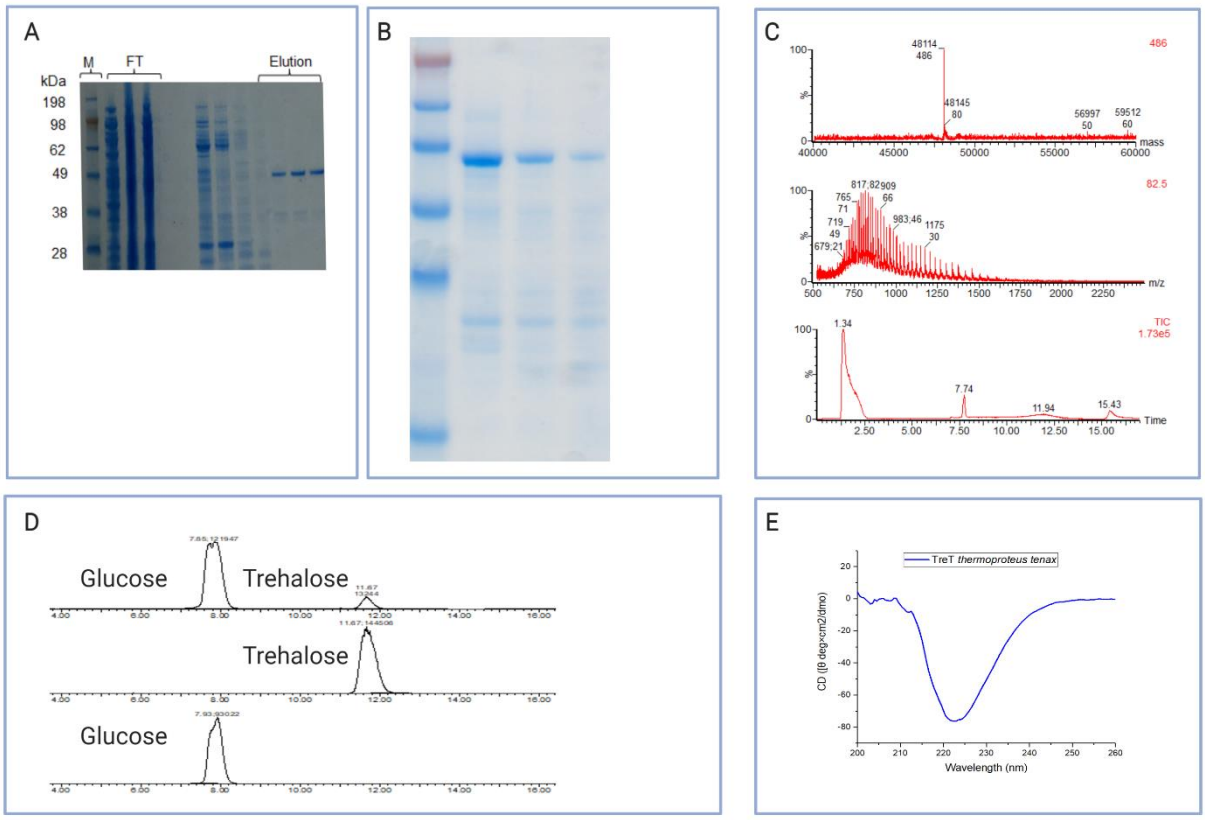


Figure S3: TreT *T. tenax* enzyme characterization and reaction analysis. A). SDS-Gel from FPLC purification of TreT *T. tenax* showing the characteristic band of the enzyme around 48 kDa. B). SDS-Gel of TreT *T. tenax* from SEC purification confirming the band at 48 kDa reprenstative of the enzyme; C). LC-MS characterization of TreT *T. tenax*, from top to bottom: deconvoluted spectra, ion series and the chromatogram of the sample; D). Enzyme reaction analysis of *T. tenax* by LC- MS. We have used standard samples for both the starting material (glucose) and the final product (trehalose) and confirmed by LC-MS analysis that the enzyme is active; E). Circular dichroism (CD) spectra of *T. tenax*.

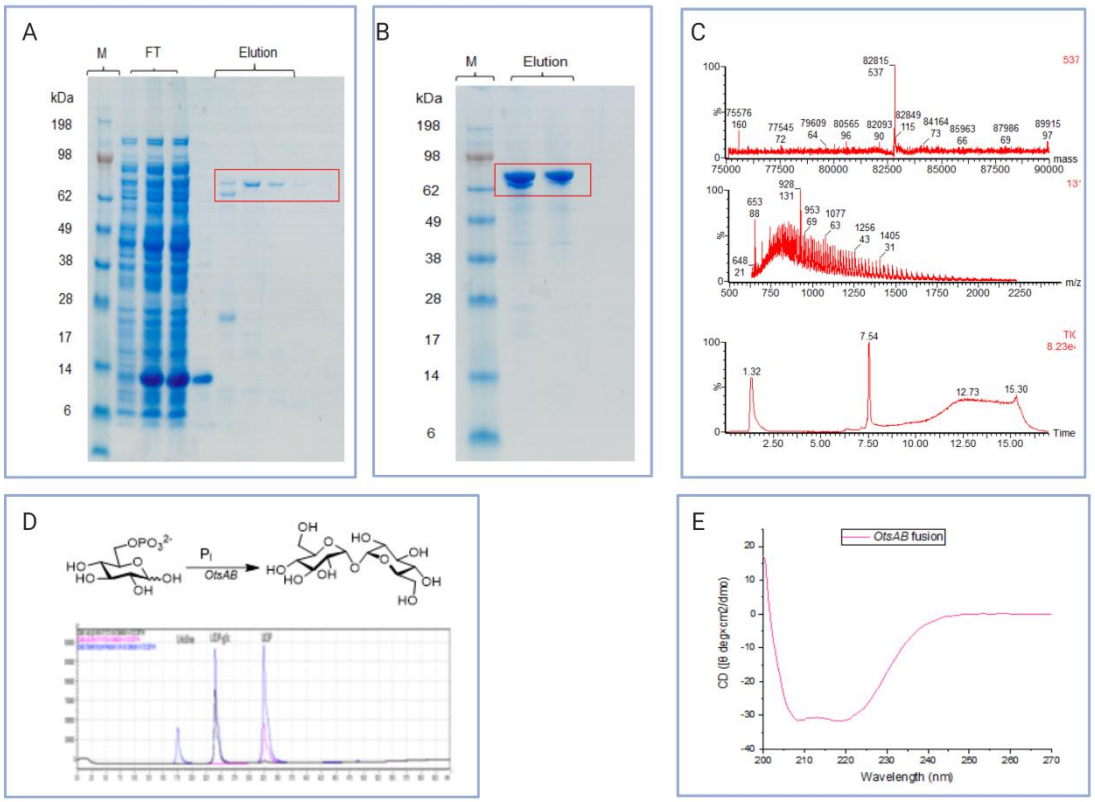
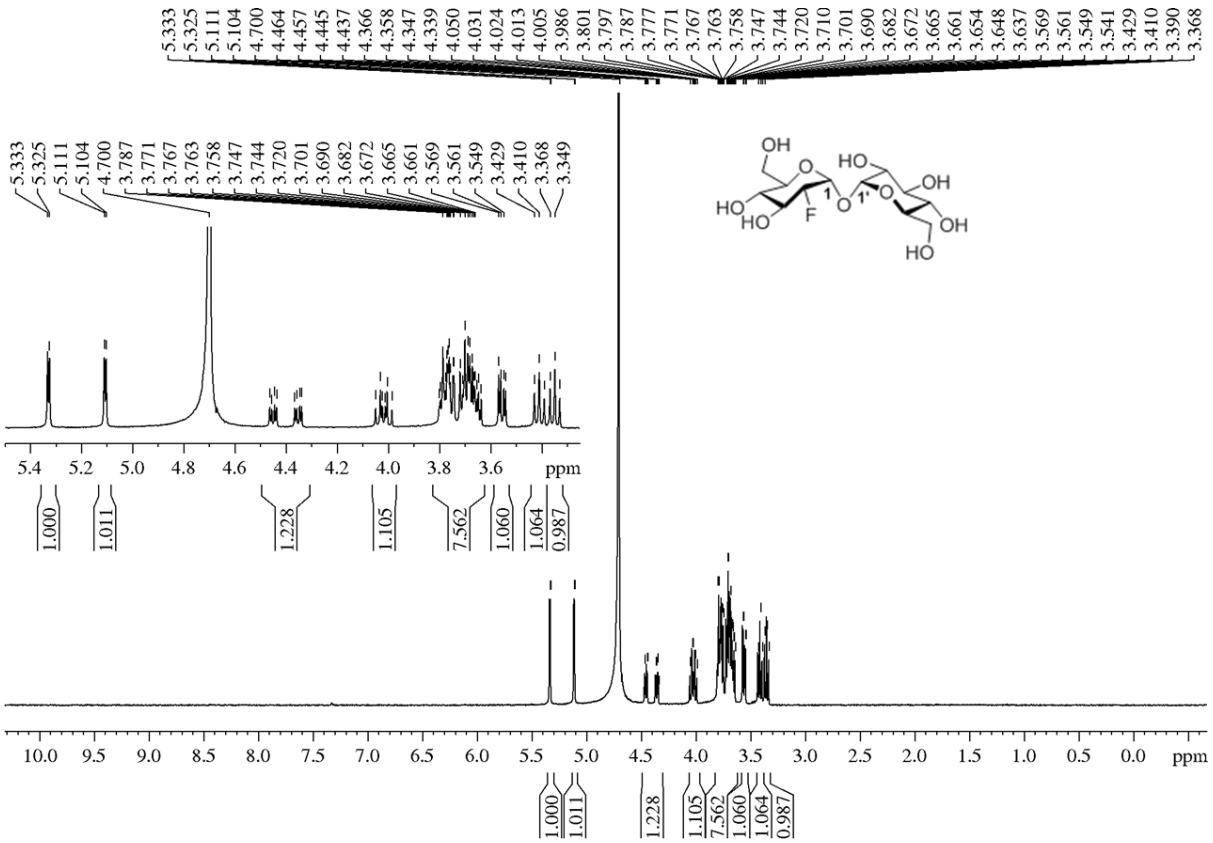
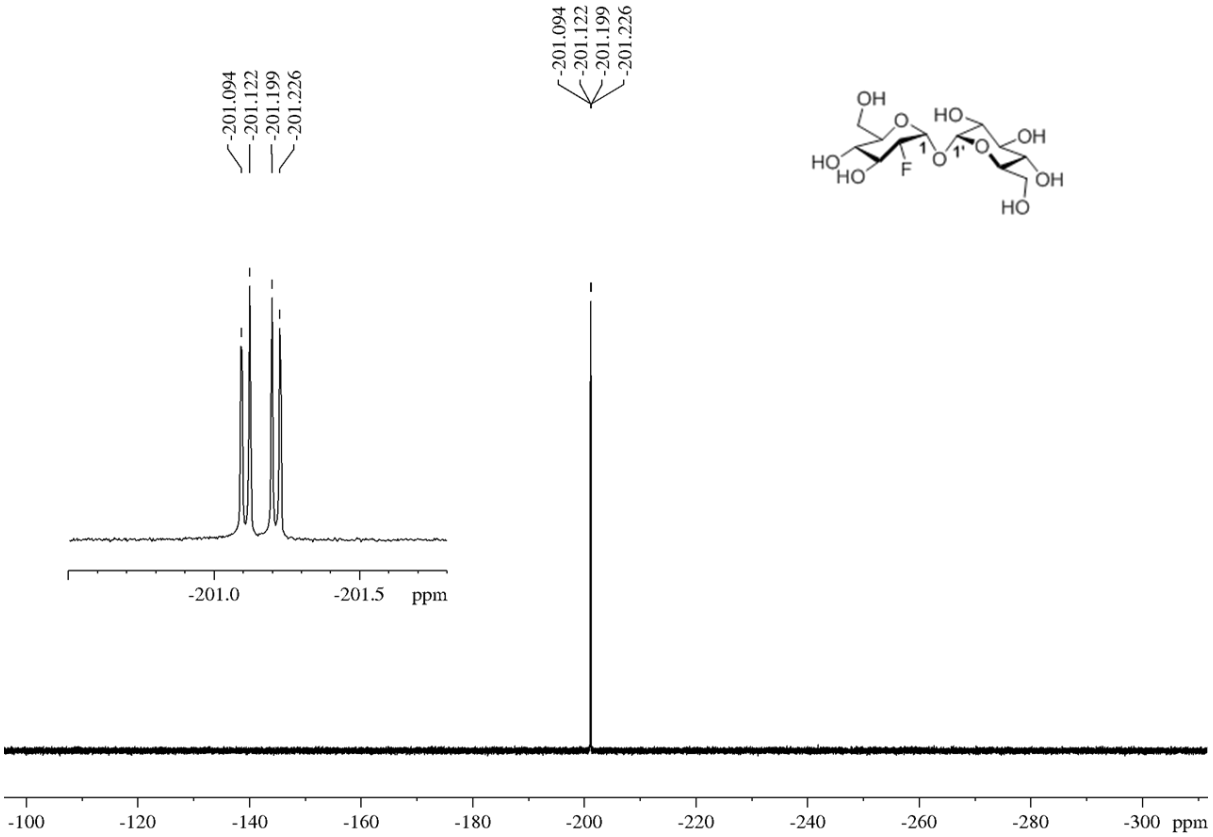


Figure S4: OtsAB fusion enzyme characterization and reaction analysis. A). SDS-Gel from FPLC purification of OtsAB fusion showing the characteristic band of the enzyme around ~ 83 kDa. B). SDS-Gel of OtsAB fusion from SEC purification confirming the band at ~ 83 kDa reprenstative of the enzyme; C). LC-MS characterization of OtsAB fusion, from top to bottom: deconvoluted spectra, ion series and the chromatogram of the sample; D). Enzyme reaction analysis of OtsAB fusion by LC- MS. We have used standard samples for both the starting material (UDP-Glc) and the final product (UDP) and confirmed by LC-MS analysis that the enzyme is active; E). Circular dichroism (CD) spectra of OtsAB fusion.



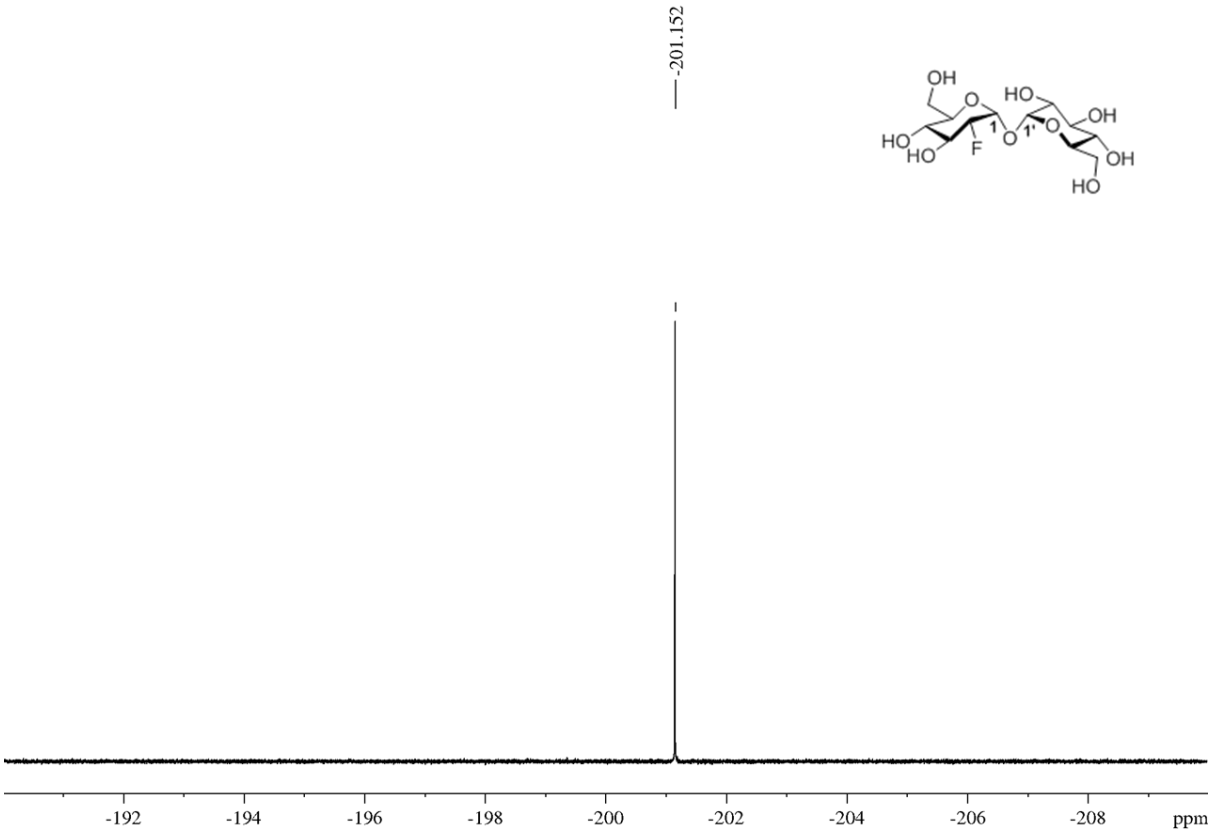
S5: ^{1}H NMR spectrum of [^{19}F]-FDT

Frequency [MHz]	500.13
SW [ppm]	19.9947
Origin	AVX500
Nucleus	^{1}H
NS	16
Solvent	D_2O
Temperature (degree C)	25



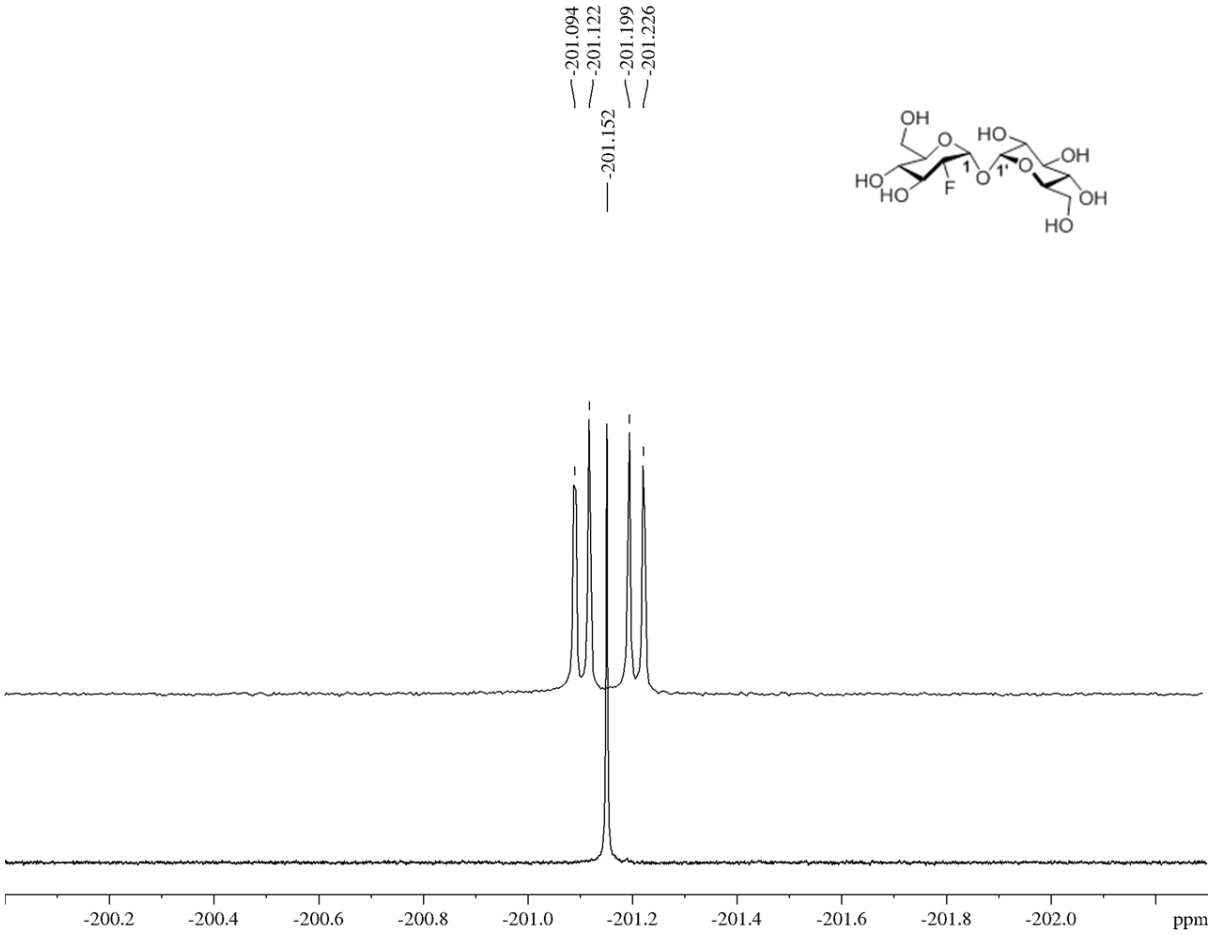
S6: ^{19}F(^{1}H coupled) NMR spectrum of [^{19}F]-FDT

Frequency [MHz)	470.13
SW [ppm]	241.5235
Origin	AVX500
Nucleus	^{19}F
NS	256
Solvent	D_2O
Temperature (degree C)	25

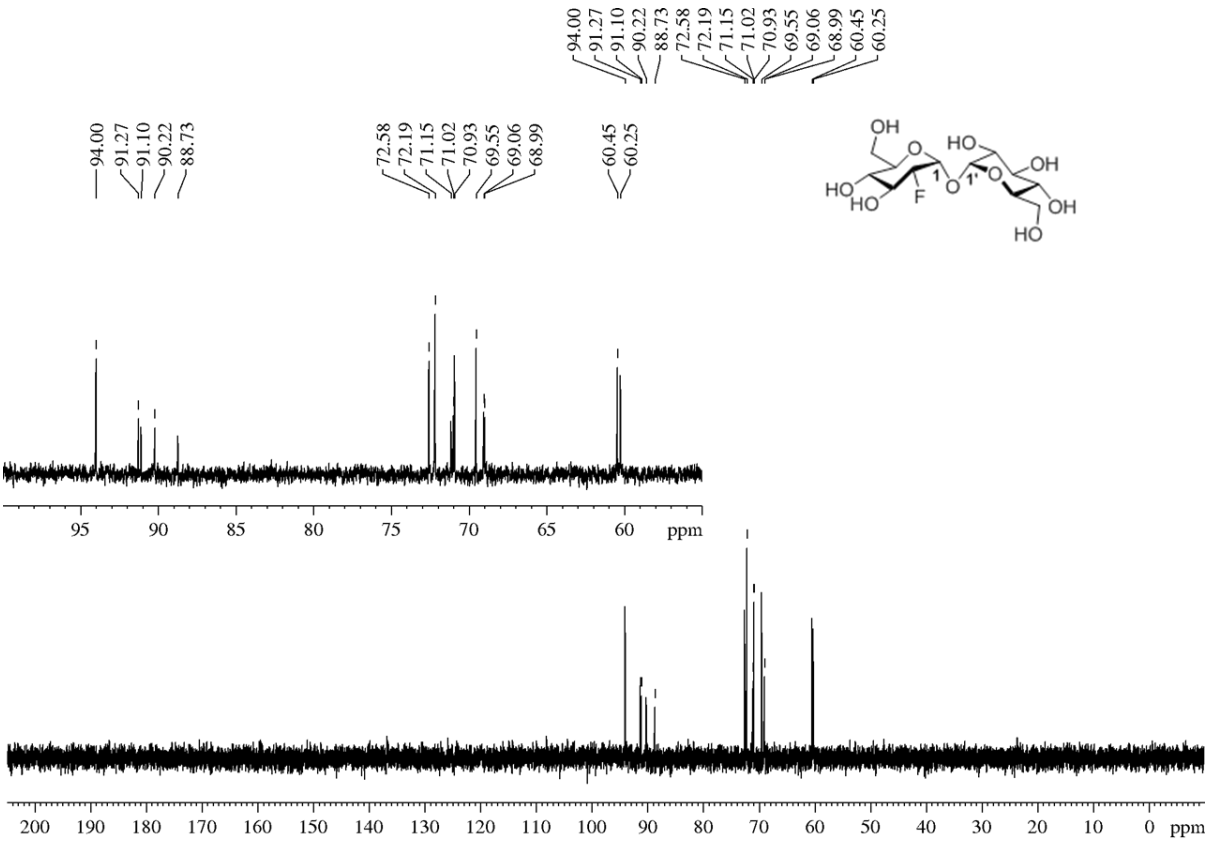


S7: ^{19}F(^{1}H decoupled) NMR spectrum of [^{19}F]- FDT

Frequency [MHz]	470.13
SW [ppm]	19.9756
Origin	AVX500
Nucleus	^{19}F
NS	32
Solvent	D_2O
D1 (sec)	10
Temperature (degree C)	25

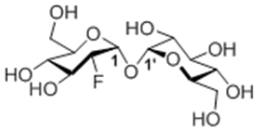


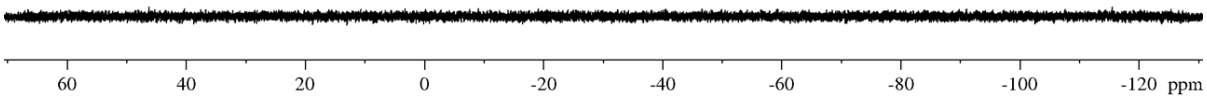
S8: ^{19}F and ^{19}F(^{1}H) Coupled NMR spectrum of [^{19}F]-FDT. Both coupled and decoupled spectra are stacked together.



S9: ^{13}C NMR spectrum of [^{19}F]-FDT

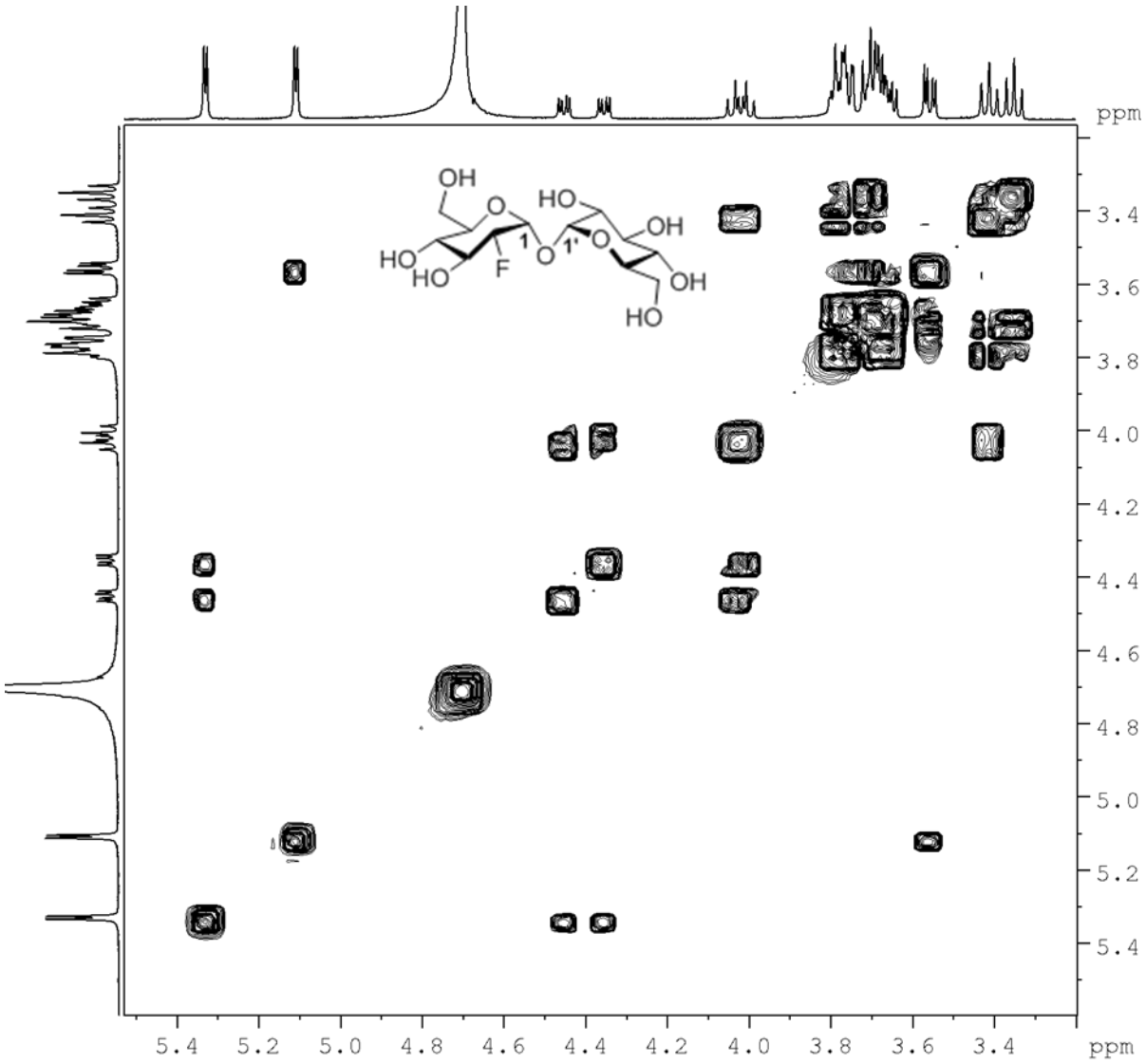
Frequency [MHz]	126
SW [ppm]	236.6369
Origin	AVX500
Nucleus	^{13}C
NS	3072
Solvent	D_2O
D1 (sec)	2
Temperature (degree C)	25





S10: ^{31}P(^{1}H Decoupled) NMR Spectrum of [^{19}F]-FDT. There is no signal for either of the reaction intermediates or reagents used that contain ^{31}P nuclei.

Frequency [MHz]	202
SW [ppm]	201.3377
Origin	AVX500
Nucleus	^{31}P
NS	64
Solvent	D_2O
D1 (sec)	2
Temperature (degree C)	25

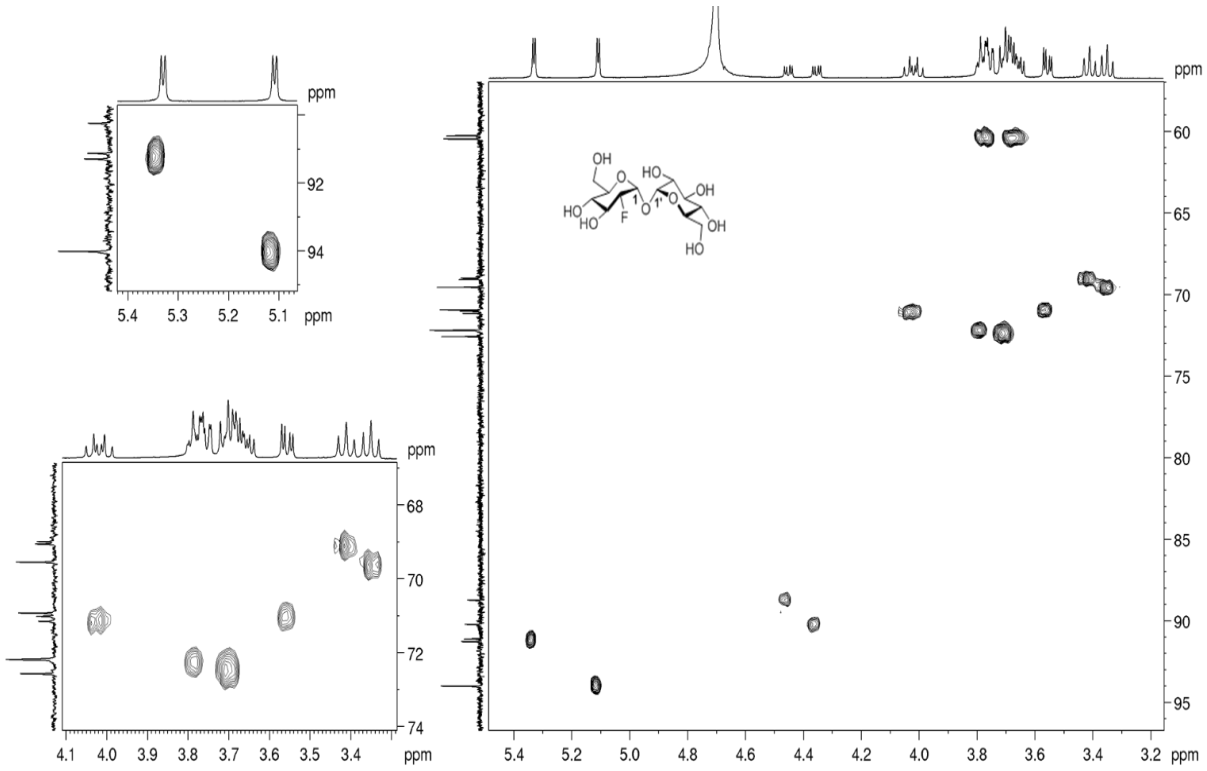


S11: COSY spectrum of [^{19}F]-FDT. *^{1}H-^{1}H COSY (Correlated Spectroscopy).*

Frequency [MHz)	500
SW [ppm]	12.0161
Origin	AVX500
Nucleus	^{1}H
NS	8
Solvent	D_2O

D1 (sec) 2

Temperature (degree C) 25



S12: HSQC Spectrum of [^{19}F]-FDT. Heteronuclear Single Quantum Coherence experiment was used to determine proton-carbon single bond correlations. In the above spectrum ^{13}C NMR spectrum is on the Y-axis whereas ^{1}H NMR spectrum is shown on the X-axis.

Frequency [MHz] ^{1}H 500 & ^{13}C 126

SW [ppm] 12.0161

Origin AVX500

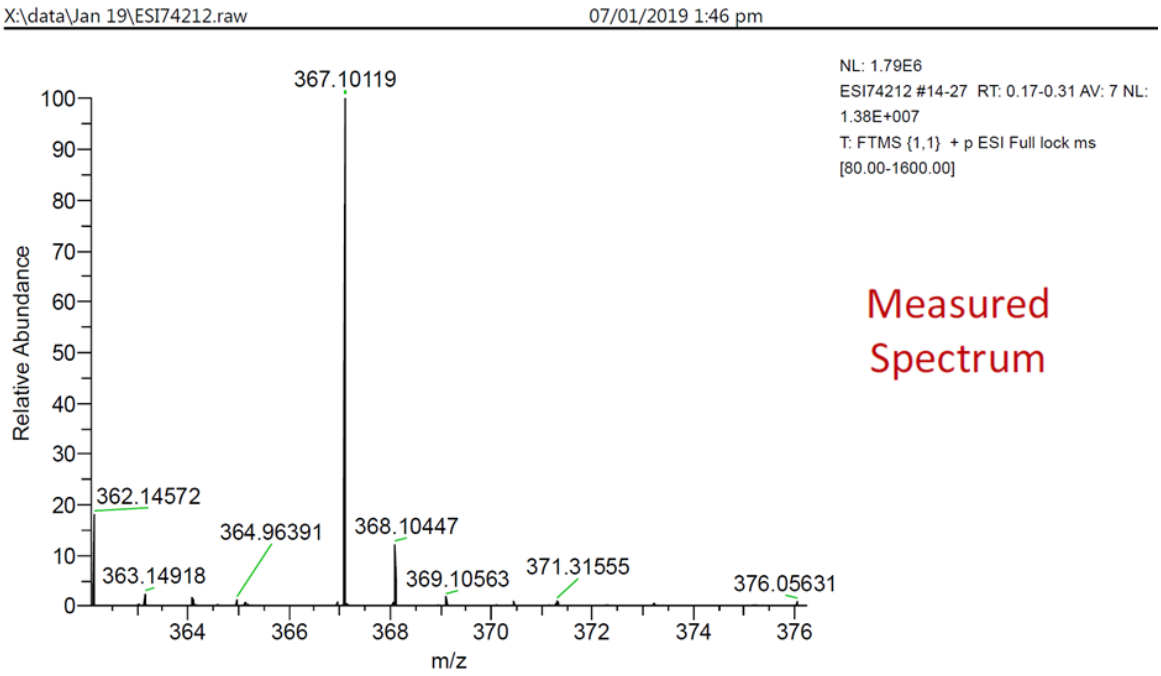
Nucleus ^{1}H – ^{13}C

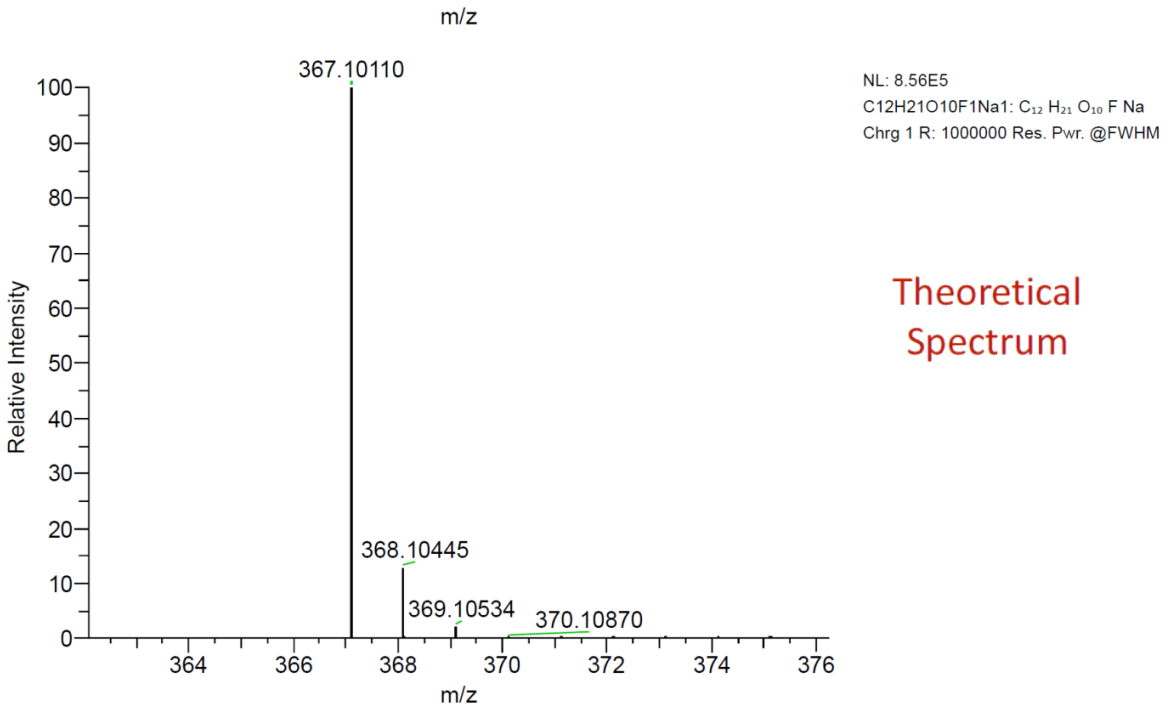
NS 8

Solvent D_2O

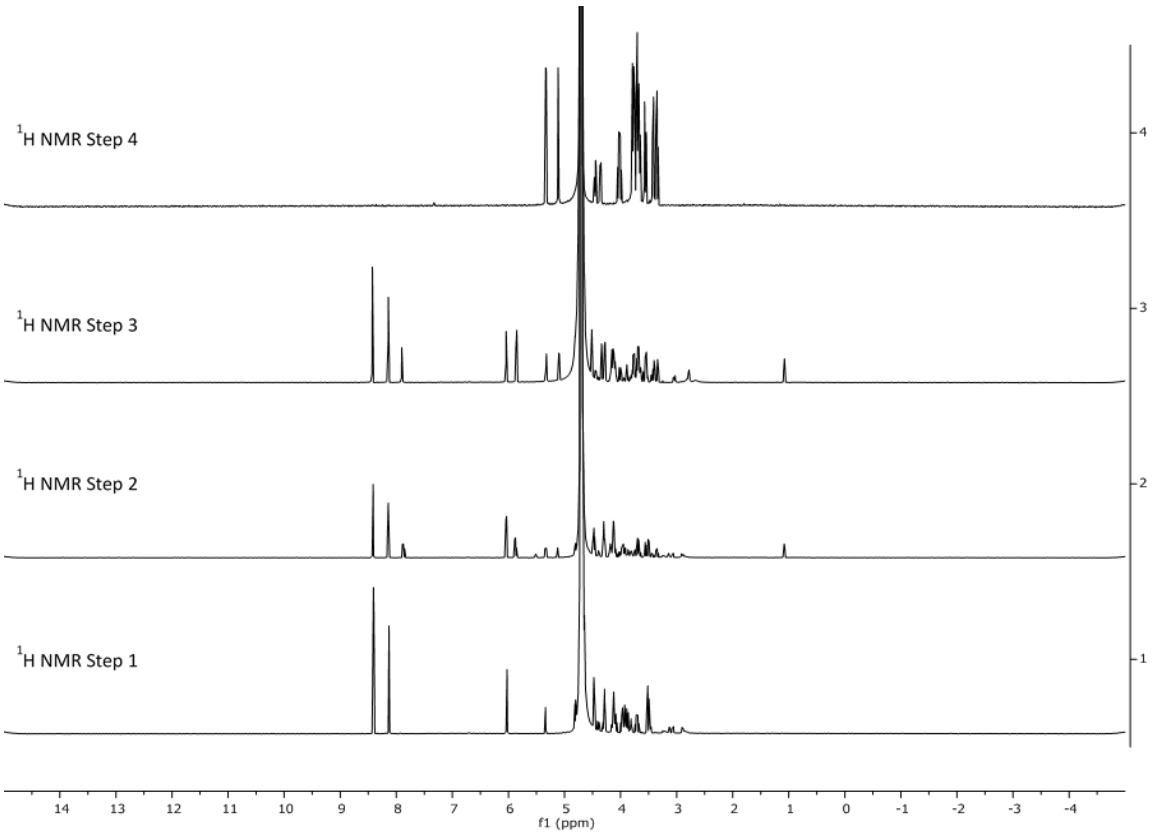
D1 (sec) 1

Temperature (degree C) 25

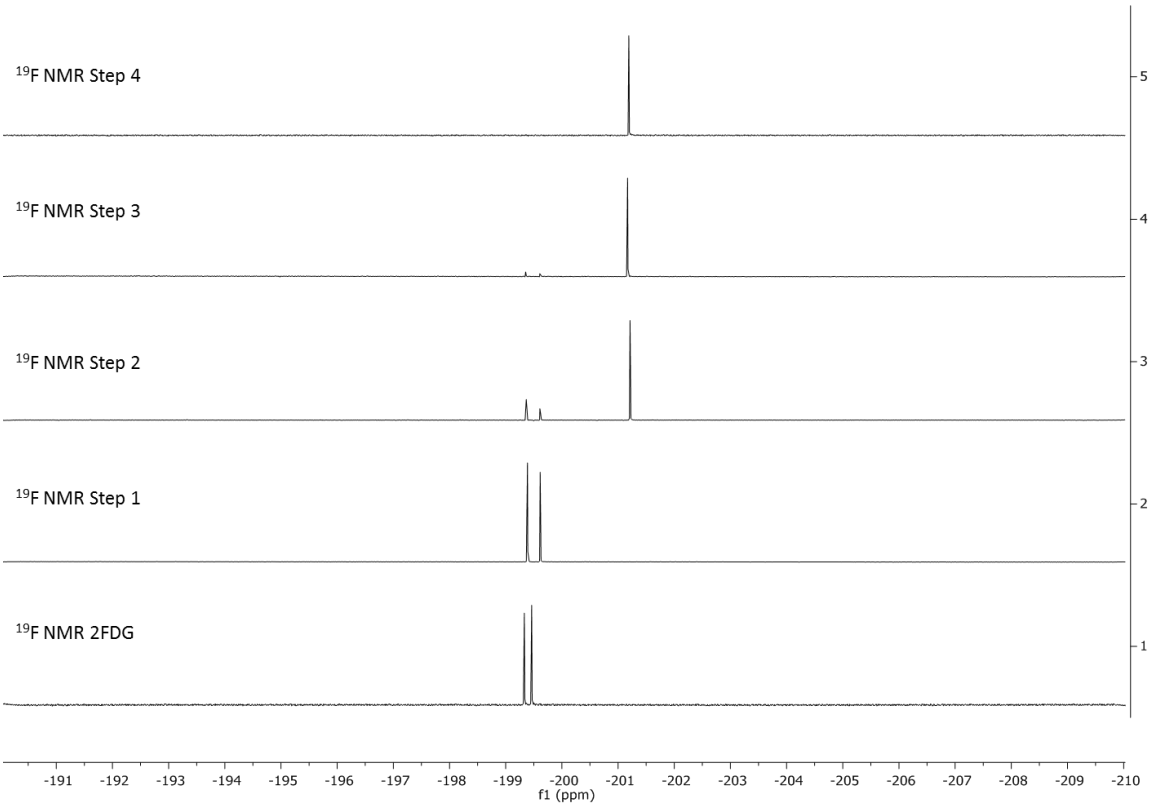




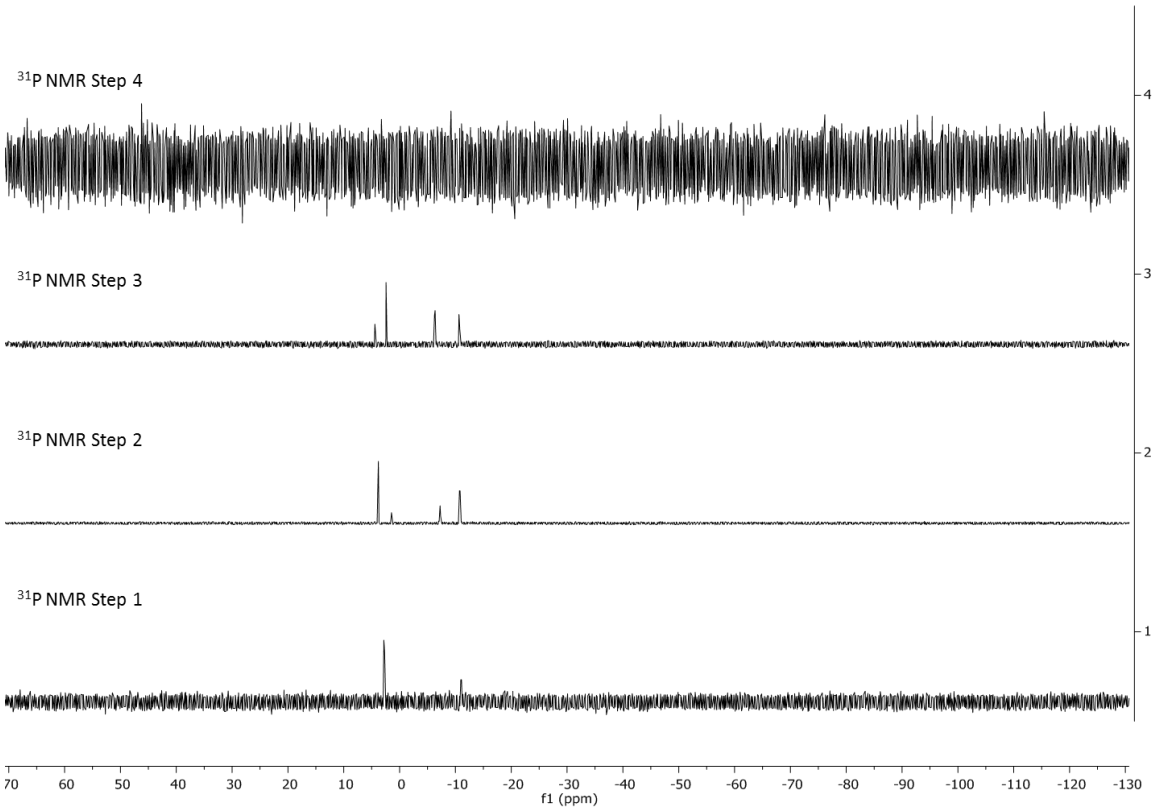
S13: ESI-MS Spectrum of [^{19}F]- FDT. 40 µg of **[^{19}F]- FDT** sample was dissolved in 1 mL 50:50 methanol de-ionised water and the accurate mass of the sample was determined. The instrument is accurate up to 4 decimal points. The sample was run on a Thermo Orbitrap Exactive mass spectrometer calibrated with standard calibration solutions that included MRFA (L-methionyl-arginyl-phenylalanyl-alanine acetate.xH_2O), Ultramark 1621, caffeine and glacial acetic acid.



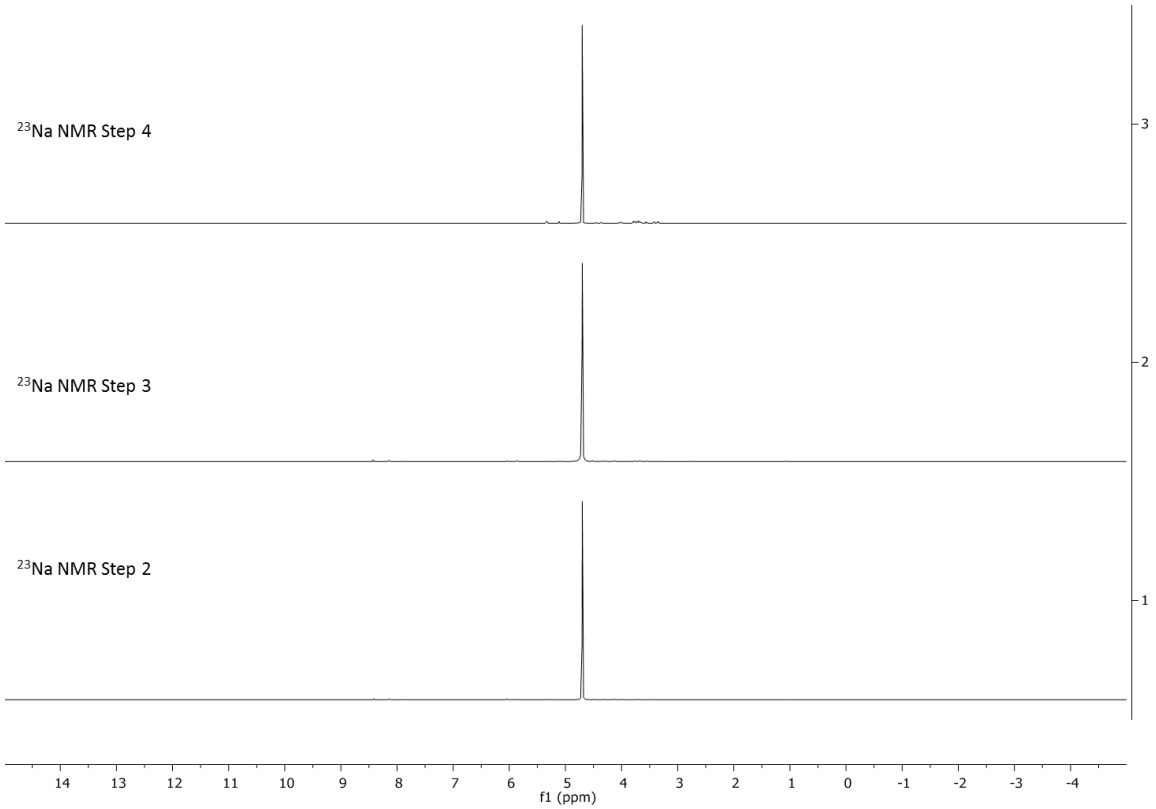
S14: ^{1}H-NMR (500 MHz) spectra of crude reaction mixtures during one-pot synthesis and purified product. Step 1 involves the conversion of **FDG** to **FDG6P**; Step 2 represents conversion of **FDG6P** to **FDT6P**; Step 3 shows the conversion of **FDT6P** to **[^{19}F]- FDT**. Step 4 is for the purified final batch of **[^{19}F]-FDT**. D_2O was used as solvent. For all crude reactions, 20 µL sample was diluted in 500 µL of D_2O; whereas for the purified sample, 2.3 mg of **[^{19}F]-FDT** was dissolved in 500 µL of D_2O.



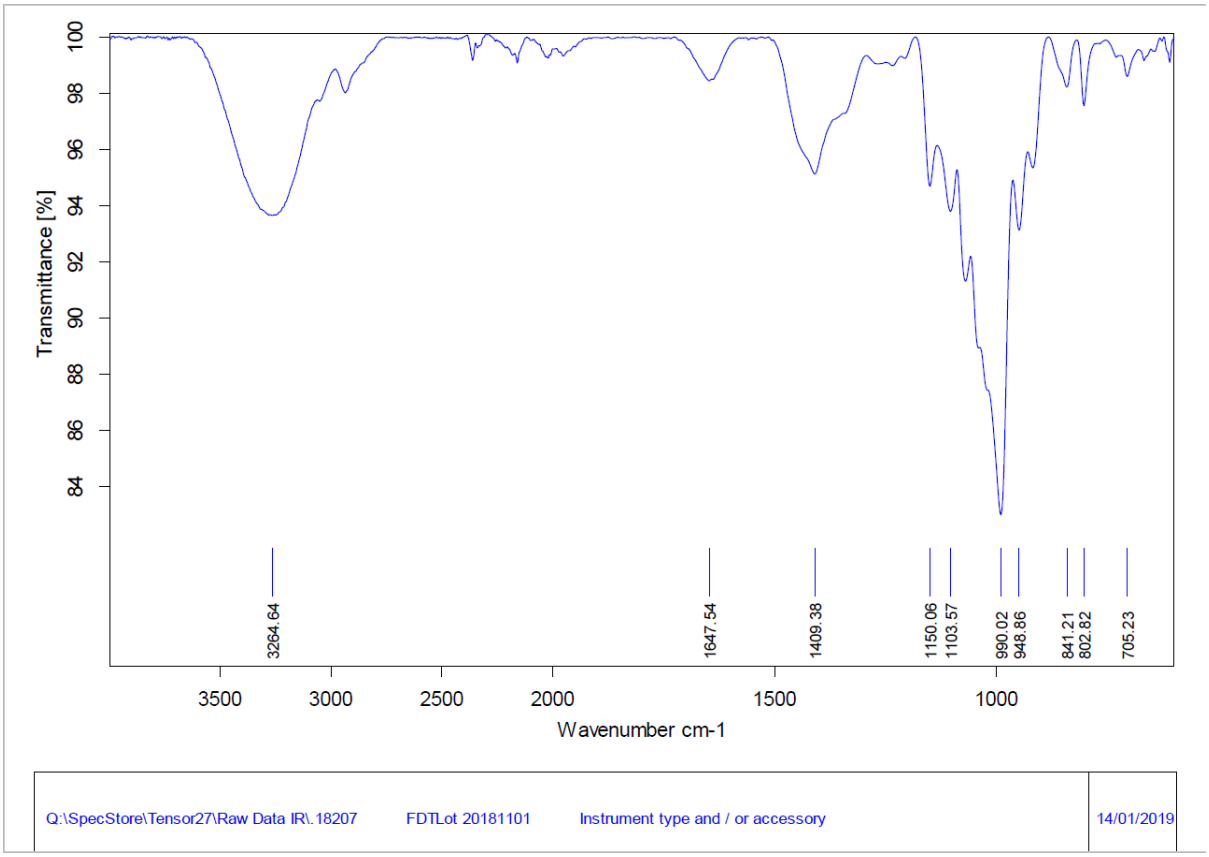
S15: ^{19}F(Decoupled) NMR (470 MHz) spectra of crude mixture and purified product of [^{19}F]-FDT. Step 1 involves the conversion of **FDG** to **FDG6P**; Step 2 represents conversion of **FDG6P** to **FDT6P**; Step 3 shows the conversion of **FDT6P** to **[^{19}F]-FDT**. Step 4 is for the purified final batch of **[^{19}F]-FDT**. D_2O was used as solvent. For all crude reactions, 20 µL sample was diluted in 500 µL of D_2O; whereas for the purified sample, 2.3 mg of **[^{19}F]-FDT** was dissolved in 500 µL of D_2O.



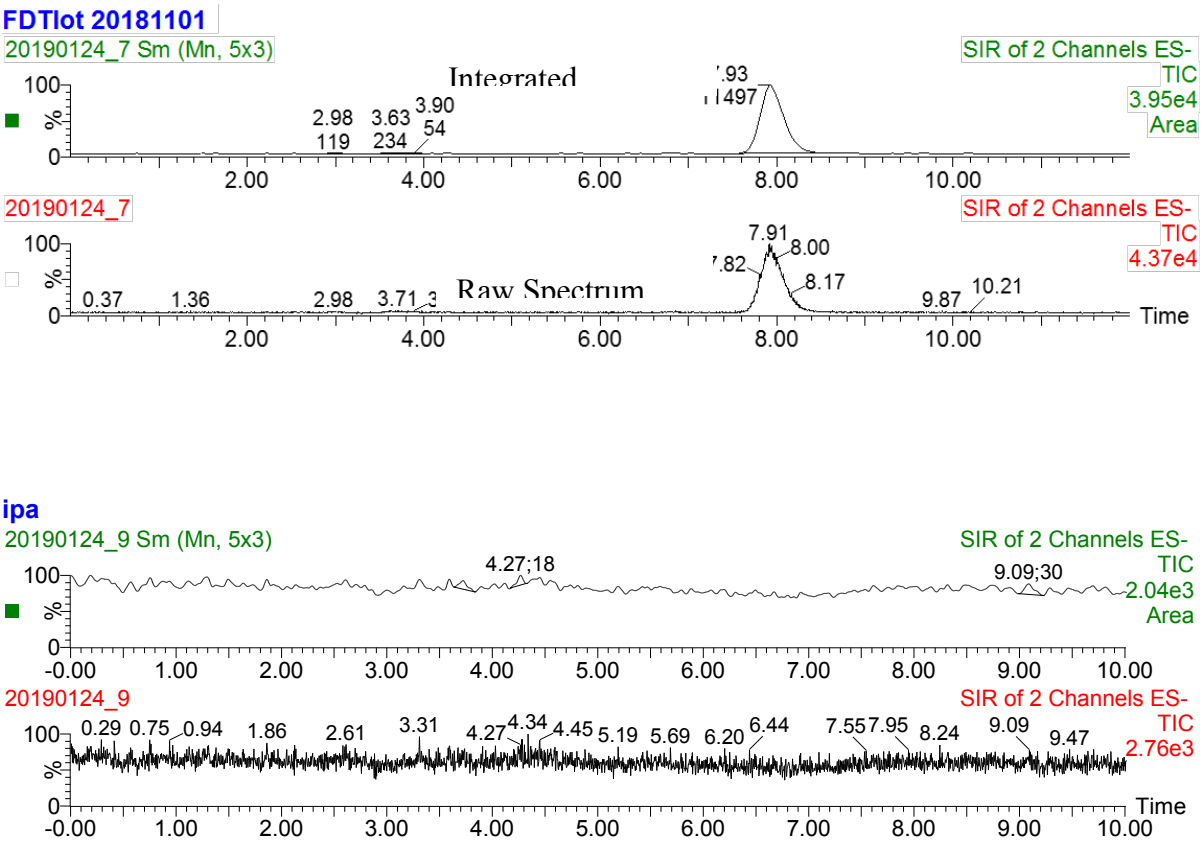
S16: ^{31}P-NMR (202 MHz) spectra of crude mixture and purified batch of [^{19}F]-FDT. Step 1 involves the conversion of **FDG** to **FDG6P**; Step 2 represents conversion of **FDG6P** to **FDT6P**; Step 3 shows the conversion of **FDT6P** to **[^{19}F]-FDT**. Step 4 is for the purified final batch of **[^{19}F]-FDT**. D_2O was used as solvent. For all crude reactions, 20 µL sample diluted in 500 µL of D_2O; whereas for the purified sample, 2.3 mg of **[^{19}F]-FDT** was dissolved in 500 µL in D_2O.



S17: ^{23}Na-NMR (132 MHz) Spectra of FDT6P & [^{19}F]-FDT Crude and [^{19}F]-FDT purified batch. Step 2 is from **FDT6P** crude mixture; Step 3 is from **[^{19}F]-FDT** crude mixture; Step 4 is from the purified product of **[^{19}F]-FDT**. All samples were analyzed in D_2O.



S18: IR Spectrum of [^{19}F]-FDT.



S19: LC-MS chromatogram of [^{19}F]-FDT and blank sample. Iso-propyl alcohol (IPA) was used as blank. In the FDTlot20181101 sample, **[^{19}F]-FDT** peak appears at a retention time of 7.93 min. The raw chromatogram was integrated using MassLynx software and the integrated counts of 11497 are from **[^{19}F]-FDT** sample

Appenices

A1: OtsA codon optimisation: Compariosn of protein sequences

E. coli

MSRLVVVSNRIAPPDEHAASAGGLAVGILGALKAAGGLWFGWSGETGNEDQPLKK

VKKGN 60

I. Cells

MSRLVVVSNRIAPPDEHAASAGGLAVGILGALKAAGGLWFGWSGETGNEDQPLKK

VKKGN 60

********** 11 **********

E. coli

ITWASFNLSEQDLDEYYNQFSNAVLWPAFHYRLDLVQFQRPAWDGYLRVNALLAD

KLLPL 120

I. cells

ITWASFNLSEQDLDEYYNQFSNAVLWPAFHYRLDLVQFQRPAWDGYLRVNALLAD

KLLPL 120

****

E. coli

LQDDDIIWIHDYHLLPFAHELRKRGVNNRIGFFLHIPFPTPEIFNALPTYDTLLEQLCD

Y 180

I. cells

LQDDDIIWIHDYHLLPFAHELRKRGVNNRIGFFLHIPFPTPEIFNALPTYDTLLEQLCD

Y 180

****

E. *coli*

DLLGFQTENDRLAFLDCLSNLTRVTTRSAKSHTAWGKAFRTEVYPIGIEPKEIAKQAA

GP 240

I. cells

DLLGFQTENDRLAFLDCLSNLTRVTTRSAKSHTAWGKAFRTEVYPIGIEPKEIAKQAA

GP 240

****

E. *coli*

LPPKLAQLKAELKNVQNIFSVERLDYSKGLPERFLAYEALLEKYPQHHGKIRYTQIAP

TS 300

I. cells

LPPKLAQLKAELKNVQNIFSVERLDYSKGLPERFLAYEALLEKYPQHHGKIRYTQIAP

TS 300

****

E. *coli*

RGDVQAYQDIRHQLENEAGRINGKYGQLGWTPLYYLNQHFDRKLLMKIFRYSDVG

LVTPL 360

I. cells

RGDVQAYQDIRHQLENEAGRINGKYGQLGWTPLYYLNQHFDRKLLMKIFRYSDVG

LVTPL 360

****

E. *coli*

RDGMNLVAKEYVAAQDPANPGVLVLSQFAGAANELTSALIVNPYDRDEVAAALDR

ALTMS 420

I. Cells

RDGMNLVAKEYVAAQDPANPGVLVLSQFAGAANELTSALIVNPYDRDEVAAALDR

ALTMS 420

****

E.coli

LAERISRHAEMLDVIVKNDINHWQECFISDLKQIVPRSAESQQRDKVATFPKLALEHH

HH 480

I.cells

LAERISRHAEMLDVIVKNDINHWQECFISDLKQIVPRSAESQQRDKVATFPKLALEHH

HH 480

****

E. coli HH-- 482

I. cells HHAA 484

**

A 2: OtsB Codon optimisation and comparison of protein sequences

E. coli

MGSSHHHHHHGTKTEEGKLVIWINGDKGYNGLAEVGKKFEKDTGIKVTVEHPDKLE

EKFP 60

I. cells ---------- 0

E.coli

QVAATGDGPDIIFWAHDRFGGYAQSGLLAEITPDKAFQDKLYPFTWDAVRYNGKLI

AYPI 120

I.cells ---------- 0

E. COLI

AVEALSLIYNKDLLPNPPKTWEEIPALDKELKAKGKSALMFNLQEPYFTWPLIAADG

GYA 180

I.cells ---------- 0

E. coli

FKYENGKYDIKDVGVDNAGAKAGLTFLVDLIKNKHMNADTDYSIAEAAFNKGETA

MTING 240

I.cells ---------- 0

E. coli

PWAWSNIDTSKVNYGVTVLPTFKGQPSKPFVGVLSAGINAASPNKELAKEFLENYLL

TDE 300

I. cells ---------- 0

E. coli

GLEAVNKDKPLGAVALKSYEEELAKDPRIAATMENAQKGEIMPNIPQMSAFWYAVX

TAVI 360

I. cells ---------- 0

E. coli

NAASGRQTVDEALKDAQTGTDYDIPTTENLYFQGHMVTEPLTETPELSAKYAWFFD

LDGT 420

I. cells ----------MSYYHHHHHHDYDIPTTENLYFQG---
TEPLTETPELSAKYAWFFDLDGT 47

: . : ********** **********

E. coli
LAEIKPHPDQVVVPDNILQGLQLLATASDGALALISGRSMVELDALAKPYRFPLAGV
HGA 480

I. cells
LAEIKPHPDQVVVPDNILQGLQLLATASDGALALISGRSMVELDALAKPYRFPLAGV
HGA 107

****

E. coli
ERRDINGKTHIVHLPDAIARDISVQLHTVIAQYPGAELEAKGMAFALHYRQAPQHED
ALM 540

I. cells
ERRDINGKTHIVHLPDAIARDISVQLHTVIAQYPGAELEAKGMAFALHYRQAPQHED
ALM 167

****

E. coli
TLAQRITQIWPQMALQQGKCVVEIKPRGTSKGEAIAAFMQEAPFIGRTPVFLGDDLT
DES 600

I. cells

TLAQRITQIWPQMALQQGKCVVEIKPRGTSKGEAIAAFMQEAPFIGRTPVFLGDDLT

DES 227

****

E. coli

GFAVVNRLGGMSVKIGTGATQASWRLAGVPDVWSWLEMITTALQQKRENNRSDD

YESFSR 660

I. cells

GFAVVNRLGGMSVKIGTGATQASWRLAGVPDVWSWLEMITTALQQKRENNRSDD

YESFSR 287

****

E. coli SI 662

I. cells SI 289

**

A3: Gene and protein sequence of TreT *P. horikoshii*

ATGGCTAGCATGACTGGTGGACAGCAAATGGGTCGCGGATCC**ATG**AAGATGTAC

GAGGTTAAGGAATTTAGTTCGGGGAAAAGAAAGCTTGAAGACTATAAAAGCATA

ATAGGGGAGGAAGAAGTTAGCAAAATCCAGGAAAAGGCCGAGAAATTGAAAGG

AAGAAGTTTCGTCCATGTGAACTCAACTTCCTTCGGAGGAGGTGTCGCCGAGATA

CTCCACAGCTTGGTACCCCTACTGAGGAGCATTGGAATTGAAGCAAGGTGGTTCG

TAATCGAGGGGCCCACGGAATTCTTCAACGTCACGAAGACCTTTCACAACGCACT

TCAAGGTAACGAATCCCTCAAGCTAACGGAGGAGATGAAAGAACTTTACCTCAA

TGTGAACAGGGAAAATTCTAAATTCATTGACCTTTCAAGCTTTGACTACGTTCTA

GTCCACGACCCCCAGCCGGCCGCCCTTATAGAGTTCTACGAGAAGAAGAGCCCA

TGGCTCTGGAGGTGCCACATAGATCTCAGCTCACCAAACAGAGAATTCTGGGAG

TTCCTGAGGAGGTTCGTGGAGAAGTACGACAGATATATCTTCCACCTTCCTGAGT

ACGTTCAGCCTGAGTTAGATAGGAATAAGGCCGTTATAATGCCTCCATCGATAGA

TCCCCTGAGCGAAAAGAACGTTGAGCTTAAGCAGACGGAAATCCTAAGAATCCT

TGAGAGATTCGACGTTGATCCGGAGAAACCTATAATAACCCAGGTCTCAAGGTT

CGATCCATGGAAAGGGATATTCGACGTTATCGAGATTTACAGAAAGGTTAAGGA

AAAGATCCCAGGAGTTCAGCTACTCCTAGTTGGGGTCATGGCCCACGACGACCC

AGAGGGATGGATCTACTTCGAAAAGACCCTAAGGAAGATAGGAGAAGACTACG

ATGTGAAAGTCCTGACGAATTTAATAGGGGTTCACGCGAGGGAGGTTAACGCCT

TCCAAAGGGCTAGCGATGTTATATTACAAATGTCGATAAGGGAAGGGTTCGGGT

TAACAGTTACCGAGGCTATGTGGAAGGGAAAACCTGTAATTGGTAGAGCAGTTG

GCGGTATTAAGTTCCAGATAGTAGATGGGGAGACTGGATTCTTGGTAAGGGATG

CAAATGAAGCCGTTGAGAAGGTGCTCTATCTCCTTAAACATCCAGAGGTATCGA

AGGAGATGGGAGCTAAGGCCAAGGAAAGGGTGAGGAAAAACTTCATAATAACT

AAACATATGGAAAGGTACTTGGATATCTTGAACTCCCTCGG**AGGA**

MASMTGGQQMGRGSMKMYEVKEFSSGKRKLEDYKSIIGEEEVSKIQEKAEKLKGRS

FVHVNSTSFGGGVAEILHSLVPLLRSIGIEARWFVIEGPTEFFNVTKTFHNALQGNESL

KLTEEMKELYLNVNRENSKFIDLSSFDYVLVHDPQPAALIEFYEKKSPWLWRCHIDL

SSPNREFWEFLRRFVEKYDRYIFHLPEYVQPELDRNKAVIMPPSIDPLSEKNVELKQT

EILRILERFDVDPEKPIITQVSRFDPWKGIFDVIEIYRKVKEKIPGVQLLLVGVMAHDD

PEGWIYFEKTLRKIGEDYDVKVLTNLIGVHAREVNAFQRASDVILQMSIREGFGLTVT

EAMWKGKPVIGRAVGGIKFQIVDGETGFLVRDANEAVEKVLYLLKHPEVSKEMGA

KAKERVRKNFIITKHMERYLDILNSLGGLEHHHHHH-

Mw with methionine: 50642.38 Da

MW without N-terminal M= 50511.19 Da

A4: Gene and protein sequence of TreT *T. tenax*

ATGGCTAGCATGACTGGTGGACAGCAAATGGGTCGCGGATCCATGATTGAACGC

TATGTGGAATTTATCGGTGAACACGAACTGAACGCTATCTTTAAATACGCTGAAC

GCCTGCGCGACCTGAGCATCCTGCATATTAATTCAACCGCCGCCGGCGGTGGCGT

GGCAGAAATTCTGCACCGTCTGATCCCGCTGATGCGCGAACTGGGTCTGAACGTG

GAATGGAAAGTTATTCGTGGCAATGAAGAATTTTTCCGCGTTACCAAAAGTTTTC

ATAACGCACTGCAGACGGGTGCTGGCTCCATTCCGCGTGAATATTTCGAAATCTA

CGATCGCTGGCAAGAAATTAATGCGGGTGAAATCCCGCTGGATTATGACGTGGT

TTTTATTCACGATCCGCAGCCGGCCGGTCTGATCCGTTACAAACGTCGCGGCGTG

TGGATTTGGCGCTGCCATATTGATATCTCCAACCCGCACCCGGAAGTTTGGGCGT

TTCTGAAACGTTATATCTCAGCCTACGACGGCGTTATTGTCTCGATCCCGGAATT

CGCCCGCGATGACCTGGATGTGCCGCAGATTAGTATCCCGCCGTCCATTGACCCG

CTGTCACCGAAAAATGTCCCGCTGCCGCGTGCGACCGTTGATCGTATCGTGCGCA

AATATGGTGTTGACCCGGAACGCCCGATTGTTCTGCAGGTCTCGCGTTTCGATCG

CGCCAAAGACCCGGTGGGCGTTATTGAAGCGTATAAACTGGCCCGTCGCCATGT

CGATGTGCAACTGGTTTACCTGGGTAGCCCGGCATCTGATGACCCGGAAGGCGA

AGAAGTCTATCGTGAAGCTCTGCGCGCAGCTGGTGATGACAAAGATATCCATCT

GCTGATGCTGCCGCCGAACAGCCACATTGAAGTGAATGCATTTCAGCGTGCGGC

CGCAGTCGTGCTGCAGAAAAGCATTCGCGAAGGTTTCGGCCTGACCGTGTCTGA

AGCTCTGTGGAAACGTCGCCCGGTTATCGGTGGCAATACCGGTGGCATTCGTATC

CAGGTTATTCATGGTGTCACGGGCTTTCTGGTCGATTCTCCGAAAGCTGCGGCCC

ACTATATCGTGTACCTGCTGAAAAACAAACGTCTGCGTCGCGAAATGGGTGCAG

CTGGCCGCGAACACGTTCGTCGCAATTTCCTGATTACGCAACAACTGCGTCGTTA

TCTGATGACCATTCTGTATCTGACCGGCCGCCATTCCGCTCCGGGACTCGAG

CACCACCACCACCACCACTGAGATCCGGCTGCTAACAAAGCCCGAA

MASMTGGQQMGRGSMIERYVEFIGEHELNAIFKYAERLRDLSILHINSTAAGGGVAEILH

RLIPLMRELGLNVEWKVIRGNEEFFRVTKSFHNALQTGAGSIPREYFEIYDRWQEINAGEIP

LDYDVVFIHDPQPAGLIRYKRRGVWIWRCHIDISNPHPEVWAFLKRYISAYDGVIVSIPEFA

RDDLDVPQISIPPSIDPLSPKNVPLPRATVDRIVRKYGVDPERPIVLQVSRFDRAKDPVGVI

EAYKLARRHVDVQLVYLGSPASDDPEGEEVYREALRAAGDDKDIHLLMLPPNSHIEVNAFQR

AAAVVLQKSIREGFGLTVSEALWKRRPVIGGNTGGIRIQVIHGVTGFLVDSPKAAAHYIVYL

LKNKRLRREMGAAGREHVRRNFLITQQLRRYLMTILYLTGRHSAPGLEHHHHHH

Gene and protein sequence of *OtsAB* fusion

TATGATGTCTCGCCTGCTGCTGGTCTCCAATCGTCTGCCGGTCACGGTCAAAGTT

GAAAAAGATACGGTTAGCGTTGTTCGTTCTGCGGGTGGTCTGGCCACCGGTCTGC

GTCGCCCGCATGAACGCTCAGGCGGTCTGTGGATTGGCTGGCCGGGTGATGTCTC

GCGTCTGAGCGAATCTCAGCGTGCCCGTGTGGATGCACAACTGGCAGAACTGCG

TTGTGTGCCGCTGACCCTGAGTGCATCCGAAGTTAGCCGCTATTACGAAGGCTAT

TCTAACCGTGTTCTGTGGCCGCTGTGTCACTACATGCTGGAACGTATTCCGCGCC

AGGACCGTGATTGGGAAGTTTATCGCAAAGTCAATGAACGTTTTGCCGATCTGGT

GGCAAAACATTATGAACCGGGCGATACCATCTGGGTCCACGACTACCAGCTGAT

GCTGGTGCCGGGTATGCTGCGTCAACGTCTGCCGGGTGCACGTATTGGTTATTTT

CATCACATCCCGTTCCCGAGCTCTGAAATTTTCAGTACGCTGCCGCGTCGCCGTG

AACTGCTGAAAGGCCTGCTGGGTGCCGATCTGATCGGTTTTCATACCGTTAGTTA

CGTCCGCCACTTCTCCGGTGCACTGCTGCGTCATCTGGGCCTGGACACGGATATT

GACCGTATTATCTGGGAAGGCCGCGATGTGCGTGTTGGTGCGTTTCCGATGGGCA

TTGACGCCCAGGCATTCGAAAGCATCGCTTCTGAACCGGGTATGCAAGAAGAAG

TTGCGAACCTGCGCCGTAGTTCCGAGGGTCAGCGCATTCTGCTGGGCATCGATCG

TCTGGACTATACCAAAGGCATTCCGCGCCGTCTGCTGGCGGTGCAGCGTGTTCTG

GAACGTACGCCGGCATGGCGTGGTCGTCTGCGTTTTATCCAGGTCACCGTGCCGT

CACGTACGCAAGTGGAAGCTTATGCGAACTACCGCGAACTGGTGAATGAACTGG

TTGGCCGTATTAACGGCCTGTATGGTACCGTTCATAATGTTCCGGTCCACTATCTG

TACCGCTCGTTCAACGAACGTCAGCTGGTTGGCCTGTACCGCGGTGCAGATGTCA

TGCTGGTGACGCCGGTTCGTGACGGTATGAATCTGGTGGCGAAAGAATTTTGTGC

CGCACGTCCGGATGATGATGGTGTGCTGGTTCTGAGCGAATTTGCGGGTGCAGCT

GCCGAACTGGGCGGTGCACTGATTGTCAATCCGTACGATGTGGACGCCATGGCA

GATGCTATCGAAAAAGCTCTGGGCATGGCGGAAGAAGAACGCCGTACCCGCATG

CATACGCTGCGTAAACAGGTTAAATCTCGTGATGTCCACTGGTGGACCTCATCGT

TTCTGGATCGCCTGCAAAGTCTGCCGGCAGTTGATGTGCGTGCCGAAGCATCCGC

ACCGGAAGCTCTGGCCCAGATGAAACAAGTTGAACGCCTGCAGCTGCTGCTGGA

TTATGATGGTACCCTGGTGGGTTATGCGCCGCGTCCGGAACTGGCGGCACCGGAT

GCTGCCCTGAAAGAACTGCTGGCCAAACTGGTGGCACGCCCGGGTATTTCAGTCT

CGATCGTGAGTGGCCGTCCGAAAGAAACGCTGGAAGAATGGCTGGGTGATCTGG

CTATGGGCCTGTATGCGGAACATGGTCTGTGGTCCCGCCCGGCTCCGGGTGAAGC

CTGGCGTATGCTGGAAGGTGTTACCTTTGATTGGAAAGAACGTGTCCGCCCGGAA

CTGGAAACGTTTTCAGCCCGCGTGCCGGGCTCGTTCGTTGAAGAAAAAACCGCTA

GCCTGGCGTGGCACTATCGTCTGGTTGATGCCGAATTTGGTGCAATTCAGAGCCG
CGAACTGCGTCTGTACCTGGCTGAAAAATTCGCGGGCCAATCTATGGATATTCTG
CCGGGTGACAAAGTGGTTGAAATCCGTCCGCGCGGCGTGCATAAAGGTCGCGTC
GTGGGCGAAGCGACCAAAGATGCCGCACCGGGTGCCCTGGTTGTCGCAATCGGC
GACGATCGTACGGATGAAGACCTGTTTGCTAGCATTCCGCCGGGCGGTCTGACCA
TCCATGCCGGTAACAAACCGACGCGCGCTGCGTTTCGTGTGAATGGCCCGGATG
AAGTGCGTGCTCTGCTGGCTGGTCTGCTGGAACCGTAAT

MNHKVHHHHHHIEGRHMMSRLLLVSNRLPVTVKVEKDTVSVVRSAGGLATGLRRP
HERSGGLWIGWPGDVSRLSESQRARVDAQLAELRCVPLTLSASEVSRYYEGYSNRV
LWPLCHYMLERIPRQDRDWEVYRKVNERFADLVAKHYEPGDTIWVHDYQLMLVPG
MLRQRLPGARIGYFHHIPFPSSEIFSTLPRRRELLKGLLGADLIGFHTVSYVRHFSGAL
LRHLGLDTDIDRIIWEGRDVRVGAFPMGIDAQAFESIASEPGMQEEVANLRRSSEGQR
ILLGIDRLDYTKGIPRRLLAVQRVLERTPAWRGRLRFIQVTVPSRTQVEAYANYRELV
NELVGRINGLYGTVHNVPVHYLYRSFNERQLVGLYRGADVMLVTPVRDGMNLVAK
EFCAARPDDDGVLVLSEFAGAAAELGGALIVNPYDVDAMADAIEKALGMAEEERRT
RMHTLRKQVKSRDVHWWTSSFLDRLQSLPAVDVRAEASAPEALAQMKQVERLQLL
LDYDGTLVGYAPRPELAAPDAALKELLAKLVARPGISVSIVSGRPKETLEEWLGDLA
MGLYAEHGLWSRPAPGEAWRMLEGVTFDWKERVRPELETFSARVPGSFVEEKTASL
AWHYRLVDAEFGAIQSRELRLYLAEKFAGQSMDILPGDKVVEIRPRGVHKGRVVGE
ATKDAAPGALVVAIGDDRTDEDLFASIPPGGLTIHAGNKPTRAAFRVNGPDEVRALL
AGLLEP-

MW= 82937 Da without N-terminus Met cleavge

A5: Gene and protein sequence of *OtsA* from insect cells

GGATCCATGAGCCGCCTGGTCGTGGTGTCCAACCGCATCGCTCCCCCTGACGAAC

ATGCCGCTAGCGCTGGTGGTCTCGCTGTCGGTATCCTCGGCGCTCTGAAGGCTGC

CGGTGGTCTGTGGTTCGGTTGGAGCGGCGAAACCGGCAACGAGGATCAGCCCCT

GAAGAAGGTGAAGAAGGGCAACATTACCTGGGCCTCCTTCAACCTCAGCGAACA

GGACCTGGACGAGTACTACAATCAGTTCTCCAACGCTGTGCTGTGGCCCGCTTTC

CATTACCGTCTGGACCTGGTGCAATTCCAACGTCCTGCTTGGGACGGTTACCTCC

GCGTGAACGCTCTCCTGGCCGACAAGCTGCTCCCCCTCCTGCAGGACGACGACAT

TATCTGGATACACGATTATCACCTGCTCCCCTTCGCTCACGAGCTGCGTAAACGC

GGCGTGAACAACCGCATTGGCTTCTTCCTGCACATCCCCTTCCCTACTCCCGAGA

TTTTCAACGCCCTGCCCACCTACGACACTCTGCTGGAACAGCTCTGTGATTACGA

CCTGCTCGGTTTCCAGACCGAAAACGACCGCCTGGCTTTCCTCGACTGCCTGAGC

AACCTGACTCGTGTCACTACCCGCTCCGCCAAGTCCCATACCGCTTGGGGTAAAG

CTTTCCGCACCGAGGTCTACCCTATCGGCATCGAACCTAAGGAGATCGCCAAGCA

AGCCGCTGGTCCTCTGCCTCCCAAACTGGCCCAGCTGAAGGCCGAGCTCAAGAA

CGTCCAGAACATCTTCTCCGTGGAGCGTCTGGACTACAGCAAGGGCCTGCCCGA

ACGCTTCCTGGCCTACGAGGCTCTCCTCGAGAAGTACCCCCAACACCACGGCAA

GATCCGCTACACCCAAATCGCCCCTACCTCCCGTGGCGATGTGCAGGCTTACCAG

GACATCCGCCACCAGCTGGAGAACGAAGCCGGTCGCATCAACGGCAAATACGGC

CAGCTCGGTTGGACCCCCCTGTATTATCTGAACCAGCACTTCGACCGCAAGCTGC

TGATGAAGATCTTCCGCTACAGCGATGTGGGCCTGGTGACTCCCCTCCGCGATGG

CATGAACCTGGTCGCTAAGGAATACGTGGCTGCCCAAGACCCCGCTAATCCCGG

TGTGCTGGTGCTGTCCCAGTTCGCTGGTGCCGCTAACGAACTGACCAGCGCCCTG

ATCGTGAATCCCTACGATCGCGACGAAGTGGCCGCCGCTCTGGACCGTGCTCTCA

CTATGAGCCTGGCTGAACGTATCTCCCGCCATGCCGAGATGCTGGACGTCATCGT

GAAGAACGACATCAACCACTGGCAAGAATGCTTCATCTCCGACCTCAAACAAAT

CGTGCCTCGTAGCGCTGAGAGCCAGCAGCGCGACAAGGTGGCCACCTTCCCTAA

GCTGGCCCTGGAGCACCATCACCACCACCACGCGGCCGC

M S R L V V V S N R I A P P D E H A A S A G G L A V G I L G A L K A A G G L W F G

W S G E T G N E D Q P L K K V K K G N I T W A S F N L S E Q D L D E Y Y N Q F S N

A V L W P A F H Y R L D L V Q F Q R P A W D G Y L R V N A L L A D K L L P L L Q

D D D I I W I H D Y H L L P F A H E L R K R G V N N R I G F F L H I P F P T P E I F N

A L P T Y D T L L E Q L C D Y D L L G F Q T E N D R L A F L D C L S N L T R V T T R

S A K S H T A W G K A F R T E V Y P I G I E P K E I A K Q A A G P L P P K L A Q L K

A E L K N V Q N I F S V E R L D Y S K G L P E R F L A Y E A L L E K Y P Q H H G K I

R Y T Q I A P T S R G D V Q A Y Q D I R H Q L E N E A G R I N G K Y G Q L G W T P

L Y Y L N Q H F D R K L L M K I F R Y S D V G L V T P L R D G M N L V A K E Y V A

A Q D P A N P G V L V L S Q F A G A A N E L T S A L I V N P Y D R D E V A A A L D

R A L T M S L A E R I S R H A E M L D V I V K N D I N H W Q E C F I S D L K Q I V P

R S A E S Q Q R D K V A T F P K L A L E H H H H H H A A A F E S R A C S L E A C G

T K L V E K Y Stop

Calculated Mass= 57005

A6: Gene and protein sequence of *OtsB* from insect cells

ATGAGCTACTACCACCACCACCACCACCACGATTACGACATCCCCACCACAGAA

AACCTCTACTTCCAGGGCACAGAACCATTGACAGAGACACCGGAACTGAGCGCT

AAGTACGCCTGGTTCTTCGACCTCGATGGAACCTTGGCTGAGATCAAGCCCCACC

CTGACCAGGTGGTCGTTCCCGATAACATCCTCCAGGGTTTGCAACTGCTCGCTAC

CGCCTCCGACGGAGCTTTGGCCCTGATCTCCGGTAGGTCTATGGTCGAGCTGGAT

GCTCTCGCCAAGCCATACAGATTCCCACTGGCTGGAGTTCACGGAGCTGAACGTC

GCGACATCAACGGCAAGACTCACATCGTGCACCTGCCCGACGCTATCGCCAGGG

ATATCTCCGTGCAACTCCACACAGTCATCGCTCAGTACCCTGGCGCTGAGCTCGA

AGCCAAGGGAATGGCTTTCGCCTTGCACTACCGTCAGGCCCCACAACACGAGGA

CGCTTTGATGACTCTGGCCCAGCGCATCACACAAATCTGGCCACAGATGGCTCTG

CAGCAGGGCAAGTGCGTGGTCGAAATCAAGCCGCGTGGTACTTCCAAGGGCGAG

GCTATCGCTGCCTTCATGCAAGAAGCCCCCTTCATCGGTCGCACCCCTGTCTTCCT

GGGCGACGATCTCACTGACGAGTCTGGCTTCGCCGTTGTGAACAGGTTGGGTGGC

ATGAGCGTGAAGATCGGAACAGGTGCTACCCAGGCCTCATGGAGACTCGCTGGA

GTCCCTGATGTTTGGTCGTGGTTGGAAATGATCACCACTGCCCTGCAACAGAAGA

GAGAGAACAACAGAAGCGACGATTACGAGTCATTCAGCAGAAGCATCTAA

M S Y Y H H H H H H D Y D I P T T E N L Y F Q G T E P L T E T P E L S A K Y A W F

F D L D G T L A E I K P H P D Q V V V P D N I L Q G L Q L L A T A S D G A L A L I S

G R S M V E L D A L A K P Y R F P L A G V H G A E R R D I N G K T H I V H L P D A I

A R D I S V Q L H T V I A Q Y P G A E L E A K G M A F A L H Y R Q A P Q H E D A L

M T L A Q R I T Q I W P Q M A L Q Q G K C V V E I K P R G T S K G E A I A A F M Q

E A P F I G R T P V F L G D D L T D E S G F A V V N R L G G M S V K I G T G A T Q A

S W R L A G V P D V W S W L E M I T T A L Q Q K R E N N R S D D Y E S F S R S I

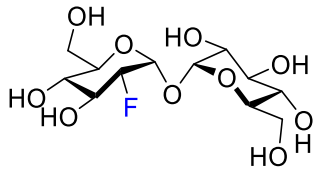
Calculated Mass= 32069.3

3 Chapter 3: Pre-clinical Studies Using [^{19}/^{18}F]FDT

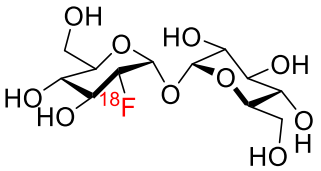
3.1 Introduction

Imaging modalities are being used increasingly to understand the molecular basis of disease from its early onset and to guide the design and development of new therapies[1,2]. New radiotracer development has to go through a similar regulatory approval path to an investigational drug. However, the need for only a trace amount of probe to conjugate with a radionuclide can allow for a reduced safety assessment for regulatory approval. Pre-clinical imaging, when used effectively can provide unique information on numerous biological processes during health and disease. Research in pre-clinical imaging allows for the identification, development and validation of biomarkers[3]. These biomarkers can be used to identify and stage the disease or predict the clinical outcome[4]. In addition, pre-clinical imaging can provide information on the safety and efficacy of the drug, its pharmacokinetics behaviour and an appropriate dose regimen of the new drug[4].

The aim of this chapter was to conduct pre-clinical studies using 'cold' and 'hot' FDT (**Scheme 4.1**) to fulfil the requirements of an investigational new drug (IND) application to the FDA. As per the FDA guidelines, an IND should contain pharmacology and toxicology information to ensure the product is safe for clinical trials[5]. It should also include biodistribution data, which could allow reasonable calculation of radiation absorbed dose to the whole body and critical organs[5, 6]. In addition, the application should have details of chemical synthesis, manufacturing, and quality control of the potential radiotracer and the route of administration to the patient[5, 7]. For safety assessment purposes, the FDA has divided radioactive diagnostic agents into two groups i.e. group I medical imaging agents and group II medical imaging agents and the results from pre-clinical studies are the basis for this classification[8]. The information obtained provides a solid platform for the smooth transition of the potential radiotracer into phase 0 or I clinical trials, although there are generally high attrition rates.



FDT ('cold')



[^{18}F] FDT ('hot')

Scheme 4.1. Schematic of 'cold' and 'hot' FDT

Due to stringent regulatory and legal requirements, as well as ever increasing public perception on the use of animals for pre-clinical studies, the choice of a suitable model for TB becomes even harder. The complexity of the TB disease poses a significant challenge to find an animal model that can accurately predict the human disease. Different animal models including various mouse strains, guinea pigs, rabbits, non-human primates and zebrafish have been used in the past to evaluate new therapies and vaccines[9]. Mice are the preferred animals as they are easy to maintain and cost effective[10, 11]. However, mice are not the natural hosts of *M. tuberculosis* and they have many important differences from human metabolism, limiting the use of this model in our understanding of TB pathogenesis[12]. Due to a lack of guidance from an appropriate animal model, several expensive clinical trials may have failed[13]. Recently, marmosets have been used as a successful model, which when infected with TB more closely replicates human disease and treatment outcomes[14].

One of the unique features of the mycobacteria is their incorporation of trehalose into TMM and TDM in their outer membrane structures through the transesterification reaction of Ag85 enzymes. Previous work in the Davis and Barry groups[15] have revealed that the Ag85 enzymes will tolerate a wide variety of modifications to the trehalose scaffold. Through extensive *in vitro* and *in vivo* work Backus *et al.*[15] demonstrated that trehalose analogues, including FITC-tre, were readily taken up by mycobacteria i*n vitro* and into the macrophages. A trehalose derivative incorporating ^{18}F would be extremely useful as a potential PET imaging probe for

TB by showing the integrity of the cell wall, and thus vitality of the bacteria. Subsequently, it may allow probing of the development and propagation of pathogens at each corresponding pathogenic stage and also the efficacy of therapeutics by monitoring the status of bacteria while under treatment. Since [^{18}F]FDG has been supplied as a source of ^{18}F and used as a PET probe, [^{18}F]FDT can be an excellent candidate for a PET tracer due to its absence in human metabolism.

The aim of this work was to establish and execute the necessary pre-clinical imaging protocols which would fulfil the IND application requirements for [^{18}F]FDT as a potential new radiotracer for TB imaging. In order to achieve this, the plan was to determine the safety and efficacy of the 'cold' FDT in animal models, as per FDA guidelines. In addition, using radiolabelled FDT, we studied the biodistribution of tracer to determine the radiation dose to critical organs, to allow estimation of the human exposure. Furthermore, we monitored the response to treatment with the four-drug standard regimen to determine if the FDT uptake would be reduced with treatment. Finally, we compared the uptake of FDT to FDG uptake in the animal model.

3.2 Results and Discussions

3.2.1 LC-MS Method Development for [^{19}F]FDT Detection

We set out to develop a liquid chromatography (LC) mass spectrometry (MS) based method, which would allow detection and quantification of the target analyte at lower concentrations. The instrument used for this analysis is Micromass Quattro Micro™ coupled with Acquity ™ ultra-performance WATERS LC system. Quattro micro atmospheric pressure ionization (API) is a high performance triple quadrupole mass spectrometer designed for routine LC-M/MS operation.

The MS method used during this analysis was based on SIR (selected ion recording)[16]. The SIR technique is typically used in situations where only a few specific masses are to be monitored. Since most of the data acquisition time is spent on these masses, the technique is far more sensitive than full range scanning. The SIR editor is used to enter the masses to be monitored, along with their dwell times, spans and Inter-Channel Delay times. A span of zero can be set to simply 'sit on' the specified mass. Up to 32 masses can be monitored using this method[17].

The ultimate goal was to develop a LC-MS method that could provide us with rapid detection, quantification of the [^{19}F]FDT both *in vitro* and *in vivo* and easy translation to contract research organisation for the toxicity studies. For the quantification and detection of the sugar molecule we used TSKgel® Amide-80 HPLC Column, initially with Method 1 as described in Table 3.1. By using this method we were able to detect and/or even separate sugars with similar properties such as trehalose and FDT (**Figure 3.1**), however, the method was limited in that the flow rate of 0.8 mL/min was not compatible with the Quattro LC-MS instrument.

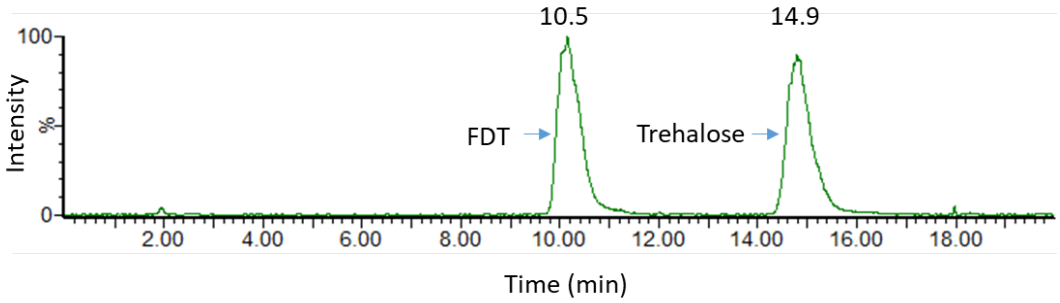


Figure 3.1. Separation of FDT and trehalose by LC-MS method 1. FDT rt is 10.5 min whereas trehalose rt is 14.9 min.

The need to divert almost half of the flow to waste meant that the accuracy of the method was in doubt. Therefore, we used the smaller column as described in Method 2. With flow rate of

0.3 mL/min, FDT rt was 8.7 min (**method 2, Figure 3.2A**)., with increasing flow rate from 0.3 mL/min to 0.4 mL/min resulted in further couple of min reduction in the FDT detection (**method 3, Figure 3.2B**). It was possible to further reduce the FDT rt by increasing the temperature to 60 °C (**method 4**). We used both method 3 and method 4 for the *in vitro* and *in vivo* samples analysis.

Table 3.1: LC-MS methods employed in the detection of FDT

Method no.	Mobile phase	Flow rate (mL/min)	Run time (min)	Temperature (°C)	FDT rt (min)
1	30/70 H_2O/MeCN	0.8	20	25	10.5
2	35/65 H_2O/MeCN	0.3	12	25	8.7
3	35/65 H_2O/MeCN	0.4	12	25	6.5
4	35/65 H_2O/MeCN	0.4	12	60	6.1

With slight modifications in the mobile phase composition, flow rate and reducing the column length, we managed to detect the [^{19}F]FDT at ~ 8.7 min (**Figure 3.2A**) or at~ 6.5 min (**Figure 3.2B)**. Increase in temperature allowed us to detect the [^{19}F]FDT even at ~ 6.1 min (**Method 4**).

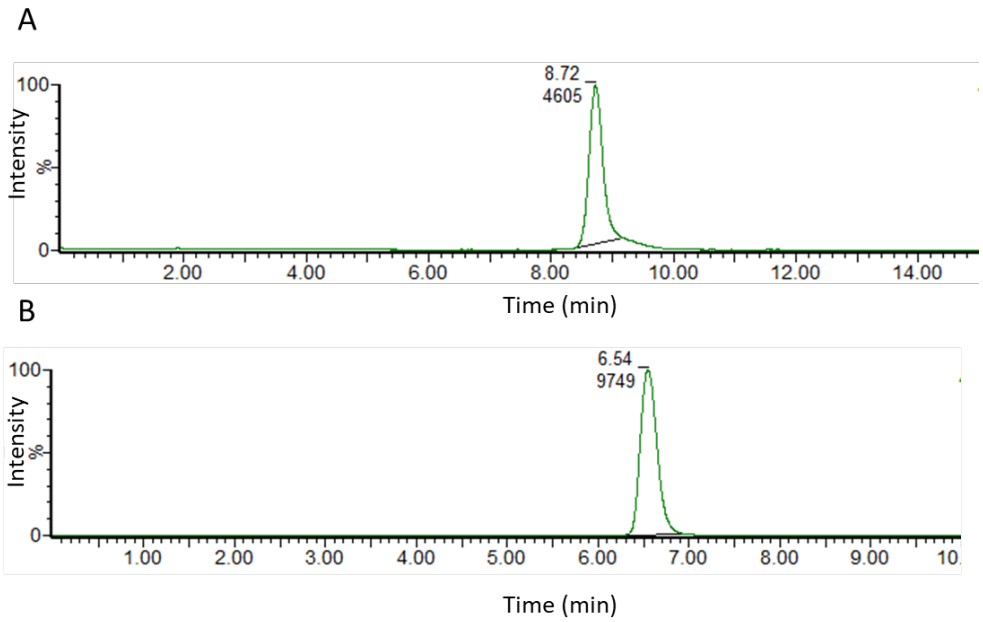


Figure 3.2. LC-MS method development for the rapid detection of FDT. A). Detection of [^{19}F]FDT with using method 2. B). Detection of [^{19}F]FDT using method 3 as specified in **Table 3.1**.

3.2.2 Sample Preparation

Plasma samples and serum contain blood proteins and other macromolecules such as phospholipids[18, 19]. The matrix effect in biological samples has been shown to be a source of variability and inaccuracy in LC-MS samples analysis[20]. Co-elution of endogenous phospholipids with the analyte can cause matrix effect ion-suppression or enhancement that can dramatically impact quantitative LC-MS analysis[21]. Various sample pre-treatment approaches have been employed to get rid of macromolecules prior to final analysis, to minimise their impact[22]. These techniques for example, include protein precipitation method (PPT)[23], solid phase extraction (SPE) method[24] and hybrid SPE[25] method. During our analysis, the PPT method has been preferred due to the fact that it is easy to use and sufficiently precipitates out the macromolecules from the plasma samples. We used a mixture of organic solvents and water to precipitate out plasma proteins during our sample preparation (see methods).

3.2.3 *In vitro* and *In vivo* detection of [^{19}F]FDT

For *in vitro* detection of [^{19}F]FDT in plasma, we spiked the plasma with known concentrations of [^{19}F]FDT, 10 µM, 20 µM, 40 µM, 120 µM, 160 µM and 300 µM, and after work up, analysed by LC-MS method 2 (**Figure 3.3A**). The instrument gave a linear response over the concentration range tested, indicating no degradation of the compound in the plasma solution (**Figure 3.3D**).

To further determine the instrument range and to detect [^{19}F]FDT in plasma, we tested another set of samples with concentrations ranging from 390 nM to 100 µM. Again the linear response from the instrument indicated that the instrument was sensitive enough to detect the compound in plasma to low hundreds nM range.

By using this method we were able to detect and quantify the amount of [^{19}F]FDT in the plasma solution and there was no degradation of the product observed *in vitro*.

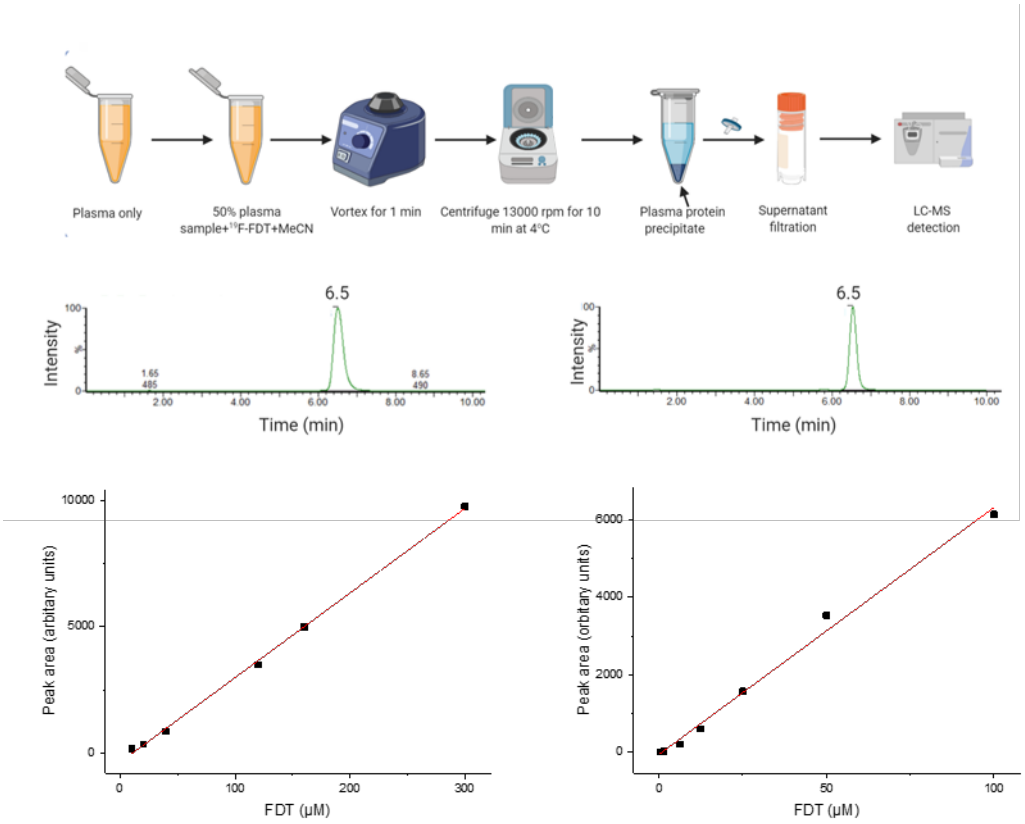


Figure 3.3. *In vitro* detection of [^{19}F] FDT by LC-MS. A) Experimental set-up of the sample preparation. Commercially available plasma samples were spiked with known concentrations of [^{19}F]

FDT, plasma proteins were then precipitated by adding up to 50% of MeCN solution and after centrifugation the samples were analysed by LC-MS. **B**) [^{19}F]FDT standard sample analysed by LC-MS method 2 with the retention time of 6.5 min. **C**) LC-MS analysis of plasma sample spiked with known amount of FDT showing the similar retention time to that of the standard sample. **D**) Calibration curve of plasma samples when spiked with FDT concentrations from 10 μM – 300 μM with $r^2 = 0.998$ and **E**) Further calibration curve showing the instrument sensitivity of up to 390 nM to accurately detect FDT with $r^2 = 0.998$.

Next we envisioned to assess the *in vivo* stability of FDT. We injected 2 different concentrations of [^{19}F]FDT solution, 50 μM and 500 μM, into the mice through tail vein injection. After 5 minutes, 700 μL of blood was drawn and plasma was separated from red cell mass by centrifugation. We analysed the [^{19}F]FDT remaining in the plasma after the work-up. As shown in **Fig. 3.4**, from the 500 μM injection sample, we were able to detect that a significant amount of [^{19}F]FDT remained in the plasma both by LC-MS and ^{19}F-NMR spectroscopy. However, samples from the mice injected with 50 μM [^{19}F]FDT, we could not detect any compound in the plasma. In essence, from this experiment it was possible to demonstrate that the compound did not break down *in vitro* and or *in vivo* within *5* minutes.

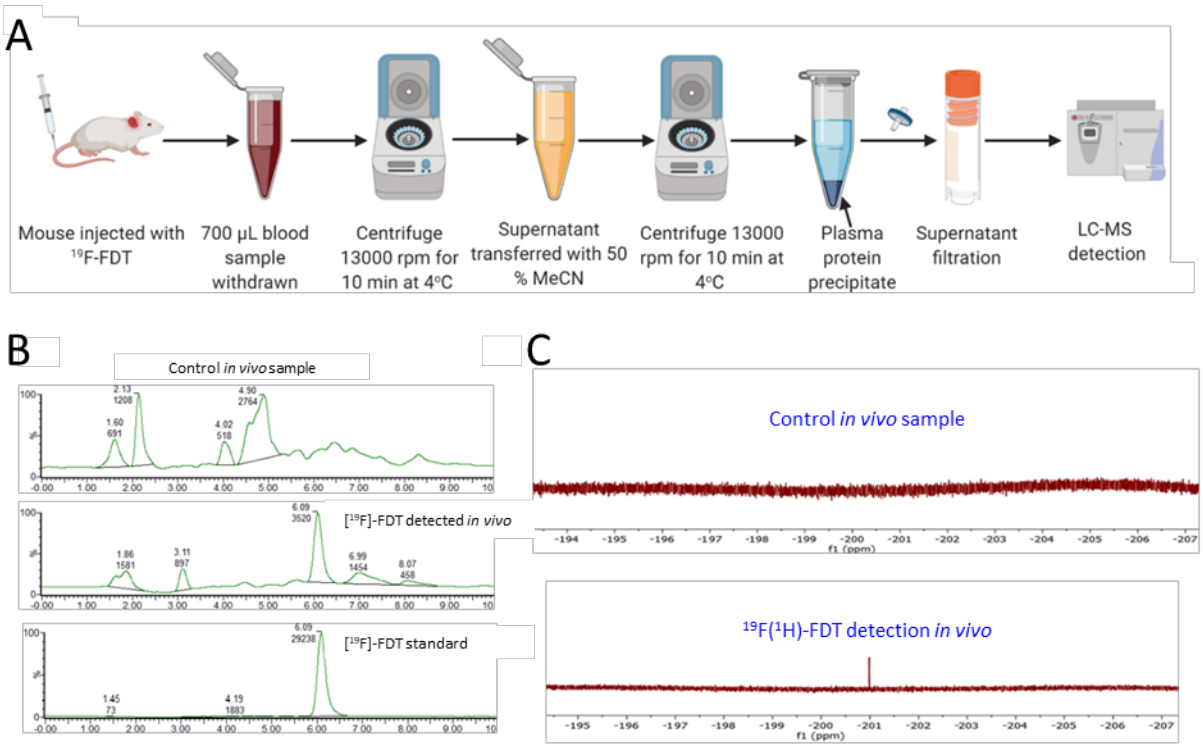


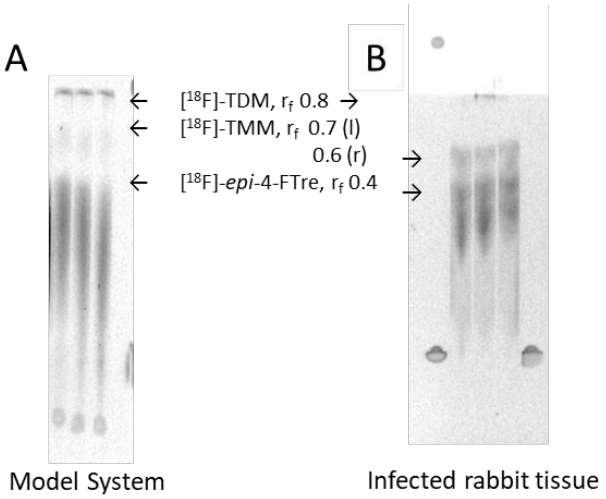
Figure 3.4. *In vivo* detection of [^{19}F]FDT by LC-MS. A) Experimental set-up for the *in vivo* detection; **B**). From top to bottom; control *in vivo* plasma sample; middle [^{19}F]FDT detection in plasma *sample in vivo* when 500 µM of the [^{19}F]FDT solution was injected in mouse and sample taken 5 min post injection; [^{19}F]FDT standard sample; **C**). From top to bottom, control *in vivo* sample and bottom [^{19}F] FDT detection *in vivo* by ^{19}F-NMR spectroscopy.

The upcoming imaging experiments were carried out by the members of our collaborator Dr Clifton Barry III lab at NIH, Bathesda. [^{19}F]FDT and enzymes expressed provided by me.

3.2.4 *In vivo* labelling of TMM in *M. tuberculosis* infected tissue

Although the Davis and Barry groups had previously shown that fluorescently labelled trehalose could be incorporated into the cell surface of *M. tuberculosis* in cultured macrophages[15], we wished to determine if the FDT incorporation was detectable *in vivo* within complex tubercular lesions within the practical imaging time allowed by ^{18}F radionuclide. To determine if it was likely to detect active incorporation of FDT in tissue, *ex vivo* mouse lung tissue was mixed with 10^6 *M. tuberculosis* bacteria/mL of lung homogenate and FDT was

added to the mixture and incubated at 37 °C for 60 min The tissue was extracted with chloroform to separate and concentrate the mycobacteria lipids before separating them by TLC and detecting by phosphor imaging. [^{18}F]FDT dimycolate (TDM) and trehalose monomycolate (TMM) were observed based on the R_f shift in radio-TLC and comparison with authentic standards of TDM and TMM (**Figure 3.5A**). Since this was successful, 8 mCi of 4-FDT was administered to a New Zealand white (NZW) rabbit 90 minutes prior to euthanasia and necropsy. Caseum from a large tubercular cavity was excised from the lung and homogenized in phosphate buffered saline. The lipids from the homogenate were extracted with chloroform and the extract was rapidly evaporated and applied to a TLC plate along with reference standards. As **Figure 3.5B** indicates, trehalose mono-mycolate was identified in the extract by phosphor imaging, indicating that exogenous FDT could be incorporated into mycobacterial lipids in tubercular lesions within a practical imaging timeframe for ^{18}F labelled probe.



C

Time (min)	% FDG	% 2-FTD
50	1.5	98.5
115	5.4	94.6
urine (120)	4.2	95.8

Figure 3.5. A) Radiolabeled FDT was incorporated in TDM and TMM *ex vivo* mouse lung spiked with *M. tuberculosis* after 60 minute incubation. **B**) Radiolabeled FDT was incorporated *in vivo* into TDM and TMM. Lipids were extracted from cavity caseum collected from a *M. tuberculosis* infected rabbit 90 min after IV injection of the probe. The lipid extract was separated by radio-TLC and the radioactivity detected by autoradiography. **C**) Table

illustrating that fluorine substitution at -2 position of the trehalose does not metabolise over time.

3.2.5 Characterization of FDT uptake timing, reproducibility, and association with bacterial numbers

A useful PET probe for diagnosing tuberculosis should have minimal signal in the absence of *M. tuberculosis* infection, particularly in the lung, where the majority of infections occur. FDT had a low background signal in the lung compared the *M. tuberculosis* infected marmoset **(Figure 3.6 A, B, C).** In order to block [^{18}F]FDT PET uptake, trehalose or [^{19}F]FDT was administered 1 h and 5 min prior to the FDT radiotracer dose. This strategy visually reduced uptake of the tracer into lesions **(Figure 3.6 D and E)** by an average of 40% **(Figure 3.6 F).** As ^{18}F has a short half-live (110 mins) it is preferred for PET imaging as the exposure to the patient and their caregivers is limited, but this property also limits the time for the molecular signal to accumulate at the site of infection. To determine if FDT accumulates in the lesions over time, we administered FDT and then imaged the animal at 30-minute intervals from60 minutes to 120 minutes, keeping the marmoset sedated and on the PET/CT scanner throughout the procedure. The FDT signal in lesions increased from 60 to 90 minutes **(Figure 3.6 G)** but there was no advantage observed in the 120 min scan signal. We also tested the reproducibility of the FDT uptake by assessing the SUV of lesions in animals scanned 48 hours apart. The SUV of lesions was found to be very similar from day to day within the short time frame **(Figure 3.6 H).** Finally, we wanted to ascertain if the FDT uptake of the individual lesions was correlated with the number of bacteria culturable from each lesion. To test this, we administered FDT to marmosets on the day prior to their scheduled necropsy and collected a PET/CT scan 90 min post injection. The resulting total SUV per lesion and the bacterial load

of the lesion were well correlated supporting the hypothesis that FDT uptake would be higher in lesions with higher Log CFU **(Figure 3.6I).**

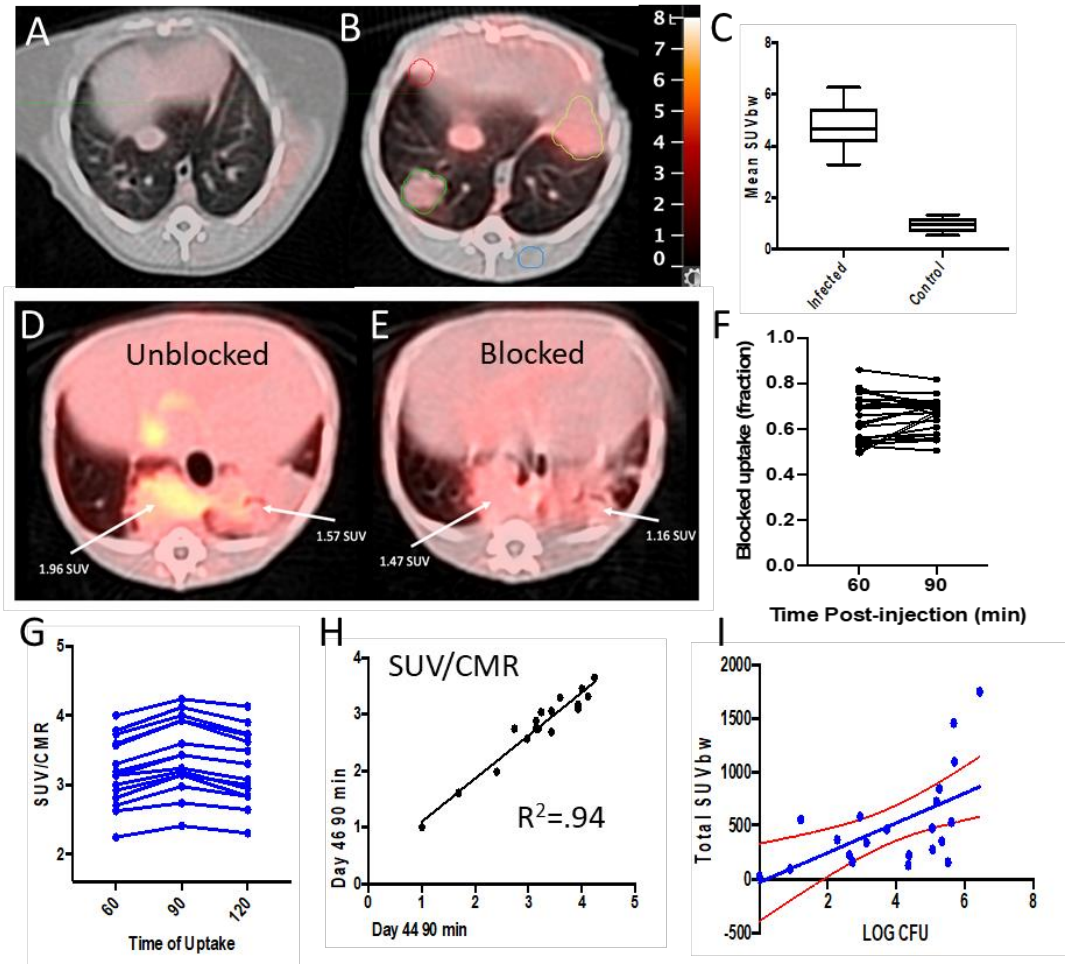


Figure 3.6. Pulmonary FDT PET uptake into tuberculous lung lesions is reproducible within 90 min with increasing signal in lesions with higher bacterial loads. A) Transverse view of FDT PET/CT of a naïve marmoset lung. **B**) Transverse view of FDT PET/CT of a M. TUBERCULOSIS -infected marmoset lung showing lesions outlined in green and red and the iliocostalis muscle used for normalization of PET uptake in blue. **C**) The FDT PET signal from M. TUBERCULOSIS -infected marmoset lungs is significantly higher that the signal from uninfected (control) marmoset lungs. The mean Standard uptake values (SUVbw) are represented as boxplots where the central bars represent the median. At least 4 lung regions of interest (ROI) were measured from 3 infected and 2 uninfected marmosets ($p<0.0001$). (**D and E**) Transverse image of FDT PET uptake (unblocked) and blocked uptake in the same infected marmoset. FDT uptake was blocked by administering 500x the dose of the

'cold' FDT split into two administrations 1h and 5 min prior to probe administration. **F**) Comparison of lesions uptake in marmosets randomized to receive [^{19}F]FDT prior to being administered FDT or to receive FDT alone. Two days later the same animals were imaged with the treatments reversed. Uptake was measure in images collected 60 min and 90 min after probe administration. Lesions in animals receiving the [^{19}F]FDT blocking dose showed significantly lower accumulation of the FDT into tubercular lesions. **G**) FDT lesion uptake (SUV/CMR) at 60, 90, and 120 mins post injection (lesions from two antibiotic treatment naïve marmosets) demonstrates that signal does not increase after 90 minutes. **H**) FDT uptake (SUV/CMR) is reproducible as illustrated when the marmosets are imaged two days apart and individual lesion SUV values are compared. **I**) FDT signals in tubercular lesion tends to increase with higher bacterial loads (p=0.003). The total SUV of each lesion was compared with the bacterial LOG colony forming units measured (Log CFU) in the lesions upon subsequent sacrifice.

3.2.6 FDT uptake in M. tuberculosis-infected marmosets and cynomolgus macaques

Unlike rabbits, no sign of metabolism was observed in marmosets; FDT maintained >95% radiochemical purity in both the blood and urine of the animals (**Figure 3.5C**). FDG labels mostly immune cells that are highly active and FDT labelling is correlated with the bacterial load of the lesions, we hypothesized that the two probes would have different labelling patterns when FDG and FDT scans were collected sequentially in M. *tuberculosis*-infected marmosets. A representative image from one of 3 sequentially scanned marmosets is presented in **Figure 3.7**. The marmoset images clearly show differential labelling of lesions. In order to analyze the different patterns of distribution, it rapidly became clear that independently analyzing regions of interest (ROI) would not allow quantitation of the different labelling patterns, as the FDG and FDT hot areas were both located within a single ROI. Using total "glycolytic" activity measurements for the entire lung also did not allow quantitation of the difference in labelling. The **Figure 3.7C** highlights the differences in the FDT and the FDG scans. This serves to show

that areas of high FDT uptake exhibit lower than average FDG uptake, and vice versa. FDG is correlated to inflammation, and FDT uptake has been shown to correlate to *M. tuberculosis* cell wall synthesis.

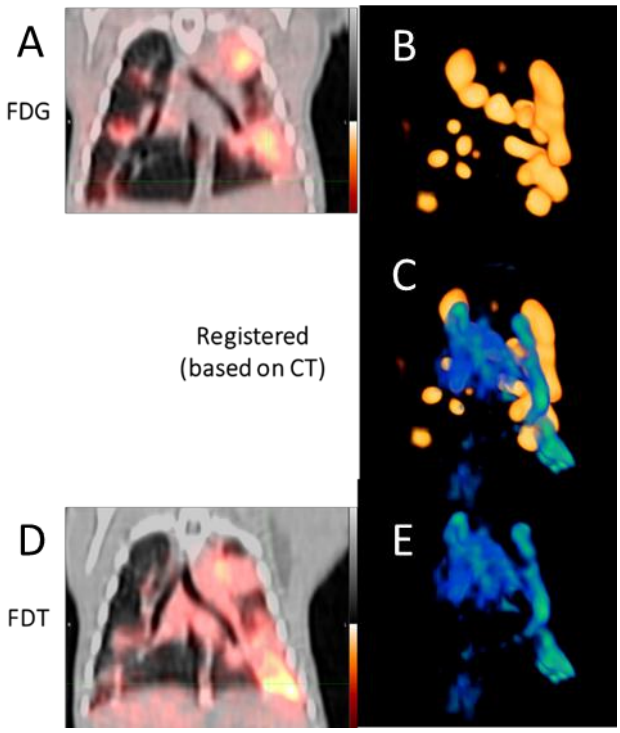


Figure 3.7 The uptake of FDG and FDT *in M. tuberculosis* infected tissues shows differences in regions of intense radioactive signal indicating the two probes are pooling in tissue regions with different characteristics. A and B) Serial FDG and **D and E**) FDT scans of the same infected marmoset were co-registered based on CT represented in **A** and **D**. The FDG signal coloured gold **B**) was then overlaid with the FDT signal **E**) coloured blue to green to indicate the differences in the regions of intense labeling.

Another challenge for the FDT probe was whether it could accurately report on treatment effect. One marmoset was treated for 5 weeks (five days per week) with first-line HRZE therapy[26] and serial FDG images (**Figure 3.8A and B)** and FDT PET images **(Figure 3.8E and F)** showed a significant reduction in SUV signal and a lower total FDT uptake **(Figure 3.8G**

and H); where the FDG showed a mixed response from in lesions FDG SUV and TLG **(Figure 3.8C and D).**

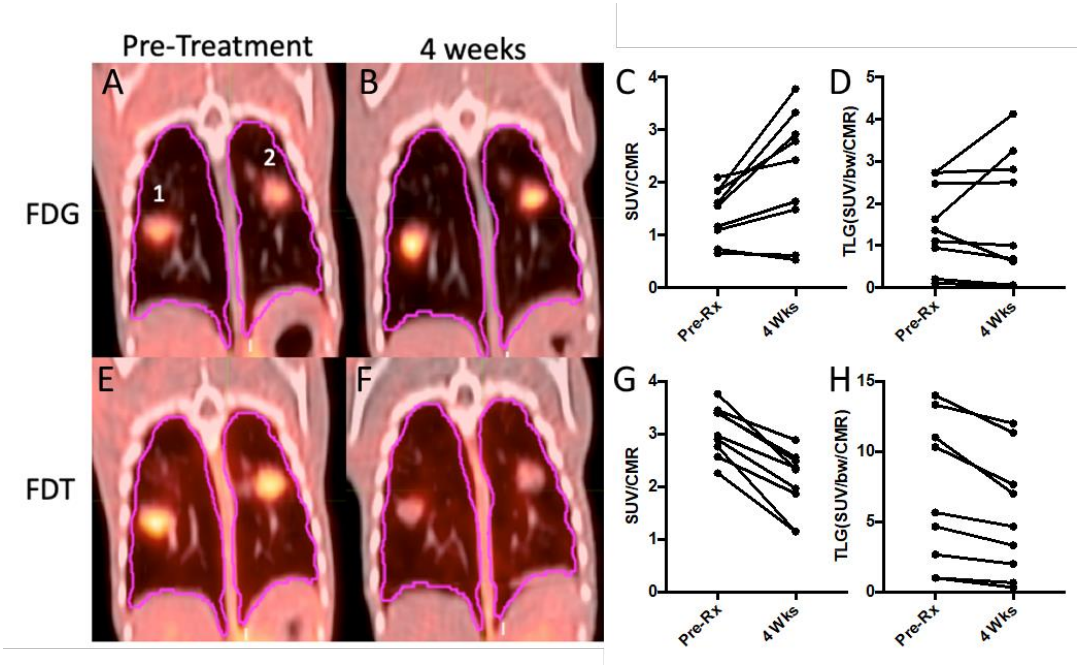


Figure 3.8 FDG and FDT scans of a *M. tuberculosis*-infected marmoset treated with HRZE for 4 weeks prior to necropsy. A) Pretreatment scan with FDG PET with two lesions indicated as 1 and 2. **B**) Marmoset imaged with FDG after 4 weeks of treatment showing same 2 lesions. **C**) The FDG SUV before and after treatment of the lung lesions was variable and often increased. **D**) The total probe uptake or TLG of the lesions showed a lesion dependent pattern. (**E and F**) Similarly timed FDT scans showed reduced SUV and total FDT uptake in the lesions after 4 weeks of treatment. Lesion 1 had 2.6 Log CFU and lesion 2 had 2.8 Log CFU when the bacterial load was determined indicating low bacterial burden in the lesions. **G**) After quadruple drug therapy, the FDT SUV of the lung lesions was significantly decreased ($p< 0001$) and **H**) the total FDT uptake in the lesions was also reduced ($p<0.005$). One representative image pair is shown of three similar treatment experiments.

To confirm the labelling differences observed in the *M. tuberculosis* -infected marmoset, we tested the FDT probe in three cynomolgus macaques infected with *M. tuberculosis*-strain Erdman **(Figure 3.9).** Here again, greater FDT uptake was associated with culturable *M.*

tuberculosis bacteria. The successful labelling of *M. tuberculosis* lesions with FDT in two primate species led us to determine the radioactivity distribution and toxicity of FDT in order to support the application of this probe in a clinical setting.

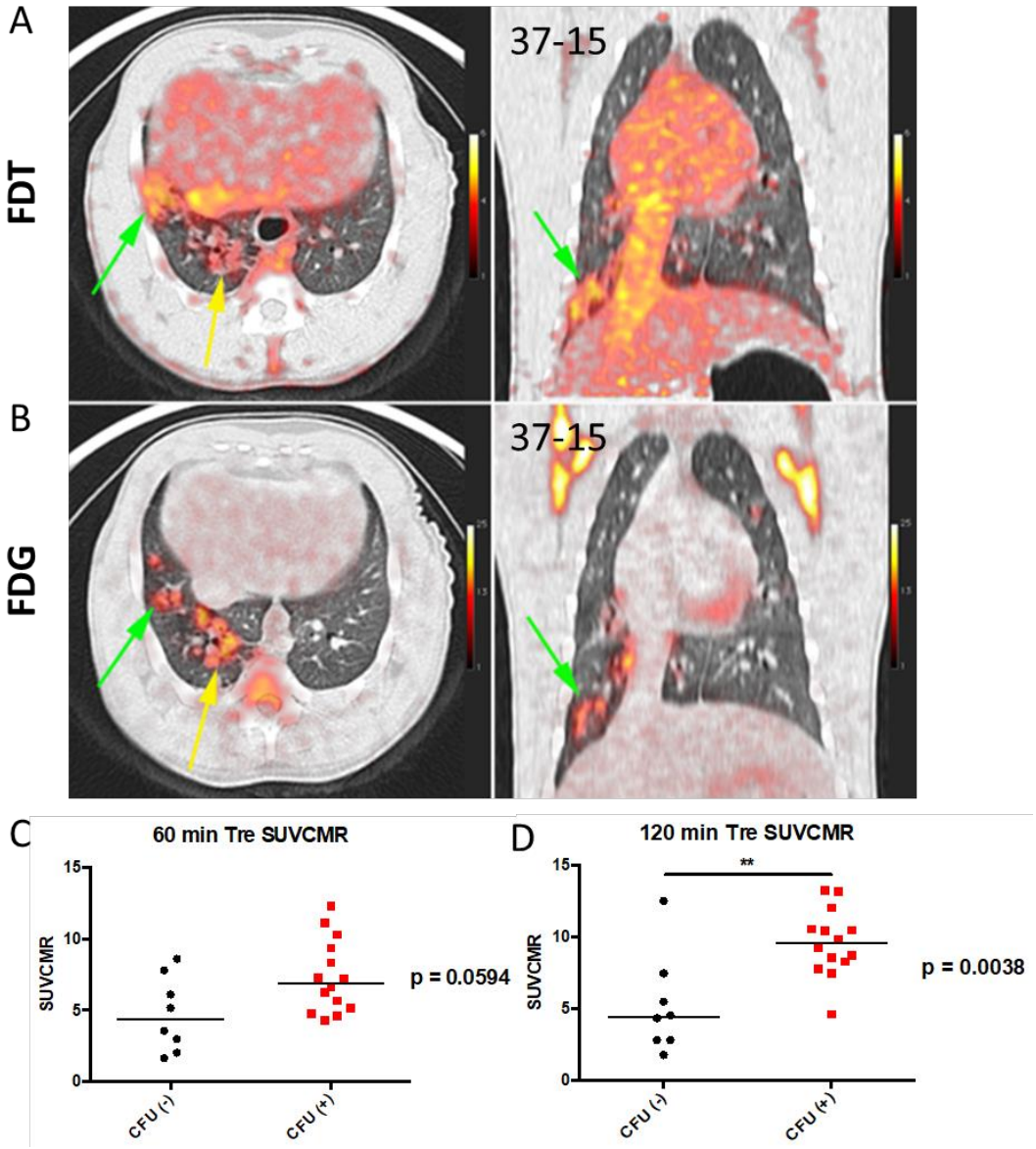


Figure 3.9. FDT and FDG scans of a *M. tuberculosis* infected cynomolgus macaque showing labeling of the tubercular lesions. A) Axial and coronal views through the lung showing lesion clusters labeling (green and yellow arrows) with the FDT probe 60 minutes post-injection. **B**) Axial and coronal views of the same lung lesion clusters labeled with FDG 60 minutes post-injection. Calibration scale in SUV. **C**) Once the animal was necropsied and the individual lesions were plated, the probe uptake of the lesions was compared to their culture status. In images captured at 60 minutes there was a trend

toward lesions with culturable bacteria having higher probe uptake. **D**) By 120 minutes, the uptake of probe was significantly higher among lesions with culturable bacteria than those without culturable bacteria. One of three representative animals with their lesion assessments is shown.

3.2.7 Biodistribution and toxicity assessment of FDT

The biodistribution of FDT was investigated in three healthy rhesus macaques by collecting 210 minutes of dynamic PET imaging, beginning after each animal was injected with 5 mCi of FDT synthesized on separate occasions. Images indicated rapid distribution from the blood stream through the tissues and accumulation in the kidney and urinary bladder (**Figure 3.10A**). Kidneys had the highest radioactivity accumulation and exposure by quantification of the PET signal from dynamic uptake studies indicating the renal clearance of the radiotracer (**Figure 3.10B**). Overall, the estimated humanized monkey body dose was low, with a mean of 0.023 rem/mCi ± 0.003 SD. Additionally, we performed biodistribution studies in two *M. tuberculosis*-infected marmosets injected with 2 mCi/kg FDT. Small samples of tissue were collected at necropsy, 120 min post-injection and the radioactivity was measured in a calibrated gamma counter. In both animals, there was little tissue uptake of the radiotracer in organs other than the kidneys **(Figure 3.10C**).

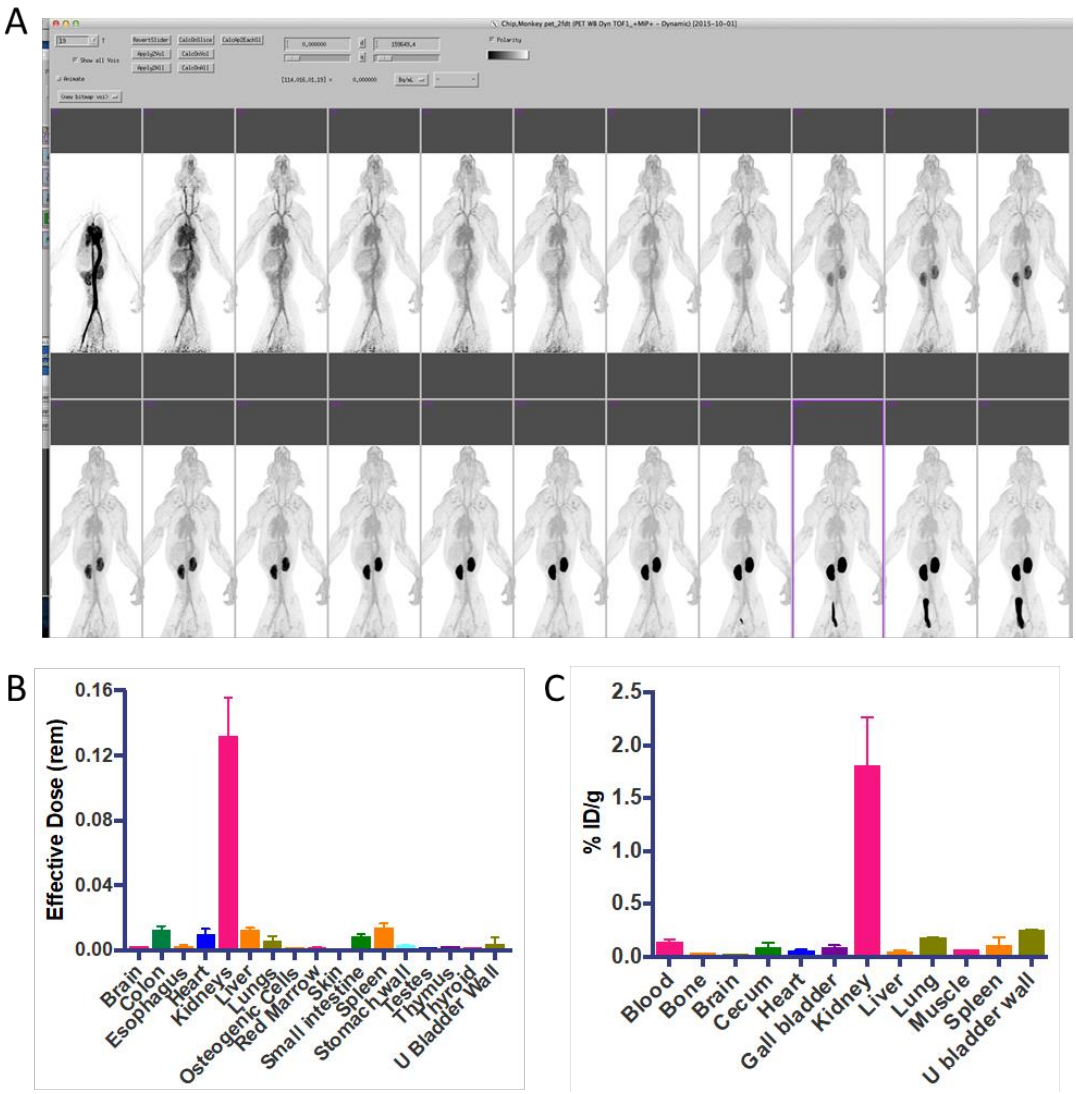


Figure 3.10 Dynamic biodistribution of FDT in naïve rhesus macaques to estimate organ exposure to FDT by quantification of PET signal in the images and by gamma counting of FDT radioactivity in excised tissues of scarificed marmosets. A) Coronal 3D projections of FDT PET activity in a representitive naïve rhesus macaque after 2, 5, and each successive 10 minutes over a 0-210 min dynamic PET scan. Rhesus macaques were administered 5 mCi of FDT for the scan. **B**) Average effective dose (rem) to rhesus tissues was estimated from summing of the PET activity per organ of the FDT given to 3 rhesus macaques. The highest exposure was observed in the kidneys and urinary bladder. **C**) Similar to the rhesus experiments, the quantification of the radioactivity in the marmoset tissues indicates the kidneys were the organs with the highest proportion of the injected dose (%ID/g) when marmosets were necropsied 120 min after being administered FDT.

3.2.8 Toxicity Studies

In order to determine the potential toxic effects of FDT administration, single and multiple intravenous (iv) dose toxicity studies of [^{19}F]FDT were conducted in rats and beagle dogs by SRI International (Menlo Park, CA) under good laboratory practice conditions. The animals were given either daily IV injections of [^{19}F]FDT at 100 times the expected human dose for seven consecutive days or a single iv injection at either 100 times or 1000 times the expected human dose once. Thereafter the animals were observed daily for mortality and morbidity, clinical observations, body weight, food consumption, clinical pathology (haematology, serum chemistry and coagulation parameters). They were humanely sacrificed either on day 9 or day 21 after the injections began and organ weights, gross pathology and histopathology were assessed. All animals survived until scheduled sacrifice. There were no adverse findings in any parameters evaluated in the study.

3.3 Conclusions

To conclude, we were able to show that [^{19}F]FDT is stable *in vitro* and *in vivo*. We tested the safety and efficacy of this compound in two animal species and did not return with any adverse findings. Through *in vivo* labelling experiments with FDT we were able to show successful FDT incorporation into mycobacterial lipids in tubercular lesions within a practical imaging timeframe for the ^{18}F radionuclide. From blocking experiments we were able to show that [^{19}F] FDT blocks the uptake of radiolabelled FDT. Data from time dependent scanning showed an optimal scanning time of 90 min post injection, suited to the short $t_{1/2}$ of ^{18}F. Scanning data from infected marmosets with both FDG and FDT revealed the differential labelling of two tracers for the TB lesions. Comparative imaging of FDG and FDT from monitoring the treatment response showed reduction of signal in FDT scans post-treatment, whereas FDG showed a mixed response. The data from biodistribution studies showed rapid clearance of the

tracer in the blood stream and accumulation in the kidneys and bladder. There was very little tissue uptake in areas other than kidneys. These pre-clinical imaging and toxicity studies support the IND application of this tracer for use in clinic as an imaging agent for tubercular disease.

3.4 Experimental

3.4.1 Animals and ethics assurance

This study was carried out in accordance with the recommendations in the Guide for the Care and Use of Laboratory Animals of the National Institutes of Health. Biodistribution studies with naive rhesus macaques were approved by the Institutional Animal Care and Use Committee (IACUC) of the NIH Clinical Centre (Bethesda, MD). The IACUC of the NIAID, NIH approved the experiments described herein with rabbits and marmosets under protocols LCID-3 and LCID-9 respectively (Permit issued to NIH Intramural Research Program as A-4149-01), and all efforts were made to provide intellectual and physical enrichment and minimize suffering. Once infected, female rabbits or marmosets of both sexes were housed individually or paired in biocontainment cages in a biological level 3 animal facility approved for the containment of *M. tuberculosis*. All NIH studies were performed in accordance with the regulations of the Division of Radiation Safety, at the National Institutes of Health (Bethesda, MD, USA). The University of Pittsburgh cynomolgus macaque studies were approved by its IACUC and Division of Radiation Safety and animals were pair housed in an approved ABSL3 facility (Regional Biocontainment Facility, Pittsburgh PA).

3.4.2 In vitro detection of [^{19}F]FDT

FDT standards were prepared in human plasma(Sigma Aldrich), whereby 20 μL plasma samples were spiked with various known concentrations of [^{19}F]FDT i.e. 10 μM, 20 μM, 40 μM, 120 μM, 160 μM, and 300 μM in 1.5 ml Eppendorf tube and diluted with up to 50% acetonitrile solution. Samples were vortexed for 1 min and centrifuged at 13000 rpm for 10 min and supernatant was analysed directly by LC-MS using LC method 2.

3.4.3 In vivo detection of [^{19}F] FDT

For the *in vivo* study, 6 white mice, CD1, male, weighing between 22-26 grams, were used. Two concentration of [^{19}F]FDT i.e. 500 μM and 50 μM (final concentration in the blood) were injected into the mice, through the tail vein injection. Prior to injection, each mouse was pre-bled (100 μL) and control samples were obtained. Five min post injection, blood samples were drawn up (775 μL) in syringe containing 75 μL sodium citrate as anticoagulant, hence total blood volume was 700 μL.

Samples were spun at 13000 rpm for 10 min and the supernatant (plasma) was used for further analysis. 200 μL of plasma sample was transferred into fresh 1.5 mL Eppendorf tube and diluted with equal amount of acetonitrile to precipitate out blood plasma protein and other macromolecules. Samples were further spun at 13000 rpm for 5 min. Supernatant was transferred into mass spectrometry vial and analyzed for the detection of sugar using LC-MS analysis method 2 & 3.

3.4.4 PET/CT instrumentation, probe administration, and image acquisition

Rabbits and marmosets at NIAID were anaesthetized and maintained during imaging as previously described[27,28]. Briefly, syringes of FDG or FDT were measured in a dose calibrator

immediately before and after injection into the animal's catheter and injected doses (~2 mCi/Kg) were calculated and recorded along with the weight of the animal. During uptake and distribution of the probes, a CT scan from the base of the skull spanning the lungs and the upper abdominal cavity was acquired as described for each species on a helical eight-slice Neurological Ceretom CT scanner (NeuroLogicia, Danvers, MA) operated as part of a hybrid pre-clinical PET/CT system utilizing a common bed[8,9]. The animal bed was then retracted into the microPET gantry (MicroPET Focus 220, Siemens Preclinical Solutions, Knoxville, TN) and sixty minutes ± 5 min post FDG injection, a series of 2 or 3, 10 minute emission scans with 75 mm thick windows with a 25 mm overlap were acquired caudal to cranial. The FDT scans were acquired beginning at 60, 90, and 120 minutes ± 5 min post injection with the same duration, window and overlap. For the blocking studies, injections of 150 mg of [^{19}F]FDT synthesized as describe above were administered 60 min and 5 min prior to the FDT tracer and the scans were acquired as before. Two animals were used in the blocking studies with one animal receiving the blocking agent while the other was administered saline only prior to the FDT tracer. Two days later the administrations were reversed so that the second animal received the blocking agent. The emission data for all scans were processed and corrected as described previously[27].

3.4.5 Uptake / Time course analysis PET/CT data analysis

For FDG glycolytic activity measurements, PET/CT images were loaded into MIM fusion software (MIM Software Inc, Cleveland, OH USA) to create lung contours using the CT 3D region growing application with upper and lower voxel threshold settings of 2 and -1024 HU respectively with hole filling and smoothing applied. Dense lesion centers were subsequently identified for inclusion in the lung region manually and the program calculated the FDG signal parameters. In addition, each lesion within the lung was marked with a 3-D region of interest

(ROI) and the SUV statistics for the ROIs were captured into excel sheets for analysis as described in[27].

3.4.6 Biodistribution in Rhesus and Marmosets

Three adult male rhesus macaques (approximately 8-12 kg) were administered 4-5 mCi/kg FDT (in ~2 mL) via saphenous vein catheter while anesthetized with ketamine and maintained with 2-4% isoflurane/97% oxygen. Dynamic whole torso PET/CT scans were collected on a Siemens mCT PET/CT camera. The PET images were reconstructed using an iterative time-of-flight algorithm to obtain 400^3 voxels with a size of $1.45 \times 1.45 \times 1.5$ mm^3. For the pharmacokinetic analyses, the PET data were divided into 22 time frames with durations 2 x 15, 4 x 30, 8 x 60, and 8 x 120 seconds. Each frame in the sequence was gathered from 4 bed positions to obtain whole-torso dynamic data in approximately 115 minutes. For each reconstructed PET scan, volumes of interest (VOIs) were drawn over major organs and PET/CT data were quantitatively evaluated using OLINDA 1.1 (Vanderbilt University, Nashville NT) to generate organ and total body estimated dose in rem/mCi by methods previously described[29]. We "humanized" the monkeys by using a human adult phantom and scaling of monkey organ size to human organ size[30].

Two marmosets were administered 2 mCi/kg FDT (in ~300 µL PBS) via tail vein catheter while anesthetized with 3% isoflurane/97% oxygen and PET/CT scans were collected as described above and a final 200 µL whole blood sample was drawn via femoral vein puncture and placed immediately into a 1.5 mL tube that was coated with potassium ethylenediamine tetraacetic acid. After euthanasia, the liver, right kidney, skeletal muscle (right quadriceps), brain, and bone (femur) and other organ samples were harvested and weighed. Each of the tissue samples

were transferred to gamma counter tubes and counted on a Wallac Wizard 1480 Gamma Counter (Perkin Elmer, Waltham, MA). Count data were converted to percent injected dose per gram using a dose calibration curve.

3.4.7 Metabolism analysis and Detection of labeled mono and dimycolates

Blood (100 µL) and urine (100-300 µL) were collected from animals and diluted 2:1 v/v with acetonitrile to sterilize them. These samples were then vortexed, centrifuged and the supernatant analyzed by either HPLC or TLC. TLC plates were visualized via exposure to a phosphor screen for 16 h prior to imaging using a phosphor screen and Typhoon FLA7000 (GE Healthcare, Pittsburgh PA). Silica gel plates used to assay the metabolism samples and lesion extracts were 150 Å Silica Gel HL 250µ m 10 x 20 cm channeled plates with a pre-adsorbent zone purchased from Analtech/iChromatography (Newark, DE). Plates were read using a BioScan AR-2000 reader.

3.4.8 Toxicity studies

For toxicity studies, 2 g of [^{19}F]FDT synthesised and tested for quality control as described in the chapter 2 of this thesis and shipped to a contract research organisation Toxicity studies were carried out by (SRI international) in two animal species i.e. rats and dogs.

For studies in rats male and female Sprague Dawley rate (15/sex/group) were given a single iv administration of [^{19}F]FDT at 1.32 mg/kg (100 times of human dose; Group 3) or 13.2 mg/kg (1000 times of human dose; Group 4) on day 7 or 1.32 mg/kg/day for 7 consecutive days (total dose 9.24 mg/kg; Group 2. A control group (15/sex; Group 1) was given 7 days of vehicle (50 mM HEPES buffer, pH 7.5 with 7.5 mM $MgCl_2$) at an equivalent dose volume of 1 mL/kg on days 1-7. Animals were sacrificed on day 9 (Main groups) or day 21 (recovery groups).

Table 3.2: Experimental Design for the toxicity Studies in Rats

Group	Treatment	Dose Level (mg/kg/day)	No. Doses	Total Dose (mg/kg)	Main groups animal	Recovery Group animals
1	Vehicle	0	7	0	10M/10F	5M/10F
2	100x human dose	1.32	7	9.24	10M/10F	5M/10F
3	100x human dose	1.32	1	1.32	10M/10F	5M/10F
4	1000x human dose	1.32	1	1.32	10M/10F	5M/10F

To assess the toxicity associated with [^{19}F]FDT in dogs, male and female Beagle dogs (5/sex) were given a daily iv injection of [^{19}F]FDT at 0.4 mg/kg/day (100 times of human dose; Group 2) for 7 consecutive days, or a single iv administration of [^{19}F]FDT at 0.4 or 4 mg/kg (100 and 1000 times of human dose in Groups 3 and 4, respectively) on Day 7. A control group (5/sex; Group 1), was given 7 days of vehicle (HEPES buffer, pH 7.5, 50 mM with $MgCl_2$ 7.5 mM), at an equivalent dose volume of 0.25 ml/kg on Days 1-7. Animals were sacrificed on Day 9 (3/sex/ group; main groups) or Day 21 (2/sex/group; recovery groups). The single dose administration for Groups 3-4 were initiated on Day 7 so that clinical pathology and necropsy occurred on the same calendar day for all Groups (1-4), thus allowing for sharing of vehicle control data for analysis of clinical pathology and necropsy results between the two dose regimens.

Table 3.3: Experimental Design for the toxicity Studies in Dogs

Group	Treatment	Dose Level (mg/kg/day)	No. Doses	Total Dose (mg/kg)	Main groups animal	Recovery Group animals
1	Vehicle	0	7	0	3M/3F	2M/2F
2	100x human dose	0.4	7	2.8	3M/3F	2M/2F
3	100x human dose	0.4	1	0.4	3M/3F	2M/2F
4	1000x human dose	4	1	4	3M/3F	2M/2F

3.5 References

1. Riemann, B.; Schafers, K. P.; Schober, O.; Schafers, M., Small animal PET in preclinical studies: opportunities and challenges. *The Quarterly Journal of Nuclear Medicine and Molecular Imaging* **2008,** *52* (3), 215-21.

2. Willmann, J. K.; van Bruggen, N.; Dinkelborg, L. M.; Gambhir, S. S., Molecular imaging in drug development. *Nature Reviews Drug Discovery* **2008,** *7* (7), 591-607.

3. Mayeux, R., Biomarkers: potential uses and limitations. *NeuroRx* **2004,** *1* (2), 182-188.

4. Pien, H. H.; Fischman, A. J.; Thrall, J. H.; Sorensen, A. G. J. D. d. t., Using imaging biomarkers to accelerate drug development and clinical trials. *Drug Discovery Today* **2005,** *10* (4), 259-266.

5. US Food and Drug Administration. 'Guidance': Investigational New Drug Applications for Positron Emission Tomography (PET) Drugs. **2012**, 1-24.

6. US Food and Drug AdministrationFood. Developing Medical Imaging Drug and Biological Products, Part 3: Design, Analysis, and Interpretations of Clinical Studies. **2004**. 1-29

7. Senderowicz, A. M., Information Needed to Conduct First-in-Human Oncology Trials in the United States: A View from a Former FDA Medical Reviewer. *Clinical Cancer Research* **2010,** *16* (6), 1719.

8. US Food and Drug Adminsitration. FDA Guidance for Industry: Developing medical imaging drug and biological Products. Part 1: Conducting Safety Assessment. **2004**, 1-16.

9. Fonseca, K. L.; Rodrigues, P. N. S.; Olsson, I. A. S.; Saraiva, M., Experimental study of tuberculosis: From animal models to complex cell systems and organoids. *PLoS Pathogens* **2017,** *13* (8), e1006421.

10. Orme, I. M., The mouse as a useful model of tuberculosis. *Tuberculosis* **2003,** *83* (1-3), 112-5.

11. Gupta, U.; Katoch, V. J. T., Animal models of tuberculosis. *Tuberculosis* **2005,** *85* (5-6), 277-293.

12. Vilaplana, C.; Cardona, P. J., The lack of a big picture in tuberculosis: the clinical point of view, the problems of experimental modeling and immunomodulation. The factors we should consider when designing novel treatment strategies. *Frontiers in Microbiology* **2014,** *5*, 55.

13. Scanga, C. A.; Flynn, J. L., Modeling tuberculosis in nonhuman primates. *Cold Spring Harb Perspect Med* **2014,** *4* (12), a018564-a018564.

14. De Rycker, M.; Horn, D.; Aldridge, B.; Amewu, R. K.; Barry, C. E., 3rd; Buckner, F. S.; Cook, S.; Ferguson, M. A. J.; Gobeau, N.; Herrmann, J.; Herrling, P.; Hope, W.; Keiser, J.; Lafuente-Monasterio, M. J.; Leeson, P. D.; Leroy, D.; Manjunatha, U. H.; McCarthy, J.; Miles, T. J.; Mizrahi, V.; Moshynets, O.; Niles, J.; Overington, J. P.; Pottage, J.; Rao, S. P. S.; Read, K. D.; Ribeiro, I.; Silver, L. L.; Southern, J.; Spangenberg, T.; Sundar, S.; Taylor, C.; Van Voorhis, W.; White, N. J.; Wyllie, S.; Wyatt, P. G.; Gilbert, I. H., Setting Our Sights on Infectious Diseases. *ACS Infectious Diseases* **2019**, 6 (1), 3-13.

15. Backus, K. M.; Boshoff, H. I.; Barry, C. S.; Boutureira, O.; Patel, M. K.; D'Hooge, F.; Lee, S. S.; Via, L. E.; Tahlan, K.; Barry, C. E., 3rd; Davis, B. G., Uptake of unnatural trehalose analogs as a reporter for Mycobacterium tuberculosis. *Nature Chemical Biology* **2011,** *7* (4), 228-35.

16. Sargent, M., Guide to achieving reliable quantitative LC-MS measurements. *Royal Society of Chemistry Analytical Methods Committee* **2013,** 1-59.

17. Vékey, K., Mass spectrometry and mass-selective detection in chromatography. *Journal of Chromatography* **2001,** *921* (2), 227-236.

18. Schuhmacher, J.; Zimmer, D.; Tesche, F.; Pickard, V., Matrix effects during analysis of plasma samples by electrospray and atmospheric pressure chemical ionization mass spectrometry: practical approaches to their elimination. *Rapid Communications in Mass Spectrometry* **2003,** *17* (17), 1950-7.

19. Matuszewski, B. K.; Constanzer, M. L.; Chavez-Eng, C. M., Matrix effect in quantitative LC/MS/MS analyses of biological fluids: a method for determination of finasteride in human plasma at picogram per milliliter concentrations. *Analytical Chemistry* **1998,** *70* (5), 882-9.

20. Ismaiel, O. A.; Halquist, M. S.; Elmamly, M. Y.; Shalaby, A.; Karnes, H. T., Monitoring phospholipids for assessment of matrix effects in a liquid chromatography-tandem mass spectrometry method for hydrocodone and pseudoephedrine in human plasma. *Journal of Chromatography. B, Analytical Technologies in the Biomedical and Life Sciences* **2007,** *859* (1), 84-93.

21. Fang, N.; Yu, S.; Ronis, M. J.; Badger, T. M., Matrix effects break the LC behavior rule for analytes in LC-MS/MS analysis of biological samples. *Experimental Biology and Medicine* **2015,** *240* (4), 488-497.

22. Jiang, L.; He, L.; Fountoulakis, M., Comparison of protein precipitation methods for sample preparation prior to proteomic analysis. *Journal of Chromatography A* **2004,** *1023* (2), 317-320.

23. Xue, Y. J.; Akinsanya, J. B.; Liu, J.; Unger, S. E., A simplified protein precipitation/mixed-mode cation-exchange solid-phase extraction, followed by high-speed

liquid chromatography/mass spectrometry, for the determination of a basic drug in human plasma. *Rapid Communications in Mass Spectrometry* **2006,** *20* (18), 2660-8.

24. Hennion, M. C., Solid-phase extraction: method development, sorbents, and coupling with liquid chromatography. *Journal of Chromatography. A* **1999,** *856* (1-2), 3-54.

25. Ahmad, S.; Kalra, H.; Gupta, A.; Raut, B.; Hussain, A.; Rahman, M. A., HybridSPE: A novel technique to reduce phospholipid-based matrix effect in LC-ESI-MS Bioanalysis. *J Pharm Bioallied Sci* **2012,** *4* (4), 267-275.

26. Via, L. E.; England, K.; Weiner, D. M.; Schimel, D.; Zimmerman, M. D.; Dayao, E.; Chen, R. Y.; Dodd, L. E.; Richardson, M.; Robbins, K. K.; Cai, Y.; Hammoud, D.; Herscovitch, P.; Dartois, V.; Flynn, J. L.; Barry, C. E., A Sterilizing Tuberculosis Treatment Regimen Is Associated with Faster Clearance of Bacteria in Cavitary Lesions in Marmosets. *Antimicrobial Agents and Chemotherapy* **2015,** *59* (7), 4181.

27. Via, L. E.; Schimel, D.; Weiner, D. M.; Dartois, V.; Dayao, E.; Cai, Y.; Yoon, Y. S.; Dreher, M. R.; Kastenmayer, R. J.; Laymon, C. M.; Carny, J. E.; Flynn, J. L.; Herscovitch, P.; Barry, C. E., 3rd, Infection dynamics and response to chemotherapy in a rabbit model of tuberculosis using [(1)(8)F]2-fluoro-deoxy-D-glucose positron emission tomography and computed tomography. *Antimicrobial agents and Chemotherapy* **2012,** *56* (8), 4391-402.

28. Via, L. E.; Weiner, D. M.; Schimel, D.; Lin, P. L.; Dayao, E.; Tankersley, S. L.; Cai, Y.; Coleman, M. T.; Tomko, J.; Paripati, P.; Orandle, M.; Kastenmayer, R. J.; Tartakovsky, M.; Rosenthal, A.; Portevin, D.; Eum, S. Y.; Lahouar, S.; Gagneux, S.; Young, D. B.; Flynn, J. L.; Barry, C. E., 3rd, Differential virulence and disease progression following Mycobacterium tuberculosis complex infection of the common marmoset (Callithrix jacchus). *Infection and Immunity* **2013,** *81* (8), 2909-19.

29. Brugarolas, P.; Sanchez-Rodriguez, J. E.; Tsai, H. M.; Basuli, F.; Cheng, S. H.; Zhang, X.; Caprariello, A. V.; Lacroix, J. J.; Freifelder, R.; Murali, D.; DeJesus, O.; Miller, R. H.; Swenson, R. E.; Chen, C. T.; Herscovitch, P.; Reich, D. S.; Bezanilla, F.; Popko, B., Development of a PET radioligand for potassium channels to image CNS demyelination. *Scientific Reports* **2018,** *8* (1), 607.

30. Macey, D. J; *A Primer for Radioimmunotherapy and Radionuclide Therapy*. American Association of Physicists in Medicine: **2001**.

3.6 Supplementary Figures

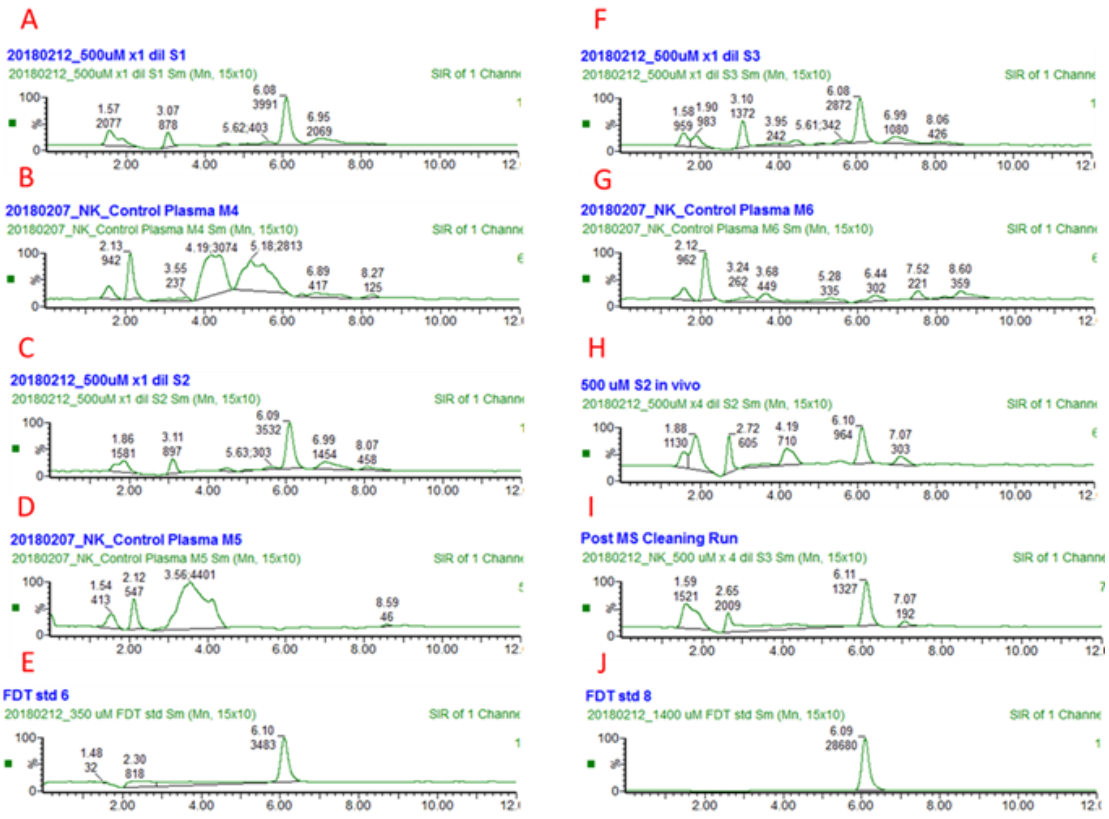


Figure S1. LC - MS Analysis of in vivo samples after pre-treatment with acetonitrile; 2**A, 2C & 2F** are the plasma samples where mice injected with 500 µM of FDT sugar. Samples were then pre-treated with equal amount of acetonitrile dilution i.e. x 1 dilution. Sample 2**B, 2D & 2G** are the corresponding control samples which were taken prior to injection of FDT. Samples 2**H & 2I** are the samples when diluted with x4 acetonitrile and 2**E & 2J** are the standard samples for FDT.

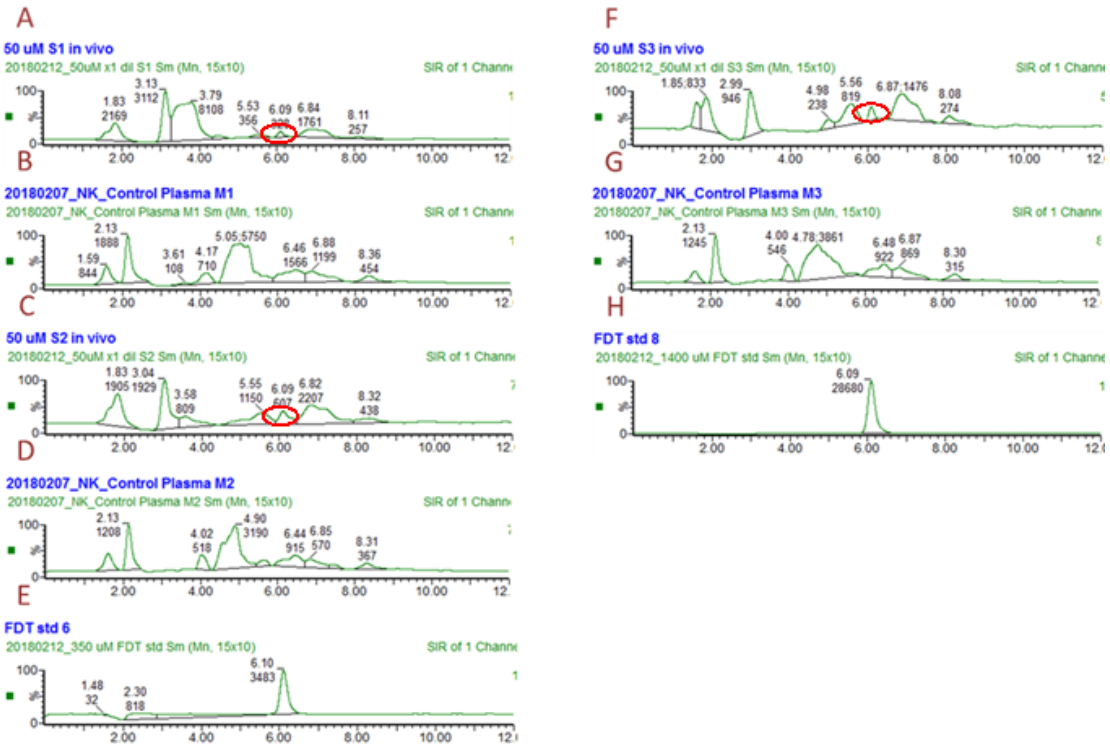


Figure S2. LC-MS Analysis of in vivo samples after pre-treatment with Acetonitrile. 3**A, 3C & 3F** are the plasma samples where mice injected with 50 µM of FDT. Samples were then pre-treated with equal amount of acetonitrile to that of plasma i.e. x1 dilution. Samples 3**B, 3D & 3G** are control samples taken prior to injection of FDT. Samples 3**E & 3H** are FDT standard samples.

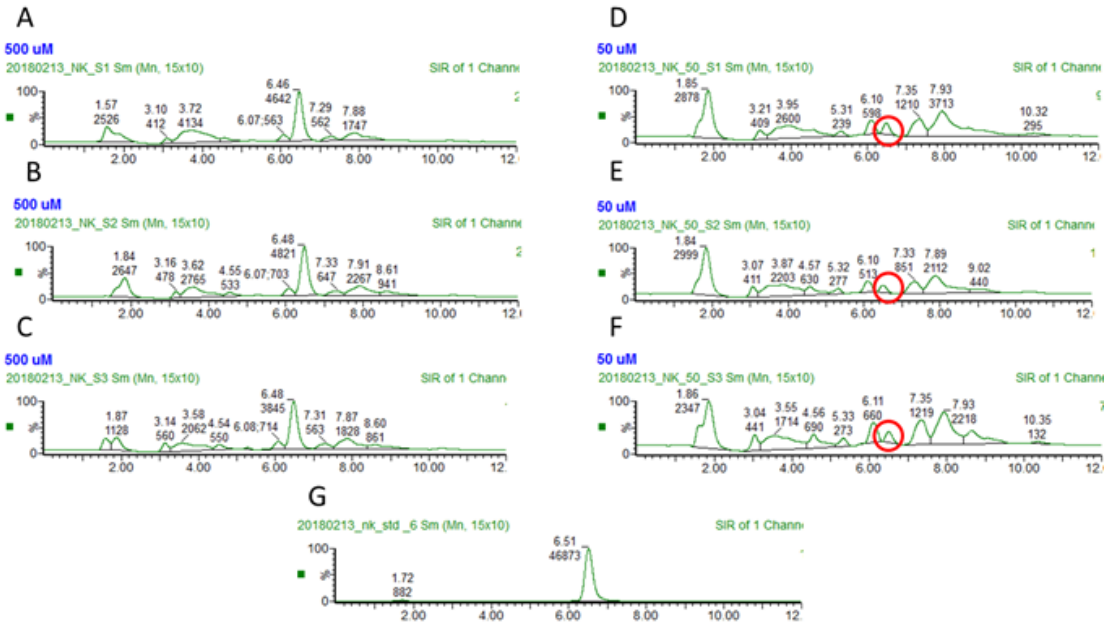


Figure S3. LC-MS analysis of mice plasma samples injected with 2FDT. Analysis was carried out at ambient temperature. Samples 4**A, 4B & 4C** represent mice samples injected with 500 µM 2FDT and samples 4**D, 4E & 4F** correspond to different mice samples injected with 50 µM 2FDT solutions (SAM. Sample **G** is 2FDT standard solution prepared in 70 % Acetonitrile solution.

4 Chapter 4: Copper-64 Labelled Monocyte Chemoattractant Protein-1 (MCP-1) as an Imaging Agent

4.1 Introduction

Chemokines constitute a superfamily of heparin-binding small proteins, usually made up of 60-100 amino acid long peptides. As their name suggests, chemokines are chemotactic cytokines, which play an important role in the immune and inflammatory response[1].

Chemokines cause chemotactic migration of leukocytes by interacting with G-Protein-Coupled Receptors (GPCRs) with the involvement of adhesion molecules and glycosaminoglycans (GAGs)[2-4]. The interaction between chemokines and their receptors are usually promiscuous. Most known receptors interact with more than one ligand and most ligands interact with more than one receptor. Apart from being involved in chemotactic movement of leukocytes, these chemokines are also involved in other functions such as angiogenesis, collagen production, the proliferation of hematopoietic precursors, and the ontogeny of the central nervous system[4]. Due to the involvement of chemokines in a large number of diseases, they are a very attractive target for pharmacological research.

To date more than 50 human chemokines have been identified with one thing in common, a cysteine motif. Chemokines are grouped into two major families (CC and CXC) and two minor families (C and CX3C), depending on the spacing of the conserved cysteine residues near the N-terminal region of the protein[5-7]. The monocyte chemoattractant protein-1 (MCP-1/CCL2) is a member of the CC chemokine family, that regulates migration and infiltration of monocytes, memory T lymphocytes, and natural killer cells.[4, 8]. Human CCL2, is composed of 76 amino acids along with a 23 amino acid long signal sequence coupled at the N-terminus, and is 13 kDa in size (**Figure 4.1**)[4, 8, 9]. The basic structure of CCL2 follows the same trend as observed for other chemokines. The structure consists of three anti-parallel β-strands a C-

terminal α-helix and an N-terminal loop containing disulphide bonds (**Fig. 4.1**). The N-terminus of the protein contains the receptor binding and dimerization site, whereas the C-terminus contains the glycosaminoglycan (GAG) binding site[9]. Although the protein contains the N-glycosylation site consensus sequence, it is not found to have N-linked sugars, however it is known to possess O-glycosylation at (one, or a number of) threonine residues[8, 10]. The heterogeneity of O-glycosylation leads to variability in its molecular weight. Importantly, it has been shown that glycosylation decreases the chemotactic activity of the protein.[4]

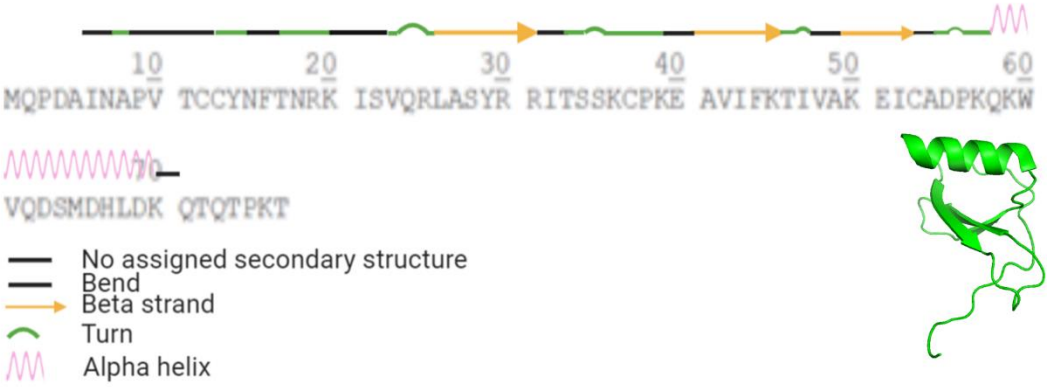


Figure 4.1. Crystal structure of CCL2 (PDB: 3IFD) and amino acid sequence.

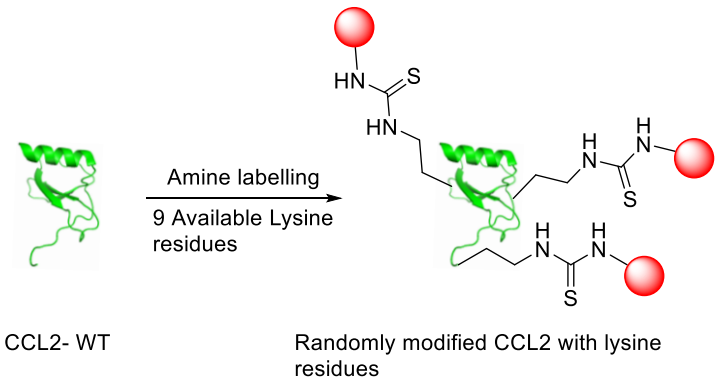
CCL2 is known to be associated with many pathological and pathophysiological processes such as infection, inflammation and arthritis[11]. During a TB infection the pathogen infects macrophages, which can then form granuloma in the tissue[12, 13]. Importantly, macrophages overexpress C-C chemokine receptor type 2 (CCR2) for which CCL2 is the natural ligand. As such, a chemically modified CCL2 labelled with a radionuclide may act as a potential imaging agent for activated macrophages at the site of infection caused by *M. tuberculosis*.

4.2 CCL2 Radiolabelling Methods

Various studies involving the labelling of CCL2 with radionuclides have been reported in the literature[14-16]. Iodine-125(^{125}I) labelled CCL2 has been used for the chemokine-receptor binding studies in intact cells and membrane fragments[14]. In addition, ^{125}I-CCL2 has also been used as a radiotracer for imaging macrophage rich experimental atherosclerotic lesions *in vivo*. However, this method has a number of limitations including reduced receptor binding affinity, and also the assay is time-consuming due to the number of wash steps needed to remove unbound chemokine.

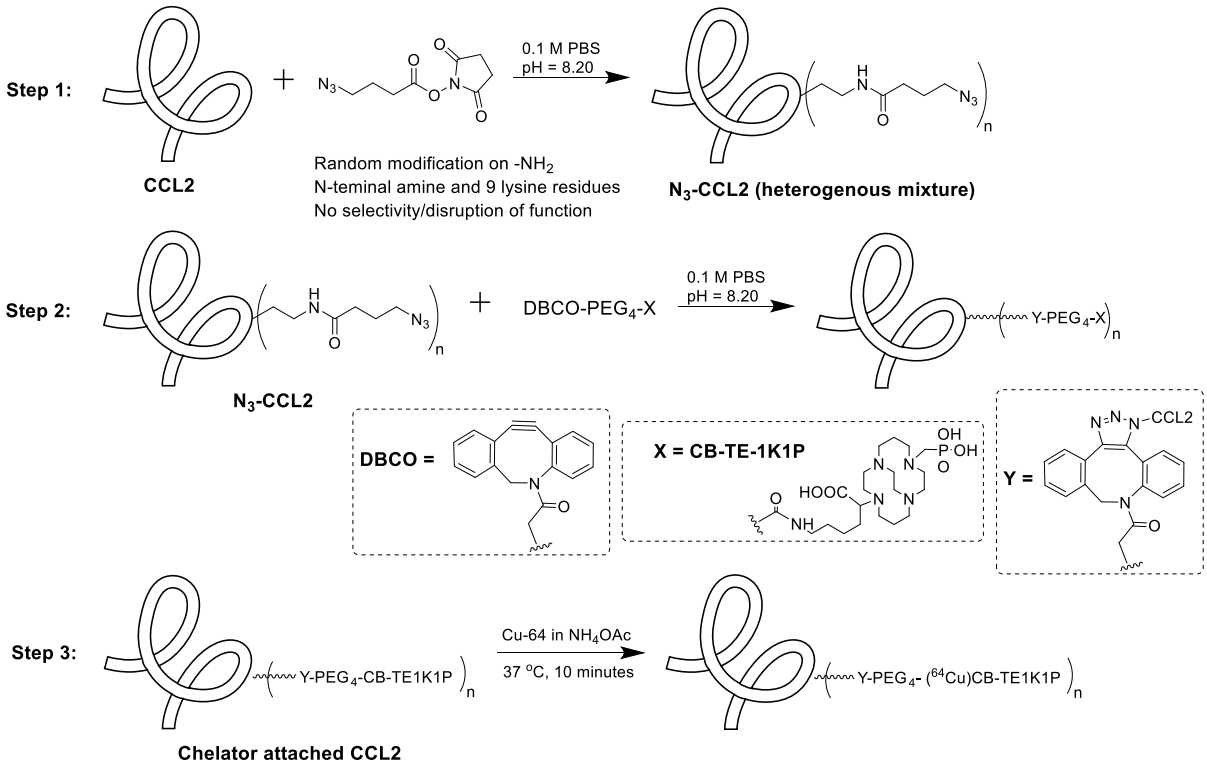
^{99m}Tc-labelled CCL2 has been used for imaging and localising the activated macrophages *in vivo*[17]. In addition, this radiotracer has also been used for the detection of inflammation in experimental atherosclerosis[15]. The radiolabelling was achieved by an indirect radiolabelling method using succinimidyl-6-hydrazinonicotinamide (HYNIC)-CCL2 and the tracer was introduced into the site of infection/inflammation non-specifically[18].

Non-specific covalent labelling through amine coupling chemistry is the simplest method for installing prosthetic groups however this leads to a random distribution of modifications on lysine residues. Unfortunately, this method is unsuitable for chemokines because the N-terminus plays a critical role in binding to the receptor causing signalling and lysine residues are frequently found at the N-terminus of chemokines[19]. However, mutants with their N-terminal amino acid deleted can still form the dimer which is thought to bind CCR2[20, 21]. In contrast, the C-terminal is relatively robust [22].



Scheme 4.1. Non-specific amine labelling of CCL2-WT. This labelling results in random modification of CCL2 with 9 available lysine residues.

Our collaborators at the University of Pittsburgh used the randomly modified CCL2 labelled with copper-64 (^{64}Cu) bifunctional chelator (BFC) as a PET imaging probe for TB[23]. Without selective modification methods, they used the common amine based protein functionalisation chemistry to introduce an azide handle on to random sites of CCL2 (**Scheme 4.2, step 1**), which resulted in the mixture of modified CCL2. In order to introduce the ^{64}Cu BFC moiety onto the protein they utilised a strain-promoted alkyne-azide cycloaddition (SPAAC)[24] reaction with a [CB-TE1K1P] DBCO-PEG$_4$-BFC bifunctional reagent (**Step 2**). Finally they installed the radionuclide ^{64}Cu through a standard radiochemistry protocol (**Step 3**).



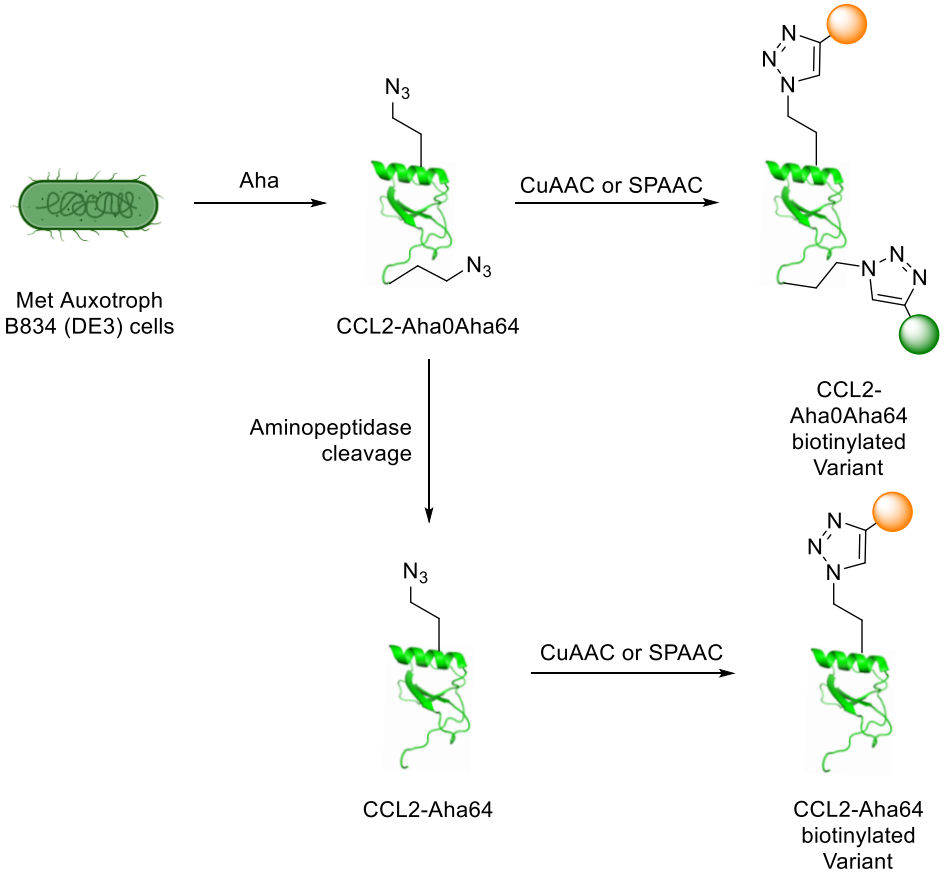
Scheme 4.2. Random Modification Strategy for synthesising ^{64}Cu labelled CCL2

Preliminary biological evaluation of the ^{64}Cu labelled CCL2 revealed that CCL2 bound to macrophages however, over modification compromised its affinity[25].

In order to overcome the problems associated with a random modification-labelling strategy, an unnatural amino acid (UAA) bearing a reactive functional handle can be installed. Site-specific labelling at an UAA residue could be a potential method for generating CCL2 based imaging probes for TB diagnosis. It has been shown that using this approach one can incorporate directly UAA bearing fluorescent chemical groups[26]. An alternative method could involve installing an UAA containing an azide or alkyne handle[27] for subsequent use in copper (I) catalysed azide-alkyne cycloaddition (CuAAC)[28] or SPAAC[24] chemistry.

With randomly modified CCL2 probes showing non-specific imaging, it was suggested that residue-specific chemically labelled CCL2 variants may be useful for imaging macrophages in

the diagnosis of TB. By using auxotrophic suppression, Dr Yiqun Geng, a previous postdoc in the Davis lab, carried out preliminary work on expression and characterisation of WT and L-azidohomoalanine (Aha) incorporation into CCL2. In the current work, we set out to extend the scope of previous work and in doing so, we incorporated Aha residues *in situ* at position 0 and position 64 of CCL2-WT, where methionine would occur naturally. Using aminopeptidase the N-terminal residue was cleaved and then we subsequently modified the residues by both copper (I) catalysed azide-alkyne cycloaddition (CuAAC)[28] and SPAAC[24] reactions with a chemical label (**Scheme 4.3**). We further confirmed the modification sites by LC-MS/MS analysis. Once the modification sites were definitively known, we tested the effects of these modifications on the protein secondary structure through physical characterisation methods. Through CCR2 binding assays, we determined the effect of modifications on the activity of the protein. Finally, the goal was to radiolabel the modified CCL2 with the PET radionuclide ^{64}Cu as a potential PET imaging agent for TB.



Scheme 4.3. Tag and modify approach to generate site specific CCL2 modification based on CuAAC and SPAAC chemistry. The N-terminal CCL2-Aha can be cleaved by aminopeptidase and modified with SPAAC reagents.

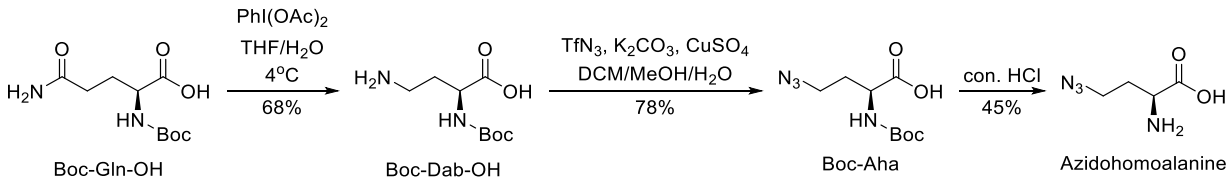
4.3 Results and Discussions

4.3.1 Synthesis of Aha

Aha was synthesised according to the literature method[29]. This method was chosen over the other published methods due to its low cost and the need for fewer purification steps. The drawback of the synthesis was the inherent danger associated with the azide transfer step[30].

Starting from commercially available N-Boc-L-glutamine, a Hoffman rearrangement with PIDA (diacetoxyiodo benzene) gave the intermediate amine, Boc-Dab-OH, in 68% yield. Azide transfer using triflic azide, prepared *in situ,* with copper sulfate solution gave the

corresponding Boc-Aha. Acid-mediated deprotection subsequently gave the Aha.HCl salt. The salt obtained was subjected to DOWEX-H^+ column chromatography to give the pure amino acid as the free base.



Scheme 4.4. Synthesis of L-Aha via a 3 steps protocol[29].

4.3.2 Aha incorporation into MCP-1, Purification and Characterisation

We successfully incorporated Aha into methionine auxotroph B834 (DE3) strain as shown in experimental section (**4.4.7**). This method has been used by several groups to label and modify proteins[31-33]. In summary after standard transformation and expression protocol, cells were harvested by centrifugation and purified by SEC on FPLC and characterised by SDS-PAGE and LC-MS (**Figure 4.2 and S2**).

The wild type (WT) CCL2 has the MW of 8811 and after analysis of the sample from purified protein by LC-MS, the mass indicated the incorporation of Aha at both sites i.e. at position 0 and position 64 as shown in the sequence below (highlighted green in the sequence).

The expression yields were low (0.2 – 0.3 mg/L), and although we did attempt to optimise the protocol, it did not result in any significant improvement in the expression yield.

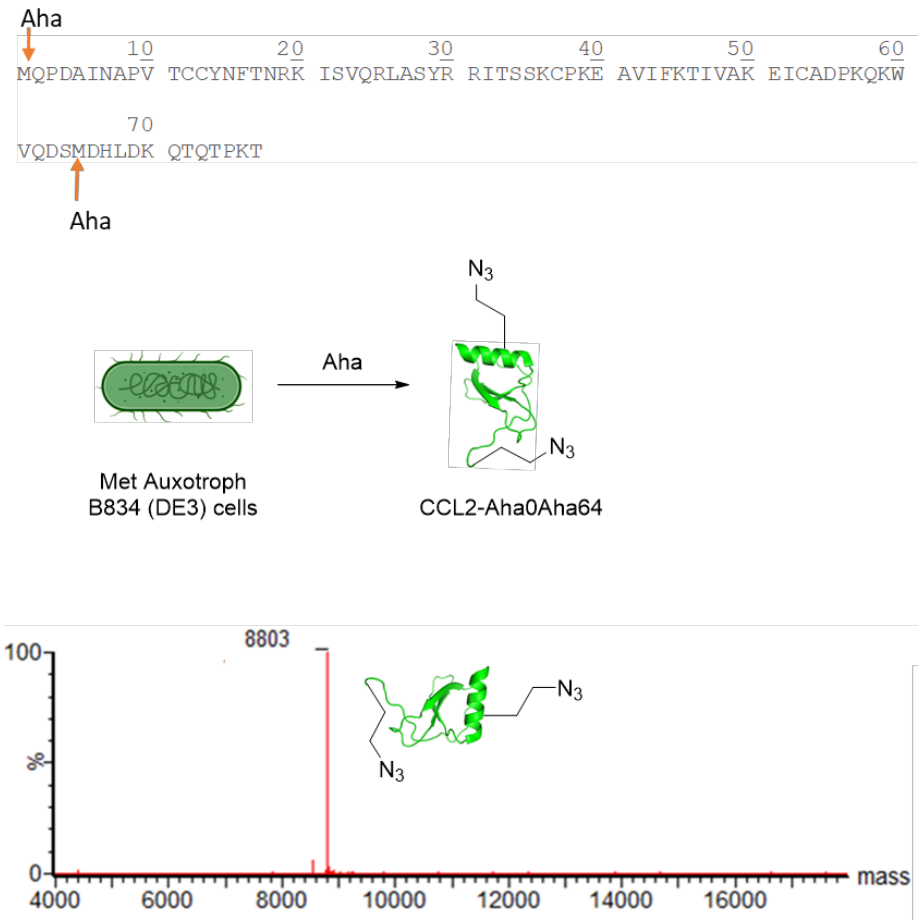


Figure 4.2. Amino Acid sequence and LC-MS characterisation of CCL2-Aha0Aha64. The mass of 8803 Da corresponds to the incorporation of Aha at both position 0 and 64. The expected mass of the protein from the amino acid sequence analysis is 8804 Da.

To further confirm that the Aha was incorporated at the both Met positions, we used LC-MS/MS to analyse individual peptide fragments after trypsin digestion. This analysis confirmed the replacement of Met with Aha at both positions 0 and 64 (**Supplementary Figure S3**).

The Aha at the N-terminus can be cleaved using the enzyme aminopeptidase. In order to test the reactions only with Aha64, we cleaved the N-terminal Aha on a 50 µg scale by adding 0.001 equivalents of aminopeptidase on ice and incubating the reaction mixture for 10 min. At this point LC-MS analysis confirmed the cleavage of N-terminus Aha giving the expected MW

of 8676 Da (**Figure 4.3**). Cleavage was further confirmed by LC-MS/MS analysis (**Supplementary Figure S4**).

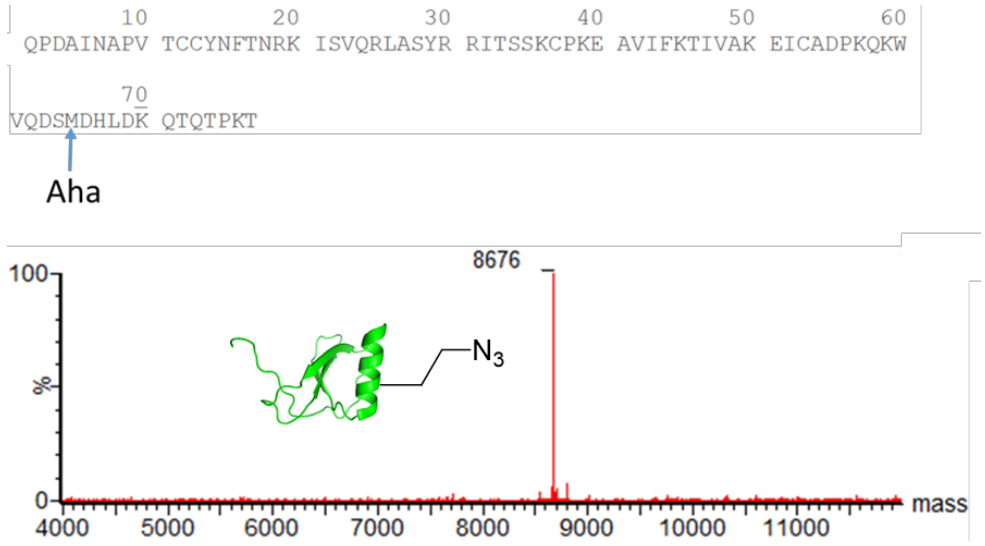


Figure 4.3: Amino acid sequence and LC-MS characterisation of the N-terminal cleavage of Aha. The mass of 8676 Da corresponds to the loss of single Aha. The modification site was further confirmed by LC-MS/MS analysis.

4.3.3 CuAAC and SPAAC Reactions with Aha0Aha64

Once we successfully incorporated the unnatural amino acid, Aha, we tested the click reactions based on CuAAC and SPAAC chemistry. For the CuAAC chemistry, we used water soluble tris (3-hydroxypropyltriazolylmethyl) amine (THPTA) ligand and complexed it with copper bromide (CuBr) solution to make copper/ligand catalyst. When CCL2-Aha was reacted with Biotin PEG4-alkyne and copper/ligand complex, only a single modification to the biotinylated derivative was observed within 30 min (**Figure 4.4 A**). We did not observe the double modification when we extended the reaction time to 2 hours or changed the number of equivalents of the copper/ligand complex and biotinylated reagent.

We also tested the click reaction of modified CCL2-Aha with dibenzocyclooctyne-PEG4-biotin (DBCO-PEG4-Biotin), effectively mimicking the SPAAC click reaction. We used 20

equivalents of biotin ligand and 1 equivalent of protein and after incubating the reaction at RT, and monitoring by LC-MS, confirmed the double modification i.e. at position 0 and position 64 in 2 hours (**Figure 4.4 B**).

We scaled-up these reactions to 200 µg scale so that enough reagent was available for biophysical assays, activity assays and LC-MS/MS analysis. The LC-MS/MS analysis of the sample confirmed the modifications of DBCO-PEG4-Biotin at position 0 and position 64 of Aha and single modification of PEG4-Biotin at position 0 only (**supplementary Figures S6 & S7**).

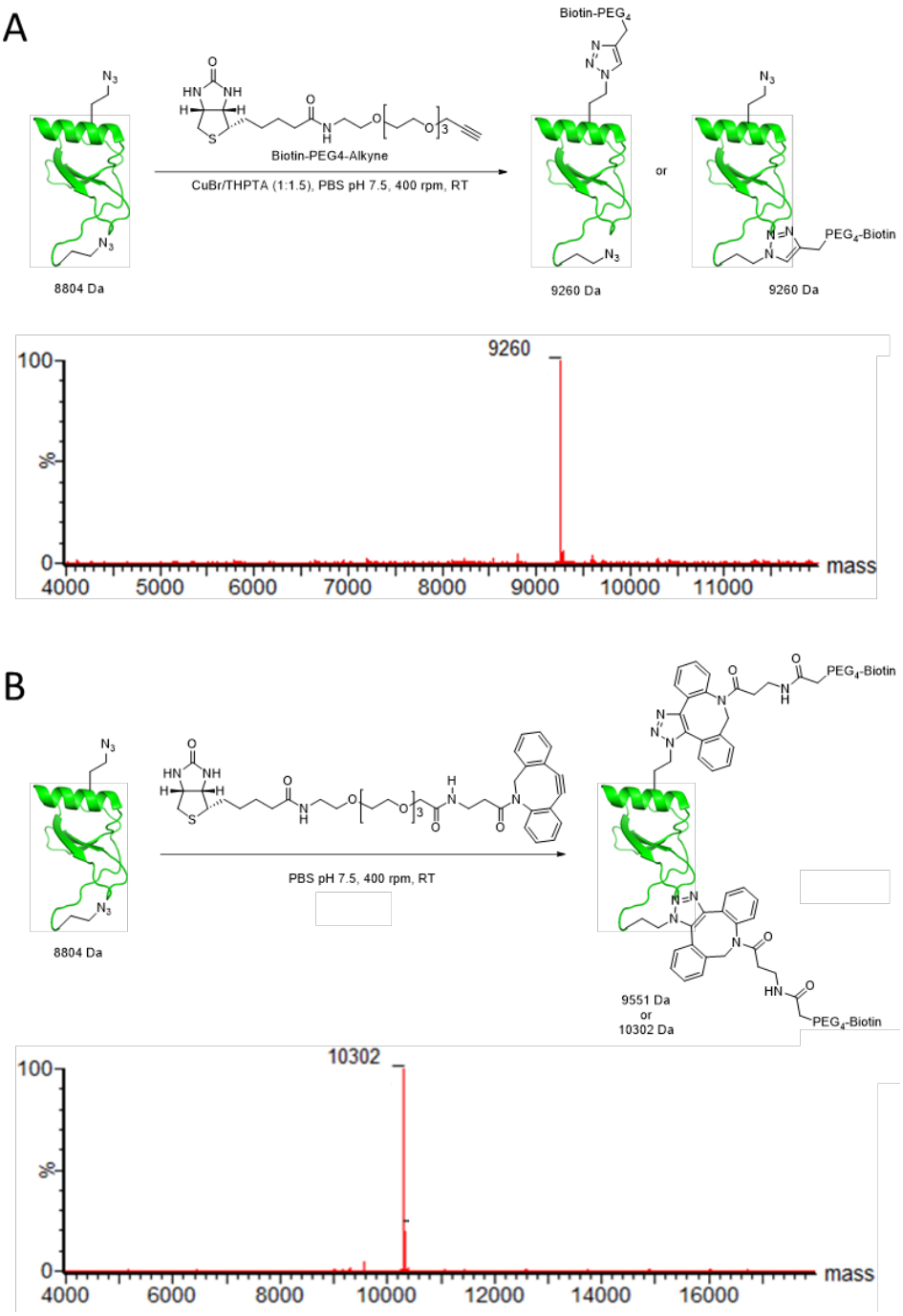


Figure 4.4. CuAAC and SPAAC Click chemistry reactions with Aha0Aha64. A) Schematic overview of the reaction of Aha0Aha64 with biotin-PEG4-alkyne in the phosphate buffer and LC-MS trace of the reaction sample indicating the conversion of Aha0Aha64 to Biotin PEG4-alkyne, although only single modification was observed. **B**) SPAAC reaction scheme with AhaAha64 and LC-MS trace showing the double modifications of Aha0Aha64 with DBCO-PEG4-biotin. Expected mass of starting material is 8804 Da and the mass of tehe product with double modification is 10302 Da.

4.3.4 CuAAC and SPAAC Reactions with Aha 64

We cleaved the N-terminal Aha by aminopeptidase and subjected the resulting protein to CuAAC and SPAAC reaction. With CuAAC chemistry, the reaction did not occur when we used the similar conditions as in the case of Aha0Aha64. We tested the reaction with higher number of equivalents of biotin ligand as well as ligand/Cu complex catalyst but there was no indication of formation of the desired modification, instead we observed only the N-terminus cleaved CCL2-Aha64 (**Figure 4.5 A**).We then introduced DBCO-PEG4-Biotin reagent into the CCL2-Aha64 and got full conversion to the modified product within 2 h, with the expected mass of 9426 Da (**Figure 4.5 B**).

We analysed both samples by LC-MS/MS to ascertain the position of the modification on the correct peptide and indeed this analysis further confirmed that in the case of DBCO-PEG4-Biotin, the modified agent was tagged at Aha64 (**Supplementary Figure S8**). There was, however, no evidence of any such modification of PEG4-Biotin reagent (**Supplementary Figure S9**), indicating that this reagent preferably reacts at the most accessible Met/Aha at the position 0.

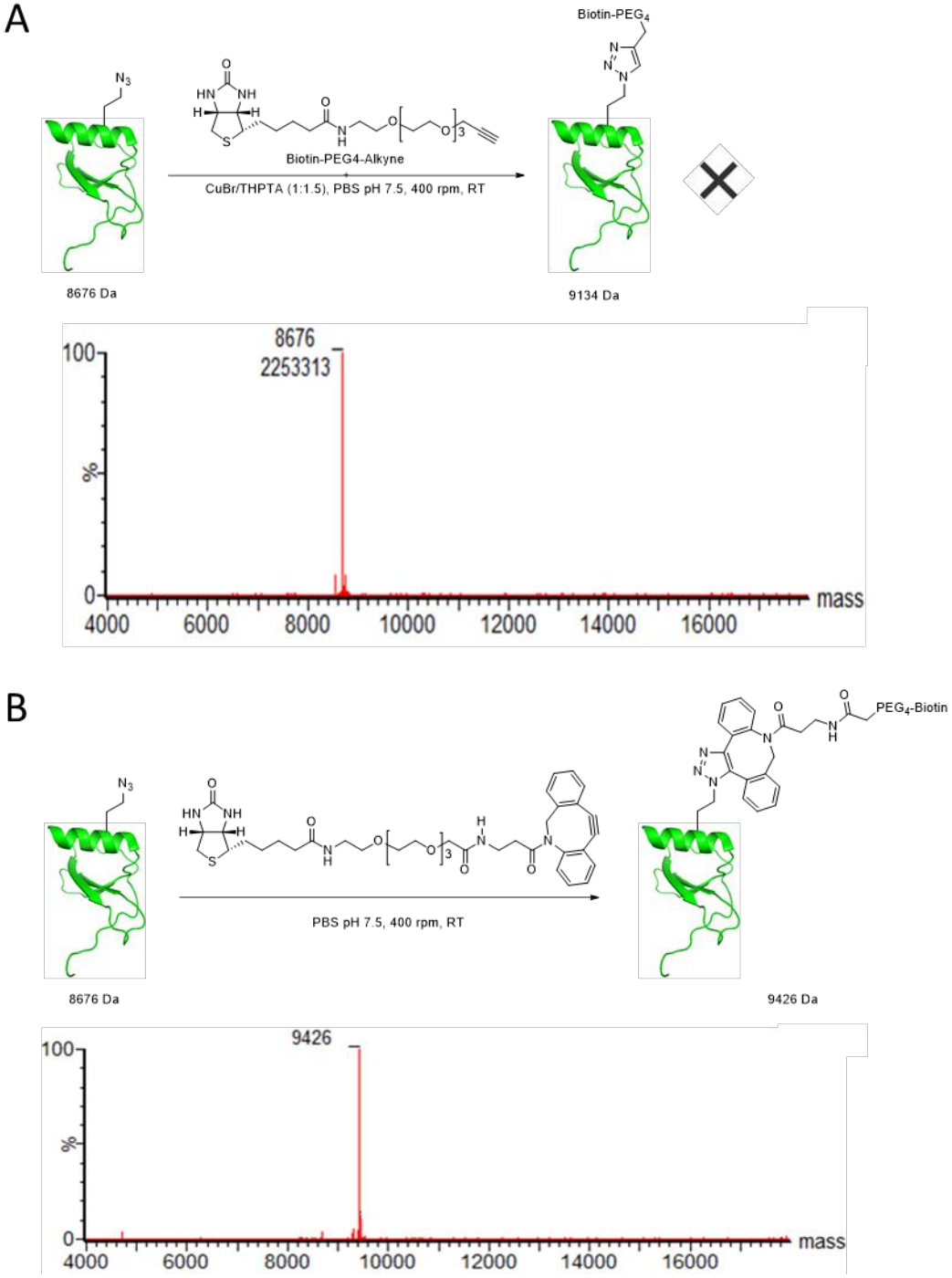


Figure 4.5. CuAAC and SPAAC Click chemistry reactions with Aha64. A) Schematic overview of the reaction of Aha64 with PEG4-biotin in the phosphate buffer at pH 7.5 and LC-MS trace of the reaction sample indicating no reaction of Aha64 with PEG4-Biotin alkyne. Expected mass with mdofied alkyne is 9134 Da, however, mass of only the starting material observed. **B**) SPAAC reaction scheme with Aha64 and LC-MS trace showing the modifications of Aha64 with DBCO-PEG4-biotin. Expected mass of starting material is 8676 Da and the expected mass of of modified product is 9426 Da.

4.3.5 Sequential Labelling of Aha0Aha64

Next we set out to trial a sequential labelling reaction. From the analysis of CuAAC and SPAAC chemistry, it is evident that PEG4-Biotin alkyne reacts at the N-terminal Aha and DBCO-PEG4-Biotin can label at both positions. Therefore, we started off with CuAAC chemistry to install the PEG4-Biotin at Aha0 and after 30 min in the same reaction mixture added the DBCO-PEG4-Biotin reagent. LC-MS analysis confirmed the modifications of both PEG4-Biotin and DBCO-PEG4-Biotin with the expected mass of 10010 Da (**Figure 4.6)**. We also analysed the positions of these modifications by LC-MS/MS which confirmed that PEG4-Biotin reagent was installed at position 0 and DBCO-PEG4-Biotin reagent tagged position 64 (**Supplementary Figure S10**). This result provides us an opportunity to install two different potential reagents, hence two different imaging probes, a fluorescence agent with CuAAC chemistry and PET imaging agent with SPAAC chemistry.

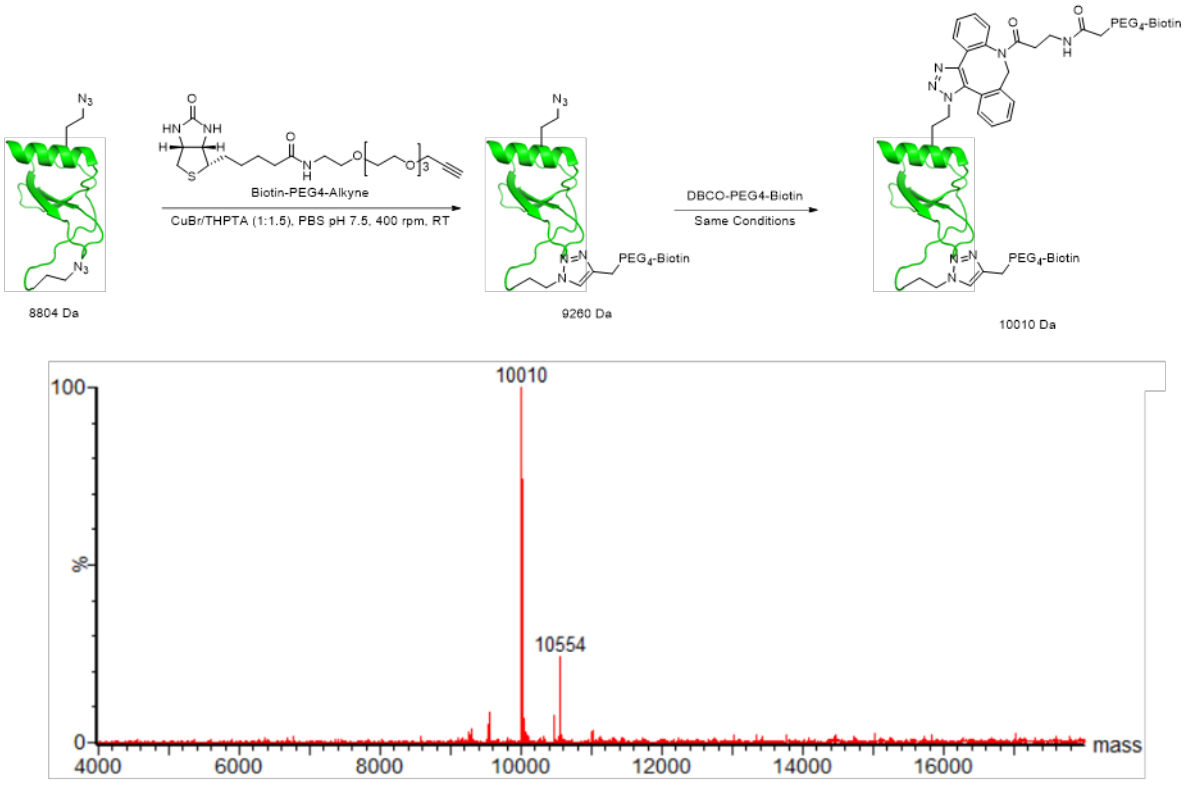


Figure 4.6. Sequential Labelling Reaction. Schematic overview of the sequential labelling of CuAAC and SPAAC reagent with Aha0Aha64. LC-MS characterisation of the final reaction, confirming the sequential modification of PEG4-Biotin and DBCO-PEG4-Biotin at position 0 and 64 respectively. Expected mass of starting material is 8804 Da. Expected mass of PEG4-biotin modification is 9260 Da and the expected mass of PEG4-Biotin modificationat the N-terminal and DBCO-PEG_4-Biotin at the C-terminal is 10010 Da. Mass observed 10010 Da indicated serial modification of PEG4-Biotin and DBCO-PEG4-Biotin at the N- and C- terminal of the CCL2 Aha0Aha64 respectively.

4.3.6 Labelling of Copper-Chelator with CCL2-Aha

The ultimate goal of this project is to develop a PET imaging agent for the detection of TB. We have identified copper-64 (^{64}Cu) as our radionuclide of choice and there are various bi-functional chelators (BFC) which could be used to radiolabel Cu[34-36]. Here we used the cross-bridge chelator DBCO-1,4,8,11-tetraazacyclotetradecane-1-(methanephosphonic acid)-8-(methanecarboxylic acid) (CB-TE1A1P)[37]. We have labelled this chelator with CCL2-Aha at

both positions by using 10 equivalents of chelator as compared to 1 equiv. of modified CCL2-Aha which resulted in ~90% conversion to the doubly modified protein in 1 h (**Figure 4.7 A**). We incubated the reaction for a further 3 h but it did not alter the conversion (**Supplementary Figure S11)**. We attempted to further optimise this reaction with an increased ratio of chelator to protein to see whether we can push this reaction to completion, but no further change in the reaction was observed. At the same time, we attempted this reaction with N-terminal cleaved Aha and as expected, the reaction was successful with the expected mass confirmed by LC-MS (**Figure 4.7 B**).

We then prepared several batches of these reactions and sent them to our collaborators at the University of Pittsburgh, where, they will develop a radiolabelling method to label the ^{64}Cu with this cold reagent. Once radiolabelled, the compound can then be tested in TB infected animal models for uptake studies, bio-distribution studies. This experiment will provide the first insight into the utility of selective CCL2 modified proteins in PET imaging of TB and provide an opportunity to compare the results from previously published randomly modified CCL2 variants.

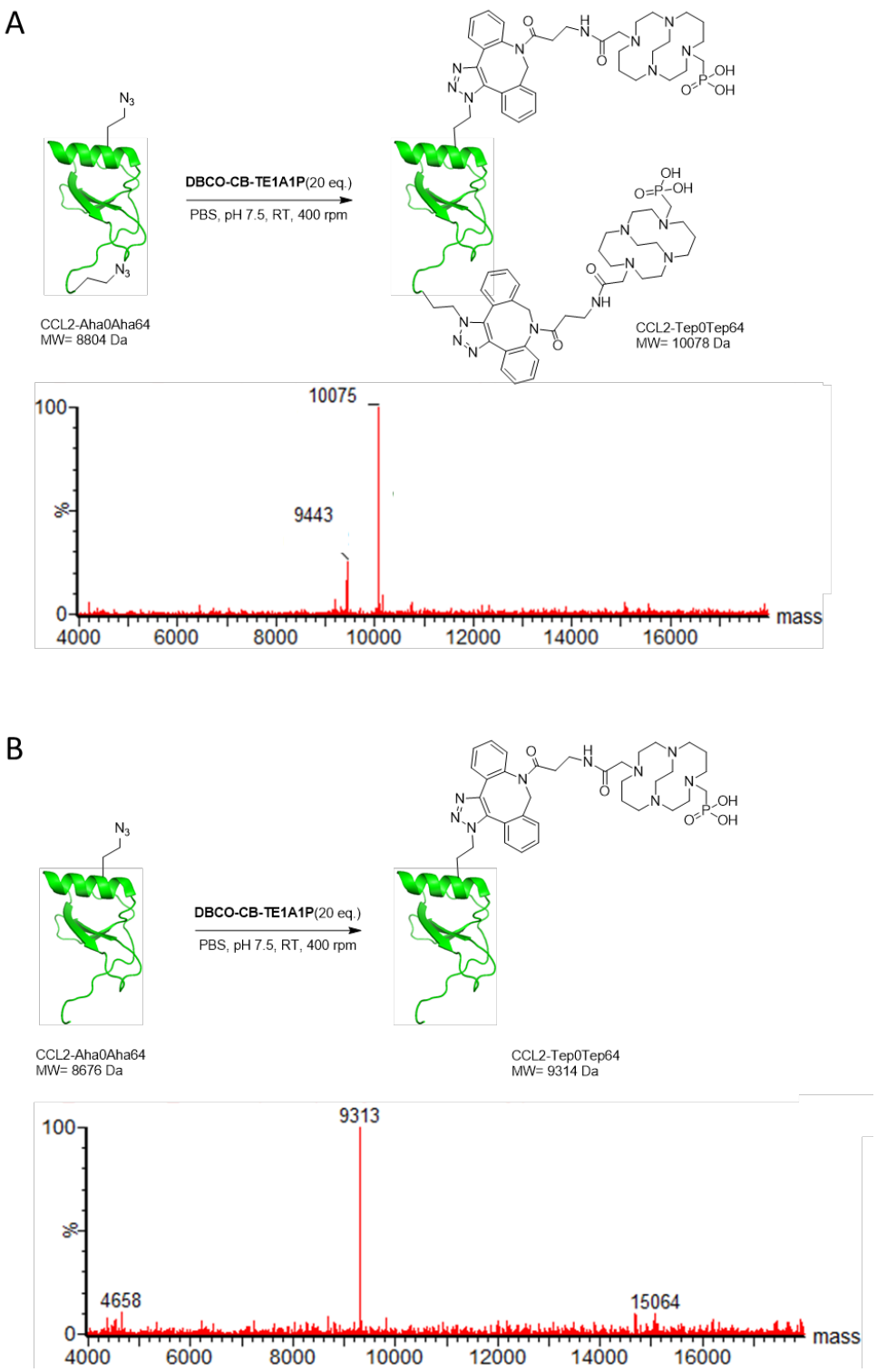
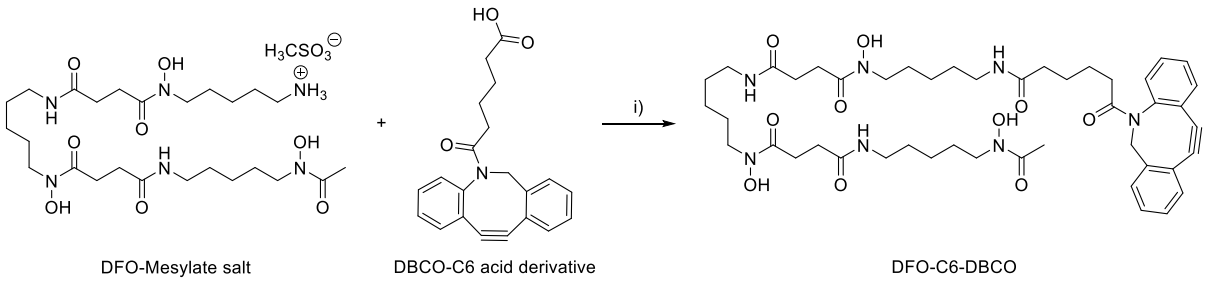


Figure 4.7. CCL2-Aha modifications with Tep reagent. A). CCL2-Aha0Aha64 reaction with DBCO-CB-TE1A1P. From LC-MS characterisation, 90% modification at both sites observed. Expected mass of starting material= 8804 Da, expected mass of doubly modified product= 10078 Da, mass found= 10076 Da **B**). CCL2-Aha64 reaction with DBCO-CB-TE1A1P. From LC-MS characterisation, full

modification with Tep reagent observed after 1 h of reaction. Expected mass of starting material= 8676 Da, expected mass of modified product= 9314 Da, mass found= 9314 Da

4.3.7 Chemical Synthesis and Labelling of CCL2-Aha64 with DFO-C6-DBCO

In addition to ^{64}Cu, we also explored the CCL2-Aha labelling with Zirconium-89 (^{89}Zr). We synthesised the BFC chelator deferoxamine alkyne (DFO-C6-DBCO) as described previously[38] by coupling the DFO-mesylate salt with commercially available DBCO-C6-acid in 57% yield. This chelator allowed the CCL2-Aha labelling using SPACC.



Scheme 4.5. Synthesis of DFO-C6-DBCO. Reagents and conditions: i). HATU, DIPEA, NMM, DMF, 48 h, r.t

For 'cold' CCL2-Aha 64 labelling, we tested the small-scale reaction by mixing 1 equiv. of protein with 50 equiv. of chelator. The reaction monitoring by LC-MS, confirmed ~ 80% conversion in 1 h. Further monitoring up to 4 h slightly improved the conversion but there was still some unlabelled CCL2-Aha 64 left (**Figure 4.8**).

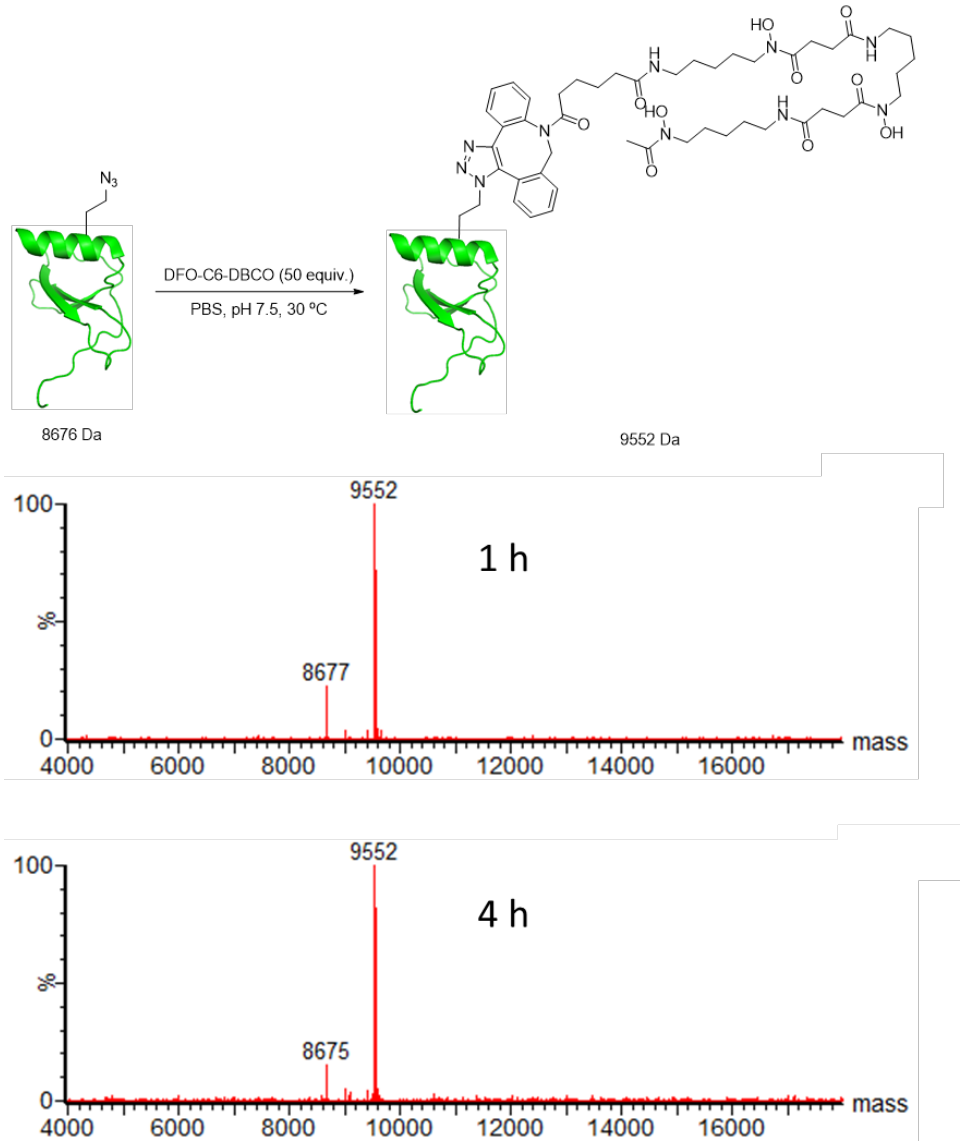


Figure 4.8. CCL2-Aha64 labelling with DFO-C6-DBCO. Reaction carried out in phosphate buffer and monitored by LC-MS over 4 h. After 1 h, the conversion was ~ 80%, which increased slightly to 90% in the next 3 h. Expected mass of starting material= 8676 Da, expected mass of modified alkyne= 9552 Da, mass observed= 9552 Da.

CCR2 binding assays were carried out by Vincent Luscombe, Department of Pathology, University of Oxford in Prof. David Greaves's group. I provided WT CCL2 and its modifications.

4.3.8 CCR2 Binding Studies on Selected Aha Modifications

For the CCR2 binding studies we used the PathHunter eXpress β-Arrestin GPCR cell assay[39-41]. These cells are engineered to co-express the ProLink™ (PK) tagged GPCR and the Enzyme Acceptor (EA) tagged β-Arrestin[42]. Activation of the GPCR-PK induces β-Arrestin-EA recruitment, forcing complementation of the two β-galactosidase enzyme fragments (EA and PK). The resulting functional enzyme hydrolyses the Galacton Star substrate to generate a chemiluminescent signal[39] (**Figure 4.9**). Independently these fragments have no β-gal activity; however, in solution they can be brought together and combine to form an active β-gal enzyme.

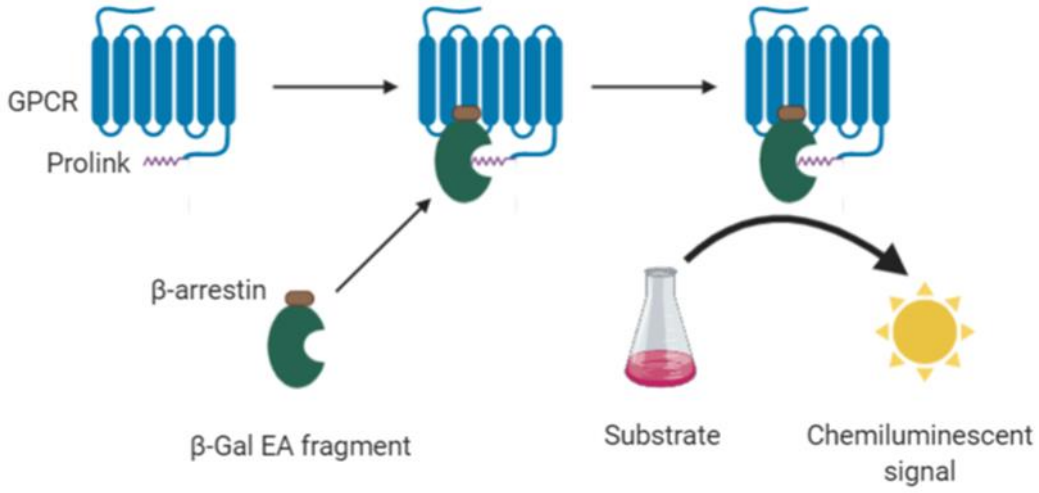


Figure 4.9. The GPCR β-Arrestin recruitment cell assay principle.

The first of the two batches tested for WT CCL2 did not have any activity. This was an old batch where chemokine potentially decomposed and lost its structure. The second batch, however, had the expected β-Arrestin EC50 at CCR2, when compared with recombinant human CCL2 (**Figure 4.10A**). As expected, any modification involving the N-terminal region resulted in loss of CCR2 activity i.e. compounds 1, 3, 4 & 5. Whereas, modifications, at position 64 did retain significant amounts of activity in the case of Aha only (84.2 nM, 65.4%)

and DBCO-PEG4-Biotin (49.6 nM, 81.6%), whereas the cross-bridge chelator showed detectable activation of CCR2 but with a reduced Emax (87.5 nM, 38%) when compared with the recombinant protein (**Figure 4.10B**).

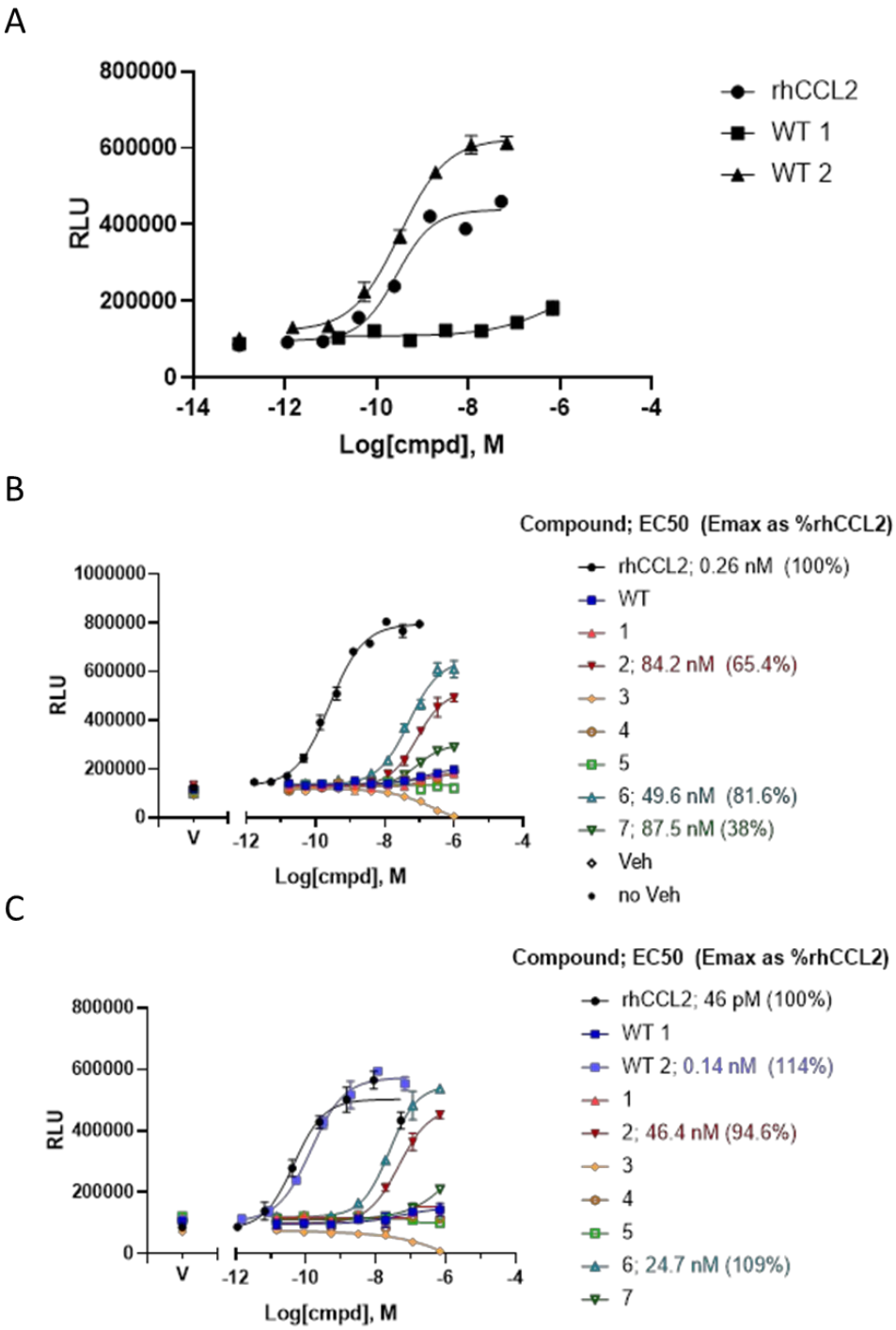


Figure 4.10. PathHunter β-Arrestin GPCR Assay using modified Aha. A) Commercially available recombinant human CCL2 was assayed against two separate batches of CCL2 expressed in house. One

of the batches did not show any activity while the recently expressed batch showed similar activity to the CCL2. Agonist was prepared in OptiMEM + 0.1% BSA. **B**) CCL2 analogues were tested for activity at CCR2 by measuring downstream β-arrestin recruitment using the DiscoverX PathHunter eXpress assay. Cells were stimulated for 90 minutes before detection reagents were added and luminescence detected. Agonist was prepared in Cell Plating Reagent. **C**) Agonist was prepared in RPMI + 0.1% BSA. Data expressed as mean relative luminescence units (RLU) ± SEM of experiment performed in duplicate.

4.3.9 Biophysical Characterisation of Aha modified MCP-1

After determining the CCR2 activity of the modified CCL2 variants, we assessed the relationship of secondary structure with modifications at CCL2. We used CD spectroscopy to study the structural properties of the CCL2 WT and modified CCL2 with Aha and variants. We used similar concentration for WT protein and the modifications. Data analysis from CD spectroscopy revealed that CCL2 WT, Aha0Aha64 with DBCO modifications did not have any bearing on secondary structure. In addition, Aha64 with DBCO and TE1A1P chelator modification, also maintained secondary structure (**Figure 4.1**1).

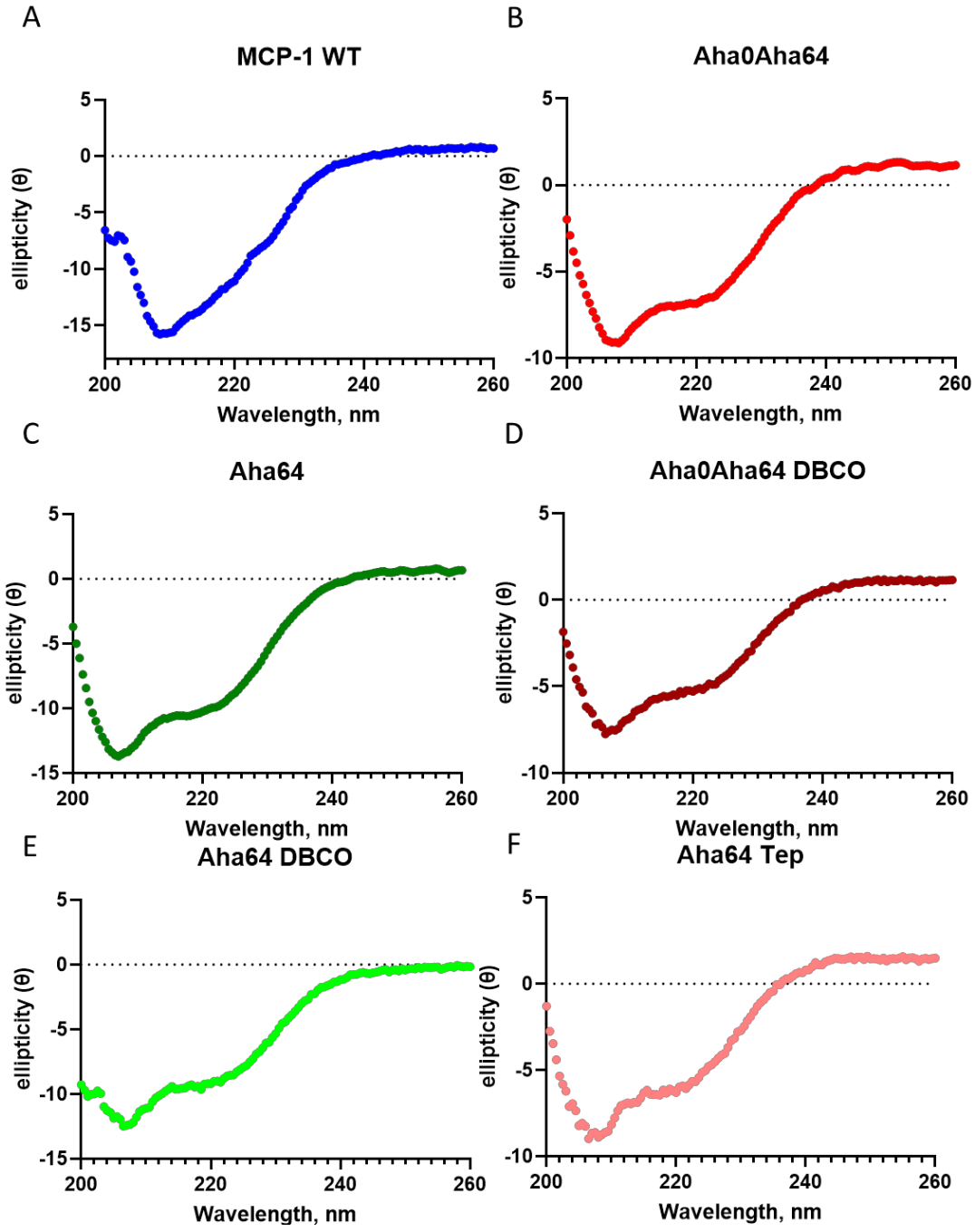


Figure 4.11. CD spectra of CCL2 WT and Aha modifications.

4.4 Conclusions

In summary, we were able to modify wild type CCL2 by the incorporation of an unnatural amino acid Aha at two sites. Using aminopeptidase we cleaved the N-terminal Aha giving access to two modified proteins, N-terminal cleaved and N-terminal retained CCL2-Aha. We modified both variants through CuAAC and SPAAC chemistry that allowed the future introduction of potential PET imaging probes for TB diagnosis. Following completion of protein assembly, and confirming the modification site through LC-MS/MS, we carried out cell assays to test the activity of wild type CCL2, CCL2-Aha and variants with probes. The preliminary data indicated that modifications at the N-terminus of the protein had an adverse effect on the CCR2 binding. On the other hand, the central Aha64 modifications did retain a significant amount of activity when tested against the rhCCL2. While information obtained from the cell assays is significant, the next step in this work will be to study the structure/activity relationship of wild CCL2, modified CCL2 and variants. Together with our collaborators, we attempted initial ^{64}Cu chelator radiolabelling of CCL2-Aha for future PET imaging of TB macrophages *in vitro* and *in vivo*. This work, after optimisation, will allow for pre-clinical PET imaging of TB macrophages. In addition, the SPAAC chemistry approach with modified CCL2-Aha could be utilized to generate fluorescent or radioisotope based probes for other imaging applications.

4.5 Experimental

4.5.1 General

The pAED-4 plasmid encoding CCL2-WT gene was obtained from Prof. T. M. Handel at University of California, San Diego. All buffer chemicals were purchased from Sigma-Aldrich and used as supplied. *E. coli* Origami 2 (DE3) and B834 (DE3) cells were purchased from Novagen. Recombinant *Aeromonas* Aminopeptidase was purchased from PEPROTECH. CuBr, CuSO4, ligand THPTA, alkyne-PEG4- biotin, DBCO-PEG4-biotin and FITC were purchased from Sigma-Aldrich. DFO-C6-DBCO was synthesied in house, DBCO-CB-TE1A1P chelator was kindly provided by Dr. Qin Zhu at University of Pittsburgh. PathHunter eXpress CCR2 CHO-K1 β-arrestin cells (93-0192E2) were purchased from DiscoverX directly as stable expressing cell lines. Recombinant human CCL2 was purchased from R & D systems (279-MC-010). White 384 well microplates were purchased from Greiner (781098).

Proteins were purified using an ÄKTA FPLC system UPC-900 (GE Healthcare Life Sciences) at 4 °C and the purification was monitored by UV absorption at 280 nm. All buffers used were prepared with Milli-Q water and sterile filtered (0.22 μm). LB-agar plates and LB media (Fisher Scientific) were used for protein expression experiments. Ampicillin Na-salt (Sigma Aldrich) and IPTG (Sigma-Aldrich) were used as H_2O-stocks as detailed below and stored at -20 °C. For biological procedures, media, glass and plastic equipment were sterilized by autoclaving (121 °C, 20 minutes) in an LTE Scientific Touchclave-R autoclave. The handling of bacterial samples and media was carried out in a well-ventilated laminar-flow hood. Protein concentrations were determined with a Thermo Scientific Nanodrop ND1000 Spectrophotometer.

Sodium dodecyl sulfate-polyacrylamide gel electrophoresis (SDS-PAGE) was carried out using pre-casted Invitrogen Novex bis-Tris gels (12%, 12 or 17 wells). For analysis, 8 μL of the desired sample was mixed with 2 μL of 5 x SDS loading dye and incubated at 95 °C for 10

min. As a reference, 5 µL of SeeBlue™ Plus2 Pre-stained Protein Standard (3-198 kDa) was added into the first lane. Electrophoresis was then performed in MES buffer with 200 V of continuous power for approximately 45 min. The gel was removed from the gel cassette and stained with Instant Blue (Expedeon Ltd.) for 90 min. The staining solution was decanted and the gel washed with water overnight prior to scanning. If a Western Blot analysis was carried out, the gel was not stained with Instant Blue, but transferred to a nitrocellulose membrane using the Thermo Fisher Scientific iBlotTM Gel Transfer Device according to the manufacturer's instructions. After the transfer, the nitrocellulose membrane was incubated with the blocking solution – BSA (2.5 g) in TBST (50 mL, 50 mM Tris, 150 mM NaCl, 0.05% Tween 20, pH 7.5) for 1 hr at room temperature. The membrane was washed with TBST (3 x 20 mL) to remove the blocking solution and then incubated with a solution of BSA (0.3 g) in TBST buffer (30 mL) containing the primary antibody for 1.5 h at room temperature or overnight at 4 °C according to the manufacturer's instructions. The membrane was washed with TBST buffer (2 x 50 mL) and water (50 mL) before incubation of the secondary antibody-alkaline phosphatase conjugate for 1 hr at room temperature. The bands were visualized on membrane by adding BCIP/NBT alkaline phosphatase substrate drop by drop.

The general chemistry procedures are described in chapter experimental section.

4.5.2 In-solution Digestion for proteomics

In a 1.5 mL Eppendorf tube 15 µL (15 µg protein) of an aliquot of desired protein sample was taken and reduced with 2 µL of 85 mM DTT in 50 mM ammonium bicarbonate (10 mM final concentration of DTT) and incubated for 40 min at 56 °C. The reaction mixture was then alkylated with 7 µL of 55 mM IAA in 50 mM ammonium bicarbonate solution (final concentration of IAA 20 mM) and incubated for 30 min in the dark at RT. The traction mixture

was then further reduced again with 3 µL of 85 mM DTT in 50 mM ammonium bicarbonate solution for 10 min in the dark at RT, in order to eliminate excess IAA.

To perform in-solution digestion trypsin was added in a 1:20 to 1:50 (W/W) ratio with regards to the total protein content of the sample. We prepared a stock-solution of 1 mg/mL and added 5 µL in the sample solution. Contents of the sample were mixed carefully and the digestion carried out overnight at 37 °C. The following day a second in-solution trypsin digestion was carried out in 80% ACN. For this digestion trypsin was added in a 1:100 ration as opposed to the total protein content of the sample. After adding 80% ACN to the final concentration, the sample was incubated at 37 °C for 3 h. Trypsin digestion was stopped by adding 5% FA and then the digested sample was dried to completion by freeze drying.We then re-dissolved the peptide in 10 µL of 0.1% FA and used Zip Tip protocol to clean up the sample.

4.5.3 Zip Tip Protocol for sample clean up

For sample clean up, we used buffer A (100% ACN) and buffer B (98% Milli-Q water, 2% ACN and 0.1% FA). The sample was acidified by adding 20 µL of 0.1% FA. Zip Tip was equilibrated by first aspirating 10 µL of buffer A into the tip and dispensing to waste. This step was repeated 3 times and carried out with buffer B as well. Once equilibrated, peptide was bound to the tip by aspirating up to 10 cycles of the reaction mixture and then washed by aspirating 10 µL of buffer B and dispense to waste and repeating one more time. Sample was then eluted from the Zip Tip into the clean recovery vial. For elution 10 µL of buffer C (50% ACN, 50% Milli-Q water and 0.1% FA) was dispensed into a clean Eppendorf tube. Elution solution was aspirated and dispensed through Zip tip at least 5 times without introducing air. We then dispensed 10 µL of buffer A into a clean Eppendorf tube, aspirated and dispensed elution solution through Zip Tip at least 5 times without introducing air. Sample was then dried under constant nitrogen flow and re-suspended in 10 µL buffer B for LC-MS/MS analysis.

4.5.4 LC-MS/MS Data Acquisition on Orbitrap Elite

Resulting tryptic peptides were analysed on a NanoAcquity-UPLC system (Waters) connected to an Orbitrap Elite mass spectrometer (Thermo Fischer Scientific) possessing an EASY-Spray nano-electrospray ion source (Thermo Fischer Scientific). The peptides were trapped on an in-house packed guard column (75 µm i.e. x 20 mm, Acclaim PepMap C18, 3µm, 100 Å) using solvent A (0.1% Formic Acid in water) at a pressure of 140 bar. The peptides were separated on an EASY-spray Acclaim PepMap® analytical column (75 µm i.d. × 50 mm, RSLC C18, 3 µm, 100 Å) using a linear gradient (length: 100 minutes, 3 % to 60 % solvent B (0.1% formic acid in acetonitrile), flow rate: 300 nL/min). The separated peptides were electrosprayed directly into the mass spectrometer operating in a data-dependent mode using a CID based method. Full scan MS spectra (scan range 350-1500 m/z, resolution 120000, AGC target $1e^6$, maximum injection time 250 ms) and subsequent CID MS/MS spectra (AGC target $5e^4$, maximum injection time 100 ms) of 10 most intense peaks were acquired in the Ion Trap. CID fragmentation was performed at 35 % of normalized collision energy and the signal intensity threshold was kept at 500 counts. The CID method used performs beam-type CID fragmentation of the peptides.

4.5.5 LC-MS/MS data analysis

The analysis was performed with Peaks 8.5. The raw MS file was searched against the respective protein sequence. Trypsin with a maximum number of 3 missed cleavages and one unspecific end was selected as the protease. Carbamido methylation (Cysteine) was set as a fixed modification, Oxidation (Methionine), Deamination (Asparagine, Glutamine) and the desired modification was set as variable modifications. Precursor mass tolerance was set as 20

ppm. Fragment mass tolerances for CID were set to 0.8 Da respectively. All spectra were manually validated. All peptides present a -10lgP> 20, spectra were manually checked and validated or disqualified.

4.5.6 β-arrestin recruitment

The recruitment of β-arrestin 2 to CCR2 was measured using the DiscoverX PathHunter® assay following the manufacturers protocol. In brief, CHO-K1 cells stably expressing human CCR2 tagged on the C-terminus with an enzyme fragment and β-arrestin fused to an N-terminal deletion mutant of beta-galactosidase were seeded in 384-well plates at a density of 2,000 cells/20µL/well in AssayComplete™ Cell Plating 0 Reagent and incubated at 37 ◦C, 5 % CO2 for 48 h. The cells were stimulated with agonist for 90 min at 37 ◦C, 5 % CO2. Cell lysis and luminescence detection were performed as per the manufacturer's protocol. Luminescence measurements were taken at 1 second/well 3h after detection reagents were added using a PHERAstar FS microplate reader (BMG Labtech) and data was analysed using Prism (GraphPad Software, La Jolla California USA, www.graphpad.com).

For CCR2 activity, we used a CHO-CCR2-β-arrestin expressing cell line from DiscoverX and the reagents from the PathHunter detection kit. We obtained the recombinant human CCL2 from R & D systems for the main control. We then used our wild type CCL2 to compare the activity with the commercially available CCL2. We used two proteins with different modifications (Aha0Aha64 and Aha64); i). Single Aha modification with PEG4-Biotin alkyne at position 1 and ii). Double Aha modification with DBCO-PEG4-Biotin. In addition, we cleaved off the N-terminal Aha by aminopeptidase, and did two further modifications; i). Modification of Aha with DBCO-PEG4-Biotin at position 64 and ii). With cross-bridge copper chelator. The concentrations of the modified proteins were kept similar to the wild type protein expressed in house.

4.5.7 Expression, Purification and characterisation of CCL2-WT

For the expression of CCL2-WT, the recombinant plasmid was transformed into Origami 2 (DE3) strain using general transformation protocol. This strain was chosen as the expression host because it has mutation in both the thioredoxin reductase (*trxB*) and glutathione reductase (*gor*) genes, which facilitates disulfide bond formation in the *E. coli* cytoplasm and eliminate the need for a refolding step.

For the expression, a single colony was used to inoculate LB broth medium (10 mL) containing ampicillin solution (10 µL, 100 mg/mL) for 16 h at 37 °C. Overnight starter culture was used to inoculate 1 L of LB broth culture media containing 1 mL of ampicillin stock solution (100 mg/mL). The culture was incubated at 37 °C until an OD600 value of 0.6 was obtained. The over-expression was induced by adding 0.5 mL of aqueous IPTG stock solution (1 M) to a final concentration of 0.5 mM and the culture was incubated at 30 °C for 1h, followed by adding 2 mL of rifampicin stock solution (10 mg/mL in 67% methanol with 0.17 N NaOH) to a final concentration of 24 µM. The culture was incubated at 30°C for additional 4 h and the cells were harvested by centrifugation (8000 rpm, 15 min, 4 °C) and flash-frozen in liquid nitrogen. The cells pellets were stored at -20 °C until further manipulation.

For the purification, the cell pellet was thawed and re-suspended in 30 mL of the binding buffer (10 mM K_2HPO_4, 150 mM NaCl, 5 mM $MgCl_2$, pH 7.5) containing one tablet of Complete® protease inhibitor cocktail (Roche) and 1.5 mg DNase (3000 U). The mixture was stirred vigorously at 4 °C for 1 hr. The suspension was subjected to sonication pulses (5 x 30 s sequences with 1 min interval in between: 2 s sonication, 2 s off, 40 % Amplitude) on ice. The lysed cells were then centrifuged (25000 rpm, 4 °C, 40 minutes) to remove the cell debris and the supernatant was collected and filtered through a 0.2 µm syringe filter. The filtered supernatant was loaded onto a pre-equilibrated 5 mL SP HP column (GE Life Sciences) with binding buffer. The column was washed with 10 column volumes (CV) of binding buffer and

the protein was eluted with a linear gradient of 0 to 100% elution buffer (10 mM K_2HPO_4, 1 M NaCl, 5 mM $MgCl_2$, pH 7.5) over 20 CV (Figure S1). The column fractions were collected and analysed by SDS-PAGE. Fractions containing CCL2-WT were combined, desalted and concentrated to a final concentration of 1.0 mg/mL by using the Vivaspin sample concentrator (MWCO 3,000 Da). The protein expression level was 0.5 mg/L culture.

The concentrated protein was further purified by size exclusion chromatography (HiLoad 16/600 Superdex 75 PG column (GE Life Sciences)). The column was washed with water (1.2 CV) followed by equilibration with the binding buffer as descried above. The protein sample was loaded onto the column and eluted with 1.2 CV of the same buffer. The purification was performed at a flow rate of 0.5 mL/min and 3 mL fractions were collected. The eluted fractions were analysed by SDS-PAGE and LC-MS, indicating a high-purity of the protein (expressed with N-terminal Met0, **Figure S1**). The protein was stored as 100 µL aliquots with the concentration of 0.4 mg/mL at -80 °C.

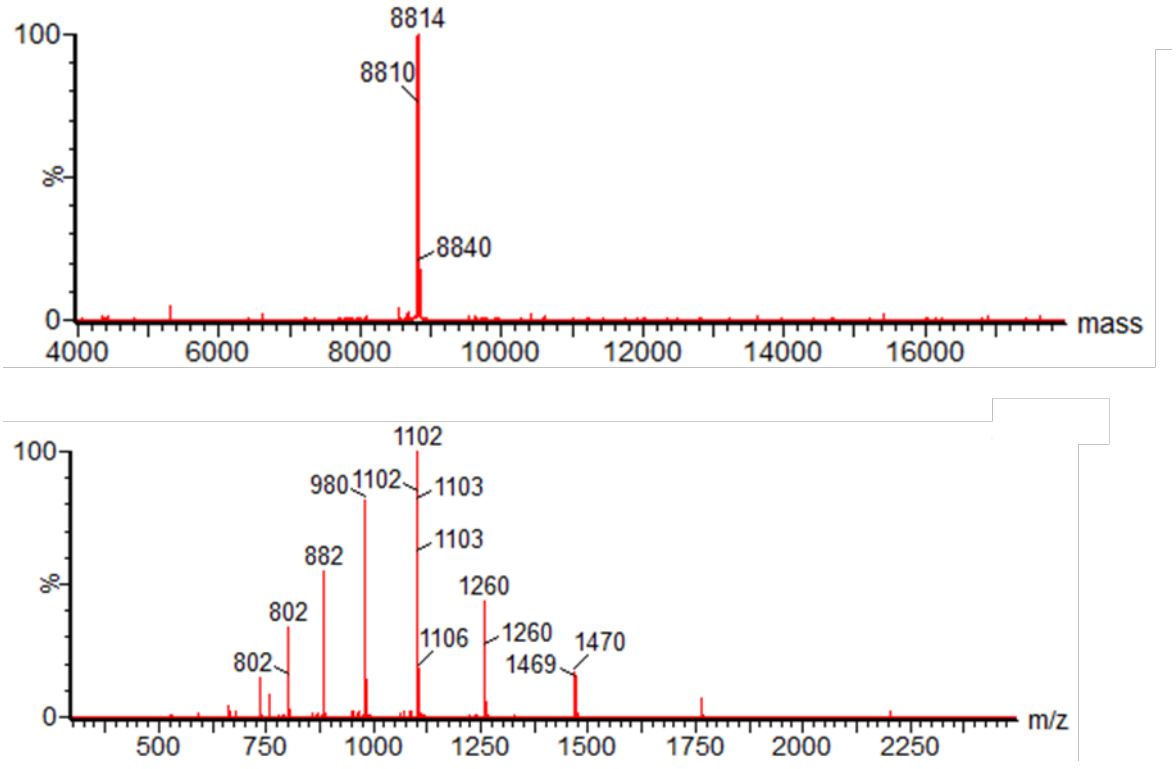


Figure S1: LC-MS characterisation of CCL2 WT

4.5.8 Incorporation of L-Azidohomoalanine into CCL2 WT

Methionine auxotrophic strain B834 (DE3) was chosen as the expression host for the unnatural amino acid L-Azidohomoalanine (Aha) incorporation. Cells and plasmid were first thawed on ice. An aliquot of plasmid DNA (2.0 μL of 44.0 ng/μL) was added to 50 μL of B834 (DE3) cells in a 14 mL polyene tube, mixed and incubated on ice for 30 min. The transformation mixture was then heat-shocked at 42 °C for 40 seconds and immediately chilled on ice for 2 min. SOC medium (300 μL) was added and the mixture incubated for 60 minutes at 37 °C with shaking at 250 rpm. The transformed cells were then plated on a freshly prepared LB agar plates containing Ampicillin (100 mg/mL) and incubated for 14 h at 37 °C. The plates were stored at 4 °C.

The following day, a single colony was used to inoculate LB broth medium (10 mL) containing ampicillin solution (10 μL, 100 mg/mL) for 16 h at 37 °C. Overnight starter culture was used to inoculate 1 L freshly prepared selenomet media containing 0.6 mL of aqueous L-Met solution (10 mg/mL, final concentration 0.04 mM) and 1 mL of ampicillin stock solution (100 mg/mL). The culture was incubated at 37 °C until an OD600 value of 0.8 was reached and centrifuged at 4700 rpm for 20 min. The cell pellet was washed with 3 x 300 mL of selenomet media (methionine free) and then re-suspended in 1 L freshly prepared selenomet media which was inoculated with L-Aha (final concentration 1 mM) and 1 mL of ampicillin stock solution (100 mg/mL). The culture was left to grow 37 °C for additional 15 min and then 30 °C for 15 min. Protein over-expression was induced by adding 0.5 mL of aqueous IPTG stock solution (1 M) to a final concentration of 0.5 mM and the culture was incubated at 30 °C for 1 h, followed by adding 2 mL of rifampicin stock solution (10 mg/mL in 67% methanol with 0.17 N NaOH) to a final concentration of 24 μM (the rifampicin addition step can be omitted without influence of the expression level). The culture was incubated at 30 °C for additional 4 h and the cells

were harvested by centrifugation (8000 rpm, 15 min, 4 °C) and flash-frozen in liquid nitrogen. The cells pellets were stored at -80 °C until further manipulation.

The cell pellet was thawed and re-suspended in 20 mL of the binding buffer (10 mM K_2HPO_4, 150 mM NaCl, 5 mM $MgCl_2$, pH 7.5) containing one tablet of Complete® protease inhibitor cocktail (Roche) and 1.5 mg DNase (3000 U). The mixture was stirred vigorously at 4°C for 1 hr. The suspension was subjected to sonication pulses (5 x 30 s sequences with 1 min interval in between: 2 s sonication, 2 s off, 40% Amplitude) on ice. The lysed cells were then centrifuged (25000 rpm, 4 °C, 45 minutes) to remove the cell debris and the supernatant was collected and filtered through a 0.2 μm syringe filter. The filtered supernatant was loaded onto a pre-equilibrated 5 mL SP HP column (GE Life Sciences) with binding buffer. The column was washed with 10 CV of binding buffer and the protein was eluted with a linear gradient of 0 to 100% elution buffer (10 mM K_2HPO_4, 1 M NaCl, 5 mM $MgCl_2$, pH 7.5) over 20 CV. The column fractions were collected and analysed by SDS-PAGE. Fractions containing the expected protein were combined, desalted and concentrated to a final concentration of 0.4 mg/mL by using the Vivaspin sample concentrator (MWCO 3,000 Da).

After the FPLC purification on a SP HP column, the concentrated impure protein was further purified by size exclusion chromatography (HiLoad 16/600 Superdex 75 PG column (GE Life Sciences)). The column was washed with water (1.2 CV) followed by equilibration with the binding buffer as descried above. The protein sample was loaded onto the column and eluted with 1.2 CV of the same buffer.

The purification was performed at a flow rate of 0.5 mL/min and 2 mL fractions were collected. The eluted fractions were analysed by SDS-PAGE and LC-MS, indicating a high-purity of the protein (**Figure S1 B & C**). The protein CCL2-Aha0Aha64 was expressed with N-terminated Aha0 incorporated except for the expected Aha64 incorporation, which was further confirmed through LC-MS/MS analysis (**Figure S6**). The protein was stored as 100 μL aliquots in the

storage buffer (10 mM K_2HPO_4, 150 mM NaCl, and 5 mM $MgCl_2$, pH 7.5) with the concentration of 1.0 mg/mL at -80 °C.

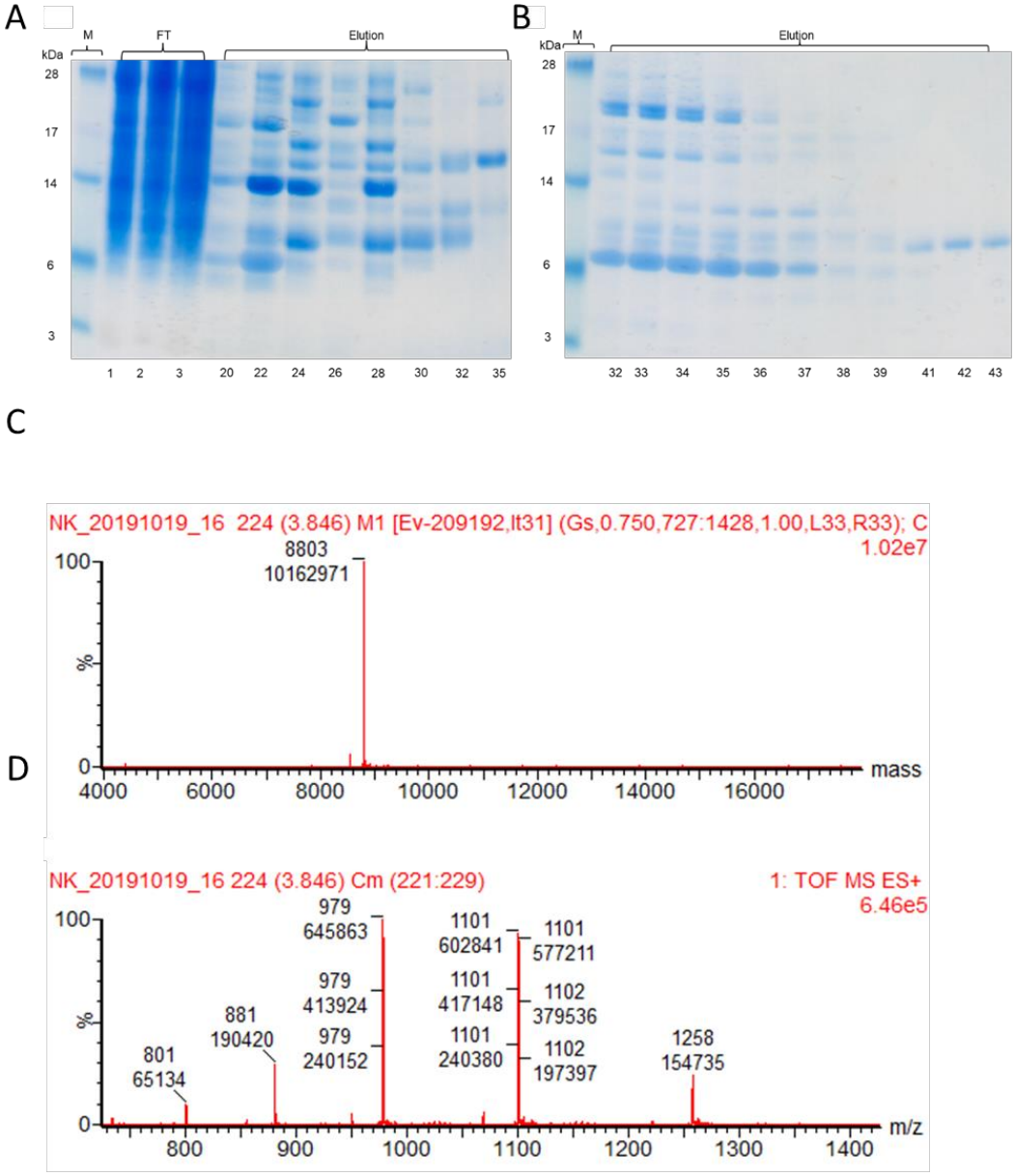


Figure S2. SDS-Gel and LC-MS characterisation of CCL2-Aha0Aha64. A). SDS-gel from FPLC purification. B). SDS-Gel characterisation of CCL2-Aha0Aha64 from SEC purification. C). LC-MS integrated spectrum of CCL2-Aha0Aha64 and D). Representative ion series from LC-MS chromatogram.

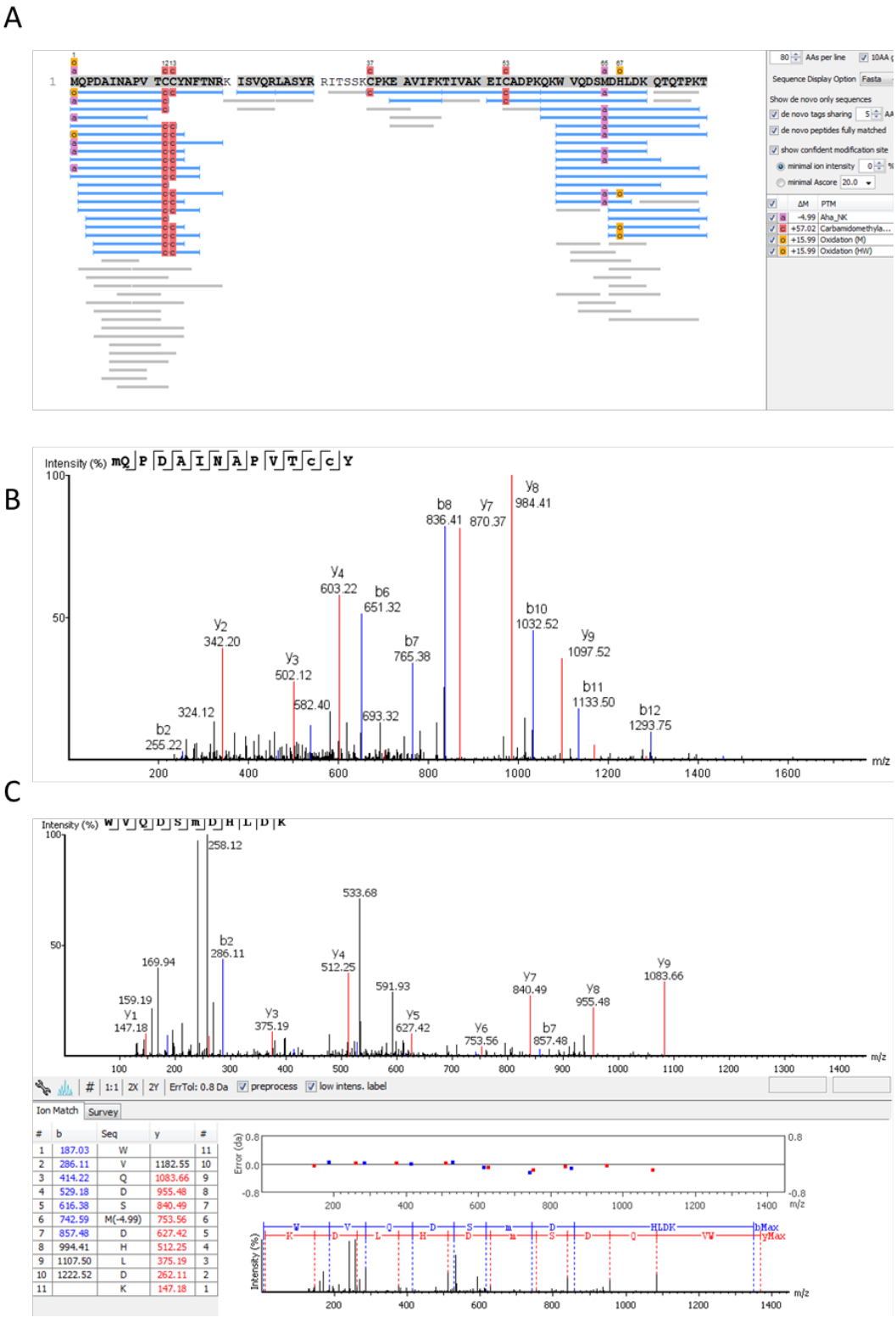
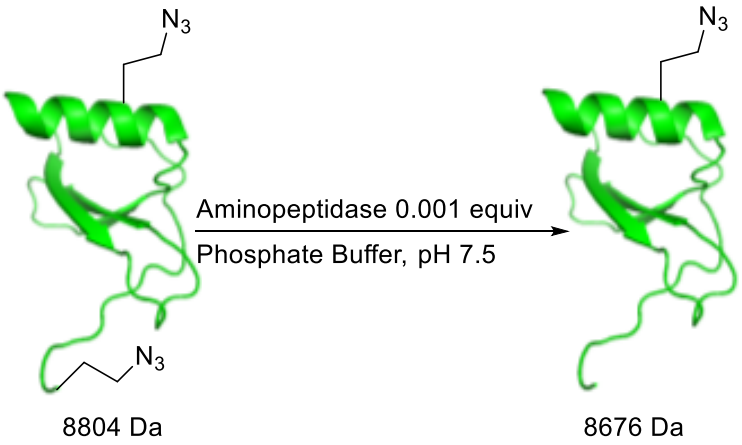


Figure S3. LC-MS/MS characterisation of Aha incorporation into CCL2. A) Sequence coverage obtained after LC-MS/MS analysis. Aha modifications identified at position 0 and

64, highlighted in purple. B) Peptide fragmentation shows the modification site of Aha0. C) Peptide fragment spectra indicating the Aha64 modification.

4.5.9 Enzymatic cleavage of N-terminal Aha



The N-terminal Aha was cleaved by adding the catalytic amount of aminopeptidase. This was achieved in 100 µL scale in 1.5 mL Eppendorf tube by adding 3.6 µL of aminopeptidase (0.1 mg/mL, 0.001 equiv.) and the protein was incubated on ice for 10 min. 3 µL of sample was taken and diluted to 40 µL in 0.1 % formic acid and analysed by LC-MS. The cleavage was confirmed by this analysis (**Fig. S3 A**) and no further cleavage was observed over time.

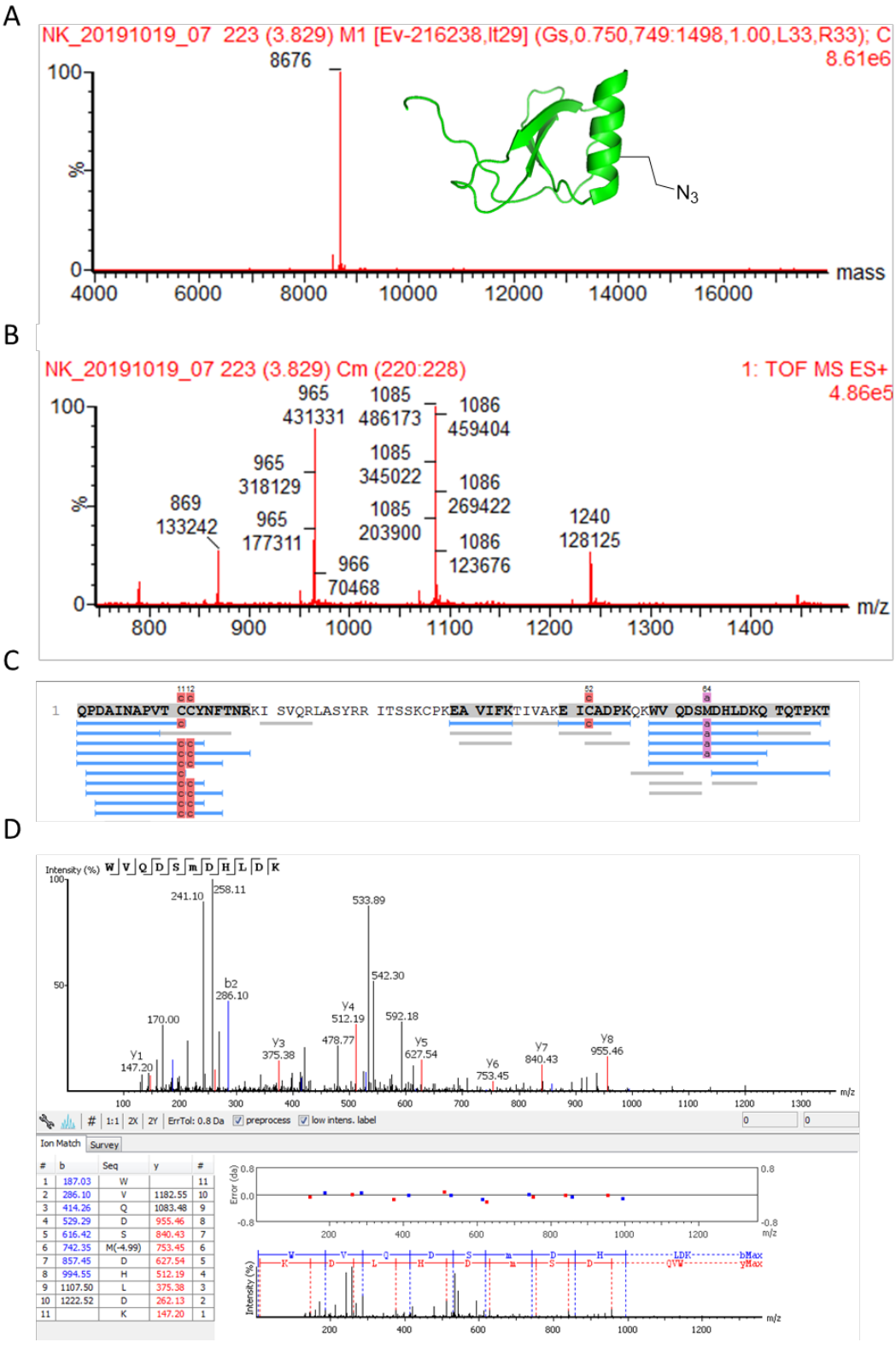
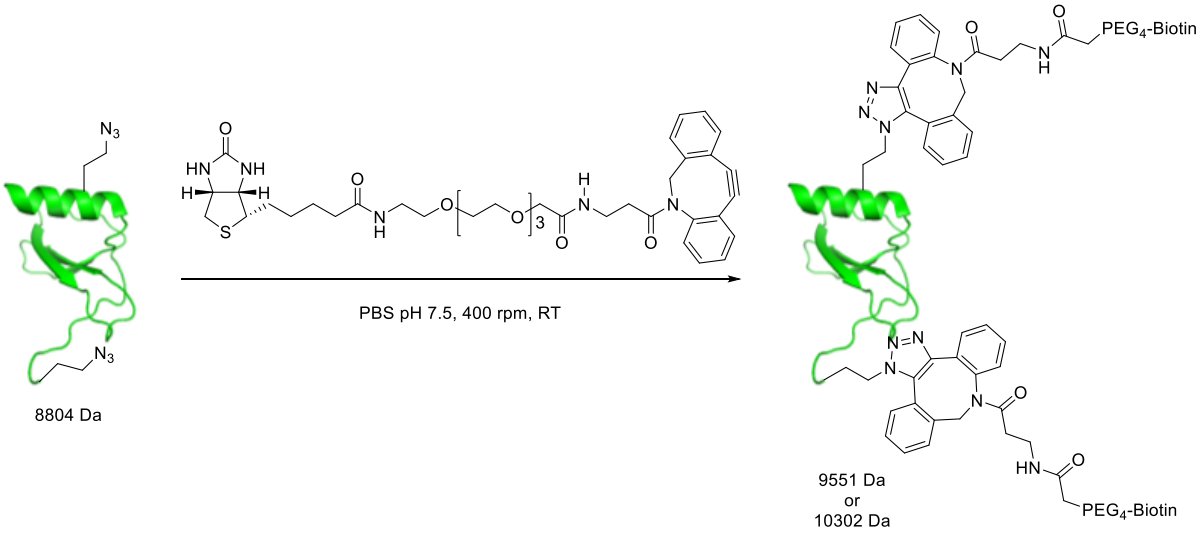


Figure S4. N-terminal cleavage of CCL2-Aha0Aha64 by aminopeptidase. A) LC-MS integrated spectrum for the characterisation of N-terminal cleavage of CCL2-Aha0Aha64, the mass 8676 corresponds to the loss of one Aha. B) Ion series from the LC-MS chromatogram.

C) Sequence coverage spectra obtained after LC-MS/MS analysis. Aha modifications identified at position 64 is shown (purple highlighted in the spectra). D) Peptide fragmentation shows the modification site of Aha at position 64.

4.6 Protein Modification using CCL2-Aha0Aha64

4.6.1 CCL2-Aha0Aha64 through SPACC chemistry



An aliquot of the CCL2-Aha0Aha64 stock solution (50 µL, c = 1.0 mg/mL, 0.114 mM) in pH 7.5 buffer was thawed on ice. 25 µL solution was pipetted into a micro centrifugation tube (0.2 mL), to which an aqueous solution of DBCO-PEG4-biotin (20.0 mg/mL, 26.7 mM, 2.1 µL, and 20 equiv.) was added. The reaction mixture was quickly vortexed (5 sec) and incubated at RT in a thermoshaker at 400 rpm. 3 µL aliquot of reaction mixture were taken at different time points and diluted to 40 µL for LC-MS monitoring of the reaction process. Full conversion was obtained in 2 hrs and the reaction mixture was then desalted by using 7k MWCO Zeba Micro Spin Desalting Columns or 3.5k MWCO Slide-A-Lyzer MINI Dialysis Unit followed by a LC-MS characterization.

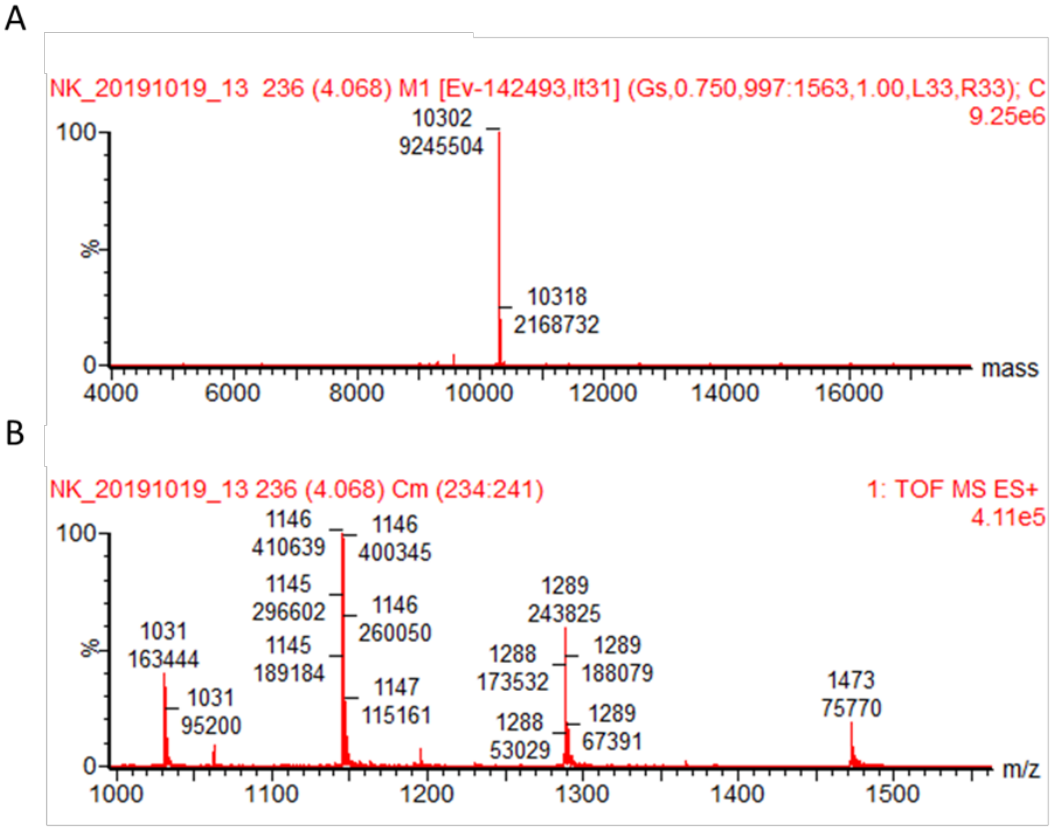


Figure S5. SPACC Chemistry reaction with double CCL2-Aha modification. A) LC-MS integrated spectrum showing the mass of 10302 that corresponds to CCL2-Aha modified DBCO-PEG4Biotin at position 0 and 64. B) the ion series from the LC-MS chromatogram.

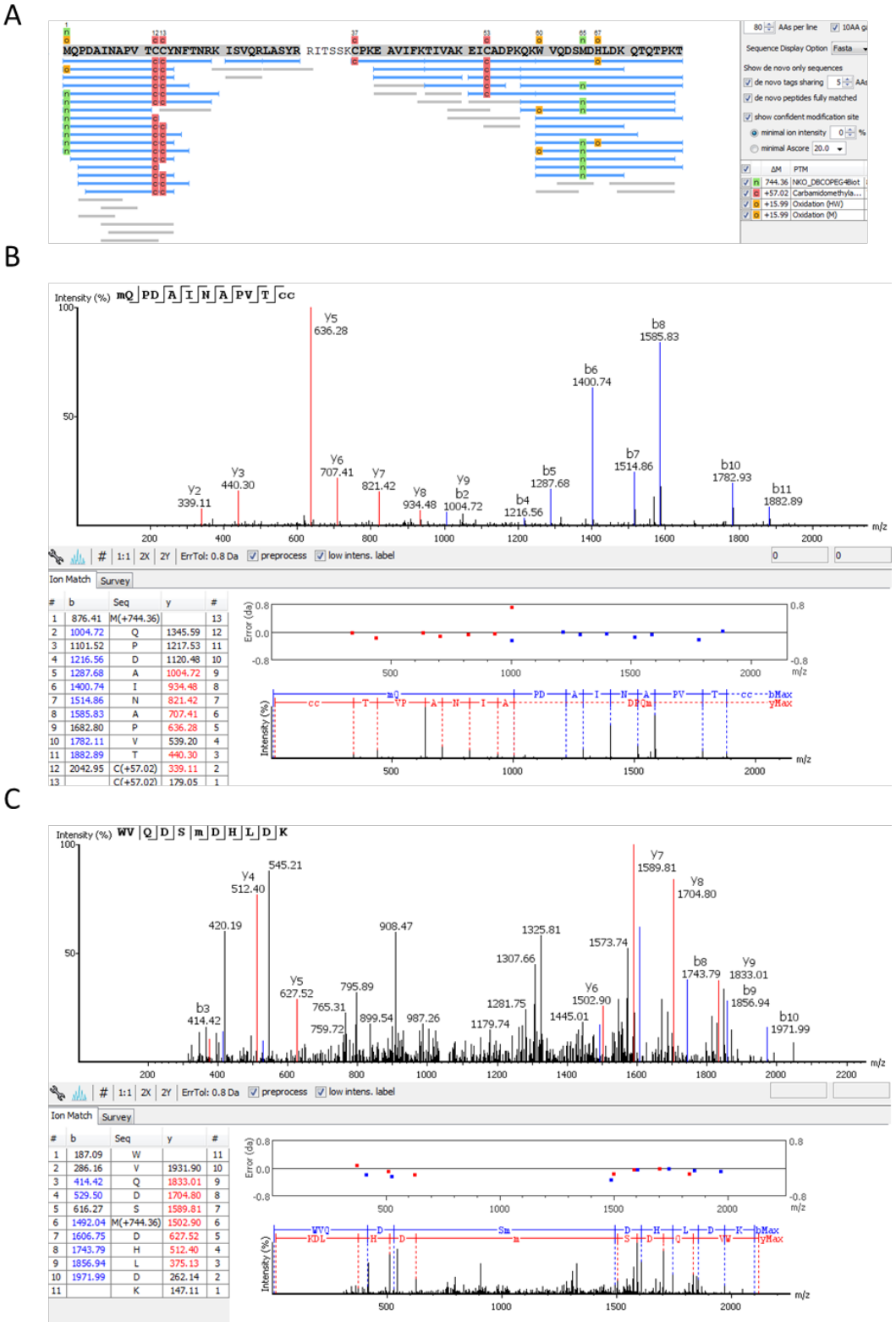
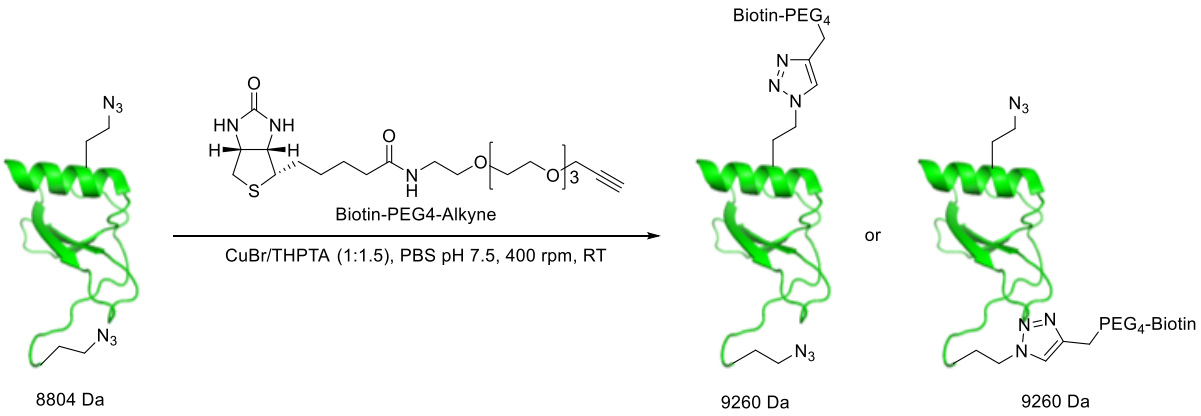


Figure S6. LC-MS/MS characterisation of CCL2-Aha modification by DBCO-PEG4Biotin reagent. A) Sequence coverage obtained after LC-MS/MS analysis. Modifications identified at position 0 and 64, highlighted in green. The corresponding mass of

744 Da is indicative of a single modification of DBCO-PEG4-Biotin reagent at each position. B) Peptide fragmentation spectra shows the modification of DBCO reagent at position 0. C) Peptide fragmentation spectra shows the modification of DBCO reagent at position 64.

4.6.2 CCL2-Aha0Aha64 through CuAAC Chemistry



10 µL of freshly prepared CuBr (10.0 mg/mL; 70 mM) acetonitrile solution was mixed with 10 µL of aqueous stock solution of THPTA (60.55 mg/mL; 140 mM) through 5 sec of vortex to make the catalyst-ligand complex at the concentration of 35 mM. On ice 25 µL of the CCL2-Aha0Aha64 stock solution (50 µL, c = 1.0 mg/mL; 0.114 mM) in pH 7.5 buffer was pipetted into a micro centrifugation tube (0.2 mL), to which 2.6 µL of an aqueous solution of alkyne-PEG4-biotin (10.0 mg/mL; 21.9 mM; 20 equiv.) was added, followed by the addition of catalyst-ligand complex solution (1.6 µL, 20 equiv.). The reaction mixture was quickly vortexed (5 sec) and incubated at RT in thermoshaker at 400 rpm. 3 µL aliquot of reaction mixture were taken at different time points and diluted to 40 µL for LC-MS monitoring of the reaction process. Full conversion was obtained after 30 min.

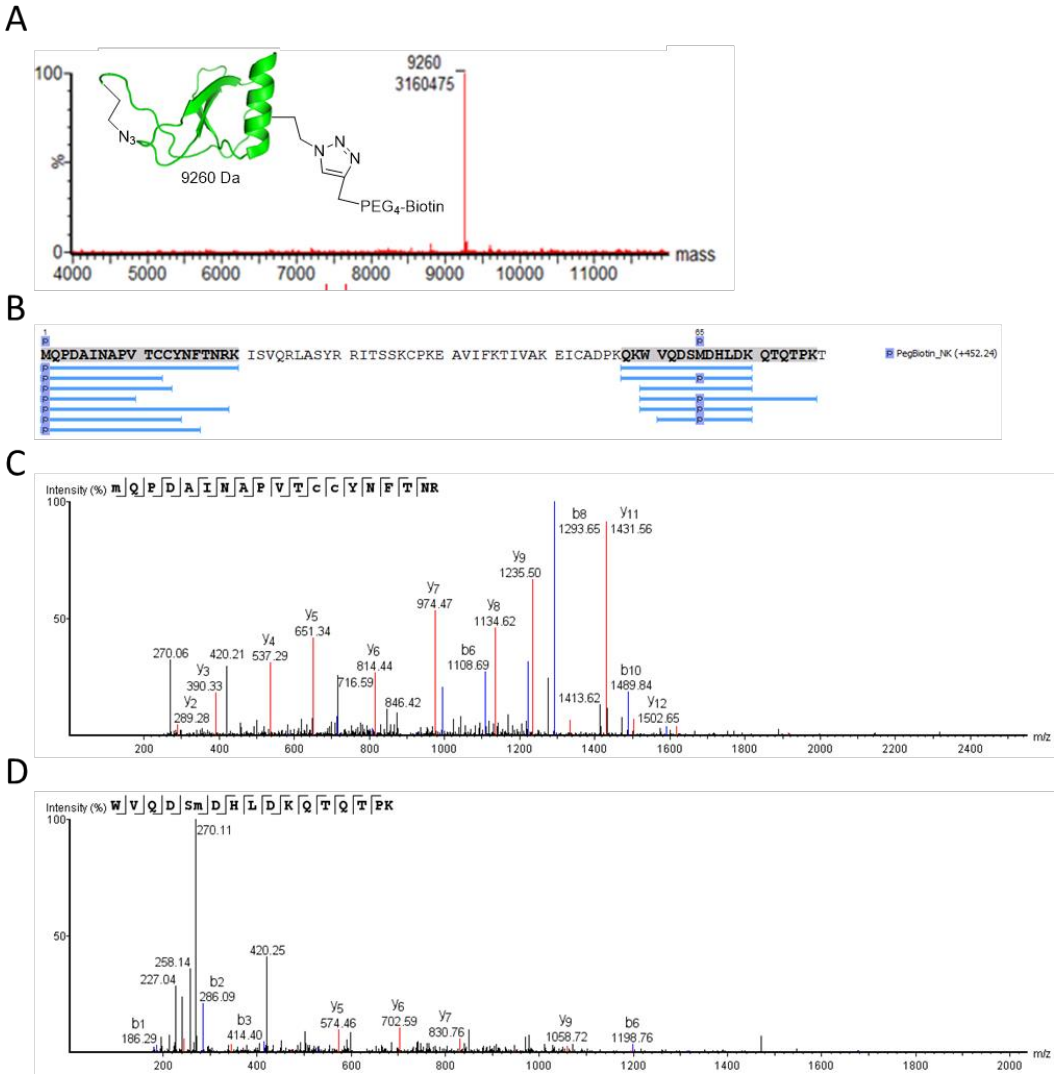
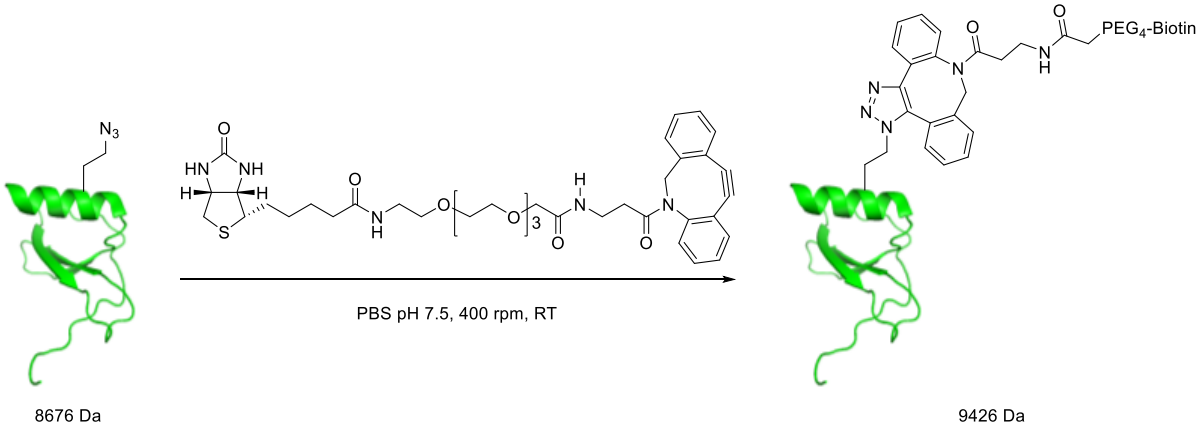


Figure S7. LC-MS and LC-MS/MS characterisation of CCL2-Aha0Aha64 CuAAC reaction. A) LC-MS spectrum indicating that modification of one biotinylated agent with CCL2-Aha0Aha64. B) Coverage spectra of the LC-MS/MS sample. Although the spectra shows the double modification, however, we did not see second modification by LC-MS. C) Individual peptide fragmentation spectra at position 0. D) Peptide fragmentation spectra at position 64.

4.6.3 CCL2-Aha64 labelling through SPAAC Chemistry



An aliquot of N-terminal cleaved CCL2-Aha (25 µL, c= 1.0 mg/mL; 0.114 mM) in pH 7.5 buffer solution was pipetted into the micro centrifuge tube, to which an aqueous solution of DBCO-PEG4-Biotin (2.1 µL, 20 mg/mL; 26.7 mM) was added. The reaction mixture was quickly vortexed and incubated at RT in a thermoshaker at 400 rpm. 3 µL aliquot of reaction mixture was taken at different time intervals and diluted to 40 µL with 0.1 % FA and analysed by LC-MS. Full conversion was achieved within 2 h.

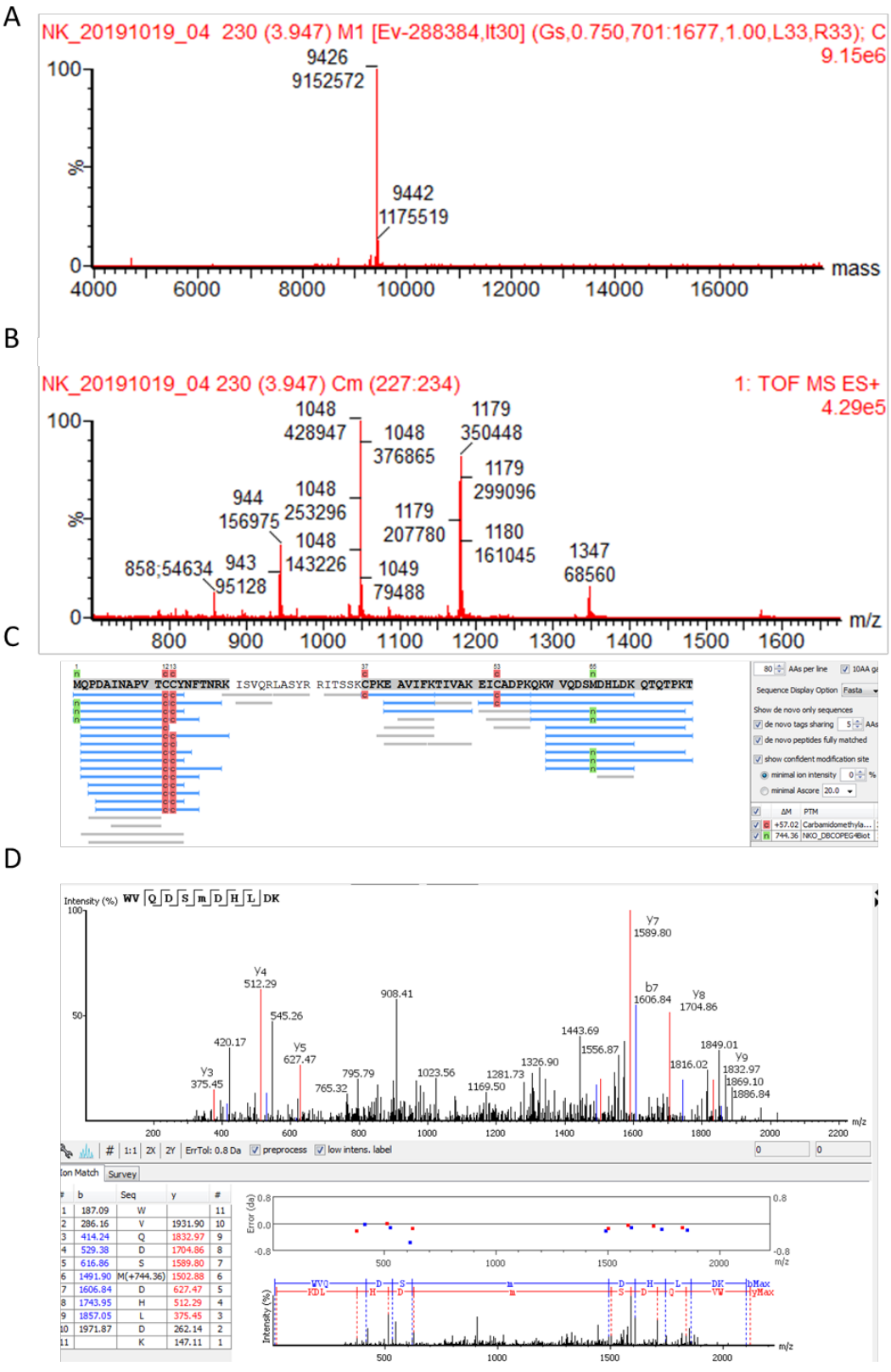
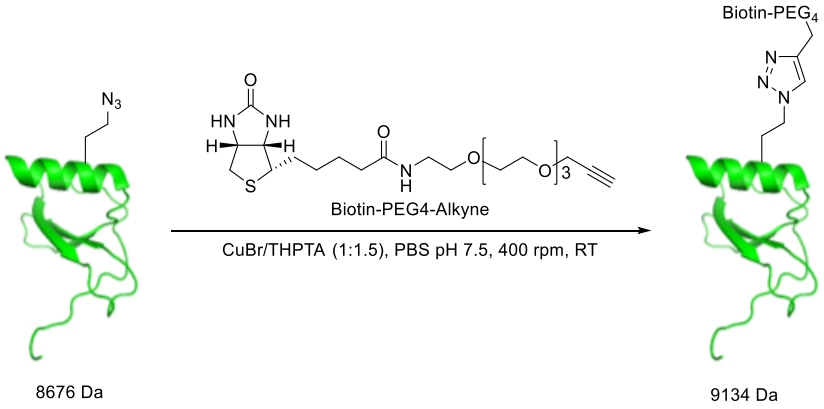


Figure S8. LC-MS and LC-MS/MS characterisation of CCL2-Aha-64 labelling via SPAAC chemistry. A) LC-MS integrated spectrum of CCL2-Aha-64 DBCO-PEG4-Biotin. The mass of 9426 Da corresponds to the single modification of CCL2-Aha with DBCO-PEG4-

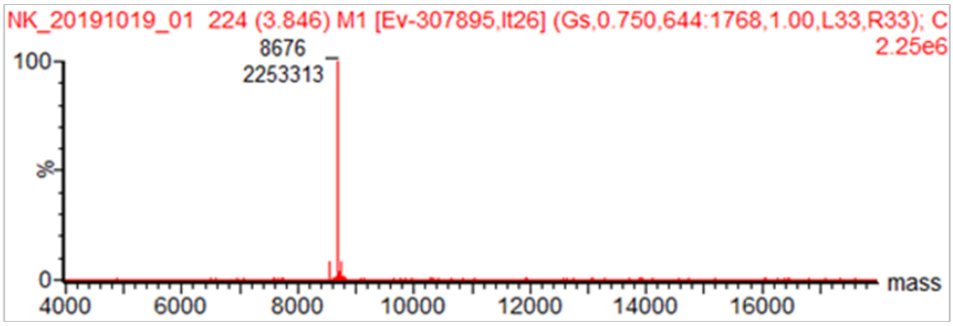
biotin reagent. B) Representative ion-series from LC-MS chromatogram. C) Sequence coverage spectra after LC-MS/MS analysis. Although the coverage spectra indicates the modification of CCL2-Aha with DBCO reagent at both positions 0 and 64, this is likely due to some residual CCL2-Aha at position 0 which was not observed during LC-MS characterisation, ended up modifying the DBCO reagent. D) Peptide fragmentation spectra shows the modification of DBCO reagent at position 64.

4.6.4 CCL2-Aha64 Reaction with alkyne PEG4-biotin



N-terminal CCL2-Aha was cleaved as previously described. 10 µL of freshly prepared CuBr (10.0 mg/mL; 70 mM) acetonitrile solution was mixed with 10 µL of aqueous stock solution of THPTA (60.55 mg/mL; 140 mM) through 5 sec of vortex to make the catalyst-ligand complex at the concentration of 35 mM.On ice 25 µL of the CCL2-Aha64 stock solution (50 µL, c = 1.0 mg/mL; 0.114 mM) in pH 7.5 buffer was pipetted into a micro centrifugation tube (0.2 mL), to which 2.6 µL of an aqueous solution of alkyne- PEG4-biotin (10.0 mg/mL; 21.9 mM; 20 equiv.) was added, followed by the addition of catalyst-ligand complex solution (1.6 µL, 20 equiv.). The reaction mixture was quickly vortexed (5 sec) and incubated at RT in thermoshaker at 400 rpm. 3 µL aliquot of reaction mixture were taken at different time points and diluted to 40 µL for LC-MS monitoring of the reaction process. No conversion was achieved after 2 h of the reaction.

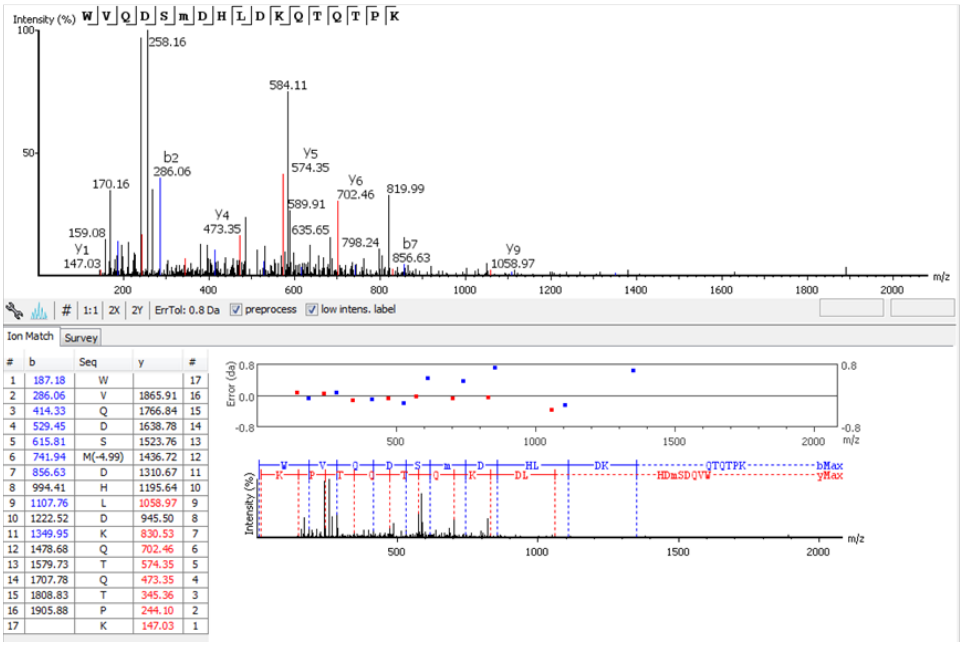
A



B



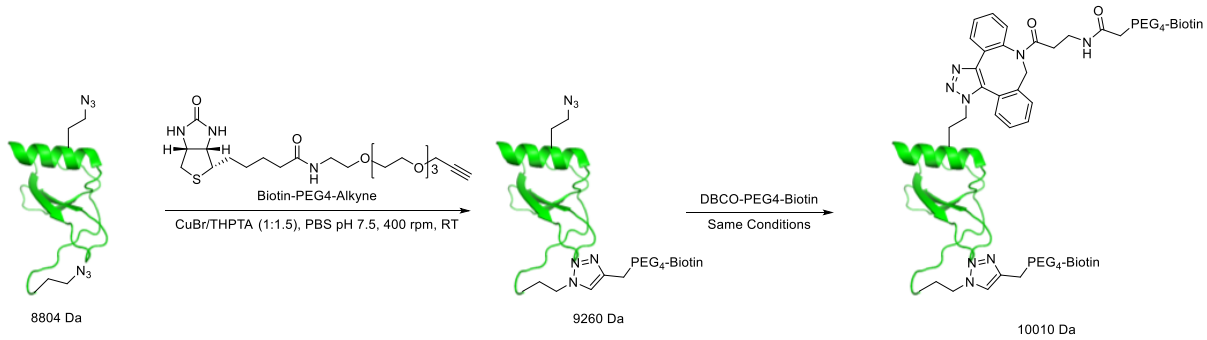
C



#	b	Seq	y	#
1	187.18	W		17
2	286.06	V	1865.91	16
3	414.33	Q	1766.84	15
4	529.45	D	1638.78	14
5	615.81	S	1523.76	13
6	741.94	M(-4.99)	1436.72	12
7	856.63	D	1310.67	11
8	994.41	H	1195.64	10
9	1107.76	L	1058.97	9
10	1222.52	D	945.50	8
11	1349.95	K	830.53	7
12	1478.68	Q	702.46	6
13	1579.73	T	574.35	5
14	1707.78	Q	473.35	4
15	1808.83	T	345.36	3
16	1905.88	P	244.10	2
17		K	147.03	1

Figure S9: CuAAC reaction characterisation for N-terminal cleaved CCL2-Aha. A) LC-MS characterisation of the reaction where no conversion was observed. B) Coverage sequence from LC-MS/MS characterisation with no modification corresponding to the mass of PEG4-Biotin at CCL2-Aha was seen. C) Corresponding peptide fragment spectra.

4.6.5 Sequential Selective labelling of CCL2-Aha with two biotin tags



5 µL of freshly prepared CuBr (10.0 mg/mL; 70 mM) acetonitrile solution was mixed with 5 µL of aqueous stock solution of THPTA (60.55 mg/mL; 140 mM) through 5 sec of vortex and diluted twice with 10 µL of water, making the catalyst-ligand complex at the concentration of 17.5 mM.

An aliquot of the CCL2-Aha0Aha64 stock solution (50 µL, c = 1.0 mg/mL, 0.114 mM) in pH 7.5 buffer was thawed on ice. 25 µL solution was pipetted into a micro centrifugation tube (0.2 mL), to which 1.1 µL of an aqueous solution of alkyne-PEG4-biotin (10.0 mg/mL; 26.7 mM, 10 equiv.) was added, followed by the addition of catalyst-ligand complex solution 1.6 µL (10 equiv.). The reaction mixture was quickly vortexed (5 sec) and incubated at RT in thermoshaker at 400 rpm. 3 µL aliquots of reaction mixture were taken at different time points and diluted to 40 µL for LC/MS monitoring of the reaction process. Full conversion of the Aha0 labelling was achieved at around 30 min. 2.1 µL solution of DBCO-PEG4-biotin (20.0 mg/mL; 26.7 mM, 20 equiv.) was added to the reaction mixture to perform the second labelling at RT by shaking at 600 rpm. 3 µL aliquots of reaction mixture were taken at different time points and diluted to 40 µL for LC/MS monitoring of the reaction process. 2 hrs later another 20 equiv. of DBCO-PEG4-biotin solution and the completion was observed at around 4 h.

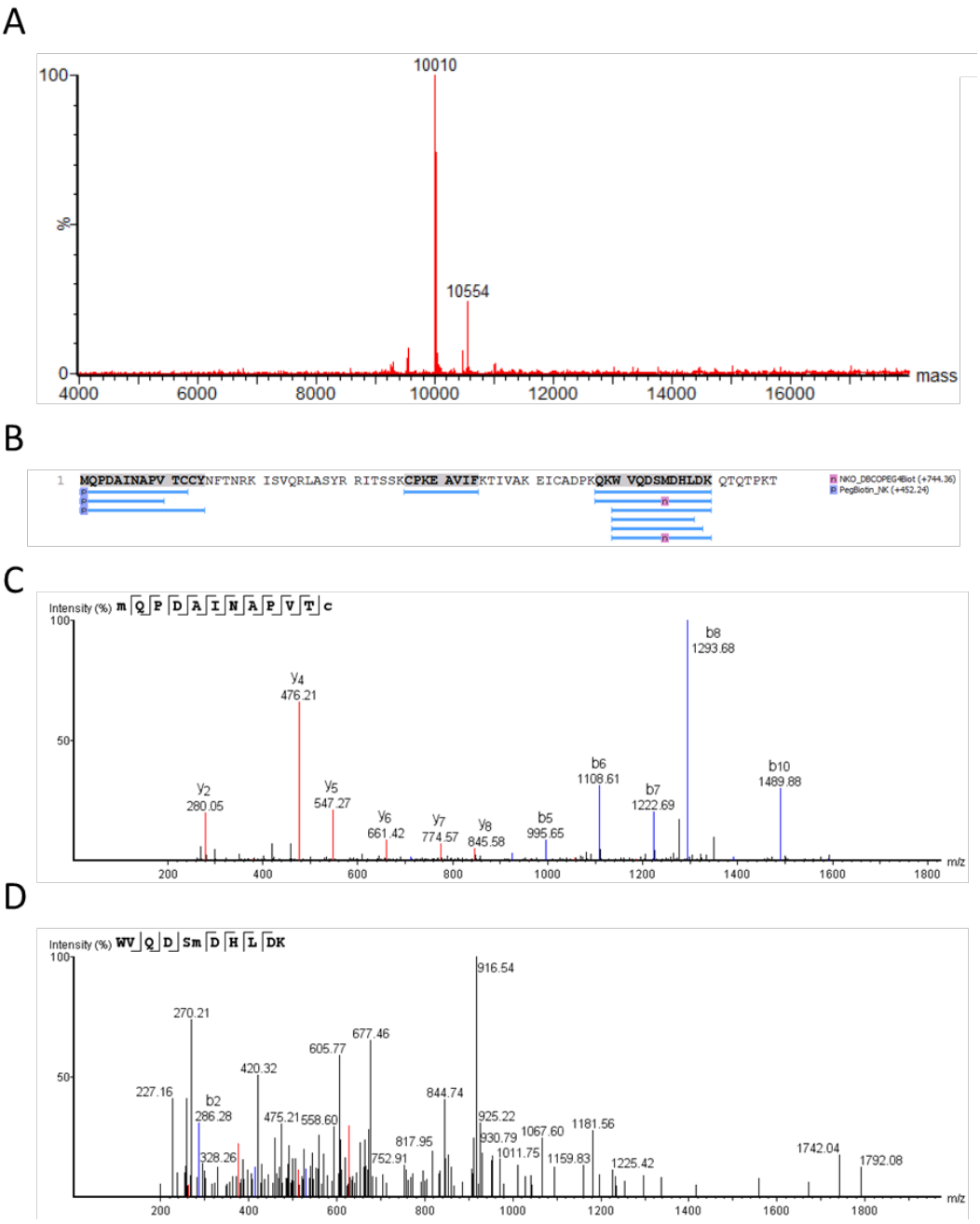
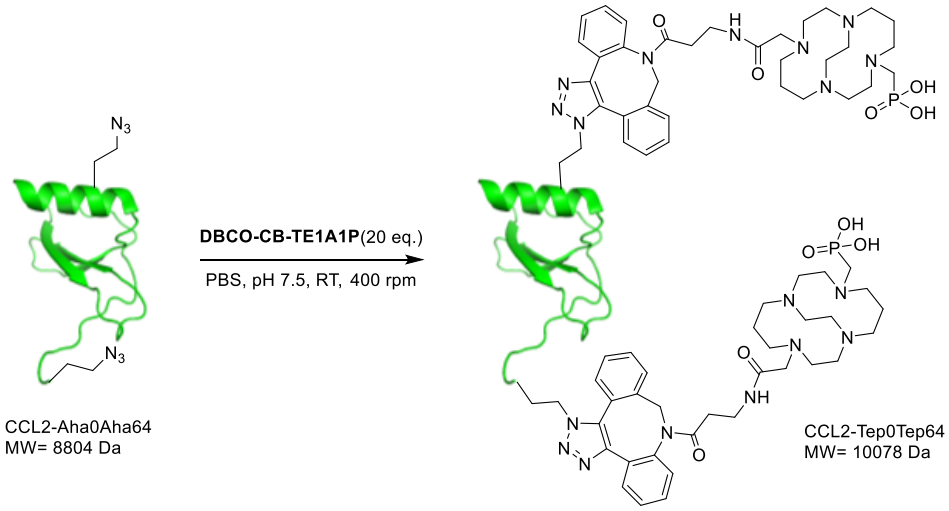
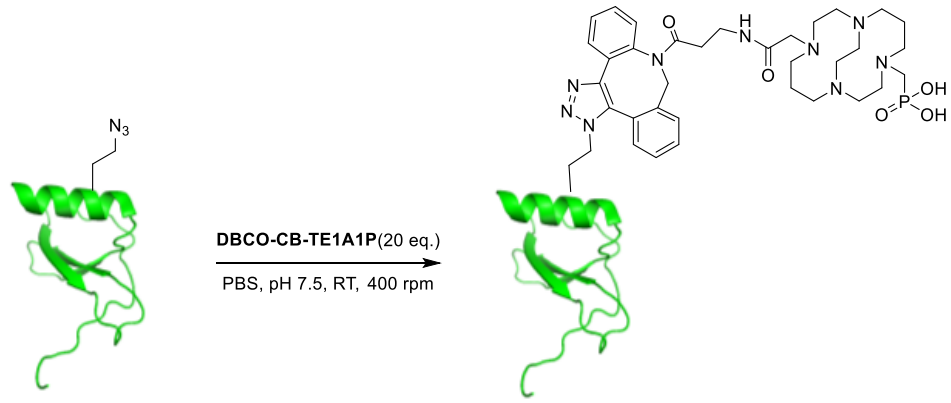


Figure S10. Sequential selective labelling of CCL2-Aha with two biotin tags. A) LC-MS characterisation of the sequential labelling reaction. The integrated spectra confirmed the dual modification, one at each site. B) Coverage spectra from LC-MS/MS characterisation. This spectra confirmed the modification at position 0 is PEG4-Biotin alkyne and at position 64 is DBCO-PEG4-Biotin. C) Fragment peptide spectra for position 0 and D). Fragment peptide spectra for position 64.

4.6.6 Site-selective labelling of CCL2-Aha with Cu chelator CB-TE1A1P



20 µL solution of CCL2-Aha0Aha64 (c = 1.0 mg/mL; 0.114 mM) in pH 7.5 buffer was pipetted into a micro centrifugation tube (0.2 mL), to which an aqueous solution of DBCO-CB-TE1A1P (3.0 mM, 10 µL, 20 equiv.) was added. The reaction mixture was quickly vortexed (5 sec) and incubated at RT in thermoshaker at 400 rpm. 3 µL aliquots of reaction mixture were taken at different time points and diluted to 40 µL for LC/MS monitoring of the reaction process. After 1 h, 90% of the product was from double modification and 10% of single modification of the chelator to CCL2-Aha. Further incubation up to 4h did not result in any further change for the formation of the product.



20 µL solution of CCL2-Aha64 (c = 1.0 mg/mL; 0.114 mM) in pH 7.5 buffer was pipetted into a micro centrifugation tube (0.2 mL), to which an aqueous solution of DBCO-CB-TE1A1P (3 mM, 10 µL, 20 equiv.) was added. The reaction mixture was quickly vortexed (5 sec) and incubated at RT in thermoshaker at 400 rpm. 3 µL aliquots of reaction mixture were taken at different time points and diluted to 40 µL for LC/MS monitoring of the reaction process.

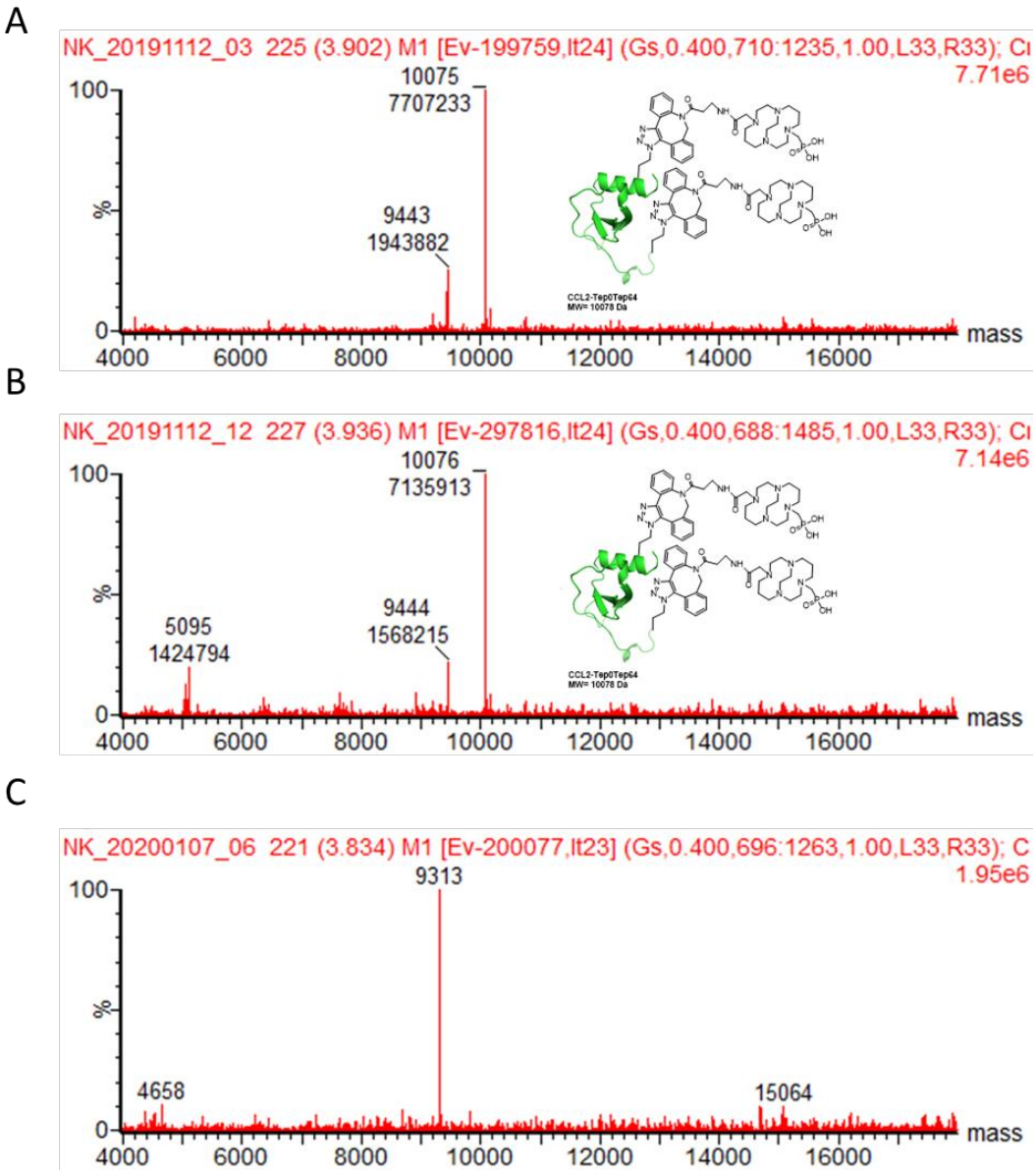
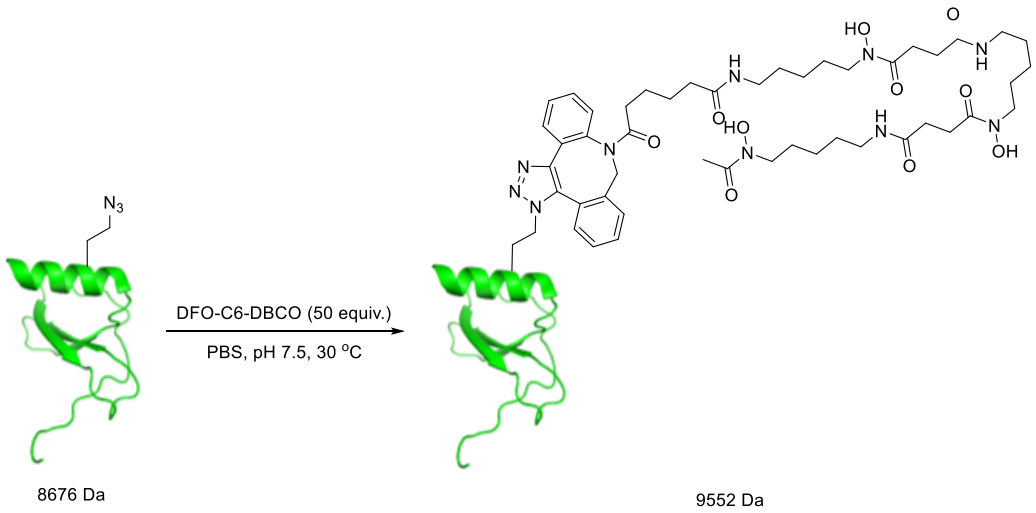


Figure S11. Labelling CCL2-Aha with Cu Chelator (DBCO-CB-TE1A1P). A) Cross-bridge copper chelator DBCO-CB-TE1AIP was labelled with Aha0Aha64. The conversion was around 90% after 1h, as there was 10% of single modification reaction was still left. B) The same reaction was analysed after 4h but that did not change the conversion. C) CCL2-Aha64 labelling with Cu chelator. Full conversion observed within 1h.

4.6.7 CCL2-Aha64 Labelling with DFO-C6-DBCO



10 µL solution of CCL2-Aha64 (c = 1.0 mg/mL, 0.114 mM in pH 7.5 buffer) was pipetted into a microcentrifugation tube (0.2 mL), to which a DMSO solution of DFO-C6-DBCO (5 mM, 2 µL, 50 equiv.) was added. The reaction mixture was quickly vortexed (5 sec) and incubated at RT in thermoshaker at 600 rpm. 3 µL aliquots of reaction mixture were taken at different time points and diluted to 40 µL for LCMS monitoring of the reaction process. 90% conversion was achieved after 4 h.

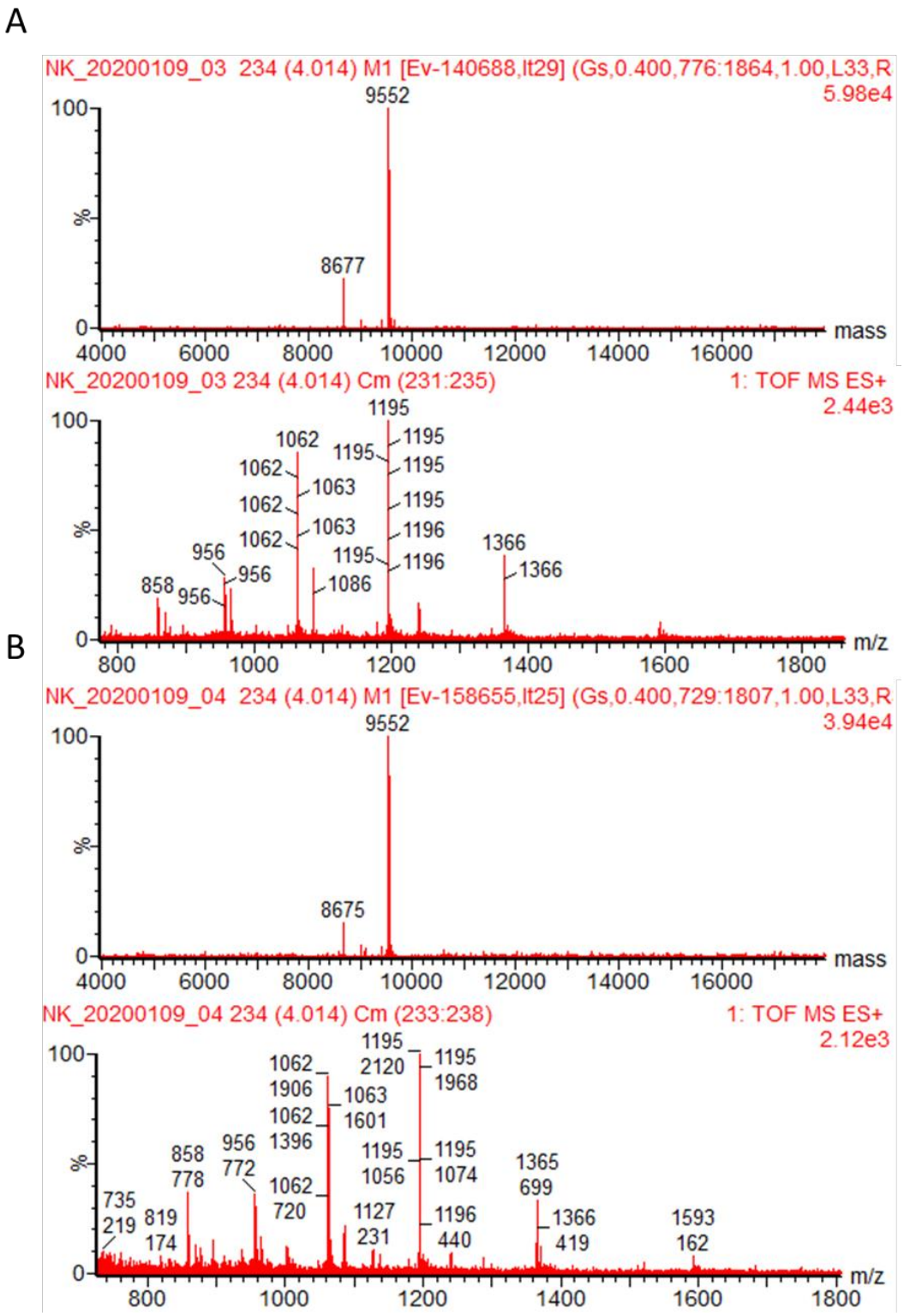
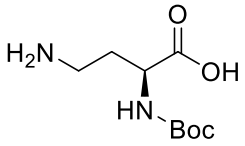


Figure S12. LC-MS characterisation of CCL2-Aha64 labelling with DFO-C6-DBCO. A) Representative integrated spectrum and ion-series of reaction sample analysed after 1 h of the reaction. B) Spectrum and ion –series after 4 h of the reaction. The over-all conversion after 4 h was ~ 90%.

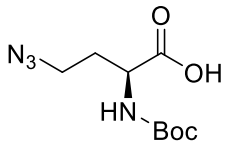
4.7 Chemical Synthesis of Azidohomoalanine (Aha)[29]

4.7.1 (S)-2-(N-tert-butoxycarbonyl)-3-azidopropanoic acid allyl ester (Boc-Dab-OH)



N-Boc-L-Glutamine (3.69 g, 15 mmol, 1 equiv.) was dissolved in a 4:1 solution of THF (36 mL) and H_2O (9 mL) in a 100 mL round-bottomed flask. The solution was cooled to 4 °C (ice cold water), and phenyliodine diacetate (PIDA; 5.79 g, 18 mmol, 1.2 equiv) was added. The reaction was stirred for 6 hours only. After 6 hours, the solvent was then removed *in vacuo*, and the resulting oil dissolved in H_2O (40 mL) and extracted with EtOAc (3 x 40 mL). The aqueous layer was then evaporated to dryness *in vacuo*, washed with cold chloroform (approx. 100 mL), and the product isolated by filtration and dried under vacuum overnight to yield the crude product as an off-white solid (2.2 g, 68% yield).^{1}H NMR (400 MHz, Deuterium Oxide) δ 3.86 (dd, J= 7.0, 5.5 Hz, 1H, Hα), 3.50 (t, *J* = 6.6, 2.4 Hz, 2H, Hβ), 2.17 – 1.81 (m, 2H, Hγ). ^{13}C NMR (101 MHz, Deuterium Oxide) δ 173.9 (C=OOH), 52.8 (Cα), 47.5 (Cγ), 29.5 (Cβ); ESI-MS- [M-H] Expected 435.0, found 435.0.

4.7.2 Synthesis of Boc-Aha

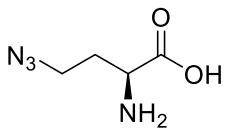


Triflic azide preparation: A solution of sodium azide (5.27 g, 81.1 mmol, 10 equiv.) in H_2O (13 mL) was stirred in a round-bottomed flask on an ice bath. Triflic anhydride (2.7 mL, 16.1 mmol, 2 equiv) was then added dropwise, after which the ice bath was removed and the reaction stirred at room temperature for 2 hours. It was then extracted with DCM (2 x 8 mL), washed

with sat. Na_2CO_3 (25 mL) and added dropwise to the flask containing Boc protected derivatives.

Boc-Aha synthesis: While the triflic azide reaction was stirring for 2 hours, Boc-Dab-OH (1.77g, 8.1 mmol, 1 equiv), K_2CO_3 (1.68 g, 12.2 mmol, 1.5 equiv) and $CuSO_4$ (20 mg, 0.08 mmol, 0.01 equiv) were dissolved in water (26 mL) and MeOH (52 mL) solution in a 250 mL round-bottomed flask. The DCM solution of triflic azide was then added dropwise, and the opaque blue reaction was stirred at room temperature for 16 hours. DCM and MeOH were then removed in-vacuo, and H_2O (25 mL) was added to give a bright blue solution with pH approx. 12 (pH paper). 6 M HCl was then added dropwise to bring the pH to 6, during which the colour was observed to change to green and foaming occurred. Potassium phosphate buffer (100 mL, 250 mM, pH 6.2) was then added, and the pH further adjusted to 3 (pH paper) with 6 M HCl. The reaction was then extracted with EtOAc (2 x100 mL), washed with brine (50 mL), dried on $MgSO_4$, filtered, and evaporated to dryness in-vacuo to give the crude product as a yellow-green oil (2.2 g, 78%). ^{1}H NMR (400 MHz, Chloroform-d) δ 5.30-4.28 (m, 1H, Boc-NH) δ 4.09 (q, 1H, *J*= 7.2 Hz, Hα), 3.43 (t, *J* = 7.5 Hz, 1H, NH), 3.45 (t, *J*= 6.7 Hz, 2H, Hβ), 2.22 – 2.07 (m, 1H, Hγ), 1.96 (m, 1H, Hγ'), 1.44 (s, 9H, Boc$(CH_3)_3$). ^{13}C NMR (101 MHz, Chloroform-d) δ 175.9 (C=OOH), 155.9 (Boc C=O), 81.0 (BocC $(CH_3)_3$, 60.8 (Cα), 47.9 (Cγ), 31.5 (Cβ), 28.4 (Boc C $(CH_3)_3$). MS-ESI- [M-H] Expected 243.0, found 243.1.

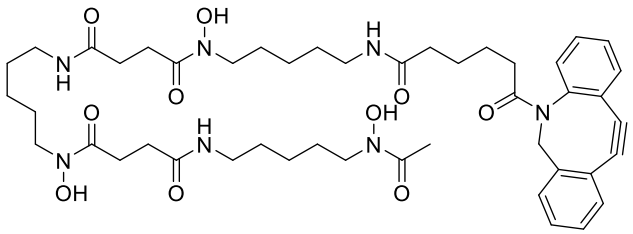
4.7.3 Synthesis of Aha



To the crude N-Boc-Aha (1.9 g, 0.009 mol) was added conc. HCl (10 mL), and the reaction stirred for 1 hour at room temperature. It was then diluted with H_2O (90 mL) and loaded onto

a Dowex (resin specs) column that had been pre-washed with H_2O (1 L), MeOH (1 L), H_2O (4 x 1 L), 1N NH_4OH (3 x 100 mL), H_2O (4 x 1 L), 1M HCl (100 mL), and H_2O (4 x 1 L). The eluent was collected and passed over the Dowex again, before washing the resin with H_2O until eluent was constant at neutral pH (6 x 1 L). The product was then eluted with 1N NH_4OH (400 mL), dried in-vacuo at 65 °C, and recrystallized by dissolving in minimal H_2O, adding minimal acetone until the solution clouded, heating at 75°C until clear again and refrigerating at 4 °C overnight to yield the product as white crystalline needles which were isolated by filtration (0.5 g, 45%)^{1}H NMR (400 MHz, Deuterium Oxide) δ 3.73 (d, J = 6.5 Hz, 1H, Hα), 3.48 (t, J = 6.3, Hz, 2H, Hβ), 2.17 – 1.98 (m, 2H, Hγ). ^{13}C NMR (101 MHz, Deuterium Oxide) δ 174.3 (C=OOH), 53.0 (Cα), 47.6 (Cγ), 29.7 (Cβ). MS-ESI- [M-1] Expected 143.1, found 143.1

4.7.4 Chemical Synthesis of DFO-C6-DBCO[38]



To a stirred solution of DBCO-C6-Acid (54 mg, 0.04 mmol) in DMF (1.28 mL), were added HATU (92.0 mg, 0.06 mmol) and DIPEA (53.2 µL, 39.2 mg, 0.08 mmol). Separately, DFO mesylate salt (105.2 mg, 0.04 mmol) was dissolved in DMF (1.28 mL) and DIPEA (53.2 µL) and NMM (120.0 µL) were added. Both solutions were stirred at room temperature for 1 h. During this time, the solution containing DBCO-C6-acid turned orange. After 1 h, the DFO-mesylate solution was added to the DBCO-C6-acid and the reaction mixture stirred for further 48 h at room temperature, under nitrogen. After this time, ice cold acetone (5 mL) was added and the reaction mixture was sonicated for 5 min. This resulted in a white solid which was separated from the liquid by centrifugation (7000 rpm). The white solid was then washed with

acetone (2 x 5 mL) and water (3 x 5 mL), with sonication and centrifugation in between the washes. Finally the resulting white solid was dried under high vacuum to afford DFO alkyne 35 mg (35 mg, 57%). ^{1}H NMR (400 MHz, DMSO-d6) 9.65 (3H, br s, OH), 7.80-7.77 (3H, m, 3 x NH), 7.63-7.56 (4H, m, CH), 7.51-7.44 (2H, m, 4 x CH), 7.40-7.29 (4H, m, 2 x CH), 7.29 (1H, m, CH), 5.04 (1H, d, *J* = 14.3 Hz, C*H*H), 3.60 (1H, d, *J* = 14.0 Hz, CH*H*), 3.46-3.41 (6H, m, 3 x CH_2), 3.02-2.97 (4H, m, 2 x CH_2), 2.94-2.89 (2H, m, CH_2), 2.59-2.55 (4H, m, 2 x CH_2), 2.28-2.24 (4H, m, 2 x CH_2), 2.16 (1H, m, C*H*H), 1.96 (3H, s, CH_3), 1.84-1.80 (2H, m, CH_2), 1.75 (1H, m, CH*H*), 1.53-1.44 (6H, m, 3 x CH_2), 1.41-1.28 (6H, m, 4 x CH_2), 1.24-1.15 (8H, m, 3 x CH_2);13C NMR (125 MHz, DMSO-d6) 172.5, 172.2, 172.0, 171.8, 170.7, 152.2, 148.9 132.9, 129.9, 129.4, 128.6, 128.5, 128.2, 127.3, 125.6, 122.9, 121.9, 114.8, 108.7, 55.2, 47.5, 47.2, 38.9, 38.7, 35.5, 34.4, 30.4, 29.3, 28.0, 26.5, 25.2, 25.0, 24.0, 23.2 MS $[M+H]^{+}$ calculated 876.4, found 876.4.

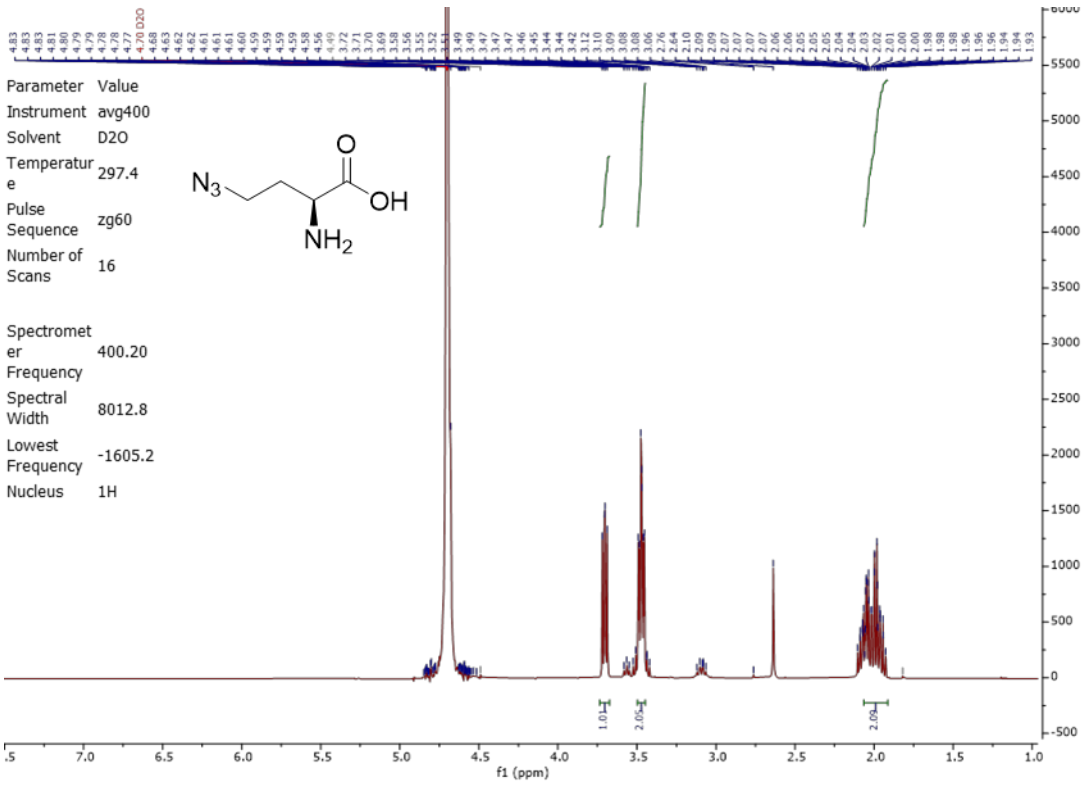


Figure S13: ^{1}H NMR spectrum of Aha

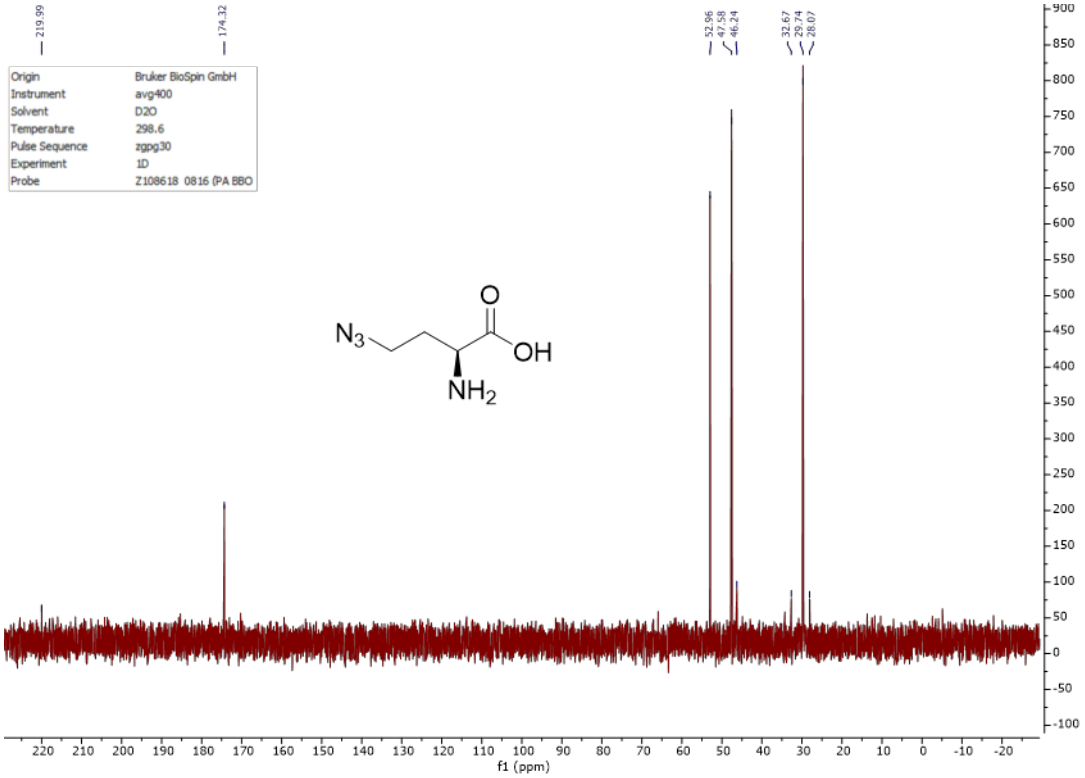


Figure S14: ^{13}C NMR spectrum of Aha

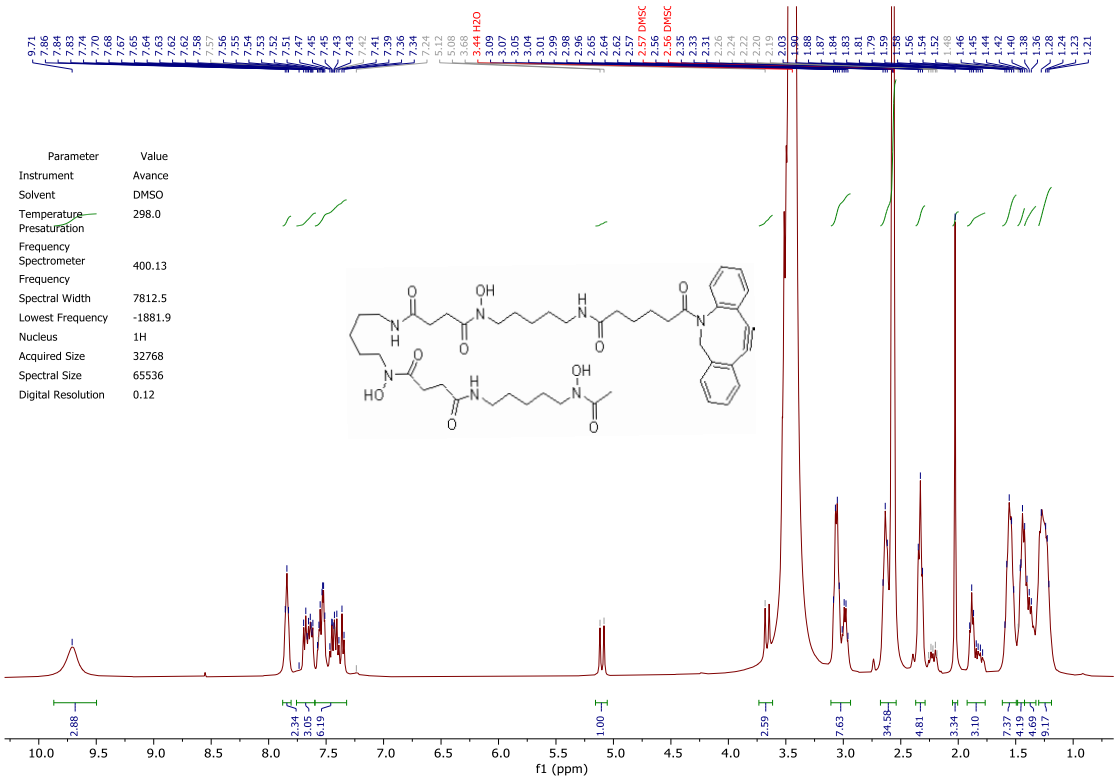


Figure S15. ^{1}H NMR spectrum of DFO-C6-DBCO

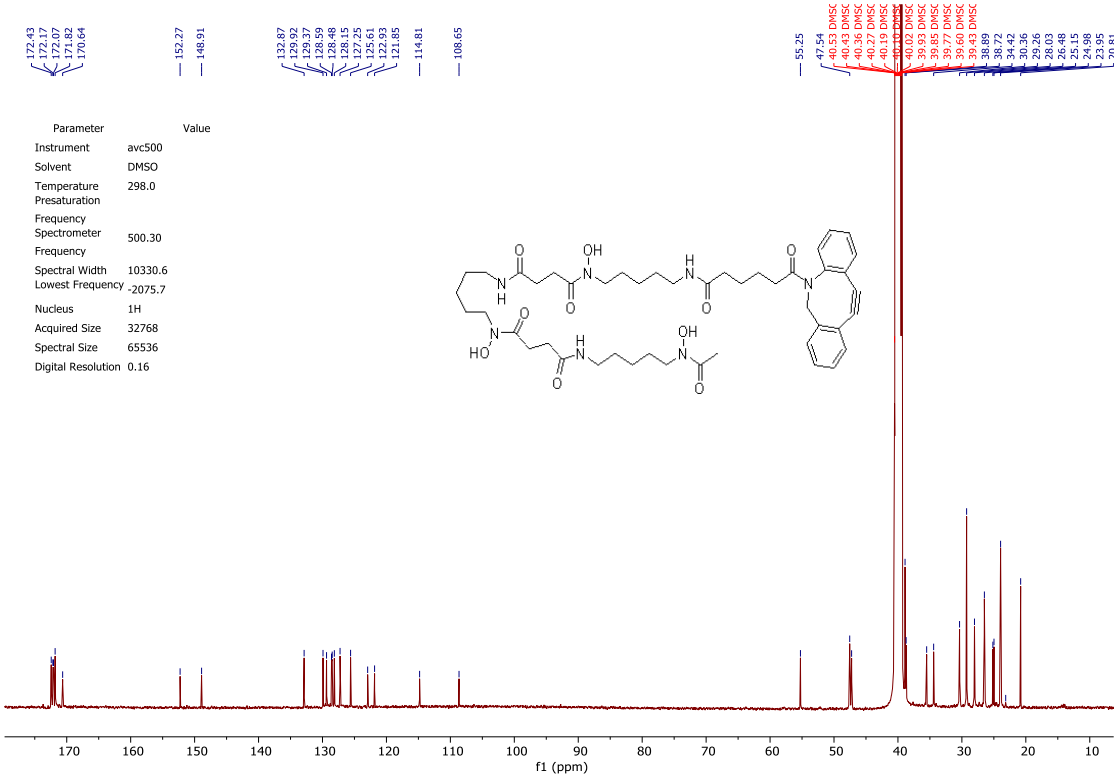


Figure S16. ^{13}C NMR spectrum of DFO-C6-DBCO

4.8 References

1. Moser, B.; Willimann, K., Chemokines: role in inflammation and immune surveillance. *Annals of the Rheumatic Diseases* **2004,** *63 Suppl 2*, ii84-ii89.

2. Hoffmann, C.; Leis, A.; Niederweis, M.; Plitzko, J. M.; Engelhardt, H., Disclosure of the mycobacterial outer membrane: cryo-electron tomography and vitreous sections reveal the lipid bilayer structure. *Proceedings of the National Academy of Sciences of the United States of America* **2008,** *105* (10), 3963-7.

3. Hyduk, S. J.; Chan, J. R.; Duffy, S. T.; Chen, M.; Peterson, M. D.; Waddell, T. K.; Digby, G. C.; Szaszi, K.; Kapus, A.; Cybulsky, M. I., Phospholipase C, calcium, and calmodulin are critical for alpha4beta1 integrin affinity up-regulation and monocyte arrest triggered by chemoattractants. *Blood* **2007,** *109* (1), 176-84.

4. Deshmane, S. L.; Kremlev, S.; Amini, S.; Sawaya, B. E., Monocyte chemoattractant protein-1 (MCP-1): an overview. *Journal of Interferon & Cytokine Research : The Official Journal of the International Society for Interferon and Cytokine Research* **2009,** *29* (6), 313-26.

5. Handel, T. M.; Domaille, P. J., Heteronuclear (1H, 13C, 15N) NMR assignments and solution structure of the monocyte chemoattractant protein-1 (MCP-1) dimer. *Biochemistry* **1996,** *35* (21), 6569-84.

6. Chung, C. W.; Cooke, R. M.; Proudfoot, A. E.; Wells, T. N., The three-dimensional solution structure of RANTES. *Biochemistry* **1995,** *34* (29), 9307-14.

7. Baggiolini, M., Chemokines and leukocyte traffic. *Nature* **1998,** *392* (6676), 565-568.

8. Zhang, Y. J.; Rutledge, B. J.; Rollins, B. J., Structure/activity analysis of human monocyte chemoattractant protein-1 (MCP-1) by mutagenesis. Identification of a mutated

protein that inhibits MCP-1-mediated monocyte chemotaxis. *The Journal of Biological Chemistry* **1994,** *269* (22), 15918-24.

9. Van Coillie, E.; Van Damme, J.; Opdenakker, G., The MCP/eotaxin subfamily of CC chemokines. *Cytokine & Growth Factor Reviews* **1999,** *10* (1), 61-86.

10. Jiang, Y.; Valente, A. J.; Williamson, M. J.; Zhang, L.; Graves, D. T., Post-translational modification of a monocyte-specific chemoattractant synthesized by glioma, osteosarcoma, and vascular smooth muscle cells. *The Journal of Biological Chemistry* **1990,** *265* (30), 18318-21.

11. Siddiqui, J. A.; Partridge, N. C., CCL2/Monocyte Chemoattractant Protein 1 and Parathyroid Hormone Action on Bone. *Frontiers in Endocrnology* **2017,** *8* (49).

12. Flynn, J. L.; Chan, J., Immunology of tuberculosis. *Annual Review of Immunology* **2001,** *19*, 93-129.

13. Sadek, M. I.; Sada, E.; Toossi, Z.; Schwander, S. K.; Rich, E. A., Chemokines induced by infection of mononuclear phagocytes with mycobacteria and present in lung alveoli during active pulmonary tuberculosis. *American Journal of Respiratory Cell and Molecular Biology* **1998,** *19* (3), 513-21.

14. Ohtsuki, K.; Hayase, M.; Akashi, K.; Kopiwoda, S.; Strauss, H. W., Detection of monocyte chemoattractant protein-1 receptor expression in experimental atherosclerotic lesions: an autoradiographic study. *Circulation* **2001,** *104* (2), 203-8.

15. Hartung, D.; Petrov, A.; Haider, N.; Fujimoto, S.; Blankenberg, F.; Fujimoto, A.; Virmani, R.; Kolodgie, F. D.; Strauss, H. W.; Narula, J., Radiolabeled Monocyte Chemotactic Protein 1 for the detection of inflammation in experimental atherosclerosis. *Journal of Nuclear Medicine* **2007,** *48* (11), 1816-21.

16. Blankenberg, F. G.; Wen, P.; Dai, M.; Zhu, D.; Panchal, S. N.; Tait, J. F.; Post, A. M.; Strauss, H. W.; Valantine, H. A., Detection of early atherosclerosis with radiolabeled monocyte chemoattractant protein-1 in prediabeteic Zucker rats. *Pediatric Radiology* **2001,** *31* (12), 827-835.

17. Blankenberg, F. G.; Tait, J. F.; Blankenberg, T. A.; Post, A. M.; Strauss, H. W., Imaging macrophages and the apoptosis of granulocytes in a rodent model of subacute and chronic abscesses with radiolabeled monocyte chemotactic peptide-1 and annexin V. *European Journal of Nuclear Medicine* **2001,** *28* (9), 1384-93.

18. Blankenberg, F. G.; Wen, P.; Dai, M.; Zhu, D.; Panchal, S. N.; Tait, J. F.; Post, A. M.; Strauss, H. W.; Valantine, H. A., Detection of early atherosclerosis with radiolabeled monocyte chemoattractant protein-1 in prediabeteic Zucker rats. *Pediatric Radiology* **2001,** *31* (12), 827-35.

19. Allen, S. J.; Crown, S. E.; Handel, T. M., Chemokine: receptor structure, interactions, and antagonism. *Annual Review of Immunology* **2007,** *25*, 787-820.

20. Zhang, Y.; Rollins, B. J., A dominant negative inhibitor indicates that monocyte chemoattractant protein 1 functions as a dimer. *Molecular and Cellular Biology* **1995,** *15* (9), 4851-5.

21. Tan, J. H.; Canals, M.; Ludeman, J. P.; Wedderburn, J.; Boston, C.; Butler, S. J.; Carrick, A. M.; Parody, T. R.; Taleski, D.; Christopoulos, A.; Payne, R. J.; Stone, M. J., Design and receptor interactions of obligate dimeric mutant of chemokine monocyte chemoattractant protein-1 (MCP-1). *The Journal of Biological Chemistry* **2012,** *287* (18), 14692-702.

22. Allen, S. J.; Hamel, D. J.; Handel, T. M., A rapid and efficient way to obtain modified chemokines for functional and biophysical studies. *Cytokine* **2011,** *55* (2), 168-73.

23. Zeng, D.; Mattila, J.; Beaino, W.; Jiang, M.; Lopresti, B.; Coleman, M.; Flynn, J.; Anderson, C., Copper-64-labeled CB-TE1K1P conjugates of MCP-1 for PET imaging of macrophages in tuberculosis granulomas. *The Journal of Nuclear Medicine* **2014,** *55* 1210-1210.

24. Agard, N. J.; Baskin, J. M.; Prescher, J. A.; Lo, A.; Bertozzi, C. R., A Comparative Study of Bioorthogonal Reactions with Azides. *ACS Chemical Biology* **2006,** *1* (10), 644-648.

25. Zeng, D.; Mattila, J.; Beaino, W.; Jiang, M.; Lopresti, B.; Coleman, M.; Flynn, J.; Anderson, C., Copper-64-labeled CB-TE1K1P conjugates of MCP-1 for PET imaging of macrophages in tuberculosis granulomas. *The Journal of Nuclear Medicine* **2014,** *55* 1210.

26. Chatterjee, A.; Guo, J.; Lee, H. S.; Schultz, P. G., A genetically encoded fluorescent probe in mammalian cells. *Journal of the American Chemical Society* **2013,** *135* (34), 12540-3.

27. Ma, Y.; Biava, H.; Contestabile, R.; Budisa, N.; di Salvo, M. L., Coupling bioorthogonal chemistries with artificial metabolism: intracellular biosynthesis of azidohomoalanine and its incorporation into recombinant proteins. *Molecules* **2014,** *19* (1), 1004-22.

28. Rostovtsev, V. V.; Green, L. G.; Fokin, V. V.; Sharpless, K. B., A Stepwise Huisgen Cycloaddition Process: Copper(I)-Catalyzed Regioselective "Ligation" of Azides and Terminal Alkynes. *Angewandte Chemie* **2002,** *41* (14), 2596-2599.

29. Link, A. J.; Vink, M. K.; Tirrell, D. A., Preparation of the functionalizable methionine surrogate azidohomoalanine via copper-catalyzed diazo transfer. *Nature Protocols* **2007,** *2* (8), 1879-8.

30. Bernardes, G. J.; Linderoth, L.; Doores, K. J.; Boutureira, O.; Davis, B. G., Site-selective traceless Staudinger ligation for glycoprotein synthesis reveals scope and limitations. *Chembiochem : a European Journal of Chemical Biology* **2011,** *12* (9), 1383-6

31. Kramer, G.; Kasper, P. T.; de Jong, L.; de Koster, C. G., Quantitation of newly synthesized proteins by pulse labeling with azidohomoalanine. *Methods in Molecular Biology* **2011,** *753*, 169-81.

32. Martell, J.; Weerapana, E., Applications of copper-catalyzed click chemistry in activity-based protein profiling. *Molecules* **2014,** *19* (2), 1378-93.

33. Zhang, X.; Lu, W.; Kwan, K.; Bhattacharyya, D.; Wei, Y., Dual-Functional-Tag-Facilitated Protein Labeling and Immobilization. *ACS Omega* **2017,** *2* (2), 522-528.

34. Cooper, M. S.; Ma, M. T.; Sunassee, K.; Shaw, K. P.; Williams, J. D.; Paul, R. L.; Donnelly, P. S.; Blower, P. J., Comparison of 64Cu-Complexing Bifunctional Chelators for Radioimmunoconjugation: Labeling Efficiency, Specific Activity, and in Vitro/in Vivo Stability. *Bioconjugate Chemistry* **2012,** *23* (5), 1029-1039.

35. Cai, Z.; Anderson, C. J., Chelators for copper radionuclides in positron emission tomography radiopharmaceuticals. *Journal of Labelled Compounds & Radiopharmaceuticals* **2014,** *57* (4), 224-30.

36. Cai, Z.; Ouyang, Q.; Zeng, D.; Nguyen, K. N.; Modi, J.; Wang, L.; White, A. G.; Rogers, B. E.; Xie, X.-Q.; Anderson, C. J., 64Cu-labeled somatostatin analogues conjugated with cross-bridged phosphonate-based chelators via strain-promoted click chemistry for PET imaging: in silico through in vivo studies. *Journal of Medicinal Chemistry* **2014,** *57* (14), 6019-6029.

37. Zeng, D.; Ouyang, Q.; Cai, Z.; Xie, X. Q.; Anderson, C. J., New cross-bridged cyclam derivative CB-TE1K1P, an improved bifunctional chelator for copper radionuclides. *Chemical Communications* **2014,** *50* (1), 43-5.

38. Marculescu, C.; Lakshminarayanan, A.; Gault, J.; Knight, J. C.; Folkes, L. K.; Spink, T.; Robinson, C. V.; Vallis, K.; Davis, B. G.; Cornelissen, B., Probing the limits of Q-tag bioconjugation of antibodies. *Chemical Communications* **2019,** *55* (76), 11342-11345.

39. Wang, T.; Li, Z.; Cvijic, M. E.; Krause, C.; Zhang, L.; Sum, C. S., Measurement of beta-Arrestin Recruitment for GPCR Targets. In *Assay Guidance Manual*, Sittampalam, G. S.; Grossman, A.; Brimacombe, K.; Arkin, M.; Auld, D.; Austin, C. P.; Baell, J.; Bejcek, B.; Caaveiro, J. M. M.; Chung, T. D. Y.; Coussens, N. P.; Dahlin, J. L.; Devanaryan, V.; Foley, T. L.; Glicksman, M.; Hall, M. D.; Haas, J. V.; Hoare, S. R. J.; Inglese, J.; Iversen, P. W.; Kahl, S. D.; Kales, S. C.; Kirshner, S.; Lal-Nag, M.; Li, Z.; McGee, J.; McManus, O.; Riss, T.; Saradjian, P.; Trask, O. J., Jr.; Weidner, J. R.; Wildey, M. J.; Xia, M.; Xu, X., Eds. *Eli Lilly & Company and the National Center for Advancing Translational Sciences* **2004**.

40. Zhao, X.; Jones, A.; Olson, K. R.; Peng, K.; Wehrman, T.; Park, A.; Mallari, R.; Nebalasca, D.; Young, S. W.; Xiao, S. H., A homogeneous enzyme fragment complementation-based beta-arrestin translocation assay for high-throughput screening of G-protein-coupled receptors. *Journal of Biomolecular Screening* **2008,** *13* (8), 737-47.

41. von Degenfeld, G.; Wehrman, T. S.; Hammer, M. M.; Blau, H. M., A universal technology for monitoring G-protein-coupled receptor activation in vitro and noninvasively in live animals. *Official Publication of the Federation of American Societies for Experimental Biology* **2007,** *21* (14), 3819-26.

42. Yan, Y. X.; Boldt-Houle, D. M.; Tillotson, B. P.; Gee, M. A.; D'Eon, B. J.; Chang, X. J.; Olesen, C. E.; Palmer, M. A., Cell-based high-throughput screening assay system for

monitoring G protein-coupled receptor activation using beta-galactosidase enzyme complementation technology. *Journal of Biomolecular Screening* **2002,** *7* (5), 451-9.



Thank you for your order!

Dear Mr. Raja Muhammad Naseer Khan Khan,

Thank you for placing your order through Copyright Clearance Center's RightsLink® service.

Order Summary

Licensee:	University of Oxford
Order Date:	Nov 24, 2019
Order Number:	4715271327336
Publication:	Cell
Title:	Host Evasion and Exploitation Schemes of Mycobacterium tuberculosis
Type of Use:	reuse in a thesis/dissertation
Order Total:	0.00 GBP

View or print complete details of your order and the publisher's terms and conditions.

Sincerely,

Copyright Clearance Center

Tel: +1-855-239-3415 / +1-978-646-2777
customercare@copyright.com
https://myaccount.copyright.com

Copyright Clearance Center RightsLink®



Thank you for your order!

Dear Mr. Raja Muhammad Naseer Khan Khan,

Thank you for placing your order through Copyright Clearance Center's RightsLink® service.

Order Summary

Licensee:	University of Oxford
Order Date:	Dec 27, 2019
Order Number:	4737101402128
Publication:	Cancer
Title:	PET/CT imaging in cancer: Current applications and future directions
Type of Use:	Dissertation/Thesis
Order Total:	0.00 GBP

View or print complete details of your order and the publisher's terms and conditions.

Sincerely,

Copyright Clearance Center

Tel: +1-855-239-3415 / +1-978-646-2777
customercare@copyright.com
https://myaccount.copyright.com

Copyright Clearance Center RightsLink®

SPRINGER NATURE

Thank you for your order!

Dear Mr. Raja Muhammad Naseer Khan Khan,

Thank you for placing your order through Copyright Clearance Center's RightsLink® service.

Order Summary

Licensee:	University of Oxford
Order Date:	Dec 27, 2019
Order Number:	4737110808608
Publication:	Nature Reviews Cancer
Title:	Molecular imaging of cancer with positron emission tomography
Type of Use:	Thesis/Dissertation
Order Total:	0.00 GBP

View or print complete details of your order and the publisher's terms and conditions.

Sincerely,

Copyright Clearance Center

Tel: +1-855-239-3415 / +1-978-646-2777
customercare@copyright.com
https://myaccount.copyright.com

Copyright Clearance Center RightsLink®

SPRINGER NATURE

Thank you for your order!

Dear Mr. Raja Muhammad Naseer Khan Khan,

Thank you for placing your order through Copyright Clearance Center's RightsLink® service.

Order Summary

Licensee:	University of Oxford
Order Date:	Feb 25, 2020
Order Number:	4775970700057
Publication:	BioMedical Engineering OnLine
Title:	Bright field microscopic cells counting method for BEVS using nonlinear convergence index sliding band filter
Type of Use:	Thesis/Dissertation
Order Total:	0.00 USD

View or print complete details of your order and the publisher's terms and conditions.

Sincerely,

Copyright Clearance Center

Tel: +1-855-239-3415 / +1-978-646-2777
customercare@copyright.com
https://myaccount.copyright.com

Copyright Clearance Center RightsLink®